NUMERICAL INVESTIGATION OF SATURATED POOL BOILING ON THIN WALLS

A thesis submitted for the degree of Doctor of Philosophy by

Antonio Sanna

School of Engineering and Design
Brunel University

Brunel UNIVERSITY WEST LONDON

May 2010

Abstract

Boiling heat transfer provides a means of removing high heat fluxes at low temperature differences in many applications in the power and process industries. A strong interest has been also developed for the cooling of silicon-based devices, such as electronic chips. However, a complete model to describe the processes involved has not been developed as yet.

This PhD project focused on the study of nucleate pool boiling via numerical simulations for a solid plate horizontally immersed in a saturated liquid with a large number of potential nucleation sites. The simulations were developed by a FORTRAN code based on a hybrid approach, combining the 3-dimensional time-dependent solution for the temperature field on the substrate with semi-empirical models for phenomena occurring on the liquid side. The starting point of the project was the modification of a previous version of the code in order to reduce the computational time (in collaboration with Dr. Nelson at Los Alamos National Laboratory) and improve the modelling of the physics of the processes.

One of the key features of the code is the flexibility in adapting to different conditions. In fact the code was used to study bubble growth, site activation frequency and superheat variations, as well as the interactions between nucleation sites. The differences in behaviour between very thin metal foils immersed in water and thicker silicon substrates in FC-72 were studied. The results were compared with experimental results produced at the University of Edinburgh and the University of Ljubljana, both partners of this project.

Both the numerical and physical modifications introduced made it possible to have simulations for a large number of sites, of the order of 100, in reasonable times, of the order of days, so that the code can be now used as a tool for the design of new test sections.

Declaration of Originality

The research presented in this thesis is the original work of the author except where otherwise specified, or where acknowledgements are made by references. This project was carried out at the School of Engineering and Design, Brunel University, under the supervision of Prof. D.B.R. Kenning and Prof. T.G. Karayiannis.

The work has not been submitted for another degree or award to any other institution.

Antonio Sanna

Acknowledgements

The present study was developed in the School of Engineering and Design at Brunel University between 2006 and 2010, financially supported by the government of the United Kingdom through the Engineering and Physical Sciences Research Council (EPSRC) with the grant EP/C532805/1.

First and foremost, I would like to express my most sincere gratitude to my supervisors Prof. David B.R. Kenning and Prof. Tassos G. Karayiannis for their constant and patient invaluable support, mainly during the difficult steps, and for the trust in offering me the opportunity to undertake this PhD. I honestly believe that their encouragement and understanding provided the motivation and the reason to finish. Also sincere thanks to Beatriz Alcala López for her help in preparing documents and dealing with the bureaucracy, as well as for the always supportive words.

I would also like to thank all the collaborators to this project and in particular Dr. Christian Hutter for sharing with me doubts, ideas and spare time during the times he visited London and Dr. Ralph Nelson from Los Alamos National Laboratory for his irreplaceable support for the technical questions regarding the rearrangement of the code. I am also grateful to Prof. Iztok Golobič and Dr. Erik Pavlovič for the very useful discussions about the code and the project and his team at the University of Ljubljana, and in particular Jure Petkovsek, for the warm welcome to the city during my time there.

A special gratitude to my friends here in London, who made this experience unique and unforgettable, who helped me through the difficult times and were always present to listen to my nonsense talks per long hours. Also a special thank to my friends back in Italy, from the present and from the past, for every bit of help that contributed to my success. A special attention to Carola, who taught me words that I believed I could never pronounce in my life.

Last, but not certainly least, I would really like to thank my parents and my siblings who stood, supported and helped me with a kind word or simply a sincere laugh.

Table of contents

ABSTRACT II

DECLARATION OF ORIGINALITY III

ACKNOWLEDGEMENTS IV

TABLE OF CONTENTS V

LIST OF FIGURES IX

LIST OF TABLES XIV

LIST OF EQUATIONS XV

NOMENCLATURE XX

1. INTRODUCTION 1

1.1. Motivation 1

1.2. Outline of the project 3

2. LITERATURE REVIEW: NUCLEATE POOL BOILING 7

2.1. Introduction to boiling heat transfer 8

2.2. Nucleate pool boiling phenomena 10

2.3. Single bubble growth: mechanistic models and experiments 14

2.4. Waiting time, inception and departure of a bubble 25

2.5. Micro-layer theory 31

2.6. Effects of the surface characteristics on the nucleation sites density 37

2.7. Interaction mechanisms 40

2.8. Coalescence 55

2.9. Empirical correlations 59

2.10. Numerical models 65

2.11. Chaos in pool nucleate boiling 77

2.12. Conclusions 80

3. NUMERICAL MODEL 83

3.1. Original version of the code 83

3.1.1. Input data 85

3.1.2. Mesh management 86

3.1.3. Physics of the model 89

3.1.4. Output data 96

3.1.5. Critical analysis and necessity of improvements 97

3.2. New version of the code 98

3.2.1. Numerical improvements 98

3.2.2. Input data 102

3.2.3. Mesh management 103

3.2.4. Improvements to the physical model 109

3.2.5. Output data 117

3.3. Summary 118

4. ANALYSIS OF THE INFLUENCE OF THE INPUT DATA 121

4.1. Introduction 121

4.2. Definition of the base case 121

4.2.1. Experimental facilities 122

4.2.2. Experimental input data for simulations 123

4.2.3. Numerical input data 125

4.2.4. Bubble growth 127

4.2.5. Superheat variations 129

4.2.6. Heat Flux and HTC distributions 132

4.3. Sensitivity analysis 135

4.3.1. Boundary conditions 136
4.3.2. Heat source 137
4.3.3. Activation superheat 138
4.3.4. Shrinking of the contact area 140
4.3.5. Heat transfer at the dome of the bubble 148
4.3.6. Heat transfer evaporation models 150
4.3.7. Standard and unrefined nucleation sites 153
4.3.8. Variation of the thickness of the substrate 156

4.4. Conclusions 158

5. VERIFICATION AND VALIDATION 160

5.1. Introduction 160

5.2. Verification of the code 161
5.2.1. Verification of the conduction model 161
5.2.2. Verification of the mesh refinement process without boiling 166
5.2.3. Verification of the mesh refinement process during boiling 167
5.2.4. Summary of the verification process 168

5.3. Validation of the code 169
5.3.1. Bubble growth analysis 169
5.3.2. Comparison of the base case: bubble growth and superheat variations 174
5.3.3. Long term superheat analysis 175
5.3.4. Validation against experiments on thin metal foils 177

5.4. Summary 190

6. LARGE DISTRIBUTIONS OF SITES 191

6.1. Preliminary analysis 191
6.1.1. Effect of the distance between a pair of sites 191
6.1.2. Effect of the site arrangement 199
6.1.3. Intermediate distribution of nucleation sites 203
6.1.4. Summary of the preliminary analysis 210

6.2. Large distribution of nucleation sites (100) on Silicon immersed in FC-72 211
6.2.1. Nominal values for activation superheat and bubble departure radius values 214
6.2.2. Nominal values for activation superheat and bubble departure radius values 223

6.3. Large distribution of nucleation sites on Titanium immersed in water 237

6.4. Summary 250

7. CONCLUSIONS 252

8. DISCUSSION AND FUTURE WORK 257

8.1. Heat evaporation at the dome of the bubble 257

8.2. Heat transfer model at the base of the bubble 259

8.3. Coalescence 263

8.3.1. Horizontal coalescence 263

8.3.2. Vertical and declining coalescence 264

8.4. Site activation, bubble departure and waiting time 265

8.5. Numerical aspects 266

9. REFERENCES 267

List of figures

Figure 2-1: Boiling curve (Nukiyama, 1934) 9
Figure 2-2: Bubble growth modes (Chester, 1978).....11
Figure 2-3: Schematic bubble growth assuming a truncated sphere shape at different times (t_1, t_2, t_3) ..12
Figure 2-4: Bubble interaction (Zhang and Shoji, 2003).....14
Figure 2-5: Bulk convection and thermal layer formation (Han and Griffith 1965b) 16
Figure 2-6: Bubble growth in a uniformly superheated liquid (a) and in a non-uniform temperature field (b) Mikic et al. (1970).....17
Figure 2-7: Cavity shape (Forest, 1982).....28
Figure 2-8: Different micro-fabricated cavity shapes (Shoji and Takagi, 2001).....29
Figure 2-9: Bubble growth stages (Tong, 1990).....30
Figure 2-10: Necking process and bubble departure (Tong, 1990) 31
Figure 2-11: Bubble growth models for bubble completely surrounded by the thermal boundary layer (a) and growing outside it (b) (Cooper, 1969).....32
Figure 2-12: Hemispherical bubble growth shape (Cooper 1969).....33
Figure 2-13: Micro-layer evaporation for a composite wall (Guo and El-Genk, 1994).....36
Figure 2-14: Site seeding: sequence of events (Calka and Judd, 1985) 42
Figure 2-15: Site interactions (Calka and Judd, 1985).....43
*Figure 2-16: Comparison of site interactions with results from Chekanov (1977) (Calka and Judd, 1985)*43
Figure 2-17: Experimental site interactions from Chopra (1992) and comparison with numercal analysis (Mallozzi et al., 2000).....45
Figure 2-18: Effect of distance on bubble departure frequency (Zhang and Shoji, 2003).....51
Figure 2-19: Variation of the averaged bubble departure frequency with cavity spacing (Shoji, 2005) 52
Figure 2-20: Effect of thermal properties and wall thickness on the averaged bubble departure frequency (Shoji et al., 2005).....54
Figure 2-21: Schematization of bubble coalescence modes: vertical (a), horizontal (b) and declining (c) .56
Figure 2-22: Experimental coalescence modes: vertical (a), horizontal (b) and declining (c) (Zhang and Shoji, 2003).....56
Figure 2-23: Comparison of numerical (a) and experimental (b) vertical coalescence (Dhir, 2006).....58
Figure 2-24: Influence area (Mikic and Rohsenow, 1969) 62
Figure 2-25: Heat transfer coefficient areas (Golobič et al., 1996).....68
Figure 2-26: Micro- and macro-regions (Stephan and Hammer, 1994) 70
Figure 2-27: Micro-region (Stephan and Hammer, 1994) 71
Figure 2-28: Phase maps (Shoji and Takagi, 2001) 78

Figure 2-29: Long time memory and average time interval of bubble growth dependence on dimensionless distance (Mosdorf and Shoji, 2004) *80*
Figure 3-1: Logic of the code *84*
Figure 3-2: Mesh distribution for cells with triangular base – irregular distribution *87*
Figure 3-3: Mesh distribution for cells with square base – regular distribution *88*
Figure 3-4: Minimum distance between active sites *89*
Figure 3-5: Geometry of a cell *90*
Figure 3-6: Geometry of the substrate (Golobič et al., 2004) *91*
Figure 3-7: Heat transfer coefficients distribution around a growing bubble (original model OR) *93*
Figure 3-8: Advancing triple contact line *95*
Figure 3-9: Temperature surface distribution *97*
Figure 3-10: Refinement methods *104*
Figure 3-11: Numerical inhibitory effect *105*
Figure 3-12: Alternate effect with no intermediate mesh refinement *106*
Figure 3-13: Reduction of the alternate bubble growth effect using the intermediate mesh refinement *107*
Figure 3-14: Simulation of the triple contact line area: *109*
Figure 3-15: Heat transfer coefficients models: a) Micro-layer model (ML); b) Contact-Line model (CL). *112*
Figure 3-16: Coalescence models *116*
Figure 3-17: Bubble growth parameters *118*
Figure 4-1: Arrangement of the micro-fabricated cavities for the second generation (left) and third generation (right) test sections *122*
Figure 4-2: Experimental setup *123*
Figure 4-3: Base case: bubble growth and superheat simulation results *128*
Figure 4-4: Base case: Superheat distribution along a line *130*
Figure 4-5: Base case: 2-dimensional superheat distribution *132*
Figure 4-6: Base case: Instantaneous heat flux (a) and HTC (b) along a line *133*
Figure 4-7: Scaled and theoretical contact line regions *134*
Figure 4-8: Base case: Heat flux and HTC 2-dimensional distribution *134*
Figure 4-9: Effect of the variation of the boundary conditions on superheat distribution along a line on the top and bottom of the substrate *136*
Figure 4-10: Effect of the variation of heat sources on superheat distribution along a line on the top and bottom of the substrate *137*
Figure 4-11: Effect of activation superheat on bubble growth and superheat *139*
Figure 4-12: Effect of the activation superheat and cavity radius on $HTC_{cl,scal}$ *and Heat Flux* *140*
Figure 4-13: Effect of the contact angle decrease modes on bubble growth and superheat *142*
Figure 4-14: Effects of the angle decrease fraction on bubble growth and superheat *144*
Figure 4-15: Effect of contact angle decrease fraction on $HTC_{cl,scal}$ *and Heat Flux* *145*

Figure 4-16: Effect of the initial value of the apparent contact angle variation for angle decrease fraction equal to 0.6 (left) and 0.9 (right) *146*
Figure 4-17: Effects of the initial apparent contact angle variation on $HTC_{cl,scal}$ *and Heat Flux*..... *148*
Figure 4-18: Effect of dome heat contribution factor on superheat and bubble growth *149*
Figure 4-19: Effect of the dome heat contribution factor and angle decrease fraction on $HTC_{cl,scaled}$ *and Heat flux*..... *150*
Figure 4-20: Superheat and HTC distributions along a line in the region around the nucleation site for micro-layer (ML) and contact line (CL) models *151*
Figure 4-21: Effects of the heat transfer evaporation models at the base of the bubble for..... *152*
Figure 4-22: Mesh distribution and contact line area for standard (a) and unrefined (b) sites..... *153*
Figure 4-23: Superheat distribution along a line for standard and unrefined sites..... *154*
Figure 4-24: Bubble growth and superheat variation for standard and unrefined sites *155*
Figure 4-25: Effects of the mesh size on $HTC_{cl,scaled}$ *and heat flux* *156*
Figure 4-26: Effect of the substrate thickness on superheat variations *157*
Figure 5-1: Comparison of theoretical and simulation (FORTRAN) results for the superheat temporal variation in the case of volumetric source..... *164*
Figure 5-2: Comparison of theoretical and simulation (FORTRAN) results for the superheat temporal variation in the case of heat flux applied to the back *165*
Figure 5-3: Comparison of the heat source effect along a line passing through the centre of the substrate *166*
Figure 5-4: Effect of n_R *on the* $HTC_{cl,scal}$ *and Heat Flux*..... *168*
Figure 5-5: Effect of the number of intermediate refinements steps *168*
Figure 5-6: Experimental bubble growths *171*
Figure 5-7: Comparison of experimental and simulated dimensionless bubble growths. a) $f_{decr} = 0.6$*; b)* $f_{decr} = 0.9$..... *172*
Figure 5-8: $HTC_{cl,scal}$ *and Heat Flux derived from simulations for the validations cases* *174*
Figure 5-9: Validation for the base case..... *175*
Figure 5-10: Long term superheat variations *176*
Figure 5-11: Dimensionless HTC_{max} *versus dimensionless time*..... *179*
Figure 5-12: Comparison between experimental (Golobič et al., 2006) and simulation results for bubble and contact radii, superheat and HTC_{max} *180*
Figure 5-13: Comparison of experimental (Golobič et al., 2006) and simulation results for a bubble growing on a thin metal foil..... *182*
Figure 5-14: Superheat distribution along a line. Comparison of experimental and simulations for Titanium (25 µm)..... *183*
Figure 5-15: HTC distribution along a line passing through the nucleation site for Titanium (25 µm)..... *184*
Figure 5-16: Heat flux distribution along a line passing through the nucleation site for Titanium (25 µm) *184*

Figure 5-17: Comparison between experimental (Golobič et al., 2009) and simulation results for bubble and contact radii, superheat and HTC_{max} for platinum (6 µm) 186
Figure 5-18: Superheat distribution along a line. Comparison of experimental and simulations for Platinum (6 µm) 187
Figure 5-19: HTC distribution along a line passing through the nucleation site for Platinum (6 µm) 189
Figure 5-20: Heat flux Heat flux distribution along a line passing through the nucleation site for Titanium (25 µm) 189
Figure 6-1: Arrangements of a pair of inline sites 192
Figure 6-2: Superheat variations for large distance between interacting sites 193
Figure 6-3: Superheat distribution along a line at two different time steps for variable (large) site distance 194
Figure 6-4: Superheat variations for close interacting sites 196
Figure 6-5: Effect of coalescence on superheat distribution along a line passing through the centres of the nucleation sites. a) C1: similar radii (S = 0.495 mm); b) C2: different radii 197
Figure 6-6: Site arrangements: inline (left); triangular (centre); square (right) 199
Figure 6-7: Effect of site arrangement on superheat in the midpoint between two adjacent sites 200
Figure 6-8: Bubble growth for S = 0.330 mm for triangular and square arrangements 202
Figure 6-9: Site distribution: a) triangular; b) square 204
Figure 6-10: Superheat distribution along a line for square and triangular arrangements of the sites 205
Figure 6-11: 2-dimensional superheat distributions for a large distribution of nucleation sites for triangular and square arrangements 206
Figure 6-12: Comparison of standard and unrefined sites for a large distribution of nucleation sites. a) whole simulations; b) last stage of simulations 208
Figure 6-13: Superheat distribution along a line for a large distribution of standard and unrefined sites 209
Figure 6-14: Site distribution for Silicon immersed in FC-72 with distance between sites 0.4 mm 213
Figure 6-15: Superheat variation at the nucleation site and bubble growth histories for the nucleation sites #1, #32, #79 and #100 215
Figure 6-16: 2-dimensional superheat distribution at t = 2.278 s 216
Figure 6-17: Superheat distribution along a line passing through the centre of the plate when the uncertainties parameters are not used 217
Figure 6-18: Bubble distribution at the standard sites at different time steps when the uncertainty parameters are not used 218
Figure 6-19: Activity of the nucleation sites over the whole simulated time 220
Figure 6-20: Average growth time and waiting time per each nucleation site 221
Figure 6-21: Occurrence of coalescence type C1 222
Figure 6-22: Superheat variation at the nucleation site and bubble growth histories for the nucleation sites #1, #32, #79 and #100. Uncertainties = 10% 224

Figure 6-23: Waiting time, growth time and period for the refined sites in case of uncertainty parameters equal to 10%.....225
Figure 6-24: Bubble distribution at the standard sites at different time steps when the uncertainty parameters are equal to 10%.....226
Figure 6-25: Superheat distribution along a line passing trough the centre of the plate.....227
Figure 6-26: 2-dimensional superheat distribution with uncertainty parameters equal to 10% 228
Figure 6-27: Activity of the nucleation sites for all the bubbles and only the large bubbles for the case with uncertainty parameter equal to 10% 230
Figure 6-28: Average activity of the nucleation sites during the quasi-steady state when using the uncertainty parameters equal to 10%. a) Total activity. b) Large bubble activity 230
Figure 6-29: Occurrence of coalescence type C1 (a, c) and C2 (b, d).....232
Figure 6-30: Bubble growth histories and superheat variations at Site #1 and the surrounding adjacent sites (#2, #4., #6, #8).....235
Figure 6-31: Bubble growth and superheat distribution along the line passing through the nucleation sites #2, #1 and #6.....236
Figure 6-32: Site distribution for titanium immersed in water with distance between sites 3.23 mm.....239
Figure 6-33: Superheat variation at the nucleation site and bubble growth histories for the nucleation sites #1, #32, #79 and #100 on titanium. Uncertainty parameters = 0% 240
Figure 6-34: Waiting time, growth time and period for the case with titanium and uncertainty parameters equal to 0.....242
Figure 6-35: Bubble distribution at the standard sites on titanium at different time steps when the uncertainty parameters are equal to 0 244
Figure 6-36: Superheat colour map and bubble and contact area radii.....245
Figure 6-37: Superheat distribution along a line passing trough the centre of the plate.....246
Figure 6-38: 2-dimensional superheat distribution.....247
Figure 6-39: Total activity of the nucleation sites: a) spatial distribution; b) depending on the nucleation site identification number 248
Figure 6-40: Bubble growth histories involving coalescence and superheat variations at Site #1 and the surrounding adjacent sites (#2, #4., #6, #8) 250
Figure 8-1: Bubble growth inside (a) and outside (b) the thermal layer (Son et al., 2008).....258
Figure 8-2: Contact line (a) and micro-layer (b) model schematics.....260
Figure 8-3: Sliding bubble.....261
Figure 8-4: Vertical coalescence, schematic representation (Hutter, 2009).....264

List of tables

Table 1: Experimental conditions and results 124
Table 2: Physical properties used as input data for simulations 125
Table 3: Simulations data 126
Table 4: Base case physical input data 127
Table 5: Activation temperatures 138
Table 6: Apparent contact angle decrease fraction values 143
Table 7: Apparent contact angle values 145
Table 8: Numerical input data for FORTRAN simulations 161
Table 9: Physical properties used as input data for FORTRAN simulations 162
Table 10: ΔT_{trans} for FORTRAN simulations 163
Table 11: Summary of experimental results 171
Table 12: Input data for thin metal foil validation (Golobič et al., 2006) 178
Table 13: Bubble growth data and superheat values at the nucleation site (Golobič et al., 2006) 178
Table 14: Input data for thin metal foil validation (Golobič et al., 2009) 185
Table 15: Bubble growth data and superheat values at the nucleation site (Golobič et al., 2009) 186
Table 16: Values of the inter-distance between large-spaced sites 192
Table 17: Superheat variations at variable distance 193
Table 18: Values of the inter-distance between close-spaced sites 196
Table 19: Values of the inter-distance between sites for square and triangular distributions 200
Table 20: Input data for a large distribution of sites for Silicon 212
Table 21: Coalescence type C1 frequencies for site #1 to #10 233
Table 22: Coalescence type C2 frequencies for site #1 to #10 234
Table 23: Input data for a large distribution of sites for titanium in water 238
Table 24: Coalescence type C1 frequencies for site #1 to #10 249
Table 25: Coalescence type C2 frequencies for site #1 to #10 249

List of equations

$$\rho_L\left[r\frac{d^2r}{dt^2}+\frac{3}{2}\dot{r}^2\right]=\Delta p-\frac{2\sigma}{r} \quad (2.1) \ldots 15$$

$$\Delta p=\frac{H_{fg}}{T\left(\dot{V}_V-\dot{V}_L\right)}\left(T_{bulk}-T_{sat}\right) \quad (2.2) \ldots 15$$

$$r^*+\log\frac{r^*-1}{r_1^*-1}=C\cdot t^{1/2} \quad (2.3) \ldots 15$$

$$\frac{1}{x_r{}^2}\frac{\partial}{\partial x_r}\left(x_r{}^2u_L\right)=0 \quad (2.4) \ldots 17$$

$$u_L=\frac{dr}{dx_r}\left(\frac{R}{x_r}\right)^2 \quad (2.5) \ldots 17$$

$$\frac{dR^*}{dt^*}=\left(t^*+1\right)^{1/2}-\left(t^*\right)^{1/2} \quad (2.6) \ldots 18$$

$$R^*=t^* \quad , \quad t^*<<1 \quad (2.7) \ldots 18$$

$$R^*=\sqrt{t^*} \quad , \quad t^*>>1 \quad (2.8) \ldots 18$$

$$\frac{dR^*}{dt^*}=\left[t^*+1+\theta\left(\frac{t^*}{t^*+t^*_{wait}}\right)^{1/2}\right]^{1/2}-\left(t^*\right)^{1/2} \quad (2.9) \ldots 19$$

$$\left(\frac{dR}{dt}\right)_{inertial}=\left[\frac{2}{3}\frac{p(T_\infty)-p(T_{bulk})}{\rho_L}\right]^{1/2} \quad (2.10) \ldots 20$$

$$\left(\frac{dR}{dt}\right)_{thermal}=\left(\frac{3}{\pi}\right)^{1/2}\frac{k_L}{H_{fg}\cdot\rho_V(T_{bulk})}\frac{T_\infty-T_{bulk}}{(\alpha_L t)^{1/2}} \quad (2.11) \ldots 20$$

$$R(t)=\frac{R_1(t)R_2(t)}{R_1(t)+R_2(t)} \quad (2.12) \ldots 22$$

$$R_{cav,\min/\max}=\frac{\delta(T_w-T_{sat})}{3(T_w-T_\infty)}\left[1\pm\sqrt{\left(1-\frac{12(T_w-T_\infty)T_{sat}\sigma}{\delta\rho_v H_{fg}(T_w-T_{sat})^2}\right)}\right] \quad (2.13) \ldots 26$$

$$T_{bulk}=T_{sat}+\frac{2\sigma T_{sat}}{H_{fg}\rho_V r_n} \quad (2.14) \ldots 26$$

$r_n = \frac{r_{cav}}{\sin\varphi}$ (2.15) 26

$R = 2.5\frac{Ja}{\mathrm{Pr}_L}\sqrt{\nu_L t}$ (2.16) 32

$R = 1.12\sqrt{\frac{k_W \rho_W c_{pW}}{k_L \rho_L c_L}} Ja\sqrt{\alpha_W t}$ (2.17) 33

$\delta_0 = C\sqrt{\nu \cdot t_g}$ (2.18) 34

$\dot{q}_{tot} = \frac{\dot{q}_{ML} t_g + \dot{q}_{\mathrm{Re}st} t_{wait}}{t_g + t_{wait}} + \dot{q}_{NC}$ (2.19) 34

$N = C_1 r_{cav}^m \left(\frac{H_{fg}\rho_V}{2T_{sat}\sigma}\right)^m (\Delta T)^m$ (2.20) 37

$\Gamma(Na) = \frac{e^{-\overline{Na}}(\overline{Na})Na}{(Na)!}$ (2.21) 38

$\frac{n}{A} = 218.8\theta_{\mathrm{rough}} - 0.4\,\mathrm{Pr}^{1.63}\frac{1}{\gamma}\Delta T^3$ (2.22) 39

$q_{boiling} = q_{total\_boiling} - \left(q_{NC} - q_{\exp erimental\_NC}\right)$ (2.23) 57

$Nu = f(\mathrm{Re}, \mathrm{Pr})$ (2.24) 59

$Nu = C \cdot \mathrm{Re}^m\,\mathrm{Pr}^{m_1}$ (2.25) 59

$\frac{c_L(T_w - T_{sat})}{H_{fg}} = C_{sf}\left[\frac{\dot{q}}{\mu_L H_{fg}}\sqrt{\frac{\sigma}{g(\rho_L - \rho_V)}}\right]^{0.33}\left(\frac{c_L\mu_L}{k_L}\right)^{1.7}$ (2.26) 59

$Nu_b = 0.0015\mathrm{Re}_b^{0.62}\cdot\mathrm{Pr}^{0.33}$ (2.27) 60

$$\frac{\dot{q}c_L\rho_L\sqrt{\pi\alpha_L}}{k_L H_{fg}\rho_V}\left(\frac{2\sigma}{\Delta p}\right)^{1/2}\left(\frac{\rho_L}{\Delta p}\right)^{1/4} = 0.0015\cdot\left[\frac{\rho_L}{\mu_L}\left(\frac{c_L\cdot\rho_L\cdot\Delta T\sqrt{\pi\alpha_L}}{H_{fg}\rho_V}\right)^2\right]^{0.62}\left(\frac{c_L\mu_L}{k_L}\right)^{0.33}$$ (2.28) 60

$Nu_b = \frac{\dot{q}\cdot R}{k_L\cdot\Delta T}$ (2.29) 60

$R = \frac{\Delta T\cdot c\rho_L\sqrt{\pi\alpha_L}}{H_{fg}\rho_V}\left(\frac{2\sigma}{\Delta p}\right)^{1/2}\left(\frac{\rho_L}{\Delta p}\right)^{1/4}$ (2.30) 60

$\dot{q} = C_I\frac{k_L}{2\sigma}\Delta p\Delta T\left(\frac{\rho_L}{\mu_L}B^2\right)^{1/4}\left(\frac{\mu\cdot c_L}{k_L}\right)^{1/3}$ (2.31) 61

$$\dot{q} = C\frac{\alpha\rho_L c_L T_{sat}}{H_{fg}\rho_V\sigma^{1/2}}\left(\frac{c_L T_{sat}\alpha^{1/2}}{\left(H_{fg}\rho_V\right)^2}\right)^{1/4}\left(\frac{\rho_L}{\mu_L}\right)^{5/8}\left(\frac{\mu_L\cdot c_L}{k_L}\right)^{1/3}\Delta p^2 \quad (2.32)$$ 61

$$\dot{q} = \frac{k_L c_L \rho_L^2}{\sigma\cdot T_{sat}\left(\rho_L-\rho_V\right)}\frac{\left(1-\chi\right)}{B_L}\left(T_w - T_{sat}\right)^3 \quad (2.33)$$ 61

$$\dot{q} = \pi D_b^2 n\cdot\dot{q}_b = \pi D_b^2 n\cdot 2\frac{k\Delta T}{\sqrt{\pi\alpha}}\sqrt{f} \quad (2.34)$$ 63

$$\dot{q}_b = B_1\left(c\cdot\Delta T\right)^{m+1}\frac{H_{fg}\mu_L}{\sqrt{\frac{\sigma}{g\left(\rho_L-\rho_V\right)}}} \quad (2.35)$$ 63

$$\frac{\dot{q}D_b}{\Delta T\cdot k_L} = 0.23\left(\frac{\dot{q}D_b}{k_L T_{sat}}\right)^{0.674}\left(\frac{\rho_V}{\rho_L}\right)^{0.297}\left(\frac{H_{fg}D_b^2}{\alpha_L^2}\right)^{0.371}\left(\frac{\rho_L-\rho_V}{\rho_L}\right)^{-1.73}\left(\frac{\alpha_L^2\rho_L}{\sigma D_b}\right)^{0.35} \quad (2.36)$$ 64

$$\frac{h}{\left(\dot{q}\right)^m} = p_r^A\cdot T_r^B\left(1-T_r\right)^C C_E \quad (2.37)$$ 64

$$\frac{h}{\left(\dot{q}\right)^m} = p_r^A\cdot\left(-\log_{10}p_r\right)^D C_E \quad (2.38)$$ 64

$$\frac{h}{\left(\dot{q}\right)^{0.67}} = 55 p_r^{0.12-0.2\log_{10}R_p}\cdot\left(-\log_{10}p_r\right)^{-0.55}M^{-0.5} \quad (2.39)$$ 65

$$\frac{\partial T}{\partial t} = \frac{k_H}{\rho_H c_H}\left[\frac{\partial^2 T}{\partial x_r^{\,2}} + \frac{1}{x_r}\frac{\partial T}{\partial x_r} + \frac{\partial^2 T}{\partial z^2}\right] + \xi\frac{Q_{vol}}{\rho c_H} \quad (2.40)$$ 68

$$S > 1.2\left(r_{mi} + r_{mj}\right) + 1.0 w_{xy} \quad (3.1)$$ 87

$$\frac{\partial T}{\partial t} = \frac{k_H}{\rho_H c_H}\left(\frac{\partial^2 T}{\partial x^2} + \frac{\partial^2 T}{\partial y^2} + \frac{\partial^2 T}{\partial z^2}\right) + \frac{Q_{vol}}{\rho_H c_H} \quad (3.2)$$ 90

$$T(\bar{t}+\Delta t; k, z) = T(\bar{t}; k, z) + \frac{Q\Delta t}{A_{v,i}\Delta z\rho_H c_H} \quad (3.3)$$ 90

$$Q = \dot{q}A_{v,k}\Delta z + A_{v,k}\frac{k_H}{\Delta z}\left[T\left(\bar{t}; k, z-1\right) - 2T\left(\bar{t}; k, z\right) + T\left(\bar{t}; k, z+1\right)\right] + \\ + \sum_j A_{h,k-j}\frac{k_H\Delta z}{S_{k,j}}\left[T\left(\bar{t}; k, z\right) - T\left(\bar{t}; j, z\right)\right] \quad (3.4)$$ 91

$$T\left|_{x=0, x=x_{ca}, y=o, y=y_{ca}; 0\le z\le\delta_H}\right. = T_{sat} \quad (3.5)$$ 91

$$\left.\frac{\partial T}{\partial z}\right|_{0\le x\le x_{ca}, 0\le y\le y_{ca}, z=0} = \alpha_{air}\left(T - T_{air}\right) \quad (3.6)$$ 92

$$HTC_{NC} = f_{enh} \cdot 0.14 \rho_L c_L \left[\frac{\gamma_{vol} g}{\upsilon_L} \left(\frac{k_L}{\rho_L c_{pL}} \right)^2 (T - T_{sat}) \right] \quad (3.7) \quad \text{...92}$$

$$HTC_{CL} = \frac{k_L}{\delta_{ML}} \quad (3.8) \quad \text{...93}$$

$$T(t, \bar{k}, z_{\delta_H}) \geq T_{act,i} \quad (3.9) \quad \text{...94}$$

$$r_{be,i}(t) \geq r_{bd,i} \quad (3.10) \quad \text{...94}$$

$$Q_{b,i}(\bar{t} + \Delta t) = Q_{b,i}(\bar{t}) + \sum_{\substack{(x_j, y_j) \in \\ \text{inner area}}} A_{v,j} HTC_{in,j} \left[T(\bar{t}; j, \delta_H) - T_{sat} \right] \Delta t + \\ + \sum_{\substack{(x_j, y_j) \in \\ \text{triple cont area}}} A_{v,j} HTC_{CL,j} \left[T(\bar{t}; j, \delta_H) - T_{sat} \right] \Delta t \quad (3.11) \quad \text{...95}$$

$$r_{eq,i}(\bar{t} + \Delta t) = \sqrt[3]{\frac{3 Q_{b,i}(\bar{t} + \Delta t)}{4 \pi \rho_L H_{fg}}} \quad (3.12) \quad \text{...95}$$

$$\Delta t < 0.3 \min\left\{ A_{v,\min}, \Delta z^2 \right\} \frac{k_H}{\rho_H c_H} \quad (3.13) \quad \text{...101}$$

$$\begin{cases} \Delta p = 2\sigma / r_{cav} & \text{(a)} \\ \log_{10} p(Pa) = 9.729 - 1562 / T(K) & \text{(b)} \end{cases} \quad (3.14) \quad \text{...110}$$

$$HTC_{NC}(t; k) = f_{enh} \cdot 314 \cdot \left[T(t; k, z) - T_{sat} \right]^{0.2} \quad (3.15) \quad \text{...111}$$

$$Q_{D,i} = f_D \left[4\pi r_{b,i}^2 f_{S,i}(t) \right] \cdot \left[k_l \frac{(T_{eff,i} - T_{sat})}{\sqrt{\pi \alpha_L (t - t_{act,i})}} \right] \Delta t \quad (3.16) \quad \text{...113}$$

$$T_{eff,i} = \frac{T_{act,i} + T_{sat}}{2} \quad (3.17) \quad \text{...113}$$

$$\varphi_i(t - t_{act,i}) = \begin{cases} \varphi_0 & \text{if} \quad r_{b,i}(t - t_{act}) < f_{\varphi,decr} r_{bd,i} \\ \varphi_0 [1 - u_{\varphi 0,i}(t - t_{act,i})] & \text{if} \quad r_{b,i}(t - t_{act}) > f_{\varphi,decr} r_{bd,i} \end{cases} \quad (3.18) \quad \text{...113}$$

$$\varphi_i(t - t_{act}) = \begin{cases} \varphi_0 & \text{if} \quad r_{b,i}(t - t_{act}) < f_{\varphi,decr} r_{bd,i} \\ \varphi_0 \dfrac{1}{1 - f_{\varphi,decr}} \left[1 - \dfrac{r_{b,i}(t - t_{act})}{r_{bd,i}} \right] & \text{if} \quad r_{b,i}(t - t_{act}) > f_{\varphi,decr} r_{bd,i} \end{cases} \quad (3.19) \quad \text{...114}$$

$$\varphi_i(t - t_{act}) = \begin{cases} \varphi_0 & \text{if} \quad r_{b,i}(t - t_{act}) < f_{\varphi,decr} r_{bd,i} \\ \varphi_0 \dfrac{1}{1 - f_{\varphi,decr}^3} \left[1 - \dfrac{r_{b,i}^3 (t - t_{act})}{r_{bd,i}^3} \right] & \text{if} \quad r_{b,i}(t - t_{act}) > f_{\varphi,decr} r_{bd,i} \end{cases} \quad (3.20) \quad \text{...114}$$

$$r_{bd,1}(t_{AC}) = 1.005\left[1+\frac{V_2(t_{BC})}{V_{bd,1}}\right]^{1/3} r_{bd,1}(t_{BC}) \quad (3.21) \ldots 116$$

$$\rho_H \delta_H c_H dT = Q_{vol}\delta_H dt - HTC(T - T_{sat})dt \quad (5.1) \ldots 163$$

$$T - T_{sat} = \frac{q''}{HTC} - \frac{q'' - HTC(T_0 - T_f)}{HTC}\exp\left(-\frac{HTC}{\rho_H c_H \delta_H}t\right) \quad (5.2) \ldots 163$$

$$q'' = 1.16 \cdot HTC(T - T_{sat}) \quad (5.3) \ldots 164$$

$$\dot{q} = -k_H \frac{dT}{dz} \quad \Rightarrow \quad \Delta T = -\frac{\dot{q}\Delta z}{k_H} \sim -0.015476K \quad (5.4) \ldots 165$$

Nomenclature

a	[m^2]	Area
A	[m/s]	Coefficient
A_1	[-]	Coefficient
A_h, A_v	[m^2]	Cell surface areas
b, B_1, B', B_L	[-]	Coefficient
B	[$m/s^{1/2}$]	Coefficient
c	[J/(kg·K)]	Specific heat
c_s	[m/s]	Propagation speed of thermal disturbances
C, C_1, C_{sf}, C_E	[-]	Coefficient
C_f	[-]	Correlation coefficient
CHF	[W/m^2]	Critical Heat Flux
D	[-]	Coefficient
D_b	[m]	Bubble departure diameter
f	[Hz]	Frequency
f_D	[-]	Dome contribution factor
f_{decr}	[-]	Apparent contact angle decrease factor
f_{enh}	[-]	Enhancing factor for natural convection Heat transfer
$f_{enh,turb}$	[-]	Enhancing factor for turbulent heat transfer Outside the contact area
f_S	[-]	Shape factor
g	[m/s^2]	Gravity acceleration
h, HTC	[$W/(m^2 \cdot K)$]	Heat transfer coefficient
H_{fg}	[J/kg]	Latent heat of evaporation
k	[W/(m·K)]	Thermal conductivity
K	[-]	Influence area coefficient
K_{bubble}	[-]	Bubble curvature
$Ja = \frac{\rho_L c_L \Delta T}{\rho_V H_{fg}}$	[-]	Jakob number

L	[-]	Lyapunov exponent
m, m_1	[-]	Constant
M	[-]	Molecular weight
n	[-]	Number of site
N	[1/m^2]	Number of sites per unit area
n_{cR}	[-]	Number of cells in the first ring
n_R	[-]	Number of rings that constitute the refined area
$n_{R,incr}$,	[-]	Number of incremental cells per ring
n_{vL}	[-]	Number of vertical layers
P	[Pa]	Pressure
$\dot{q}$	[W/m^2]	Heat flux
Q	[J]	Heat contributions
Q_{vol}	[W/m^3]	Volumetric heat source
r, R	[m]	Bubble radius
r_0	[m]	Critical radius
r_i, r_s, r_{infl}, r_h	[m]	Heat transfer coefficient area radii
R_p,	[m]	Roughness
S	[m]	Distance
t	[s]	Time
T	[K]	Temperature
T_{eff}	[K]	Effective temperature
u	[m/s]	Velocity
V	[m^3]	Volume
$\dot{V}$	[m^3/kg]	Specific volume
x, y, z	[m]	Cartesian coordinates
x_r	[m]	Radial coordinate
w_{xy},	[m]	Mesh width

Greek symbols

α	[m^2/s]	Thermal diffusivity
β	[-]	Contact angle

γ	[-]	Surface-liquid interaction parameter
γ_{vol}	[1/K]	Volumetric thermal expansion coefficient
Γ	[-]	Probability function
δ	[m]	Thickness
Δp	[Pa]	Pressure drop
Δt	[s]	Time step
ΔT	[K]	Superheat
Δz	[m]	Thickness of the layer
θ	[-]	Subcooling factor
θ_{le}	[m]	Contact line width
θ_{rough}	[-]	Roughness parameter
κ	[-]	Liquid-to-solid thermal conductivity ratio
μ_L	[-]	Liquid viscosity
v	[-]	Shape parameter
v_L	[m^2/s]	Liquid kinematic viscosity
ξ	[-]	Heat source parameter
ρ	[kg/m^3]	Density
σ	[Pa·m]	Surface tension
φ, ϕ	[-]	Contact angle
χ	[-]	Void fraction

Subscripts

AC	After coalescence
act	Activation
adv	Advancing
air	Air
base	Base of the bubble
BC	Before coalescence
b	Bubble
bd	Bubble departure
bottom	Bottom

bulk	Liquid bulk characteristics
c	Contact area
c1, *c2*	Coalescence events
cav	Cavity
CL	Contact line
d	Departure
D, dome	Dome of the bubble
dry	Dry area
dyn	Dynamic
e	Evaporation
eq	Equivalent
f	Micro-layer film
g	Growth
H	Heater substrate
i, *j*, *k*	Generic site
in	Initial value
infl	Influence
L	Liquid
lat	Lateral
le	Contact line
m	Mesh
max	Maximum
min	Minimum
ML	Micro-layer
n	Nucleus
NC	Natural convection
NS	Nucleation site
OR	Original version of the code
r	Reduced value
rec	Receding
Rest	Restored conditions
sat	Saturation
scal	Scaled
SEN	Sensor

sim	Simulated
stat	Static
top	Top
tot	Total
trans	Transient time
W	Wall
wait	Waiting period
V	Vapour
Vol	Volume
0	Initial value
φ	Contact angle
∞	Bulk value

Superscripts

*	Dimensionless value

1. Introduction

1.1.Motivation

Boiling heat transfer provides a means of removing high heat fluxes at low temperature differences in many applications in the power and process industries. A strong interest has also been developed for the cooling of silicon-based devices, such as electronic chips. However, several potential difficulties are encountered when investigating the phenomena involved in cooling by boiling, such as non-linearity of the processes, non-uniformity of the characteristics of the materials (substrates and liquids, which may lead to non-regularities in the distribution of the temperature across the substrate or of the active nucleation sites) and hysteresis (which is connected to particular conditions of excess temperatures in activating the boiling process much larger than theoretically expected). Because of the complexity and the large range of variation in the parameters involved (for instance from micro-scale for the dimensions of the nucleus of a bubble or the scale of particular phenomena during the bubble growth to millimetres for the size of the departing bubble) boiling heat transfer has not been completely understood so far, and many key questions remain open to discussion despite the numerous efforts carried out in the last decades. Recently, the continuously increasing computational power and the ever more accurate and precise experimental devices greatly helped in shedding some light, but the higher the level of details achieved, the more complicate the phenomena appear, so that some authors have also questioned the sheer possibility of completely understanding or modelling the process.

Boiling may be employed in a wide range of applications such as forced flow through micro-channels or by immersing flat surfaces in a pool of liquid with no imposed liquid flows. The international research community is investigating several aspects of the phenomena from different points of view. This study will concentrate on nucleate pool boiling at atmospheric pressure and saturation conditions, constituting only a limited area of boiling phenomena. Dhir (2006) reviewed the approaches used in the past years to address the problem of a single bubble growing under pool boiling conditions, and identified two possible approaches: the first one was based on empirical or mechanism-based correlations, while a possible alternative was found in the use of

mechanistic numerical models, aiming at reproducing the bubble growth via simulations of the involved processes. A dedicated model was also suggested, constituting one of the first complete approaches to numerically predict the nucleate boiling heat transfer on the base of bubble dynamics and heat transfer mechanisms. However, the suggested solution assumed a constant surface temperature on the substrate, which led to a thermally decoupled plate. A similar model was also developed by the group led by Stephan (compare for instance Stephan et al., 2006) but considering a transient temperature in the wall, although limited to the study of an isolated bubble. This PhD project instead aims to study pool boiling phenomena via numerical simulations for a solid plate horizontally immersed in a liquid at saturation conditions with focus on interactions between a large number of potential nucleation sites (of the order of 100 nucleation sites), able to produce results in reasonable time (of the order of days). The code could then be used as a tool to design test sections able to maximize the heat transfer and reduce the average superheat, by varying the array of closely-spaced nucleation sites of specified micro-geometry. In order to achieve that, the numerical model cannot completely describe both the liquid and the solid sides, because the computational power for the aimed number of sites would exceed the current capabilities. To obtain a solution for this large number of nucleation sites, the current approach combines empirical models with the complete solution of the temperature field in the solid substrate (hybrid code). The fluid side will not be solved and used instead as a boundary condition for the substrate continuously varying with time and space, apart otherwise for the presence of the growing bubbles (the shapes and sizes of which change with time) when sites become active. The original idea of this approach was developed at Los Alamos National Laboratory (LANL) as described by Pasamehmetoglu and Nelson (1991), and subsequently modified at the University of Ljubljana, as described in Golobič et al., (2004). The code was then acquired by Brunel University and then modified in a joint project in collaboration with the Universities of Edinburgh and Ljubljana and LANL. In particular, Dr R. Nelson at LANL provided an essential contribution to the rearrangement of the syntax of the model in order to make it suitable for parallel computations, while the teams at the Universities of Edinburgh and Ljubljana provided experimental insights and results used for the improvement of the physical model and for the validation process. The code is now based on the FORTRAN language and solves the temperature 3-dimensional space and time equation for a solid plate which is horizontally immersed in a liquid at saturation conditions. Pool

nucleate boiling occurs at fixed locations called nucleation sites that simulate artificial cavities on the top surface if the activation conditions (based on a simple superheat criterion) are satisfied. The superheat is determined by a heat source applied to the substrate, either volumetric or superficial on the back. The bubbles then grow until departure (which is determined by conditions on their maximum size). The bubble dimensions, and in particular the dimensions of the contact area, will be used to specify the heat transfer coefficients between the liquid and the solid on the upper surface. One of the key points of the numerical model is related to the mesh refinement approach, which locally modifies the mesh distribution only in the areas involved in the boiling process, i.e. around active nucleation sites, and only during its activation. Moreover, the code is flexible and adaptable to different conditions and situations, such as the use of different substrate materials and fluids (the code has been successfully used for simulations of stainless, titanium and platinum foils immersed in water as well as silicon wafers in FC-72, by simply modifying the heat transfer coefficient correlations obtained through theoretical or experimental analyses). The position of the potential nucleation sites is also an input datum for each simulation, together with the bubble growth characteristics (for instance the departure radius and shape) and can be easily modified. Another advantage of the model is the possibility to introduce sub-models (simplified in order not to excessively slow down the simulations) to take into account any particular phenomena considered important. Following this approach, several sub-models have been recently introduced to improve the physics of the processes related to the bubble growth (including modification of the bubble size during the growth, heat transfer contribution at the dome of the bubble contact area and a crude model for coalescence). Further efforts are necessary to make the code applicable to a wider range of situations in order to complete the verification and validation process, although the first studies have been already carried out.

1.2. Outline of the project

This study will start with a review of the various contributions to the understanding of the pool nucleate boiling phenomena, organised in subjects according to the considered theme. However, due to the large amount of concepts and solutions suggested during the past years and to the strong correlation of the different aspects addressed by the same investigation, sometimes the same concept may be referred to different sections. The review will begin with a general summary of the possible

involved phenomena, distinguishing between those related to the growth of a single (or also called isolated) bubble and the interactions that this may have with the surrounding environment. For the single bubble growth, several empirical correlations and models will be described in a chronological order, although some of the earliest correlations are still commonly in use. In a hybrid code, these correlations may be used to replace complicated physical phenomena and constitute a base to evaluate the importance of the specific contribution (as it could be for instance for the heat evaporation at the dome of the bubble, where the complete evaporation model based on the solution of the Navier-Stokes equations may be replaced by simpler semi-empirical time-dependent models). Connected to the bubble growth, the analysis of the suggested models for the inception (or nucleation) and departure of a bubble will also be analysed with particular focus on the (theoretical and experimental) results of the dependence of these phenomena on the mutual characteristics of liquid and solid, and on the process used to treat the surface before the experiments. In fact, the bubble growth has been observed to depend strongly on the geometric characteristics of the cavity in which it nucleates, as well as on the capability that the fluid has to cover or advance in it. This aspect consequently affects the time during which the nucleation site is not active, called waiting time. Several bubble growth models are based on the micro-layer model theory, which assumes that a thin layer of liquid is present during the whole growth of the bubble below the bubble itself, so that the dome of the bubble is not in direct contact with the solid substrate. By contrast, the contact line model assumes that the vapour in the lower part of the bubble (supposed to grow with the shape of a truncated sphere) is in direct contact with the wall, so that a zero heat transfer coefficient is expected. Despite the significant number of different investigations, a complete understanding of the mechanisms was not achieved: moreover the study of an isolated bubble is not sufficient to describe the heat transfer mechanisms for a substrate, because of the possible presence of strong interactions between sites both on the substrate and fluid sides (respectively thermal and hydrodynamic interactions). The effects of the site distribution were also observed to affect the overall heat transfer removal. Of particular interest were phenomena such as seeding and inhibition of the sites, intended as the capability that one site has to respectively promote or reduce the activity of a neighbouring site. The intensity of these mechanisms was often studied with a statistical approach, due to both the large number of participating factors and to the involved uncertainty parameters. The interaction mechanisms were observed to depend on the distance between the sites, noticing that

the effects generally faded with increasing distance. Among the interaction mechanisms, an important interaction occurring at small distances is coalescence (of which three modes were identified: horizontal, declining and vertical), involving merging of two or more bubbles in one large bubble. In addition to the study of the single phenomena and the evaluation of each contribution and interactions in a mechanistic model, the most commonly used approach at the beginning was the identification of empirical correlations, based on combined properties of fluid and solid, in order to have a macroscopic idea of the entity of the heat flux according to the specific range of conditions. Often based on dimensionless numbers, this approach has partly given way to the development of more accurate mechanistic numerical models, able to provide information with more details on local phenomena. This has been made possible by the increasing computational power and the higher accuracy of experimental facilities. Among these models, some remarks on the original model at the base of the numerical code used during this project will be mentioned. The literature review will be completed by some comments about the possible presence of chaotic behaviour in boiling, an aspect that has recently received increasing interest.

The analysis will proceed with the description and critical analysis of the original version of the numerical model, as acquired from the University of Ljubljana, with particular focus on its weaknesses or aspects that could have been improved. The modification introduced during this project, both from the numerical and physical points of view, will be then illustrated and the reasons behind modifications explained. A sensitivity analysis will be carried out to understand the influence of the input data and of the used models and improvements on the numerical code, with focus on a single bubble growing on silicon substrate (0.38 mm thick) immersed in water at atmospheric pressure and saturation conditions. The results will be compared with a base case aimed at reproducing a series of experimental results developed at the University of Edinburgh. These results, together with others from both University of Edinburgh (also on a silicon substrate, 0.38 mm thick at different pressures) and University of Ljubljana (on thin metal foils, such as titanium, 25 μm thick and platinum, 6 μm thick) will be analysed during the validation process to prove the capability of the code to correctly reproduce the bubble growth for an isolated bubble. Results from the validation process will be then used for simulations on both silicon and titanium involving a much larger number (100) of nucleation sites, assuming that the previous results from the single bubble growth are still applicable to these conditions. Future verification of this

assumption would be required, by comparison of the numerical results with experiments. Concluding remarks and future work will complete the analysis.

2. Literature Review: Nucleate Pool Boiling

This section reviews the models and concepts developed over the years involving the nucleate boiling process, identifying the most accredited theories. These will constitute the basis for the improvement and development of a numerical code able to simulate the heat transfer between a solid substrate and a saturated liquid with a large number of micro-cavities acting as potential nucleation sites. The code, as will be explained in detail in the later chapters, is based on a hybrid approach, which combines physical models with semi-empirical solutions. This compromise is necessary to allow simulations to be run in reasonable time in order to provide a design method for micro-fabricated test sections. It is therefore necessary to assemble a solid background of theories that have been suggested, both related to single bubble growth and to possible interactions between bubbles growing at adjacent sites, in order to decide which of them are sufficiently important to be implemented in the code.

The study will start with the description of general boiling heat transfer phenomena, followed by a particular focus on nucleate boiling. The identification of the different phases of single bubble growth (nucleation, growth, detachment and rise) will be of fundamental importance.

The different approaches in representing the micro-layer model will be separately analysed because of its complexity. This model will be compared with the triple contact line heat transfer model at the base of the bubble, which assumes that there is strong evaporation in a narrow region of large bubble surface curvature that separates the contact area with the wall from the dome of the bubble. The effects of the substrate characteristics on the nucleation site density and interaction mechanisms, including coalescence and creation of vapour stems, will then be investigated. A description of empirical, mechanistic and numerical models for nucleate boiling will conclude with a short analysis of the possibility of chaos. The empirical models were the first to be developed: they aimed to provide direct correlations based on the experimental analysis of the effects of the characteristics of the substrate and the fluid on the process.

Particularly, the models focused on determining the heat flux dependence on the average temperature at the heated wall for a wide range of conditions, employing an approach similar to the one used in natural convection studies. The main objective was the determination of the maximum wall temperature in order to avoid critical heat flux (*CHF*) and consequent damage of the characteristics of the substrate. A different approach was used in the mechanistic models, which used correlations derived from theoretical studies of the involved phenomena. However, despite the numerous efforts, the complexity of the process impeded the creation of a valid simple mechanistic model. With the development and improvement of computer capabilities, the mechanistic models evolved into numerical codes, using mechanistic models as well but elaborated with a more sophisticated and non-linear approach. Nowadays, two main different approaches are used for numerical codes, both subject to limitations to reduce computational times. The first aims to completely solve the thermal and fluid-dynamic equations in the substrate and liquid, analysing in detail micro-scale phenomena but limited to a small number of nucleation sites. The second aims to develop a more global analysis of the process, focusing on the interactions between the sites now interpreted as a network. It combines the complete solution of some physical processes with semi-empirical models. This approach has the disadvantage of a stronger dependence on experimental results compared to the first approach, but in principle can be used to simulate more realistic conditions.

The complete analysis will be organised in terms of subjects instead of in chronological order, so the same reviewed paper or concept may be presented in more than one section. The effect of thermal-hydraulic system variables was also the subject of numerous studies. In particular, the dependence of the bubble size and shape on the pressure of the system or on the sub-cooling, the effect of the different liquids and materials for the plates are of fundamental importance. A detailed analysis of all the effects is behind the objectives of this study, and investigated in numerous reviews.

2.1. Introduction to boiling heat transfer

Boiling heat transfer is defined as a heat transfer mode with change of phase from liquid to vapour. Two different modes can be identified: pool boiling and flow boiling. Pool boiling occurs when a body (for instance a plate or a wire) is immersed in a liquid essentially in state of rest, while flow boiling is defined as a mode where the status is strongly affected by externally generated agitation forces. For each mode several

behaviours can be identified, differing for instance for the size, shape and velocity of the bubbles, their thermal and mechanical interactions and frequency.

One of the first systematic studies of boiling phenomena was developed by Nukiyama (1934): a series of experiments with wires of different materials (iron, fuse wires, platinum, nickel and nichrome) and diameters was run using water at atmospheric pressure. Three different regimes were identified, as shown in Figure 2-1, corresponding to regions a-b, b-c, and c-d for the heat flux ($\dot{q}$) and to regions a'-b', b'-c', and c'-d' for the heat transfer coefficient *HTC* versus the wall superheat (i.e. the difference between the wall average temperature and the liquid saturation temperature). The liquid close to the wall is assumed to be agitated by the movement of the bubbles, the degree of agitation increasing with increasing wall superheat.

In region *a-b*, the liquid is superheated and tends to evaporate forming bubbles where surface irregularities as scratches or cavities act as nucleation sites. This phenomenon is generally called nucleate boiling *(*Tong and Tang, 1997*)*. The heat transfer rate per wall superheat increases with increasing superheat, because of the effect of evaporation and agitation due to bubble movements. Two different mechanisms can be identified in this region: local boiling and bulk boiling. The first one

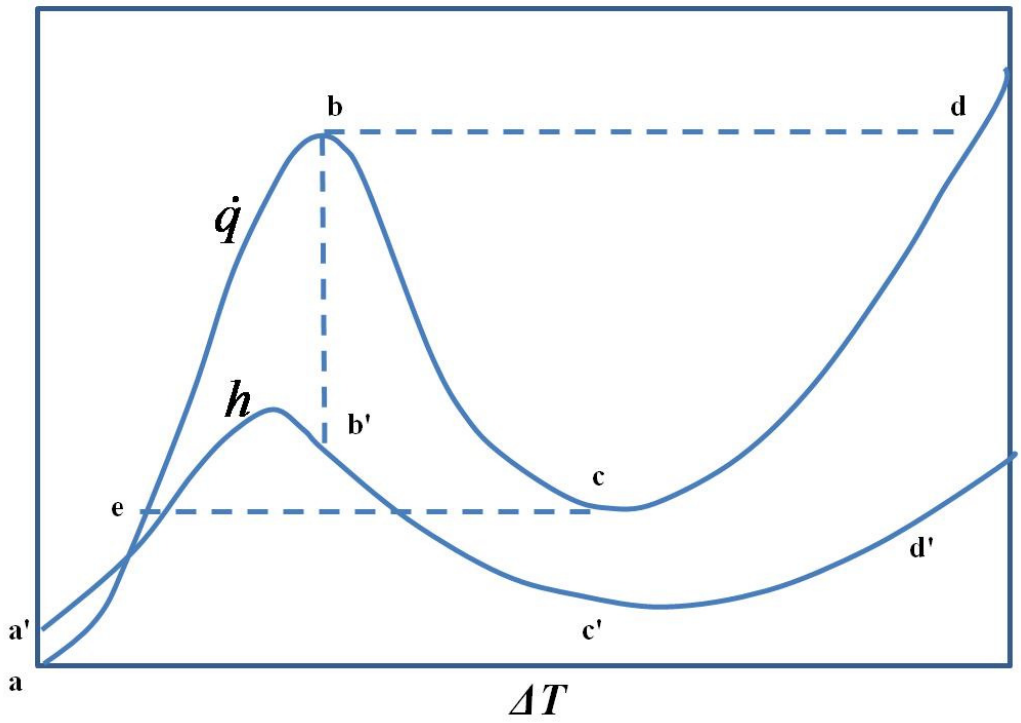

Figure 2-1: Boiling curve (Nukiyama, 1934)

occurs in a sub-cooled liquid: the bubbles formed at the heated surface tend to collapse before departure or immediately after that. The latter occurs at saturated conditions, with the bubbles moving away from the nucleation site at departure; new liquid immediately replaces the area where the bubble was growing, guaranteeing continuous contact between the liquid and the heated wall. The heat flux in nucleate boiling cannot be increased indefinitely. When the population of bubbles becomes too high (point *b*), the liquid is no longer able to reach the heated wall, and an insulating vapour film covers the heated wall, obstructing the outgoing bubbles. A decrease in heat transfer occurs and consecutively a sudden increase in the surface temperature. This phenomenon is known as boiling crisis, and the maximum heat flux that can be imposed to the wall before having boiling crisis is called critical heat flux (*CHF*).

The region *b-c* is defined as transition boiling: in this area, if the power input is maintained or increased, the wall superheat increases because of the lower heat transfer removal at the wall. This status is unstable and it quickly evolves following the curve *b-d* until the wall temperature reaches the new equilibrium at point *d*. This effect is due to the presence of a gas blanket in direct contact with the wall that alternatively replaces the liquid film causing oscillations in the heat transfer removal and then in the wall temperature. Once the point *d* is reached, if the power input is slowly reduced, the curve will not reverse along *d-b*, but along *d-c*, and then suddenly to point *e* along the curve *d-e*, because of the hysteresis of the system. In the region beyond point *d*, a stable vapour film is formed, with a heat transfer coefficient significantly lower than for nucleate boiling, leading to a higher wall superheat for a fixed power input. During the experiments with thin wires, most of the examined metals were melting after point *b*, so that only experiments using a platinum wire 0.14 mm in diameter could show the existence of point *d* (Nukiyama, 1934).

The review will now focus on nucleate pool boiling.

2.2.Nucleate pool boiling phenomena

Before proceeding with the review, it is important to provide a short summary of some notions of bubble growth and interactions as a basis for the following study. A bubble can be defined as a single (or isolated) bubble if its growth is independent on bubbles growing at adjacent nucleation sites. A description of the bubble phases was provided amongst the others by Basic et al. (2006). The five phases identified as results of numerical simulations are listed below:

a) Hemispherical expansion, during the first stage of the bubble growth, starting from nucleation.
b) Vertical elongation, when centre of gravity moves upwards; the bubble assumes here a less spherical shape.
c) Base shrinking, when the necking process starts.
d) Bubble departure.
e) Bubble rising in the liquid bulk.

This classification represents a possible evolution of the bubble growth, but the exact phases and shapes strongly depend on the fluid, substrate and heat source characteristics. For instance, in the detailed review about bubble growth phenomena, Kenning (1999) cited the model of Chester (1978) for the different bubble growth modes from a cavity, Figure 2-2. A distinction between slow and fast growth was supposed. For slow growth a further distinction was made, depending on whether the triple contact line was confined into the cavity (A) or was moving outside it (B). A model for the fast growth with formation of micro-layer was also hypothesised (C). Nowadays, the bubble is often assumed to grow as a truncated sphere, as shown at different time steps (t) in Figure 2-3, with the shape defined by the bubble radius (r_b) and the apparent contact angle (φ), i.e. the apparent angle formed by the bubble dome in proximity of the wall. Further details about the models will be provided in the following Section 2.3.

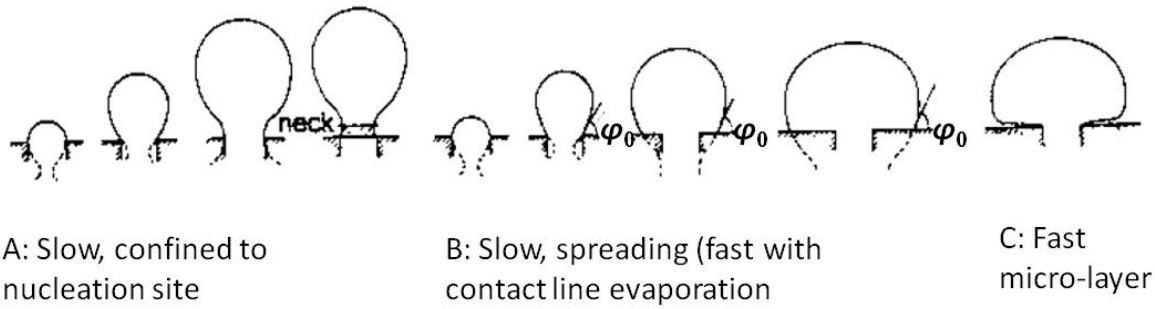

Figure 2-2: Bubble growth modes (Chester, 1978)

Cooper and Lloyd (1969) identified four main contributions determining the bubble shape, and specifically, the inertial, surface tension, viscous and gravitational forces. Predominance of the inertia term would lead to a hemispherical shape with a large, spread base, while surface tension is more likely to lead to a more spherical shape. Zeng et al. (1993) developed a mechanistic model to derive the bubble departure diameter: to do so, the forces acting on the bubble at departure needed to balance the inertial contribution in order to have departure, were evaluated. In the first instance, the considered forces were surface tension, unsteady growth, buoyancy, contact pressure and lift force generated by the wake of the bubble previously departed from the same nucleation site. The inertial contribution was supposed negligible because of the small acceleration of the vapour bubble. According to Lee and Nydahl (1989), the surface tension force at departure was considered not dominant, and then neglected. The contact pressure and lift force contributions were also assumed to be not relevant, so that only buoyancy and unsteady growth forces were accounted. Comparison of the suggested model with previous correlations was also presented, showing that for sub-atmospheric and atmospheric conditions and earth gravity conditions, the suggested model provided the best fit. Attention must be drawn to the formulation used to calculate the bubble radius, because a constant wall superheat is assumed. This condition is referred to be possibly unrealistic, as experimentally observed by Kenning (1992). According to Lee and Nydahl (1989), in the calculation of the force balance, the size of the bubble plays a fundamental role; variations in the variables of the system are very important, so that for example a reduction of the pressure allows larger bubble diameters and then larger buoyancy force. The effect of the pressure on bubble diameters was attributed by Kim et al. (2007) to the higher Jacob number (defined as $Ja = \frac{\rho_L c_L \Delta T}{\rho_V H_{fg}}$) and to the

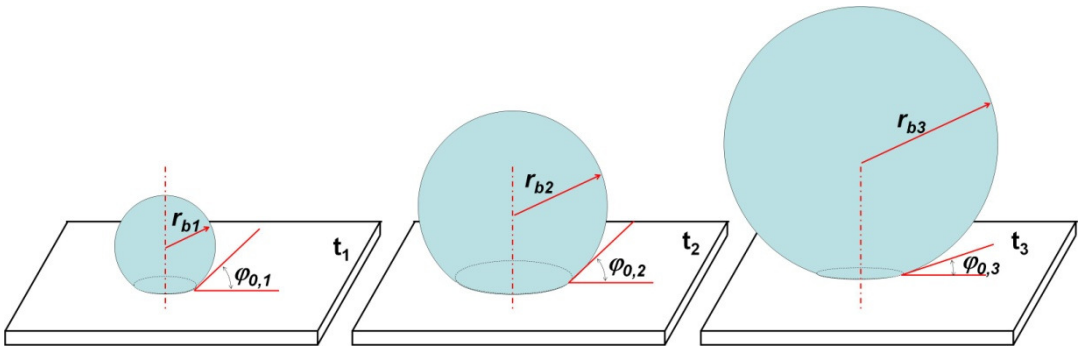

Figure 2-3: Schematic bubble growth assuming a truncated sphere shape at different times (t_1, t_2, t_3)

dimensionless pressure potential, defined as the difference between the vapour pressure at the wall temperature and the pressure of the system divided by the pressure of the system. The comparison of the dimensionless growth versus the dimensionless time for different experiments did not show apparent dependence on the pressure.

From the point of view of the formation and growth of the bubble and their effects on the heat transfer at the heated wall, several theories have been developed over the years. He et al. (2001) and Tong and Tang (1997) summarised the main approaches used to study nucleate pool boiling and to predict heat transfer between the heated wall and the liquid when an heat source is imposed to the substrate and the wall is assumed isothermal:

- Bubble agitation model. This model is based on the use of dimensionless correlations (usually involving Nusselt and Reynolds numbers) derived from experimental results. The main process considered is the displacement and movement of water caused by bubble growth and departure.
- Vapour-liquid exchange. The bubble is assumed to act as a micro-pump that absorbs heat during the bubble growth and releases it to the bulk liquid when departed, guaranteeing high heat transfer rates at the surface.
- Micro-layer evaporation. The high heat transfer rates in boiling are essentially attributed to the micro-layer evaporation below the bubble or at the triple contact line region (also called meniscus), i.e. the area where the dome of the bubble undergoes a strong variation in curvature. The bubble appears as a truncated sphere and the triple contact line identifies the region where vapour, liquid and solid wall seems to intersect.
- Transient conduction in the liquid. The heat removal is associated to the transient variation of temperature in the area around a bubble. Following bubble departure, part of the superheated liquid is removed by the effect of a vortex created by the bubble wake. Fresh liquid flows afterwards in the area where the bubble was located.

A more detailed description of the mentioned approaches will be provided in Section 2.3 and in Section 2.5 with focus on the micro-layer theory. The complexity of nucleate pool boiling is further increased by the non-linearity of involved phenomena and in particular by the interactions of the bubble with the surroundings. Zhang and

Shoji (2003) identified four types of interactions (1-4) between 2 bubbles, as shown in Figure 2-4:

- Interaction 1 occurs between the growing bubble and the liquid bulk, and it is present for both an isolated and non-isolated bubble.
- Interaction 2 occurs between two adjacent growing bubbles. Two different sub-categories may be distinguished, and in particular, the so called here hydrodynamic interaction and coalescence, the latter occurring when two (or more) bubbles merge together.
- Interaction 3 involves a growing bubble and the heated wall below. As for interaction 1, interaction 3 occurs for both isolated and non-isolated bubbles.
- Interaction 4 accounts for thermal interactions through the heated wall between bubbles growing at adjacent sites.

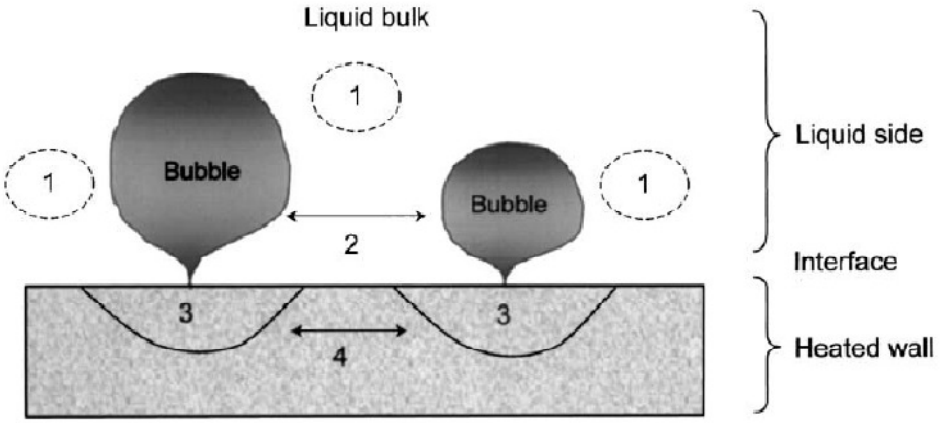

Figure 2-4: Bubble interaction (Zhang and Shoji, 2003)

2.3.Single bubble growth: mechanistic models and experiments

The single bubble growth is a complex process, and many researchers investigated the involved phenomena. The developed theories were often opposing and conflicting, due both to the incapacity of measurements to provide detailed data at microscopic scale and to the complexity and the non-linearity of phenomena. One of the first analyses of bubble growth for an isolated bubble was developed by Plesset and Zwick (1954). Three different contributions to the growth of a spherical bubble in a superheated region were identified: inertia, surface tension and pressure difference between liquid and vapour respectively outside and inside the bubble. The analysis (restricted to water with maximum superheat of approximately 10 K) assumed constant pressure and temperature for the vapour inside the bubble and negligible effects of compressibility and viscosity.

Moreover, the temperature drop between the superheated liquid and the dome of the bubble was attributed to conduction in the liquid occurring in a thin layer significantly smaller than the radius of the bubble itself, called "thin thermal boundary layer". An explicit formulation of the temperature drop depending on the bubble radius and growth rate was derived, under the assumption that the bubble growth could be divided in two stages. During the initial stage the bubble radius depends linearly on time ($r \propto t$), while during the final stage the radius depends on the square root of time ($r \propto \sqrt{t}$). The bubble is supposed to start from a nucleus at unstable equilibrium, growing with an initial slow bubble growth rate, followed by a rapid increase that leads to a maximum growth rate and a continuous decrease afterwards. A slightly different approach was attempted by Forster and Zuber (1954) for the growth of an isolated, spherically symmetric bubble. The extended Rayleigh solution (Equation 2.1) was combined with the Clausius-Clapeyron condition (Equation 2.2) to connect the pressure to the temperature differences. It was shown that during its first stage, the bubble starts growing slowly from the critical size, i.e. proportional to $t^{3/2}$, if hydrodynamic forces are not considered.

$$\rho_L \left[r \frac{d^2 r}{dt^2} + \frac{3}{2} \dot{r}^2 \right] = \Delta p - \frac{2\sigma}{r} \tag{2.1}$$

$$\Delta p = \frac{H_{fg}}{T\left(\dot{V}_V - \dot{V}_L\right)} \left(T_{bulk} - T_{sat}\right) \tag{2.2}$$

Indicating with r_0 the critical radius of the bubble (defined as that value at which the bubble is at equilibrium with the superheated liquid) and $r^* = \frac{r}{r_0}$ the dimensionless radius, and considering the bubble growth after the initial phase, the dimensionless bubble radius is obtained by solution of Equation 2.3. The coefficient C depends on thermodynamic conditions. The end of the initial phase is assumed when the dimensionless radius is such that the growth rate from superheat is comparable to the rate from evaporation.

$$r^* + \log \frac{r^* - 1}{r_1^* - 1} = C \cdot t^{1/2} \tag{2.3}$$

Successively, Han and Griffith (1965a and 1965b) developed an analysis for the single bubble growth on the base of a theory based on "bulk convection of the transient thermal layer", as shown in Figure 2-5. This theory assumes that at departure, a bubble brings part of the heated liquid thermal layer to the bulk liquid (stage 1). New cold liquid moves then from the colder regions towards the area previously occupied by the bubble base, and is heated during the waiting time (stage 2). When the bubble starts growing, the thermal layer rises (stage 3) and surrounds the bubble dome (stage 4), until it is removed by bubble departure. Both the heater and liquid bulk temperatures are assumed uniform; inertia and surface tension effects on the pressure inside the bubble are neglected. The one dimensional solution is developed for the three periods identified for the bubble cycle: the unbinding period, the departure period and the waiting period.

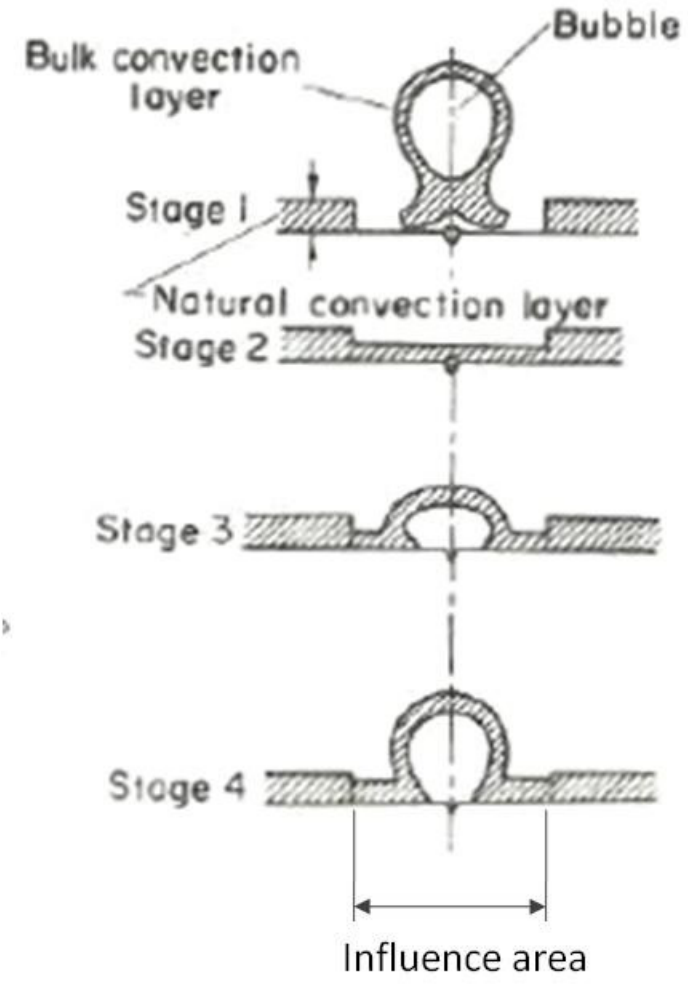

Figure 2-5: Bulk convection and thermal layer formation (Han and Griffith 1965b)

The unbinding period is defined as starting after initiation, until the bubble is still significantly under the effect of inertia and surface tension effects. The bubble radius at the beginning is shown to increase very slowly. The departure period refers to the stage when the heat transfer is assumed to be the only significant contribution to the bubble growth. After bubble departure, the effects of a liquid vortex generated by departure were supposed to bring fresh liquid to an area with a diameter approximately equal to the double of the departure diameter, called "influence area". Experimental results developed on a 16 ct gold plate in distilled and degassed water showed a significant randomness for both waiting times and bubble departure radii.

Mikic et al. (1970) developed a model for a single bubble growing either completely immersed in a uniformly superheated liquid (a) or in a non-uniform temperature field (b), as shown in Figure 2-6. For both the models the analysis started from the continuity equation, assuming the incompressibility of the liquid, Equation 2.4, with u_L the liquid velocity. If negligible mass transfer at the liquid-vapour interface is assumed, Equation 2.5 can be derived.

$$\frac{1}{x_r^{\,2}}\frac{\partial}{\partial x_r}\left(x_r^{\,2}u_L\right)=0 \qquad \textbf{(2.4)}$$

$$u_L=\frac{dr}{dx_r}\left(\frac{R}{x_r}\right)^2 \qquad \textbf{(2.5)}$$

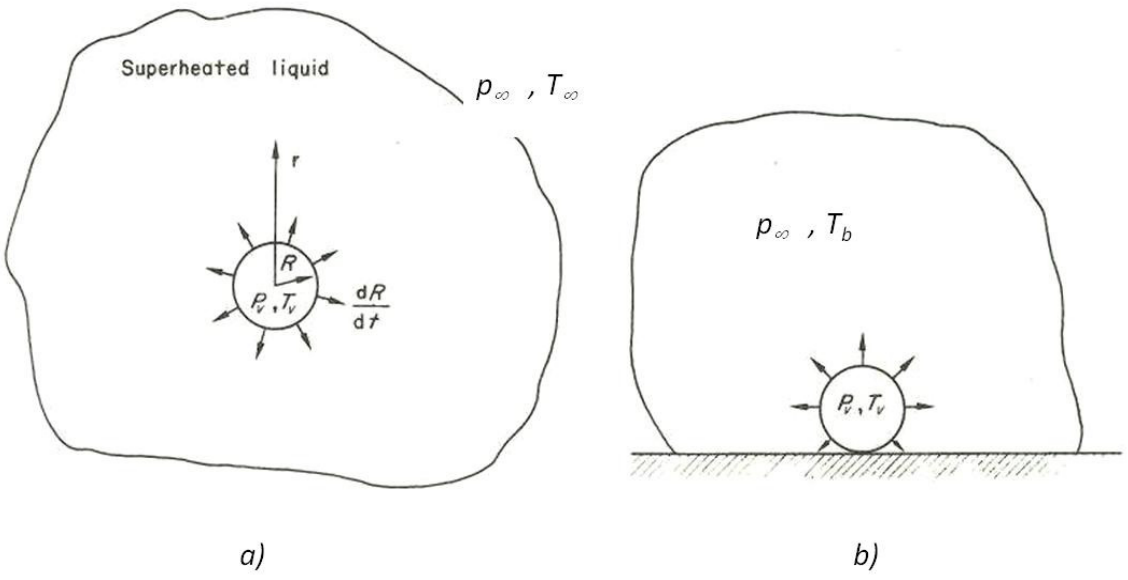

Figure 2-6: Bubble growth in a uniformly superheated liquid (a) and in a non-uniform temperature field (b) Mikic et al. (1970)

For the bubble growth in a uniformly superheated liquid the dimensionless expression in Equation 2.6 was obtained,

$$\frac{dR^*}{dt^*} = \left(t^* + 1\right)^{1/2} - \left(t^*\right)^{1/2} \qquad \textbf{(2.6)}$$

where $R^* = \frac{A}{B^2} R$ and $t^* = \frac{A^2}{B^2} t$, with $A = \left[b \frac{H_{fg} \rho_L \left(T_\infty - T_{sat}\right)}{\rho_L T_{sat}} \right]^{1/2}$, the geometric form factor $b = \frac{2}{3}$ and $B = \left(\frac{12}{\pi} \alpha_L \right)^{1/2} Ja = \left(\frac{12}{\pi} \alpha_L \right)^{1/2} \frac{c_L \rho_L \left(T_\infty - T_{sat}\right)}{H_{fg} \rho_V}$. This equation was derived assuming that the linearised form of Clausius-Clayperon equation is applicable and that the vapour temperature is not subjected to large variations during the bubble growth. Equation 2.7 was derived for the initial stage of the bubble growth ($t^* << 1$), i.e. when inertia forces are dominant; otherwise use Equation 2.8 ($t^* >> 1$), i.e. when the bubble growth is controlled by heat transfer.

$$R^* = t^* \quad , \; t^* << 1 \qquad \textbf{(2.7)}$$

$$R^* = \sqrt{t^*} \; , \; t^* >> 1 \qquad \textbf{(2.8)}$$

Equation 2.6 was compared with experimental results and showed good agreement, even if this expression is not able to describe the correct bubble growth during the early stage, due to the probably not appropriate assumption that the bubble starts growing from a zero radius instead of from a nucleus. Nevertheless, it was highlighted that the uncertainties in the early stage of the bubble growth do not affect prediction for the later stage. For a bubble growing close to a heated wall, with a non-uniform distribution of temperature, an expression similar to Equation 2.6 was derived, as shown in Equation 2.9. The superheat is now represented by the difference between the wall temperature T_W and the saturation temperature T_{sat} with $\theta = \frac{T_W - T_{bulk}}{T_W - T_{sat}}$ ($\theta = 1$ when the bulk temperature T_{bulk} is at saturated conditions) and A and B, as defined before, but with $b = \frac{\pi}{7}$.

$$\frac{dR^*}{dt^*} = \left[t^* + 1 + \theta \left(\frac{t^*}{t^* + t^*_{wait}} \right)^{1/2} \right]^{1/2} - \left(t^* \right)^{1/2} \qquad \textbf{(2.9)}$$

A correction to this model was suggested by Theofanous and Patel (1976): the previous correlations and experiments were referred to be valid only for low heat fluxes conditions, in which the use of linearization of the Clausius-Clapeyron equation for the vapour pressure and of a constant vapour density were justified. An increase in superheat would lead to a wrong estimation of the bubble growth rate using the model suggested by Mikic et al. (1970). Instead, the use of density and pressure linearization factors lead to different bubble growth rates in both the cases (inertia and heat transfer controlled). In the suggested model the bubble radius has a more complicate expression (even if formally similar), so that the time dependent value must be obtained by numerical integration of the bubble growth equations, depending on the "initial-to-final vapour density ratio". A comparison of the new and previous models showed that for low values of these parameters the solutions coincide, while for larger values the solutions converge only for the asymptotic models (inertia and heat-transfer controlled). Olek et al. (1990), further analysed the model proposed by comparing their results obtained using the Fourier equation (with a parabolic distribution of temperature) with a more complex hyperbolic heat conduction equation. Moreover, the dependence of the growth rate on the superheat has been generalised respect to the model proposed by Mikic et al. (1970). The assumption of hyperbolic temperature variation predicts a more accurate bubble growth rate during the early stage of the bubble growth, while for longer times (assuming that the initial growth is similar) the two models are coincident. The discrepancy for short times is due to the use of the Fourier heat conduction formulation that assumes that the energy is instantaneously transferred, such a condition is physically unacceptable when high heat fluxes are transferred in short times. This effect can be evident, for instance, with fluids such as Helium II, where the dimensionless time ($t^* = \frac{c_S t}{2\alpha}$, with c_s the propagation speed of thermal disturbances) is less than 1. For this reason, the hyperbolic formulation introduces a term depending on the derivative of the heat flux and on a relaxation time in the Fourier equation, and it is explicitly solved only in the case of spherical geometry in a semi-infinite body. When the relaxation time is as large as it can be for Helium II at low temperatures, its effect

can become relevant for short times, while it is of influence for most practical conditions. For longer times, i.e. when the conduction phenomena are controlling the bubble growth, the time dependences are again the same in both the solutions, but in the case of the hyperbolic model, the coefficient depends on the Jacob number *Ja*. However, particularly at low pressure conditions, the parabolic and hyperbolic conduction controlled growth models may significantly differ from the one suggested by Mikic et al. (1970).

Prosperetti and Plesset (1978) proposed a model for a spherical bubble growing in superheated liquid approximated as a thin thermal layer. The model is valid only for bubbles of which the final radius is approximately one order of magnitude larger than the initial one, so that the effect of surface tension becomes important. The use of the Clausius-Clayperon equation in the model described by Mikic et al. (1970) was criticised since it was not able to reproduce the inertial mechanisms for not low superheats; a linearization of the gradient of pressure replaced it. A good agreement with previous literature results at low superheats was shown by using this solution. The liquid is supposed to be at uniform temperature T_∞, used to evaluate the pressure inside the bubble different from the pressure supposed for the liquid itself. The pressure of the liquid corresponds to the "boiling" temperature $T_{bulk} < T_\infty$, the difference defined as superheat. During the early stage of bubble growth (inertial effects dominant), an upper bound for the growth rate is expressed as in Equation 2.10, while for larger radii (thermal effects dominant), the expression is as in Equation 2.11.

$$\left(\frac{dR}{dt}\right)_{inertial} = \left[\frac{2}{3}\frac{p(T_\infty) - p(T_{bulk})}{\rho_L}\right]^{1/2} \qquad \textbf{(2.10)}$$

$$\left(\frac{dR}{dt}\right)_{thermal} = \left(\frac{3}{\pi}\right)^{1/2} \frac{k_L}{H_{fg} \cdot \rho_V(T_{bulk})} \frac{T_\infty - T_{bulk}}{(\alpha_L t)^{1/2}} \qquad \textbf{(2.11)}$$

The above equations are coupled to the energy equation solved (with the approximation of thin thermal boundary layer) for the temperature by using a linearised expression for the pressure. A scaled solution, able to provide a good level of accuracy on the base of physical, although simplified, models was suggested. A comparison between scaled and non-scaled formulations shows a good agreement of the scaled

bubble growth radii, although this is limited to the final stage of the bubble growth, i.e. when the bubble radius is at least one order of magnitude larger than the nucleus radius. The authors pointed out that the formulation indicated by Mikic et al. (1970) has a good agreement with their formulation, even though it is based on an "unsatisfactory" physical analysis and obtained as interpolation of two asymptotic behaviours.

Cooper and Lloyd (1969) hypothesised that the contribution of micro-layer evaporation to hemispherical bubbles growing on smooth surfaces could be significant, even if the theory could not be universally proved. In fact it was admitted that in some cases, predictions without consideration of the micro-layer evaporation were also able to reproduce bubble growth rates in a very good agreement with experimental results. A detailed analysis of micro-layer theories will be provided in Section 2.5, while here only the effects on the bubble growth will be analysed. Stralen et al. (1975) identified two mayor contributions for the bubble growth, i.e. the evaporation at the micro-layer (at the base of the bubble) and the "relaxation" of the micro-layer (for evaporation occurring at the dome, either at the entire surface or only the lower part). For each of these two models the authors reviewed the existent correlations suggested until then, and compared their applicability. For the micro-layer evaporation at the base of the bubble, the models suggested by Cooper, Ouwerkerk, Pohlhausen and others were compared. The first two models were criticised because of the inappropriate approach: the two different asymptotic contributions (i.e. hydrodynamically controlled case and in the thermally controlled case) were calculated and then superimposed. This approach led to an incorrect evaluation of the mutually involved Reynolds numbers affecting the micro-layer thickness. Instead, the model of Pohlhausen was used as a starting point for the development of a new model. This model assumes the existence of two stages: the initial bubble growth (when the radius is directly proportional to the time) and the final stage (when the bubble grows hemispherically and the radius is proportional to the square root of the time). For the relaxation micro-layer contribution, the authors summarized the correlations for the asymptotic models (isothermal and isobaric bubble growth) as occurring at the initial and regime stages. To account for the conjugation between the two stages, the authors suggested Equation 2.12, where $R_1(t)$ represents the radius obtained by the Rayleigh solution (linear dependence on time) and $R_2(t)$ represents the radius obtained by asymptotic micro-layer evaporation (square root dependence on time). If the excess enthalpy of the evaporation is accounted for by a

time-dependent micro-layer superheat, different formulations for $R_1(t)$ and $R_2(t)$ must be used: these formulations were provided also for binary systems.

$$R(t) = \frac{R_1(t)R_2(t)}{R_1(t) + R_2(t)} \tag{2.12}$$

One of the biggest efforts was to quantify the different heat contributions to bubble growth and heat removal from the surface, with solutions often conflicting. With this objective, Lee and Nydahl (1989) numerically solved the axial symmetric Navier-Stokes and energy equations to simulate a bubble growth in water with an imposed superheat of 8.5 K with micro-layer formation from nucleation to departure. The mesh distribution was refined in proximity of the triple contact line. An isothermal wall and specified micro-layer and bubble shapes were assumed. The results of simulations showed that a significant part of the energy contributing to bubble growth and generally to heat transfer from the wall was provided by micro-layer evaporation. According to their simulations, departure was determined by a balance of drag and buoyancy forces, while surface tension contribution was considered to be one order of magnitude less. Later, Demiray and Kim (2004) analysed the thermal response of micro-heaters regularly arranged over an area of 1 x 1 mm^2 at different degrees of sub-cooling. Each heater (0.1 x 0.1 mm^2, platinum deposited on a quartz wafer) was designed in order to keep the average temperature constant. The bulk liquid temperature (FC-72 for these specific experiments, T_{sat} = 57 °C) was kept constant at sub-cooling conditions (low sub-cooling, T_{bulk} = 52°C; high sub-cooling, T_{bulk} = 41°C). Analysis of the heat transfer produced by the heaters (assumed entirely contributing to the bubble growth) showed a peak during the initial stage of bubble growth when the bubble was believed to have a hemispherical shape. The peak was, according to Demiray and Kim (2004), probably due to evaporation of a thin micro-layer. A steep decrease in heat transfer followed, attributed to the formation of a dry spot below the bubble. After a maximum, the contact area started shrinking. Just before departure, i.e. when the necking process started, an increase in heat flux was observed in the central area due to rewetting of the surface by the surrounding liquid. The height of the initial heat flux peaks decreased for successive bubble growths for low sub-cooling. After analysis of the total generation of heat flux at the wall, it was concluded that micro-layer and contact line evaporation contribution were insufficient to account for the whole bubble growth. Instead, transient micro-

conduction and micro-convection outside the bubble were believed to play a more important role. Analysis of the effect of sub-cooling showed that significant waiting times were observed for low sub-cooling; higher bubble departure frequency, smaller bubble departure diameters and very short waiting times occurred for higher sub-cooling. A similar analysis with FC-72, using the same type of small heaters, was developed by Myers et al. (2005). It was concluded that the total heat transferred from the wall directly to the bubble could be quantified in less than 23% of the total heat required for the bubble growth, under imposed heat flux conditions. Very high heater voltages (and consequently wall superheat) were required in this case to have nucleation. Visual analysis of the shape of the shadow of the bubble seemed to confirm the hemispherical shape during the first stage of the growth (as found by Demiray and Kim, 2004), followed by a spherical growth and then a necking process before departure. An increase in input heat flux led to coalescence phenomena. A substantial disagreement between the previous theories supporting micro-layer evaporation as essential contribution to the bubble growth (as in Cooper and Lloyd, 1969), and the findings of Myers et al. (2005) and Demiray and Kim (2004), supporting the micro-convection theory, was possibly attributed to the different Jacob numbers, much larger in the last case.

Golobič et al. (2006) investigated temperature variations and bubble coalescence (vertical, horizontal and declining) by varying the imposed heat flux on a thin titanium foil (25 μm thick) in water at atmospheric pressure. InfraRed (IR) thermography and a high-speed camera were used. For a low heat flux (50 kW/m^2) a single bubble sequence was studied: the bubble was growing as a truncated sphere. The temperature at the centre of the contact area undergoes a strong reduction, while no significant changes were detected outside the contact area. A clear identification whether strong evaporation occurred at the triple contact line or diffused over the contact area was not possible. Analysis of the temperature variations showed a crater-like shape for the heat transfer, while the heat transfer coefficient presented an approximately flat distribution in correspondence of the contact area, with a small but not zero value. Recently, Golobič et al. (2009) experimentally investigated the growth of single bubbles for a very thin (6 μm) platinum foil in water, with 2-dimensional temperature measurements on the back of the plate using high-speed infrared camera with spatial resolution of 40 μm. Two different behaviours were observed for fast and slow growths. During the presented fast growth, the bubble appeared to grow very quickly for the first 2 ms, i.e. until the contact

area reached a maximum. Then, the contact area started shrinking and detachment occurred at approximately 9 ms. During the first stage of the fast growth, a quick temperature drop occurred in the contact area up to 3 ms after nucleation. The temperature then started to rise again, but with a central depression. Analysis of the heat flux (numerically derived, together with the heat flux coefficient, from temperature variations) showed an initial (at 1 ms) high "mountain peak" at the nucleation site, followed by a crater shape (at 2 ms) and then (at 3 ms) a local depression in correspondence of the moving contact line; at 7 ms the contact line depression disappeared and it is replaced by a central depression. Comparison of results for the heat transfer coefficient seemed to attribute the heat flux reduction to the temperature variations. The typical profile of strong evaporation at the triple contact line did not seem to be supported by analysis of the heat transfer coefficient. However, any conclusion for heat flux and heat transfer coefficient must be weighted with caution, since the noise and fast changes in temperature may introduce possible computational errors. Analysis of the slow growth (approximately 50 ms, initiating at generally lower superheats than for the fast growth) showed a tendency of the bubble to sway and slide during the last stage, for no apparent reason. Moreover, the temperature presented a central peak after the initial stage of bubble growth. For all the analysed cases, the nonzero heat transfer over the whole contact area seemed to indicate the presence of liquid in contact with the wall. A general inconsistency between the experimental evidence and the two suggested models for heat transfer (micro-layer evaporation and triple contact line evaporation) was however evident even though not clarified.

Kiger and Moghaddam (2008) experimentally investigated the heat contributions to bubble growth and heat removal for a single bubble growing on a silicon substrate coated with benzocyclobutene and cooled by FC-72. Numerous sensors with temperature accuracy of ± 0.1 K were located radially around three close-spaced cavities in order to have a spatial resolution of 22-40 μm. Analysis of the temperature histories as measured by each sensor suggested the presence of micro-layer evaporation in correspondence of the triple contact line, moving outward as the contact area expanded. The contact area expansion phase was identified as "micro-layer evaporation region": temporal drops (~ 1 ms) of the temperature for the sensor crossed by the contact line were observed. Successively, as the contact area shrank, similar drops were also noticeable because of the rewetting of the surface: this phase was identified as "transient conduction phase". However, the temperature variations seemed to be limited

to a narrow area very similar to the triple contact line area. The heat flux was numerically derived from the temperature variations, showing for the considered case spikes of 20-40 kW/m^2 in correspondence of the temperature drops. Micro-layer evaporation was calculated to contribute only for ~ 21.6% to the total bubble growth in the considered case. The total heat flux generated in the projected bubble area (i.e. the surface area corresponding to the maximum bubble radius) had a much smaller contribution than the total heat necessary for the bubble growth, showing that the heat contribution from the liquid outside the projected area could be severely relevant. Contributions of micro-layer, transient conduction and micro-convection were investigated at different wall temperatures (significantly higher than the saturation temperature of the fluid). Micro-convection, defined as natural convection enhanced by the effect of the bubble growth around the bubble itself, was considered to contribute approximately 2.3 times with respect to pure natural convection. While micro-layer evaporation and transient conduction were not strongly affected by temperature variations, the micro-convection contribution significantly increased with increasing temperature. In a successive study, Moghaddam and Kiger (2009) presented a similar study using a wall temperature lower than for the previous work, so that waiting time was considerable. This case showed a significnalty smaller growth time (even though the rewetting periods were comparable) with almost twice the cooling rates.

2.4. Waiting time, inception and departure of a bubble

Bubble inception (i.e. the creation of a small nucleus able to grow and develop into a bubble), waiting time (i.e. the time elapsing between departure of one bubble and nucleation of a new one at the same nucleation site), and bubble departure have been thoroughly studied during the past years. Still, the involved mechanisms, strictly interacting between them, have not been completely clarified. One of the first approaches developed to study bubble inception was presented by Hsu (1962). It was based on the identification of the most favourable cavity radius. After bubble departure, the region previously occupied by the contact area was supposed to be covered by a liquid layer, which will be heated up, so that the thermal boundary layer thickness will increase. The time necessary for the thermal layer to reach its maximum size (i.e. when the temperature will not increase anymore) was connected to the waiting time. When the temperature in the thermal layer was higher than the temperature of the bubble nucleus, the bubble was supposed to start growing and the waiting time to end. For any given

waiting time and under the conditions that the cavity was filled with vapour/gas and the cavity walls were at constant and uniform temperature, the extremes $R_{cav,min}$ and $R_{cav,max}$ of the range of possible cavity dimensions suitable for initiation were identified, as shown in Equation 2.13.

$$R_{cav,\min/\max} = \frac{\delta(T_w - T_{sat})}{3(T_w - T_\infty)}\left[1 \pm \sqrt{\left(1 - \frac{12(T_w - T_\infty)T_{sat}\sigma}{\delta\rho_v H_{fg}(T_w - T_{sat})^2}\right)}\right] \quad \textbf{(2.13)}$$

However, the condition on the dimension of the cavity was not sufficient to guarantee activation; it was supposed necessary that the thermal layer temperature exceeded the saturation temperature in order to balance the surface tension forces, as expressed by Equation 2.14. The minimum superheat necessary for activation depended on the bubble nucleus radius (r_n) related to the mouth cavity radius (r_{cav}) by the shape of the nucleus, i.e. by its contact angle φ as expressed in Equation 2.15. For contact angle equal to 90°, i.e. for hemispherical nucleus, the bubble nucleus radius and the mouth cavity radius coincided.

$$T_{bulk} = T_{sat} + \frac{2\sigma T_{sat}}{H_{fg}\rho_V r_n} \quad \textbf{(2.14)}$$

$$r_n = \frac{r_{cav}}{\sin\varphi} \quad \textbf{(2.15)}$$

Han and Griffith (1965a) defined the initiation criterion by comparison with potential flow theory: during the waiting time, the thermal conductive layer, previously shown in Figure 2-5, was supposed to grow heated by conduction and its thickness was used to determine the minimum waiting period, and then the most favourable cavity radius. The minimum and maximum cavity radii necessary to have nucleation were derived by equating the fluid temperature to the bubble nucleus temperature assuming the maximum thermal layer thickness equal to its value for natural convection. Activation was supposed to occur only if gas was trapped in the cavity. Direct comparison of the theory with experimental results developed on a 16 ct gold 0.005 inches (~ 0.127 mm) thick plate prepared with emery treatment in orthogonal directions) immersed in distilled and degassed water was not possible. However, the

measured waiting times were larger than the minimum waiting time derived by the theory, so that the results were not in disagreement with the theory. The original project of having fixed cavity sizes on the surface was impossible to be developed because the finished surface was not considered smooth enough. Kenning et al. (2001) hypothesised that inception of a bubble depended on the wall superheat at the nucleation site. It was found by analysis of nucleate boiling on horizontal, vertical and inclined plates that each nucleation site could have different activation superheat, depending on the conditions. This phenomenon should be carefully considered in nucleate boiling numerical models mostly when using probabilistic site distributions: in fact, it was pointed out that relatively small variation of ±10% in each of these two parameters may significanlty affect the results. Analysis of the experimental results showed also that the assumption of Mikic and Rohsenow (1969) of an influence area with a diameter approximately equal to the double of the departure diameter was not confirmed by evidence. Long period experiments are needed to define irregularities and deviation from the average value.

The approach of Forest (1982) was instead based on the evaluation of the stability of vapour nuclei in cavities with axial symmetry but with no other limitations on the shape, e.g. as shown in Figure 2-7. The potential dimensions of the nucleus with respect to the "critical" radius, its rate of increase/decrease and the minimization of Helmholtz free energy were accounted. The walls were assumed to be smooth and homogenous and at constant superheat. In particular, a detailed analysis was developed for a conical cavity, distinguishing between hydrophilic (i.e. with a positive curvature radius of the nucleus for each point of the cavity) and hydrophobic (i.e. with a positive curvature radius when the triple contact line lies outside the cavity and negative inside) conditions. For both the cases, a minimum in curvature radius was identified as necessary condition to have bubble inception without dissolution of the nucleus. A loss of stability was supposed to lead to spontaneous growth of the nucleus and then inception of the bubble. Wang and Dhir (1993b) developed a theoretical analysis of criteria for activation of a cavity area, also based on analysis of Helmholtz free energy. The gas/vapour entrapment was retained as necessary condition for the formation and activation of pre-nuclei requiring a minimum superheat. A truncated sphere shape for the cavities is assumed, extendable to all the kinds of approximately regular cavities where it is possible to identify the three different curvatures of the front of the pre-nucleus. For the mentioned case, the condition for entrapment was identified in a

contact angle larger than the cavity mouth angle. The criterion for stability of the vapour bubble embryo was verified when the dimensionless modified curvature and the dimensionless volume of the vapour bubble nucleus were both either increasing or decreasing at the same time. Nucleation was assumed to occur when the dimensionless modified curvature had a maximum.

The effects of the cavity shape were investigated by Shoji and Takagi (2001) via experiments on a copper disk (0.1 mm thick) with micro-fabricated cavities immersed in a boiling chamber with distilled water at atmospheric pressure. Three cavity shapes, as shown in Figure 2-8, and sizes were evaluated and tested separately: conical on the left (50 µm diameter and 30 µm depth; 100 µm diameter and 50 µm depth), cylindrical in the middle (50 µm diameter and 30 µm depth; 100 µm diameter and 50 µm depth) and re-entrant on the right (100 µm diameter and 50 µm depth). The temperature series were measured by radiation thermometers at different heat fluxes (generated by laser irradiation). Conical cavities showed strong intermittence and low ability to hold bubble

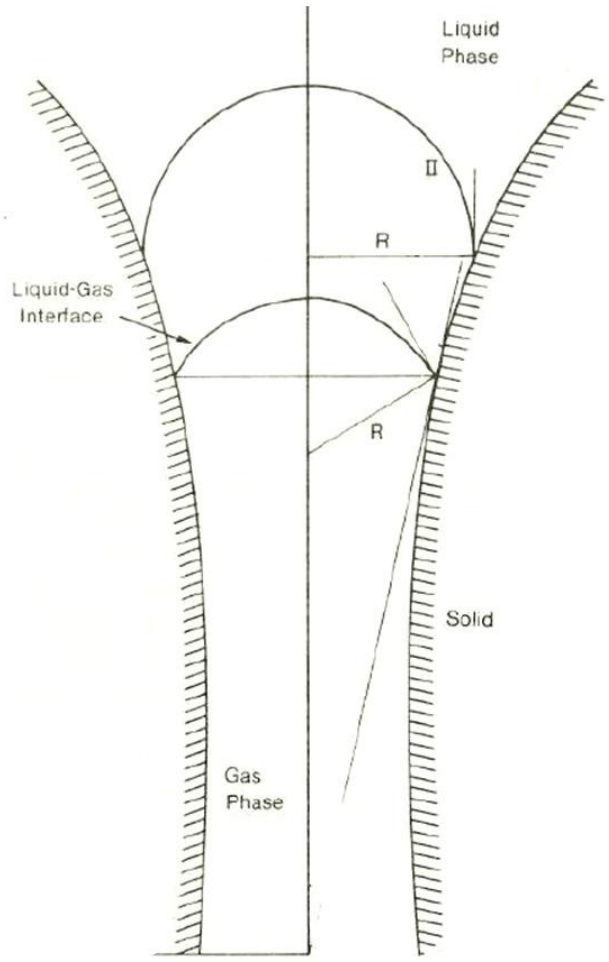

Figure 2-7: Cavity shape (Forest, 1982)

nuclei. Triangular waves with large variations in temperature and large waiting time were detected mostly for low heat fluxes and small cavity size. In these cases the temperature recovered during the waiting time so that at nucleation a drastic reduction of the measured temperature occurred. For larger cavities, higher stability was common also at low heat fluxes. The first bubble after a significant waiting time was followed by a series of smaller and more spherical bubbles with smaller temperature drops. However, stable activity was shown only occasionally for small cavities. Cylindrical and re-entrant cavities showed significantly higher stability and almost zero waiting times also at low heat fluxes, highlighting the higher capability of the cavity to hold a nucleus. Smaller temperature variations and bubble sizes than for conical cavities were detected, with a shape more similar to a perfect sphere. For all the types of cavities, vertical coalescence was observed: the frequency increased with increasing heat fluxes.

The effect of the contact angle on boiling incipience was investigated by Tong et al. (1990). Wettability of the surface was considered one of the most affecting variables for the process. Nucleation was supposed to be either homogeneous (if nucleation occurs only from vapour nuclei) or heterogeneous (vapour or gas are trapped in the cavities and generate the embryonic nuclei). The contact angle was classified according to the movement of the triple contact line: it is defined "static" (β_{stat}) if the triple contact line is considered stationary and "dynamic" (β_{dyn}) otherwise. Static and dynamic contact angles were further classified in advancing and receding. For the dynamic angle, the distinction depends on whether the liquid-vapour interface is moving towards the vapour/gas region (advancing, $\beta_{dyn,adv}$) or away from it (receding, $\beta_{dyn,rec}$). During bubble growth in a conical cavity with cone angle $2\varphi_{cav}$, four stages can be identified, see Figure 2-9: an initial phase where the contact angle adjusts due to hysteresis (a), followed by an in-cavity growth (b), growth at the cavity mouth (c) and finally the growth outside the cavity (d). For each phase, the contact angles were identified. Considering heterogeneous nucleation, the trapping process was assumed to be possible for dynamic contact angles larger than the cavity cone angle (criterion attributed to Bankoff, 1958). The ratio of the bubble to cavity mouth radii was plotted versus the

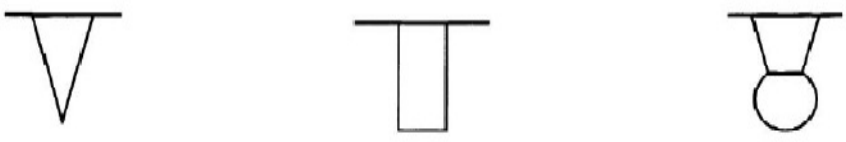

Figure 2-8: Different micro-fabricated cavity shapes (Shoji and Takagi, 2001)

difference between dynamic and static contact angles: it appeared that, fixing the static contact angle, an increase of the dynamic contact angle led to an increase of the bubble to cavity mouth radii ratio, i.e. of the embryonic curvature. For highly wetting liquids, this parameter was always lower than one, while greater for low and moderately wetting liquids and small cavity cone angles. The proposed results were compared to previous results (reported from Lorentz, 1972), developed by using a static instead of dynamic contact angle. Only a small difference was noticed in the curves despite the more complex analytical formulation; the difference increased with increasing cavity cone angles. In Tong et al. (1990), the necking process, called "snapping" process, was also explained, as shown in Figure 2-10. The bubble initially expands (a) and starts to elongate (b), the bubble neck starts to form (c), the triple contact line moves inside the cavity (d) and finally the neck disappears (e). This process was considered very important for the creation of a new nucleus, generated by the vapour or gas left in the cavity during the snapping process. The minimum radius of the embryonic nucleus, called "critical radius", was then connected to the superheat needed for bubble initiation, and then compared with results from use of Clausius-Clayperon condition (that assumes a linear saturation curve), showing lower initiation superheats in the considered case.

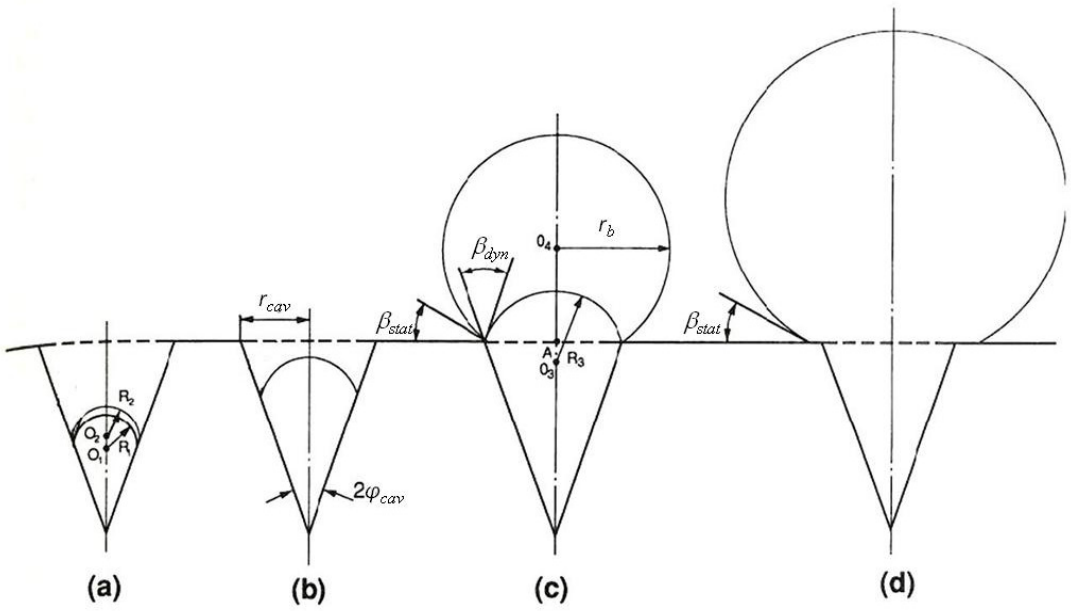

Figure 2-9: Bubble growth stages (Tong, 1990)

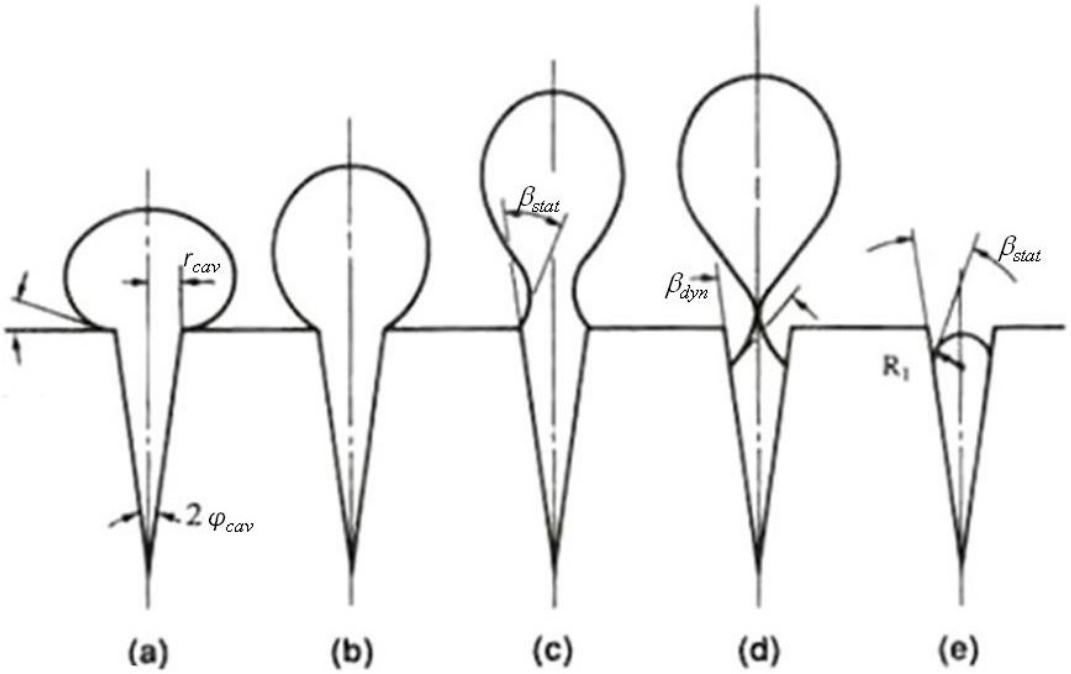

Figure 2-10: Necking process and bubble departure (Tong, 1990)

2.5.Micro-layer theory

Aspects of the micro-layer theory have been already analysed before, even though with focus of their effects on the bubble growth. However, due to the complexity of the phenomena and to the different studies developed over the years, a separate section was necessary to provide a complete description. Moore and Mesler (1961) are reported by Tong and Tang (1997) to be the first ones to introduce the idea of micro-layer evaporation as main contribution to the bubble growth. Many authors (e.g. Cooper and Lloyds, 1969, Stralen et al., 1975, Mikic and Rohsenow, 1969, just to indicate some) investigated the existence and the importance of its contribution to the bubble growth and to heat removal from a surface. Cooper (1969) developed a theoretical study aimed more to define a background for future developments than to provide an accurate and comprehensive description of all possible cases. Two models were distinguished for bubble growth, as shown in Figure 2-11. In the first case (a), the bubble is completely surrounded during its growth by a thermal boundary layer, defined as the thickness of liquid that produces the temperature drop from the wall value to the liquid bulk value by accounting only for conduction in the liquid itself. For a larger bubble, the radius is greatly larger than the thermal boundary layer (b). The analysis here was applicable only to case (b): the thermal boundary layer contribution was assumed to be not very

relevant to bubble growth. It was also assumed that the pressure in the bubble was almost uniform, and inertia and viscosity had a negligible effect. The bubble was supposed to grow with an almost hemispherical shape, with a conductive micro-layer forming below the contact area with a central dry spot, see Figure 2-12. An explicit solution for the bubble radius as function of time, both for poorly conducting liquids on a high conductive wall (and particularly for non-metallic liquid boiling at almost atmospheric pressure) and for highly conductive liquids (liquid metals) was derived, see respectively Equation 2.16 and Equation 2.17 below. In particular, it was pointed out that for metallic liquids (i.e. sodium, highly conductive) the micro-layer contribution can be of the same order as the heat flow at the dome of the bubble; for non-metallic fluids, instead, very high pressure may lead to small bubbles with size comparable to the thermal boundary layer thickness, making this formulation inexact.

$$R = 2.5\frac{Ja}{\mathrm{Pr}_L}\sqrt{\nu_L t} \qquad \textbf{(2.16)}$$

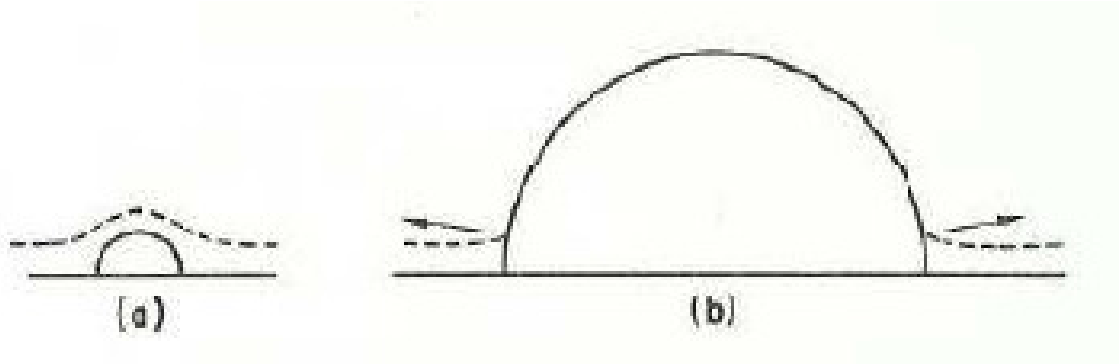

Figure 2-11: Bubble growth models for bubble completely surrounded by the thermal boundary layer (a) and growing outside it (b) (Cooper, 1969)

$$R = 1.12\sqrt{\frac{k_W \rho_W c_{pW}}{k_L \rho_L c_L}} Ja \sqrt{\alpha_W t} \qquad \textbf{(2.17)}$$

At the same time, Cooper and Lloyd (1969) experimentally studied the contribution of the micro-layer to bubble growth from the analysis of temperature histories for toluene and isopropyl alcohol on glass and toluene on ceramic with three different sets of heat fluxes, three sets of liquid bulk temperatures and three sets of system pressures. The glass or ceramic sheets were heated from below by radiation and were cooled at the upper surface. Film resistance thermometers were used at the liquid-heater interface in order to deduce the temperature histories from which the heat flux was calculated by integration. Contrarily to previous models, the temperature in the heater was not supposed uniform to be in this case, but variable with time and space. The presence of a thin micro-layer was supposed to have an initial thickness equal to δ_0. Three different methods were studied to obtain this value and then compared, showing a reasonably good agreement mostly for smaller bubbles. A limiting assumption is related to the bubble growth, supposed to be hemispherical, with micro-layer evaporation through the bubble base, evaporation from the thermal boundary layer and condensation into the bulk of fluid on the upper part of the dome of the bubble. According to these

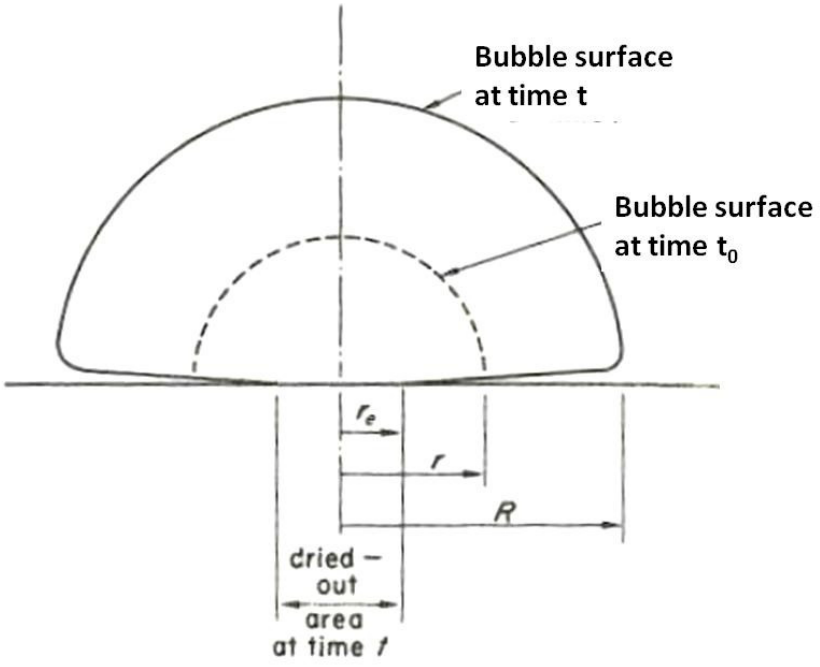

Figure 2-12: Hemispherical bubble growth shape (Cooper 1969)

conditions, an expression for the initial micro-layer thickness is shown in Equation 2.18, with $C = 0.8$ from theoretical considerations and between 0.5 and 1.0 from experiments. The effect of the macro-layer evaporation may become significant for bubbles that rapidly grow to a large size.

$$\delta_0 = C\sqrt{\nu \cdot t_g} \tag{2.18}$$

Judd and Hwang (1976) developed a model to predict the total heat flux on the base of their experimental findings, accounting for micro-layer evaporation, natural convection and nucleate boiling contributions. The micro-layer contribution to heat removal was accounted as the product of the energy due to evaporation of the micro-layer for a single bubble, the average bubble frequency and the site density. The natural convection contribution was calculated as the product of the average natural convection heat flux and the fraction of area where this contribution is involved over the total area. The nucleate boiling component was calculated as the product of the average heat flux needed to form the superheated layer and the average fraction of area affected by micro-layer evaporation and nucleate boiling (including the influence area defined as the portion of area such that the thermal layer contained in there is transported to the surrounding liquid). According to their findings, the micro-layer evaporation component plays a relevant role in determining the total heat transfer. Benjamin and Balakrishnan (1996) considered an approach similar to the one suggested by Judd and Hwang (1976) to find the total heat flux ($\dot{q}_{tot}$) removed from a surface. Three different heat contributions were identified and weighted according to the average time they occurred, as in Equation 2.19. The contributions were the heat flux due to evaporation of micro-layer ($\dot{q}_{ML}$) during the bubble growth (t_g), the heat flux removed when the thermal boundary layer is restored after departure of a bubble ($\dot{q}_{Rest}$) during the waiting time (t_{wait}), and the heat flux for natural convection ($\dot{q}_{NC}$). The waiting time and the growth time are complementary.

$$\dot{q}_{tot} = \frac{\dot{q}_{ML} t_g + \dot{q}_{Rest} t_{wait}}{t_g + t_{wait}} + \dot{q}_{NC} \tag{2.19}$$

The micro-layer evaporation contribution was determined on the base of Ünal (1976) assumptions for the determination of micro-layer thickness. The micro-layer was assumed to evaporate almost completely at the end of the bubble growth. After bubble departure, fresh liquid was supposed to come in contact to the surface so that the thermal boundary layer could be restored; pure conduction was assumed between the bubble departure and the new activation, i.e. during the waiting time. It was assumed that the area affected by bubble departure and re-formation of the thermal boundary layer (area of influence) has a diameter equal to the double of the bubble departure diameter (a similar assumption was used in Mikic and Rohsenow, 1969). Both $\dot{q}_{ML}$ and $\dot{q}_{\mathrm{Re}st}$ included the nucleation site density in their formulations, calculated on the base of roughness, wall superheat and a parameter involving liquid and heater thermal properties. A hypothesis of not interference between neighbouring sites, valid only for low heat flux regimes, was also used. The final correlation was compared with experimental results presented in the paper and also from literature showing a good agreement in the range of application.

Guo and El-Genk (1994) carried out a numerical investigation of the micro-layer evaporation during nucleate boiling for a composite wall, as shown in Figure 2-13. A 1-dimensional model was used during the waiting time substituted by an axial-symmetric 2-dimensional conductive model during bubble growth, with a dry spot (with negligible heat transfer coefficient) in correspondence of the central part of the contact area. The micro-layer was calculated at each time step by using an evaporation model. Its thermal and liquid-vapour interfacial resistances (adjusted by the use of an accommodation coefficient) were accounted in calculations. The liquid flow and heat convection in lateral direction and thermal capacity were assumed negligible because of the small thickness. Numerical simulations were carried out and compared with experimental results from Koffman and Plesset (1983) for a pyrex glass substrate (3.2 mm thick) coated with SnO_2 (30 μm think). The model over-predicted the micro-layer thickness (δ_{ML}), probably because of successive nucleation from the same nucleation site and consequent variation of the dry spot area size were not correctly calculated. This effect was numerically investigated by varying the length of the waiting time. It was noticed that the dry spot for the second bubble was more similar to the first one for increasing waiting times. Strong variations in heat flux (and then in the temperature in the substrate along the radial direction) could be observed, mostly in correspondence to the radially

moving triple contact line. The effects of material and thickness of the substrate were also investigated, concluding that an increase of the lateral conduction effect increases the evaporation rate and then the growth rate of the dry spot. The results were compared with simulations imposing an isothermal wall (as assumed in several mechanistic models): over-prediction of the dry spot radius was shown for the latter, principally for thin substrates where lateral conduction could play a very important role. Also Mitrovic (1998) presented an analysis of the micro-layer based on simplification of the Navier-Stokes equations applicable to models assuming a smooth surface. The micro-layer profile is assumed to be fixed in space, with stationary film evaporation. The necessity of the existence of a wedge-shaped micro-layer under the bubble, with a central dry

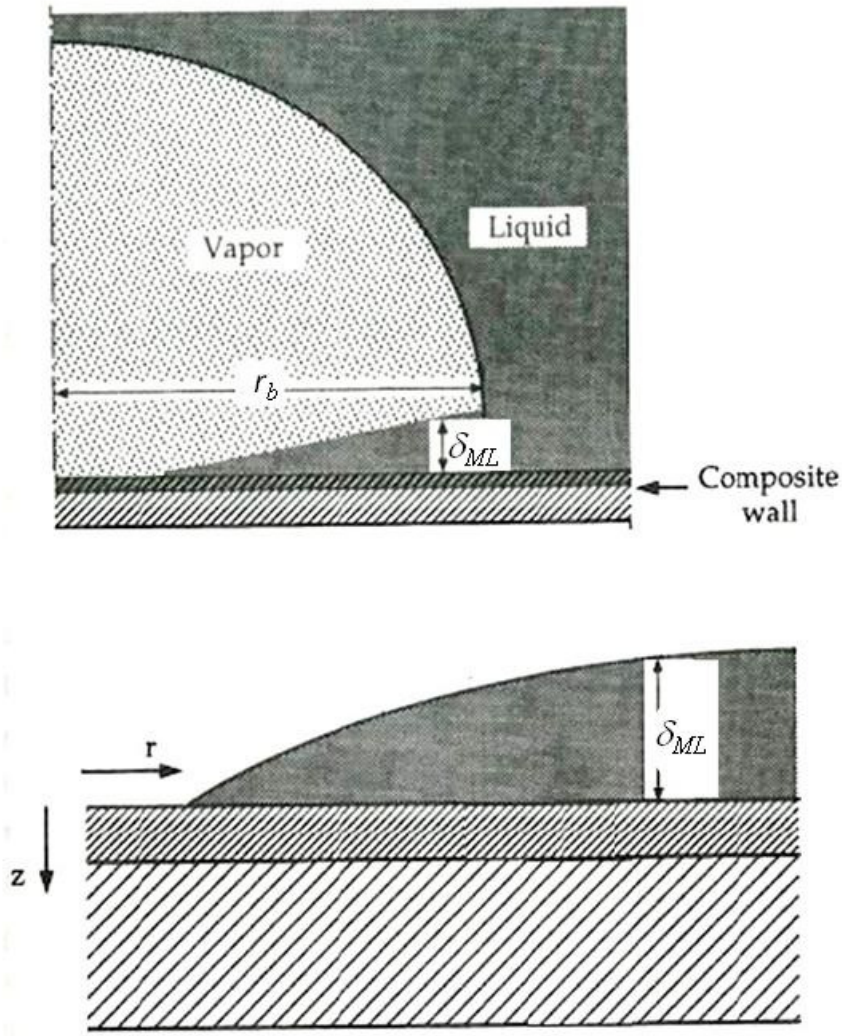

Figure 2-13: Micro-layer evaporation for a composite wall (Guo and El-Genk, 1994)

zone with direct contact between vapour and wall in the central region of the contact area, was justified by the impossibility of creation of the bubble nucleus otherwise (except for the case of homogeneous nucleation). Comparison with previously existent literature models simulating the micro-layer and the triple contact line evolution showed inconsistencies in previous models assuming motionless triple contact line and no fluid velocity in direction orthogonal to the plate.

2.6. Effects of the surface characteristics on the nucleation sites density

The models suggested for a single bubble growth are not usable to describe the heat transfer coefficient and heat removal from a surface in industrial applications. The first approach to solve this inconvenience was the evaluation of the heat removed by a single bubble with the assumption that it was valid for all the bubbles. The single bubble model was then applied to a larger surface by combining the effect of one bubble with the population of bubbles. The problems in using this approach are mostly connected to irregularities in activation of the sites and to overlapping of the effects of two or more close-spaced nucleation sites. One of the first models was proposed by Mikic and Rohsenow (1969). The number of active sites per unit area of heated surface (N) was obtained by combination of dimensionless groups, Equation 2.20: a power law dependence on the cavity radius (exponent = m) and the Clausius-Clapeyron condition was used. Two different approaches were used, depending on the characteristic of the liquid at the operating conditions and on a particular cavity radius (r_{cav}) corresponding to an active site density equal to one. The first approach used coefficients and power exponents determined by interpolation of the available data for different liquids and heater materials in one very general correlation, with the great advantage of applicability to a great variety of conditions, but with a significant loss of accuracy. The second approach was based on the choice of specific coefficients and power exponents for each liquid-heater couple, with a very high precision in prevision inside the range of applicability, but requiring experimental results for each prevision, with a consequent loss of generalization.

$$N = C_1 r_{cav}^m \left(\frac{H_{fg} \rho_V}{2 T_{sat} \sigma} \right)^m (\Delta T)^m \qquad \textbf{(2.20)}$$

An analysis of the spatial site distribution of active sites was carried out by Sultan and Judd (1978), starting from the point of view that surface roughness cannot characterise nucleate boiling properly, considered only an indirect measure of the distribution of active sites. Experiments with copper and water at atmospheric pressure and with variable heat fluxes and bulk sub-cooling showed that sub-cooling has only a slight effect on superheat and on cumulative percentage of bubble flux density. Instead, an increase in sub-cooling led to an initial increase and a subsequent decrease in the average bubble frequency. An increase in heat flux led to a significant in the number of the active site density. A formulation for the probability $\Gamma(Na)$ of finding *N* active sites in an area *a* was theorised to have a Poisson distribution, as shown in Equation 2.21.

$$\Gamma(Na) = \frac{e^{-\overline{Na}}(\overline{Na})Na}{(Na)!} \qquad \textbf{(2.21)}$$

Shoukri and Judd (1978) suggested that nucleate boiling was related to the bubble flux density (defined as "the rate of bubble emission per unit area of the boiling surface") that accounts for both the variation of activity for each site and of bubble site activity at the same time, more than for each of them separately. The bubble flux density was correlated to the frequency of bubble departure in a range of maximum and minimum cavity mouth radii. A different approach was attempted by Yang and Kim (1988). It was suggested that the nucleation site density could be obtained as the product of the average nucleation density and the integrals of two different site distributions (functions of the contact angle and of the cavity radius), so that a complete separation of the effects was supposed. A Poisson distribution was assumed for the cavity radius function and a normal distribution for the contact angle function. The cavity depth and the cavity mouth radius were experimentally measured, so that the cavity angle could be derived. The lower boundary used for integration of the cavity size distribution was related to the surface tension and wall superheat, while the upper boundary was related to the material and finish of the surface, generally preferred to the higher maximum entrapment radius. For the contact angle distribution, the function was integrated between 0 and 90°. The theoretical model was compared with some experimental results showing a reasonable agreement, but the considered data were not enough for a complete validation. Also Wang and Dhir (1993a) analysed the effect of cavity shape and size on the number of active nucleation sites. The experimental results were

obtained for a very smooth polished vertical surface and they are possibly not applicable for a horizontal surface. The cavities generating stable nuclei were supposed to have a pseudo-truncated sphere shape, called “reservoir type” cavity; deviation from the perfect shape were accounted by a shape parameter in the definition of the cavity diameter. Even though cavities with conical shape were maintained to be more common than the reservoir type ones, the large mouth diameter and the low depth of the first ones make them not likely to allow nucleation. The distribution of cavities was initially identified and categorised: the size and mouth angle of the cavity (defined as the side angle at the mouth of the cavity) were related to the wettability of the surface through the contact angle. A final correlation of the density of active sites to the superheat or to the heat flux was then derived. The cavity mouth diameter was experimentally determined as the equivalent diameter for the cavity mouth area. A distinction was made between the number of cavities and the number of active cavities, used to define respectively the cumulative site density and the cumulative active site density. The cumulative site density was experimentally obtained with a microscopic analysis of a sample of a second surface obtained with the same standard procedure as the test one. The nucleation site distribution was described by a Poisson distribution. For the considered cases, an explicit dependence of the active cavity diameter on the wall superheat was suggested. The effect of the contact angle (as average value of its receding and advancing values) was studied by modifying the wettability of the fluid (experimentally obtained by oxidation of the surface). According to their findings, an increase in wettability leads to a decrease of the active nucleation cavities.

Several methods of derivation of the nucleation site density were based on measurement of the surface characteristics. In this ambit, Benjamin and Balakrishnan (1996, 1997) suggested the correlation given below in Equation 2.22 valid for several liquid-surface combinations. The liquids used were n-hexane, distilled water, acetone and carbon tetrachloride, and the surface materials were stainless steel and aluminium. The correlation is based on the dimensionless roughness parameter (θ_{rough}), depending on the measurement of the roughness (obtained with the “Perth-o-meter” method) intended as the average value of the absolute values of the ordinate.

$$\frac{n}{A} = 218.8\theta_{\text{rough}}^{-0.4}\,\text{Pr}^{1.63}\frac{1}{\gamma}\Delta T^{3} \qquad \textbf{(2.22)}$$

The correlations for the nucleation site density and dimensionless roughness parameter were obtained by interpolation of experimental data, both newly generated and from literature. The nucleation site density was supposed to depend on Prandtl number (in order to account for the liquid viscosity), on γ (a surface-liquid interaction parameter defined as "the ratio of thermal diffusivity of the solid to the liquid and the heat content of the solid to the liquid") and on superheat. A decreasing-increasing behaviour characterised the dependence of the site density on roughness, with a local minimum. Instead, Qi et al. (2004) suggested the use of statistical methods based on metrology technology analysis of industrial surfaces in order to predict the active nucleation site distribution. Using a gas nucleation facility similar to the one described in Eddington et al. (1978) with brass and stainless steel plates immersed in depressurised water, the nucleation site distribution for different values of depressurisation was determined. In particular, a higher bubble density was observed for the brass surface. Since the static liquid/solid contact angles were very similar for the two materials, the different site densities were attributed to the surface structure. From here, the idea originates to statistically analyse the surface, scanning it along specific directions (randomly chosen), and automatic computing the potential activation cavities from the shape of the surface profile (with specific criteria for cavities residing inside other cavities). Using Bankoff's criterion (Bankoff, 1958) to establish if activation was possible at variable depressurisation values, a very poor agreement between prediction and experiments for stainless steel was found. For brass, the results were much more similar, but the authors themselves were sceptical whether it was "purely fortuitous". The predictive method determined very low probabilities of finding a cavity. The method was therefore considered unsatisfactory to be used to predict nucleation site densities for commercial purposes.

2.7. Interaction mechanisms

Since a method correlating directly the heat transfer rates based on the active nucleation site density cannot provide a useful instrument of prediction because possible interactions between sites are not accounted for, the analysis of the effects of one site on the others must be evaluated. This phenomenon becomes particularly important at high heat flux. One of the first theories on the effect of one site on the activity of a second one (either improving or inhibiting it) was suggested by Eddington et al. (1978). Site activation was analysed by using two different techniques, 1) by gas bubble nucleation

and 2) by vapour bubble nucleation. Variation of the pressure in the gas nucleation experiments was intended to reproduce the different superheat or sub-cooling levels during vapour bubble nucleation, for pressure respectively lower and higher than the vapour pressure at saturation. The experiments, developed on a brass surface, were not intended to be completely comprehensive because of the small amount of available data, but to provide a new approach in studying nucleation boiling. A large number of stable sites that were active during gas bubble nucleation seemed to be inactive for vapour bubble nucleation (~ 65%). The inactivity phenomenon was explained with a possible "thermal interference" between sites located in the area of influence of an active site, the latter supposed to have a diameter equal to the double of the bubble departure diameter. A "seeding effect" (defined as the activation of an unstable site by an adjacent stable active site) was not detected during these experiment, but was referred as important in another series of experiments described in Eddington and Kenning (1979).

The presence of thermal interference and site seeding effects was confirmed by Judd and Lavdas (1980). Regarding thermal interference, it was noticed from analysis of visual experiments that one site may stop its activation after the bubble contact area at an adjacent site covers the first nucleation site. It was concluded that the nucleus existing at the first site could have been displaced by the second bubble. Similarly, it was detected that one site could become active after departure of a bubble at an adjacent one: this effect was attributed to the formation of a new nucleus at the first site after the dry spot of the adjacent one had receded. The concept of influence area was also reviewed: a coefficient $1 < K < 4$ (decreasing if the influence areas overlap) was defined as the ratio of the energy extraction area to the projected bubble area at departure. The energy extraction area was defined according to the concept of influence area defined by Judd and Hwang (1976).

A detailed possible sequence of events for site seeding was indicated in Calka and Judd (1985), as shown in Figure 2-14. At step 1, a bubble starts growing at site A while site B is inactive, and once the micro-layer is formed (step 2) the contact area continues to grow until it reaches its maximum size: the contact area of bubble at site A has now covered site B (step 3). Then, it shrinks until departure (step 4), with a small vapour nucleus deposited at site B that starts growing (step 5) and departs (step 6). Using a transparent glass surface immersed in dichloromethane, the site interactions between 24 identified active sites were analysed at different experimental conditions (variable pressure and heat flux). Comparison of the histograms of the probability density

functions (gamma distributions based on the shape parameter v) for two different couples of sites showed that the choice of a gamma distribution was satisfactory. Plotting of the shape parameter, v, versus the dimensionless separation distance (S/D_b, where D_b is a cautionary average value of the departure bubble diameter chosen accordingly to their previous experiments, presented in Judd and Hwang, 1976) is shown in Figure 2-15: a unique relationship could be clearly identified. A shape parameter greater than one implies a "promotive" effect while "inhibitive" effects occur for values smaller than one; no interaction was supposed if $v \sim 1$.For dimensionless separation distance lower than one, the shape parameter is larger than one, showing a promoting effect (compatible with the aforementioned seeding effect); for dimensionless distance larger than three, no interaction is evident (shape parameter tends to one). An inhibitory effect (thermal interference), not completely understood, for shape parameter values between one and three is present. The results were reported to be in disagreement with results from Chekanov[1] (1977), as shown in Figure 2-16.

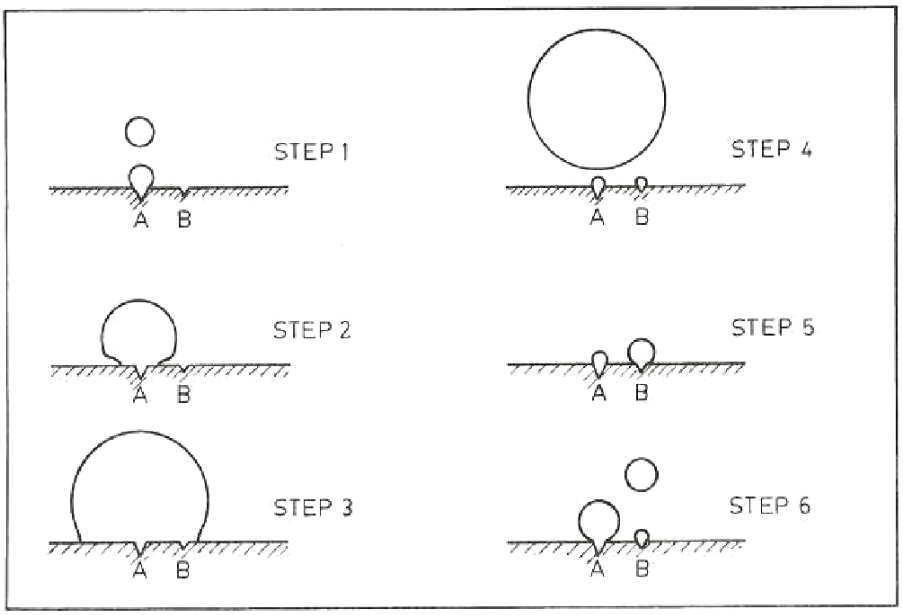

Figure 2-14: Site seeding: sequence of events (Calka and Judd, 1985)

[1] Paper in Russian, so comments are deduced from citations in the work of Calka and Judd (1985)

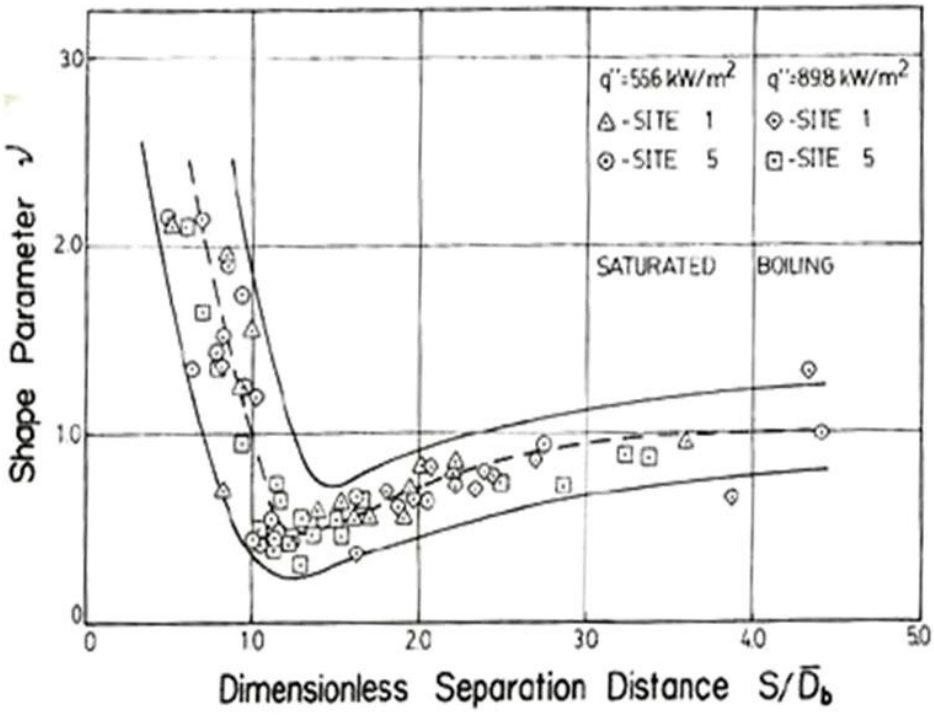

Figure 2-15: Site interactions (Calka and Judd, 1985)

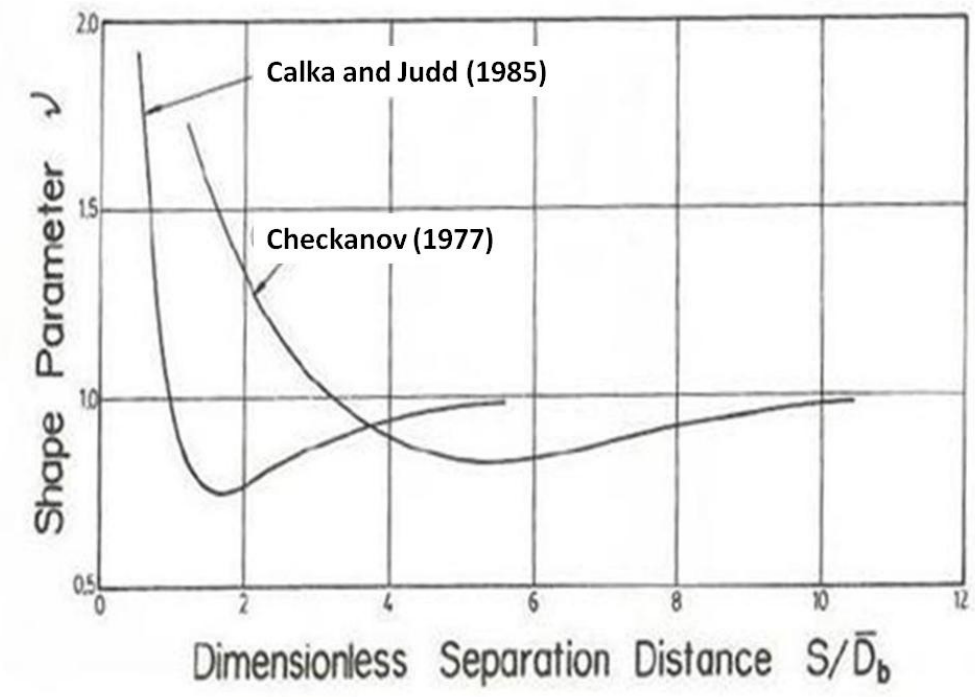

Figure 2-16: Comparison of site interactions with results from Chekanov (1977) (Calka and Judd, 1985)

The non-linearity of the systems due to interaction between sites was studied by Sultan and Judd (1983). The dependence of the time t (defined as the elapsed time between bubble formations) at two adjacent nucleation sites located at distance S was studied for different sub-cooling values and input heat fluxes. It was shown that at saturation conditions the influence disappeared for distance approximately equal to the double of the bubble diameter. Particularly, plots of (t- t_g) versus (S- R_b) showed a good fitting if compared with the predictive correlation[2] based on heat diffusion theory in the heating surface, suggesting that the site activation can depend on bubble growth (t_g) instead of on waiting time. Influence between adjacent nucleation sites was considered very relevant: assumption of applying isolated bubble growth theories for industrial surfaces would lead to incorrect results. Successively Judd and Chopra (1993) also investigated the inhibitory and promoting effects on adjacent sites, assuming a gamma function of shape parameter v for the nucleation site distribution. Anyhow, the presence of a small amount of vapour trapped in a cavity was supposed necessary for bubble inception. The identification of the site distribution of all the sites as they became active during the experiments was carried out. The variation of t after applying different input heat flux and saturation pressure in the liquid was analysed. An increase in saturation pressure led to smaller bubble radii and then larger S/D_b ratio. The associated gamma distribution revealed that the S/D_b ratio by itself does not play a fundamental role in modifying the site activation at adjacent sites, while each of the two variables (S and D_b) does, in conjunction with the active site distribution. The presence of a dominant site at a very close distance ($S/D_b < 1$) can deposit a small nucleus of vapour in the cavity corresponding to a second nucleation site, with a "promotive" effect. At the contrary, when the ratio increases, "inhibitive" ($1 < S/D_b < 3$) or "independent" ($S/D_b > 3$) effects can be observed. A different behaviour can appear for two dominant sites located close to each other: inhibitive effect, mostly at high heat fluxes, can be observed.

Mallozzi et al. (2000) developed a numerical method to match experimental results from Chopra (1992) to continue the study of the effect of nucleation sites interactions. Previous literature results were investigated, noticing common results for $S/\overline{D}_b < 1$, but contradictory effect for $1 < S/\overline{D}_b < 3$; for the last interval, according to Calka and Judd (1985), an inhibitory effect was evident, while the reported results of Knowles (1984) for a similar surface showed an essential indifference, attributed by

[2] The correlation is reported to be derived in Sultan (1981), not available

Judd (1988) to the different length of time that the surface had been used for. A numerical analysis of the experimental results, called BoilSim, assumed a Poisson distribution for the site distribution, with distinction between dominant (continuously active) and passive (irregularly or not active) nucleation sites. A probability of 50% that a passive site becomes active because of seeding of adjacent sites (either dominant or passive) was imposed. Because of the required numerical power, only 10 active nucleation sites were simulated. In particular, the experiments of Chopra (1992) were numerically reproduced, with one dominant site and two passive sites, located at different distances from the dominant site. A good qualitative agreement in identifying the influence areas was achieved, as shown in Figure 2-17, with promotive effect for $S/\overline{D}_b < 1$ and no effect for $S/\overline{D}_b > 3$, even though the inhibitive effect present in some of the cases for $1 < S/\overline{D}_b < 3$ was underestimated.

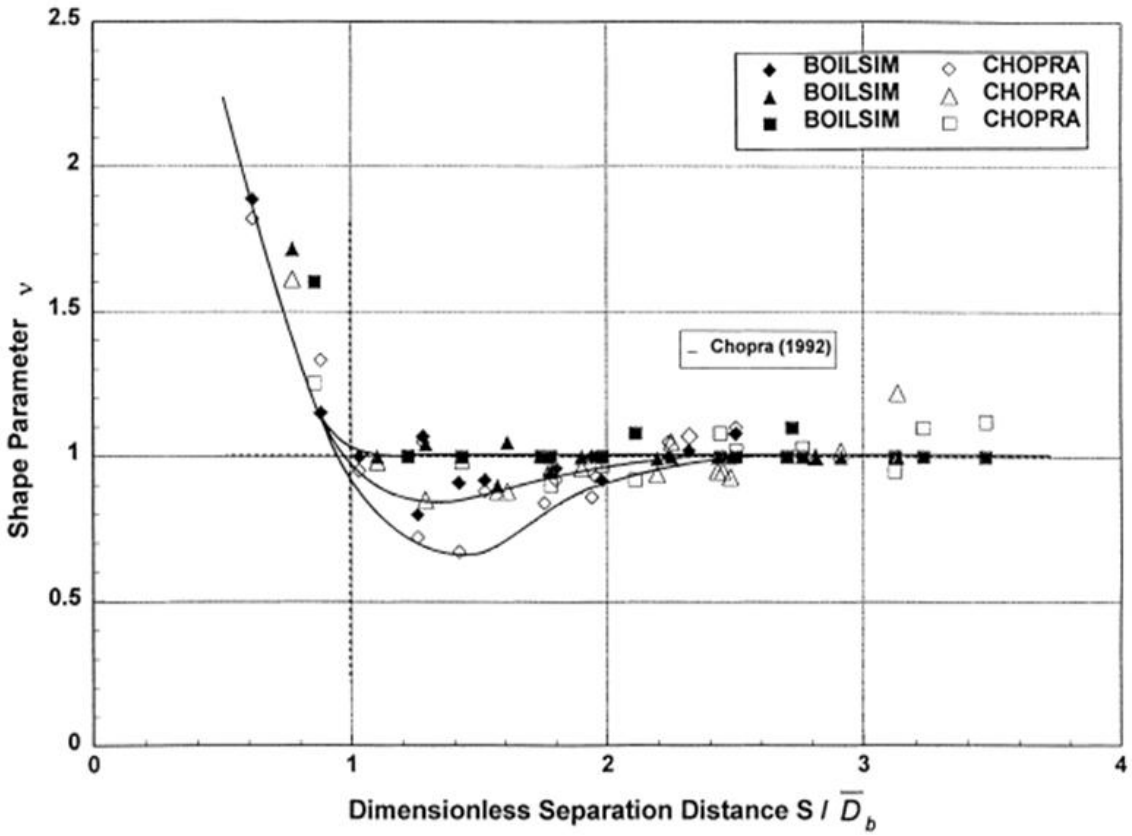

Figure 2-17: Experimental site interactions from Chopra (1992) and comparison with numercal analysis (Mallozzi et al., 2000)

Kenning (1992) demonstrated the importance of accounting for spatial variations of superheat on solid plates, mainly for small thickness. Deterministic models assuming a uniform superheat oversimplify the problem and may be valid only in a small range of conditions. For the experiments, a 0.13 mm thick stainless steel plate immersed in water was used, with spatial temperature distributions detected by thermochromic liquid crystals. Three series of experiments were run for the same plate (initially subjected to vigorous boiling), varying the surface final treatment in order to modify the wettability. The first surface was not polished after the initial boiling, while for the second and third surfaces, the polishing process was performed in order to obtain respectively a poorly-wetted and a highly wetted surface. Analysis of results showed important spatial variations of superheat (from 20 to 150% respect to the average spatial value), with a strong effect of wettability. Characteristic ring-shaped cold areas were identified in correspondence to some nucleation sites. For the poorly-wetted surface, a large population of sites, that were continuously active was noticed, clashing with the well-wetted case, for which only a small number of sites, acting intermittently and with larger bubble sizes was imputed. A different behaviour was supposed to possibly occur for thick plates that cannot be studied with thermochromic liquid crystal because of the attenuation factor $\sqrt{\alpha / f}$ (with α the thermal diffusivity and f the average bubble frequency). The temperature distortion through the plate for measurements on the back of the plate may significantly affect the results. The site distribution and spacing are considered to play a fundamental role depending on the types of surface, fluid and pressure. Hysteresis (mostly for well-wetting fluids), interaction between sites and irregular behaviour of the sites (e.g. intermittency) were supposed to strongly increase spatial variations. A large influence of these phenomena should discourage from using models with active site densities. In particular, if interaction between sites is relevant, mechanistic models assuming isolated sites with not overlapping influence areas should be revised. Interactions between sites were also investigated by Kenning and Yan (1996). Thermo-chromic liquid crystals were used during nucleate boiling of sub-cooled water at atmospheric conditions on a thin stainless steel plate (0.13 mm thick), electrically heated with variable input power. At the same time, site activity was visually recorded. Lateral conduction is minimised by the small thickness and local variation in temperature maximised. Water was degasified, but the concentration of gas

was not controllable since the water was kept in an open tank. The drawback of the use of liquid crystal thermography is the low frequency response with respect to thermocouples, compensated by the possibility of having an extensive image of the whole area instead of just at specific locations. Several analyses were performed at variable contact angles obtained using different liquids and variable heat source. Variation in wettability led to completely different bubble growth phenomena and temperature distribution. The case of high wettability (contact angle 20°) was specifically analysed. Increase of the heat source led to an increase of the average number of active sites that generated columns of rising bubbles for high heat power. It was noticed that contribution from convection decreased for increasing heat flux. The average superheat was approximately 15 K for an applied heat source equivalent to 50 kW/(m^2K). Analysis of the time evolution of the wall temperature showed a continued decrease in proximity of the nucleation site during the whole bubble growth, in obvious contradiction with the dry spot theory that supposes a partial recovery of the temperature at the centre of the contact area. Another important observation is related to the area of influence that seemed to be equal to no more than the bubble size, contrarily to the theory of Mikic and Rohsenow (1969), which supposed it approximately equal to the double of the bubble departure radius. Symmetry of the bubble was evident only for isolated bubble, while for interacting sites, the distortion in shape seemed significant. Formation of a micro-layer with variable thickness was assumed: still, its complete evaporation and formation of the dry spot was not confirmed by experiments that instead showed a central heat flux peak in correspondence of the nucleation site, with a decrease towards the contact line. An enhanced heat transfer in the area immediately outside the area defined by projection of the bubble radius was also noticed, possibly due to convective effects. High heat transfer was observed also after bubble departure: for an isolated bubble, during the waiting time the temperature recovered until it reached an activation value specific for each site. The sites identified during the examined time showed different activation temperatures and activities; activities strongly varied with the experimental conditions. Analysis of close-spaced sites showed that a site may be deactivated by cooling from an adjacent site with lower activation superheat, if the first nucleation site is located in its influence area. But still, a rule based only on activation of the site with lower superheat may lead to erroneous results since a third site may interfere with them. For instance, a high superheat site generating

bubbles with large radii may affect adjacent sites with lower superheats but smaller influence areas.

Another approach to experimentally evaluate site interactions was attempted by Golobič and Gjerkeš (2001). A laser setup for copper and titanium plates was used, concentrating the heat source in a restricted area (heated spot) out of a possibly larger heated area in order to obtain activation at specific locations. Up to four locations with different input heat flux were analysed. It was observed that for isolated bubbles and small heated spot the bubble departure diameter depended on the heated spot area, while for larger heated spot the effect was not relevant. Influence of surroundings on site activations was analysed by tuning the input heat flux on the larger area: its increase led to a different response for the two metal materials (copper and titanium), due to the different thermal capacity, and to an increase of the bubble departure diameter. The experiments highlighted that the level of interaction increased with shorter distances between nucleation sites, producing a variation in activity for both the sites, either reducing the activity of both or increasing it for the first one and decreasing it for the second one. Stronger effects were generally evident if the distance to bubble departure diameter radius ratio is approximately one or lower than that. In case of very short distance between two identically heated sites, one site may inhibit the second. The behaviour for three or four sites was also investigated: the input heat flux for some of them was kept constant, while it was gradually increased for the others. This procedure was able to highlight the strong inhibitory effect of the distance between adjacent nucleation sites, and the general decrease of the activity of a nucleation site when surrounded by other active nucleation sites. In a following paper (Golobič and Gjerkeš, 2002) the effect of the distance was further investigated. Two different series of experiments were run. For the first series the previous experimental set-up was used, with a plate heated by a large radius laser device (surface heat source); for the second, an electrically heated plate was used (volumetric heat source). The first experiment aimed to identify the location of sites suitable for activation by using the small radius laser beam. It was noticed that the activity strongly depended on the position, with difference in activity equal to the double in some cases. For the second experiment, the input heat provided by a large radius laser beam was increased until a single (“natural”) nucleation site activated. At this point, a second site (“artificial”) was activated by a second laser beam with smaller radius at variable distance from the first one. A reduction of the distance led to a lower activity for the “natural” site and an increase of

the latent heat flow rate (corrected to take into account the edge effects); however, the sum of the latent heat rates for the two sites decreased with shorter distance. A third experiment was run with the electrically heated plate. Also in this case a "natural" site was identified, and two small radius laser beams were directed to the same location. The corrected latent heat rate decreased with distance, and the "natural" site could also stop its activity if the "artificial" site became too close. The small radius of the laser beam (1.74 mm) is still considered too large in order for the experimental setup to be used to investigate micro-characteristic of the surface.

McSharry et al. (2002) developed a new method to numerically reconstruct the results of experiments with image capturing of the temperature detected by liquid crystals. The analysis of response was initially attempted by Empirical Orthogonal Functions (EOFs) and judged unsatisfactory in describing the physical processes occurring in a plate with several active nucleation sites. Instead, the use of Non-orthogonal Empirical Functions (NEFs) but it was considered a better alternative. For each analysed time step and for each active nucleation site, the procedure first identified the active sites from temperature variation respect to the average value and then the radial-symmetric non-constant NEFs were used to reconstruct the variations. A drawback of this technique is that some sites activated only seldom (so that considering them as active nucleation sites could lead to a false evaluation) and that sites located close to each other in a group may appear as one single nucleation site. In a following paper, Hardenberg et al. (2002) showed the applicability of this method to the Kenning and Yan (1996) experimental results with an improved method for error and spurious cases reduction by use of post-processing of data. A large number of active nucleation sites was successfully identified, with the important conclusion that the concept of nucleation site as single cavity cannot be appropriate in some cases, as for instance for very close-spaced cavities appearing as single ones. A further investigation was carried out by Hardenberg et al. (2004): 16 site clusters were identified (possibly attributable to individual nucleation sites), 2 or 3 regions with a more diffuse activity, and finally many occasional sites (possibly associated with stabilised nuclei due to entrapment of gas). A statistical analysis of results considering a site as primary and evaluating the correlation of this one with all the others (made independent on time) was carried out: for the particular series of considered experiments an essential non-correlation between events was generally deduced, apart from two situations. The first situation is a promotional effect for dimensionless spacing (S/R_1, with R_1 equal to the computed NEF

radius for the primary considered site) between 0.25 and 1.75 and for time delay between events lower than 25 ms. Hydrodynamic effects were supposed to be responsible for this effect, and particularly coalescence (it must be considered that circular NEFs are possibly not appropriate to describe elongated bubble shapes). The second situation is the inhibitory effect occurring for very small dimensionless spacing ($S/R_1 < 0.25$) and delay between events between 25 ms and 100 ms. Comparison with previous studies led to identify in the thermal diffusivity of the heater an important variable to be considered for interaction between sites since it plays a fundamental role in transmission of thermal interactions. The cases of non-influence for all the other situations, apparently in disaccord with previous studies (Judd and Chopra, 1993, Zhang and Shoji, 2003), were possibly attributed to the different characteristics of the experiments and particularly to the different thermal diffusivity of the heater.

A series of experiments on surfaces with artificial cavities located at specific positions to study site interactions and in particular coalescence was developed by Shoji and co-workers. Zhang and Shoji (2003) analysed the effect of distance between two adjacent artificial cavities on bubble departure frequency. The authors focused on the effects that the distance S, or better the dimensionless distance S/D_b, had on hydrodynamic interaction and coalescence. A laser beam was used to heat the wall and radiation thermometers were used to measure the wall temperature without direct interference of the measurements on the experiments. The 0.2 mm thick silicon plate was immersed in distilled water at saturation conditions. The distance between the nucleation sites was varied: the effect on the average value of the bubble departure frequency for different laser power is shown in Figure 2-18. In particular, four areas were identified:

- $S/D_b > 3$, Independent (I) region. No significant interaction was detected in this area, and the bubble departure frequency is similar to the one for an isolated bubble.
- $2 < S/D_b < 3$, Hydrodynamic (H) interaction only. This interaction was calculated by comparison of the convective heat transfer coefficient in case of two bubbles with the heat transfer coefficient for an isolated bubble. A promotive effect for bubble departure was deduced for this interaction.
- $1.5 < S/D_b < 2$, Hydrodynamic (H) and Thermal (T) interactions. The cooling effect transmitted through the heated wall (thermal interaction) due to strong evaporation can negatively affect the bubble departure frequency. For this

reason this interaction has been assumed to have an inhibitory effect. Predominance of either thermal or hydrodynamic interactions in this area determines the total effect, but a clear reduction with respect to the region of only hydrodynamic effect is evident.

- S/D_b < 1.5, Hydrodynamic (H), Thermal (T) and Coalescence (C) effects. Coalescence, acting only at very short distance, has a strong promotive effect, with consequent increase in bubble departure frequency, mostly if combined with thermal interaction. A complete description of the coalescence effects will be provided in the next section.

Shoji et al. (2005) summarised results from a series of experiments on facilities similar to the ones described in Zhang and Shoji (2003), but using different types of cavity shapes (conical, cylindrical and re-entrant), dimensions, spacing, arrangement (inline and triangular), heater materials (copper and silicon) and liquids (water and iso-

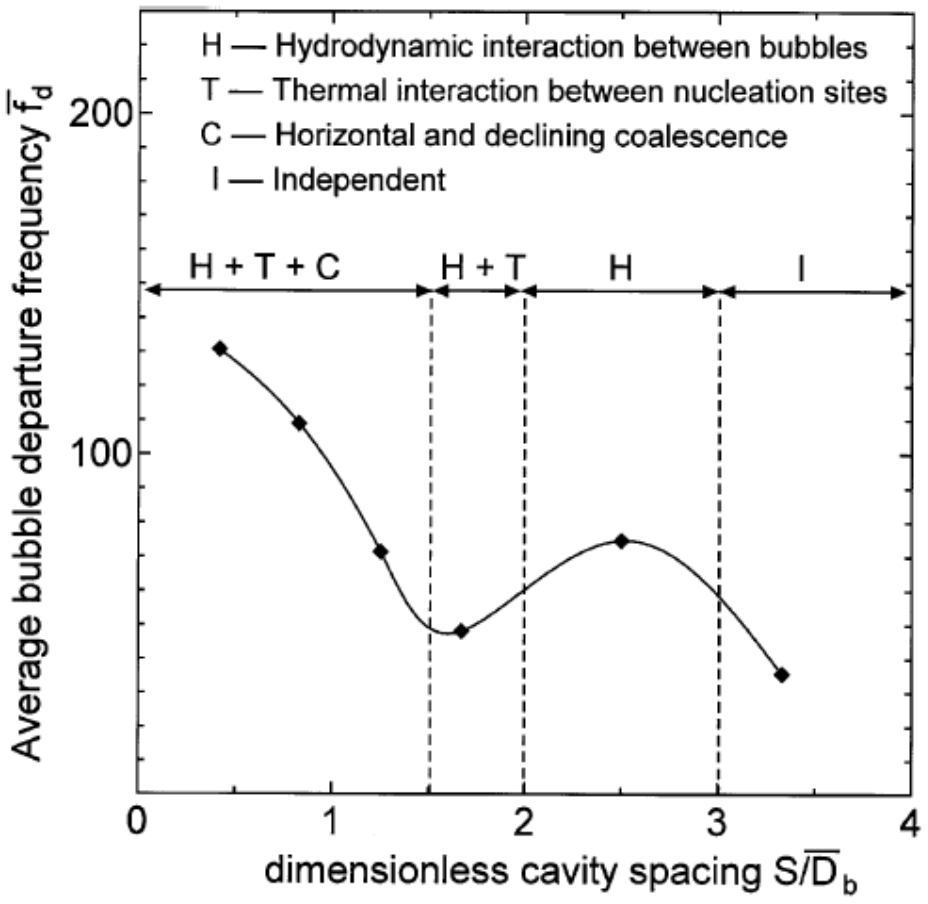

Figure 2-18: Effect of distance on bubble departure frequency (Zhang and Shoji, 2003)

propanol).

- Analysis of the cavity shape showed that conical cavities required higher superheat, and have higher instability and lower capability to entrap vapour nuclei with respect to cylindrical and re-entrant shapes. Much larger waiting periods were also observed.
- Analysis of the effect of size of cylindrical single cavities showed a weak effect of variation of the diameter for a fixed depth. Instead, a reduction of the cavity depth led to less regular histories for bubble radii, periods and temperatures.
- Experiments with twin cylindrical (10 µm in diameter and 80 µm deep) cavities and variable spacing showed a smaller average bubble radius for twin cavities if compared with single ones. This effect was attributed to the possible lower surface temperature due to higher latent heat transfer and convective heat contribution. For large distance ($S/D > 3$, S the spacing and D defined as "equivalent bubble departure diameter" $D = \sqrt{\frac{\sigma}{g(\rho_L - \rho_V)}}$), the behaviour resembled the one for a single cavity. Decrease of the spacing increased vertical

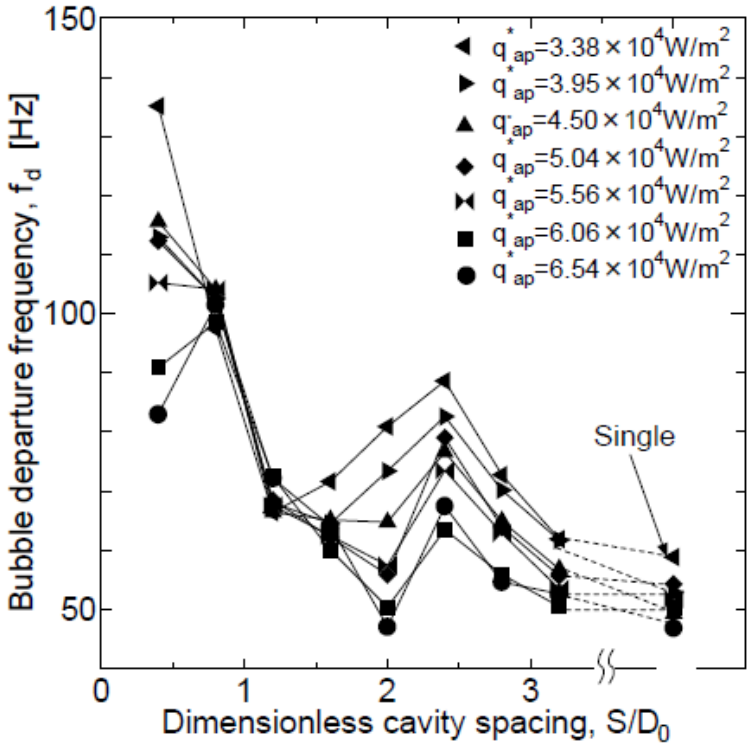

Figure 2-19: Variation of the averaged bubble departure frequency with cavity spacing (Shoji, 2005)

coalescence occurrence and if $S/D \leq 1$ horizontal and declining coalescence became likely. A reduction of the spacing led also to an increase in bubble departure frequency, as shown in Figure 2-19, while an increase of the applied heat flux for a fixed spacing determined an increase of the bubble frequency and radius. Reducing of the spacing also caused a more intense cooling effect, attributed not to an increase of the latent heat transfer contribution but to a more effective convective effect. Moreover, for a fixed heat flux, an increase in spacing led to an increase of equivalent bubble departure diameter for small dimensionless distance, followed by a decrease and a final increase for dimensionless spacing approximately larger than 2.5. On the contrary, for $S/D_0 < 1$, the bubble frequency had an initial increase or decrease depending on the heat flux; following, a decrease, increase and decrease again for large dimensionless spacing could be identified. The mutual correlation effect between temperature variations was very high for low spacing, rapidly decreasing for higher values.

- Experiments with two silicon plates (0.2 and 2.0 mm thick) and one copper plate (0.2 mm thick) showed that the bubble frequency increased following either a reduction of the thickness or alternatively an increase in thermal conductivity. As shown in Figure 2-20, a contrary effect was noticed on bubble diameter and local temperature drops,. This demonstrated the dependence of thermal interactions on wall properties.
- The analysis of effect of site arrangement, inline and triangular, showed that triple cavities generate higher bubble frequencies with respect to twin cavities, with the highest value for inline disposition. Also the heat transfer seemed to be improved by the triple cavities and particularly by inline arrangement. A detailed analysis of triple cavities was provided in Chaptun et al. (2004). Bubble coalescence became important only for dimensionless spacing lower than 1.5. For very small dimensionless distance (< 0.8), thermal interaction was more important in inline pattern than in the triangular one, while for dimensionless distance between 0.8 and 1.5 the effect reversed. Thermal interaction is not very relevant for larger distances. Hydrodynamic interaction in triple cavities is less important than in twin cavities, possibly due to the fact that a third bubble further increased the wake effect modifying the bubble behaviour.

- The use of different liquids (water and iso-propanol, even though with different input heat fluxes) had not strong influence, apart for a small increase of influence of hydrodynamic effects when using iso-propanol.

Mosdorf and Shoji (2006) developed a frequency analysis to investigate temperature fluctuation for single and twin cavities on silicon with artificial cavities immersed in water. It was assumed that temperature variations at low frequencies (5-14 Hz) are generated by changes in heat transfer conditions while variations at higher frequencies (15-150 Hz) are caused by dynamic of adjacent bubble growths. A Fourier transformation for a discrete series of temperature values was carried out to obtain the power spectrum, with the drawback of not providing dependence on time. A continuous wavelet transformation was used instead to create the wavelet power spectrum 3-dimensinal maps, able to provide the relevance of the temperature variation at all the times and frequencies. Analysis of the power spectrum for a single cavity showed the presence of two characteristic frequencies (24 and 34 Hz) and the wavelet power spectrum showed in which period of time each frequency was relevant. Analysis of results for twin cavities showed a much more complicated behaviour, varying with the

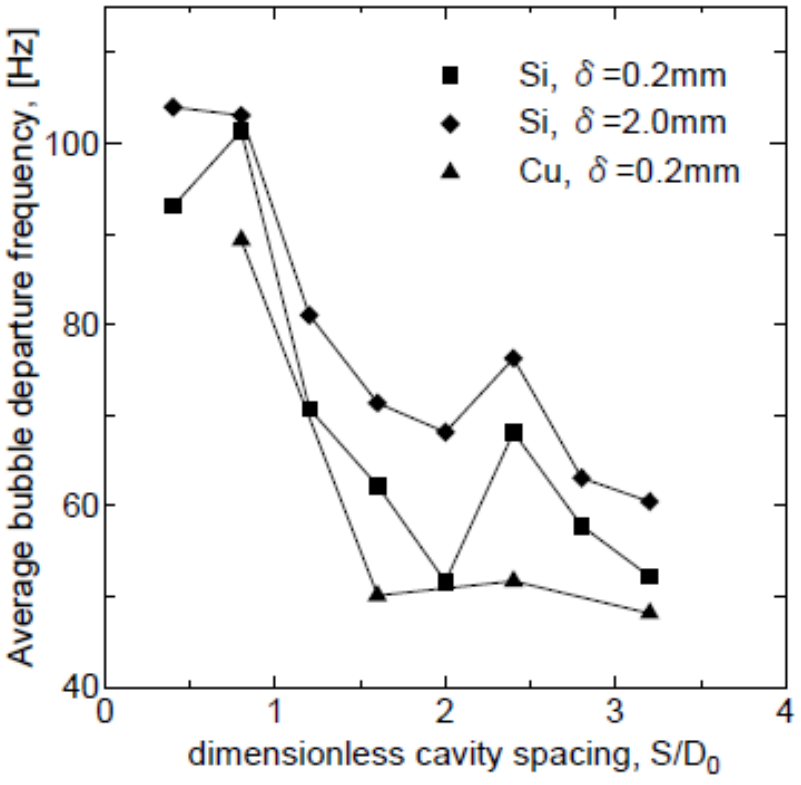

Figure 2-20: Effect of thermal properties and wall thickness on the averaged bubble departure frequency (Shoji et al., 2005)

spacing between cavities. In general, the temperature variation could either resemble the one for a single cavity or present two types of changes. The first change occurred for high frequency and low amplitude while the second one was likely for low frequency and high amplitude. A more useful instrument to describe the intensity of interaction depending on the dimensionless distance was provided by the "coefficient of correlation of time changes of wavelet power spectrum" (C_f) that depends on the frequency for different ranges of frequencies. Two ranges were analysed: one for low frequencies (5-14 Hz corresponding to variation in heat transfer conditions) and one for higher values (15-150 Hz, for dynamic interactions). In particular for low frequencies, C_f has two peaks and a minimum and tends to zero (no interaction) for dimensionless distance larger than three. The first peak corresponds to creation of a single bubble after coalescence; an increase of the distance leads to smaller probability of coalescence (lower synchronisation, in correspondence of the local minimum) followed by a second local peak (for $S/D \sim 1.67$), probably due to lower effects of dynamic interactions. In fact, approximately at the same distance, analysis of results for large frequencies showed positive C_f (synchronisation) for low distance ($S/D < 1.67$) and negative values otherwise.

2.8. Coalescence

Of particular importance while studying bubble interaction is coalescence, i.e. merging of two or more bubbles to form a larger bubble incorporating the sum of the volumes. Three different types of coalescence were clearly distinguished by Zhang and Shoji (2003), i.e. vertical (a), horizontal (b) and declining (c). The modes are schematically shown in Figure 2-21, while the experimental sequences as observed by Zhang and Shoji (2003) are shown in Figure 2-22. Vertical coalescence occurs between a bubble still growing attached to the heated wall and a bubble just departed from the same nucleation site. Horizontal coalescence occurs between two bubbles still attached at the wall and growing at adjacent nucleation sites. Declining coalescence occurs between a bubble still attached and a bubble already departed from an adjacent nucleation site. Since vertical coalescence occurs for single and interacting sites, its effect was neglected and only the other two types were accounted. Golobič et al. (2006) investigated bubble coalescence (vertical, horizontal and declining) by varying the imposed heat flux on a thin titanium foil (25 μm thick) in water at atmospheric pressure. IR thermography and a high-speed camera were used. Occurrence of vertical

coalescence produced neither large variations in cooling at the contact area nor long-range disturbance in temperature. A particular effect was noticed for horizontal coalescence: temperature disturbance propagation towards the centre of one of the merging bubbles was observed, with slight increase in temperature. A rare chain coalescence sequence was also observed after a period of essential no activity.

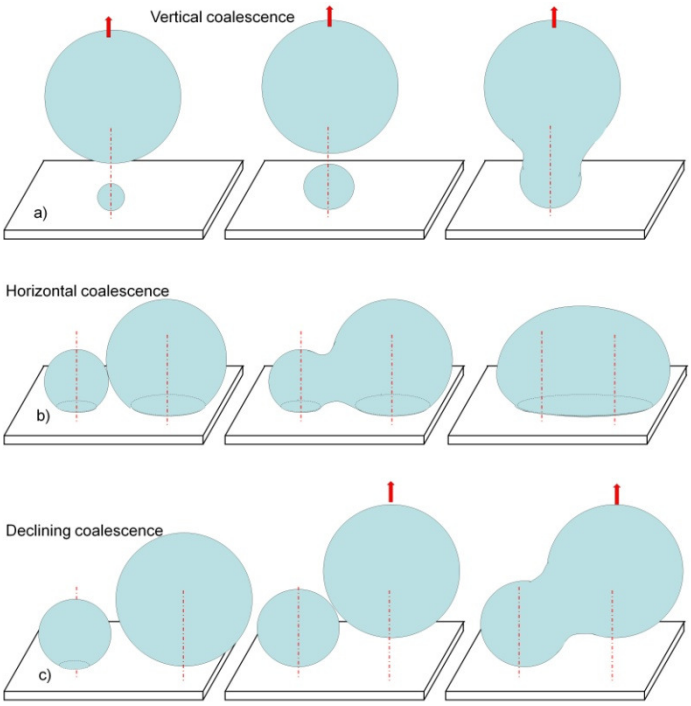

Figure 2-21: Schematization of bubble coalescence modes: vertical (a), horizontal (b) and declining (c)

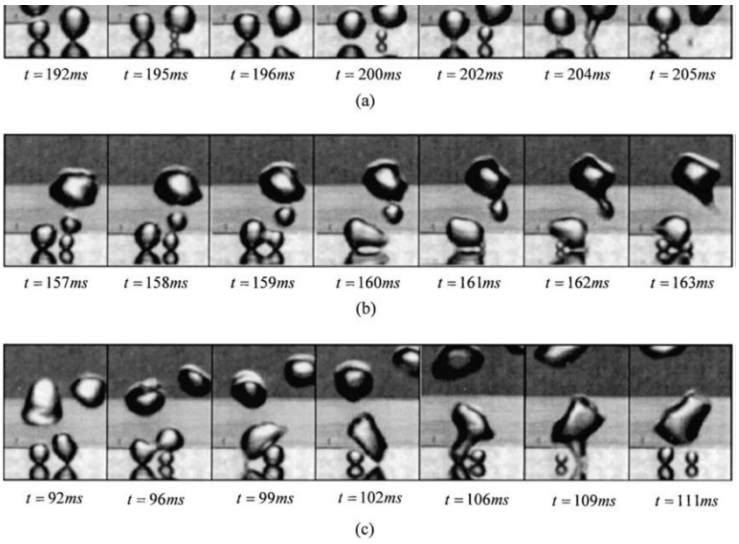

Figure 2-22: Experimental coalescence modes: vertical (a), horizontal (b) and declining (c) (Zhang and Shoji, 2003)

Chen and Chung (2002) focused on experimental studies of coalescence between two bubbles under sub-cooled conditions. The experimental system consisted of 96 heaters (0.27 x 0.27 mm^2) that could be independently activated to generate a bubble. Heat flux and temperature were measured and compared with visual results for bubble growth. The distance between activated bubbles was chosen in order for bubbles to grow independently during the first stage of the bubble growth and allow coalescence afterwards. The boiling heat flux was deduced by the difference of the total heat flux during boiling and the total heat flux during natural convection minus the experimentally calculated natural convection heat flux, as shown in Equation 2.23.

$$q_{boiling} = q_{total\_boiling} - \left(q_{NC} - q_{experimental\_NC}\right) \quad \textbf{(2.23)}$$

Using this procedure, heat dispersion and lateral conduction could be evaluated. Analysis of heat flux histories during a single bubble growth showed the presence of peaks corresponding to bubble departure (due to the rewetting of the surface by colder bulk fluid), followed by a steep decrease. When the following bubble started growing, a new smaller peak was identifiable, followed by a new decrease in heat flux due to the low heat flux in the dry spot area. When the necking process began, a shrinking of the dry spot and then an increase of the heat flux occurred. Before departure, strong vibration phenomena could be observed. Analysis of the bubble growth process involving horizontal coalescence of two bubbles showed that, while the first stage of the bubble growth is qualitatively similar to the single bubble growth, coalescence caused a large heat flux peak. Deformation of coalesced bubbles into an oval shape was also observed. In general, coalescence produced an increase in heat flux both because of the new peak corresponding to the instant when coalescence occurs and because of rewetting due to change in shape. An increase in departure frequency was also observed.

A numerical model to simulate vertical coalescence was developed by Son et al. (2002). The numerical results were compared with the experimental data for an isolated nucleation site. A variable contact angle was used as input datum: an increase in its value led to greater growth period and bubble departure radius, while no variation was observed for the ratio of bubble volume at departure to growth period. In order to evaluate the effects on coalescence, the waiting time was parametrically varied. For the largest waiting time analysed, vertical coalescence was not occurring, while a decrease

of its value led to single, double or multiple merging of the small bubble just created at the surface into the already departed bubble(s). The merged bubble moved upwards with velocity higher than that of a not-coalesced bubble. Coalescence was demonstrated to depend on the waiting time and then, for a real cavity, on the wall superheat. Analysis of the heat transfer contributions via the Nusselt number components showed that vertical coalescence (even in the multiple cases) did not strongly affect the total heat flux. Later, Dhir (2006) numerically investigated vertical and horizontal (twin of triple cavities) coalescence with a numerical code; good agreement with images from experimental results was found, as shown in Figure 2-23. Results for horizontal coalescence highlighted the presence of a liquid bridge between the two bubbles before assuming a spherical shape. Analysis of the equivalent bubble departure diameter showed that this variable underwent a significant reduction in case of triple coalescence respect to the single bubble case; this effect was attributed to the higher lift force.

Myers et al. (2005) instead focused on a study of the average temperature during coalescence. A reduction of temperature occurred due to higher cooling effect, but the largest drop of temperature occurred after bubble departure, when the fresh liquid replaced the area where the bubble was growing. Multiple coalescence also occurred for high heat flux.

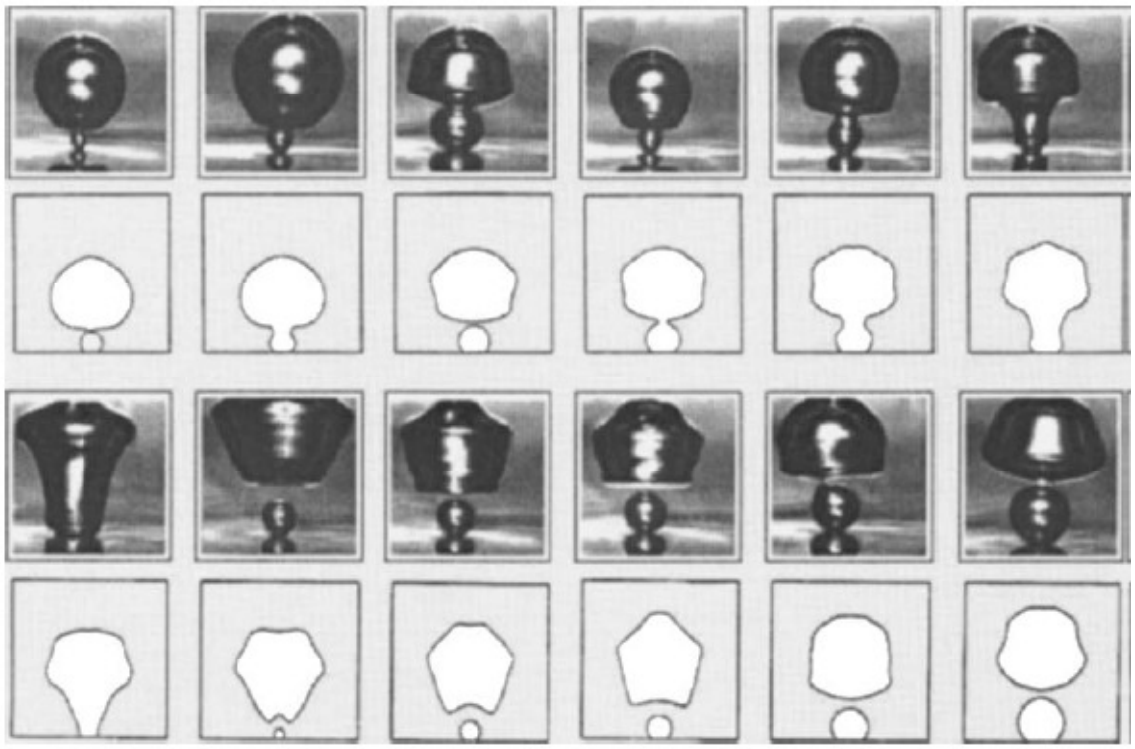

Figure 2-23: Comparison of numerical (a) and experimental (b) vertical coalescence (Dhir, 2006)

2.9.Empirical correlations

Over the years, several approaches have been attempted to provide a global description of nucleate boiling heat transfer. The first attempts were based on correlations involving several dimensionless numbers, such as the bubble Reynolds number ($\mathrm{Re}_b = \frac{\rho_V u_b D_b}{\mu_L}$), bubble Nusselt number ($Nu_b = \frac{\dot{q}}{k_L(\rho_{Ll} - \rho_V)}$) and Prandtl number ($\mathrm{Pr} = \frac{c_L \mu_L}{k_L}$), and correlated as shown for instance in Equation 2.24. Correlations based on empirical data were often on the form of power expressions, as for example Equation 2.25, (with *C*, *m* and *n* empirical constants) or derived by analogy with other phenomena, i.e. forced convection, assuming that agitation during nucleate pool boiling increased the movement of the bubble after detachment and generate high heat transfer fluxes.

$$Nu = f(\mathrm{Re}, \mathrm{Pr}) \tag{2.24}$$

$$Nu = C \cdot \mathrm{Re}^{m} \mathrm{Pr}^{m_1} \tag{2.25}$$

This type of correlations has usually limited applicability to narrow ranges of pressure, liquids and surfaces characteristics. The choice of the characteristic variables to be used in the dimensionless groups was based on the physical phenomenon believed to be more important during the analysis. One of the earliest correlations, and widely used for a long time after its formulation, was suggested by Rohsenow (1952), Equation 2.26.

$$\frac{c_L(T_w - T_{sat})}{H_{fg}} = C_{sf}\left[\frac{\dot{q}}{\mu_L H_{fg}}\sqrt{\frac{\sigma}{g(\rho_L - \rho_V)}}\right]^{0.33}\left(\frac{c_L \mu_L}{k_L}\right)^{1.7} \tag{2.26}$$

C_{sf} is a constant that depends on the characteristics of the fluid-surface combination and its value depends on experimental conditions. The term on the left side represents the ratio of liquid superheat enthalpy at the surface temperature to the latent enthalpy of evaporation. The expression can be related to Equation 2.25 with $C = 1/C_{sf}$, $m = 0.667$ and $m_1 = -0.7$. A different solution was suggested by Forster and Zuber

(1955), Equation 2.27 or equivalently Equation 2.28. Their analysis was based on the assumption that the product of the characteristic length and velocity in bubble Reynolds number Re_b is constant for a given superheat and pressure and a function only of thermodynamic properties of the liquid and vapour. The use of the bubble growth rate instead of the vertical bubble velocity in Re_b (as previously used in Rohsenow, 1952) related the heat removal to the bubble growth process more than to its departure.

$$Nu_b = 0.0015 \mathrm{Re}_b^{0.62} \cdot \mathrm{Pr}^{0.33} \tag{2.27}$$

$$\frac{\dot{q} c_L \rho_L \sqrt{\pi \alpha_L}}{k_L H_{fg} \rho_V} \left(\frac{2\sigma}{\Delta p} \right)^{1/2} \left(\frac{\rho_L}{\Delta p} \right)^{1/4} = 0.0015 \cdot \left[\frac{\rho_L}{\mu_L} \left(\frac{c_L \cdot \rho_L \cdot \Delta T \sqrt{\pi \alpha_L}}{H_{fg} \rho_V} \right)^2 \right]^{0.62} \left(\frac{c_L \mu_L}{k_L} \right)^{0.33} \tag{2.28}$$

The bubble Nusselt number was calculated as in Equation 2.29 with the radius R defined in Equation 2.30 from considerations of bubble dynamics.

$$Nu_b = \frac{\dot{q} \cdot R}{k_L \cdot \Delta T} \tag{2.29}$$

$$R = \frac{\Delta T \cdot c \rho_L \sqrt{\pi \alpha_L}}{H_{fg} \rho_V} \left(\frac{2\sigma}{\Delta p} \right)^{1/2} \left(\frac{\rho_L}{\Delta p} \right)^{1/4} \tag{2.30}$$

Engelberg-Forster and Greif (1959) tried a different approach. First, the possible contributions to enhancement of heat transfer coefficient in sub-cooled liquids during nucleate boiling suggested so far were analysed. The most relevant contribution was identified in the vapour-liquid exchange mechanism process that causes the hot vapour to be removed from the proximity of the heated surface and released in the liquid region at lower temperature, as if the bubble acted as a micro-pump. Two different correlations for the heat flux were provided. The first correlation, Equation 2.31 (with $B = \frac{c_p \rho_L \sqrt{\pi \alpha_L} \cdot T_{sat}}{\left(H_{fg} \rho_V \right)^2} \Delta p$), used a dedicated coefficient (C_I) per each liquid so that it is accurately applicable to a wide range of pressures. It is obtained on the base of physical

argumentations for the determination of the exponents of the dimensionless groups, under the assumption of highly superheated liquids. The second correlation, given in Equation 2.32, is supposed to be valid for all liquids, even if with accuracy significantly lower than for the previous correlation, with *C* a general constant.

$$\dot{q} = C_I \frac{k_L}{2\sigma} \Delta p \Delta T \left(\frac{\rho_L}{\mu_L} B^2 \right)^{1/4} \left(\frac{\mu \cdot c_L}{k_L} \right)^{1/3} \tag{2.31}$$

$$\dot{q} = C \frac{\alpha \rho_L c_L T_{sat}}{H_{fg} \rho_V \sigma^{1/2}} \left(\frac{c_L T_{sat} \alpha^{1/2}}{\left(H_{fg} \rho_V \right)^2} \right)^{1/4} \left(\frac{\rho_L}{\mu_L} \right)^{5/8} \left(\frac{\mu_L \cdot c_L}{k_L} \right)^{1/3} \Delta p^2 \tag{2.32}$$

Levy (1959) derived a general expression valid for all liquids (independent on the operating pressure) and heater materials. The analysis was carried out for a liquid at saturation conditions. The suggested formulation (Equation 2.33) correlates the heat flux removed from the heater to the third power of liquid superheat (considered constant, since the wall temperature is assumed constant).

$$\dot{q} = \frac{k_L c_L \rho_L^2}{\sigma \cdot T_{sat} \left(\rho_L - \rho_V \right)} \frac{\left(1 - \chi \right)}{B_L} \left(T_w - T_{sat} \right)^3 \tag{2.33}$$

The parameter B_L was empirically derived from experiments and assumed dependant on the liquid properties: in particular, the choice of the author was oriented on the product $\rho_V H_{fg}^2$. The quantity *(1-χ)* accounted for the presence of a small amount of vapour (in order to extend the range of applicability). However, the chosen formulation for B_L and the use of the vapour quality fraction were object of criticism because of missing evidence of physical explanation.

The relationships between the bubble departure diameter and the departure frequency were reviewed by Ivey (1967). Three different models were identified, depending on the boiling regime: the hydrodynamic, transition and thermodynamic regions. In the first one, inertia, viscous force and surface tension were neglected while main contributions are from buoyancy and drag forces. In the transition region the contribution of the surface tension was considered relevant. For the latter area, only thermodynamic contributions were relevant, i.e. those depending on the heat transferred

to the bubble. For each region, a power law correlation between frequency, departure diameter and acceleration of gravity was provided on the base of theoretical consideration and analysis of experimental data.

Mikic and Rohsenov (1969) evaluated the mechanisms at the base of the heat removal from a heated surface, maintaining that the main mechanism for heat removal was transient conduction to the superheated layer around sites associated with bubble departure. The heat was removed by micro-layer evaporation at the contact area and by the effect of superheated layer replacement by action of a vortex ring created in the wake of the bubble, affecting an area around the nucleation site with a diameter approximately equal to the double of the bubble departure diameter, Figure 2-24. The theory takes up some of the aspects suggested by Han and Griffith (1965a and 1965b) for the bulk convection and thermal layer formation theory. The authors developed a new correlation considering the average heat flux ($\dot{q}$) as a function of the cavity density, the average frequency for bubble departure, the bubble departure diameter and the wall superheat, according to Equation 2.34. The average heat flux due to boiling was defined in Equation 2.35. The following assumptions were made:

- The influence areas of adjacent sites do not overlap.
- The contact area is much smaller than the area of influence (defined as the area of the heated surface that a departing bubble affects by removing a part of the superheated layer by action of the vortex ring created in the wake of the bubble).
- The heat removed at the contact area because of the micro-layer evaporation is much smaller than the average heat flux over the area of influence of diameter D_{inf}.

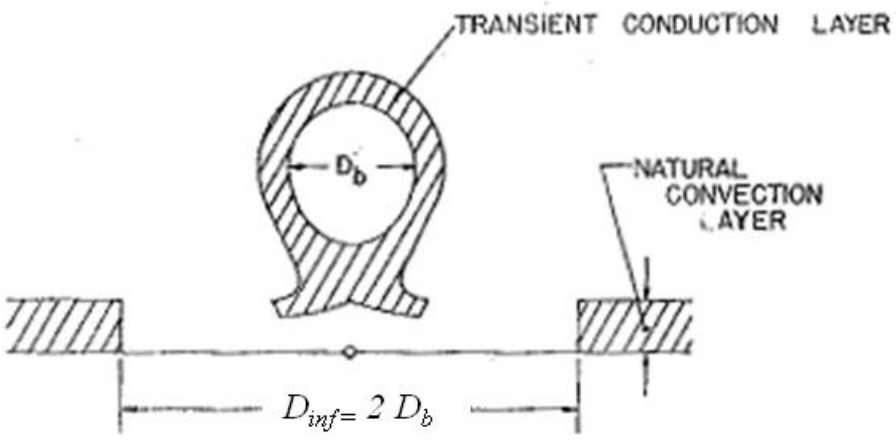

Figure 2-24: Influence area (Mikic and Rohsenow, 1969)

$$\dot{q} = \pi D_b^2 n \cdot \dot{q}_b = \pi D_b^2 n \cdot 2 \frac{k\Delta T}{\sqrt{\pi \alpha}} \sqrt{f} \quad \textbf{(2.34)}$$

$$\dot{q}_b = B_1 (c \cdot \Delta T)^{m+1} \frac{H_{fg} \mu_L}{\sqrt{\frac{\sigma}{g(\rho_L - \rho_V)}}} \quad \textbf{(2.35)}$$

The parameter *c* depended only on the thermal-hydraulic properties of the fluid (including saturation temperature) and B_1 was constant for a given liquid-surface combination; formulations for these two parameters were also provided. A variation of this model was suggested by Haider and Webb (1997): analysis of experimental results from literature highlighted the incapability of the Mikic and Rohsenow model (1969) based on pure conduction in the thermal layer to take into account the high heat flux rates. Micro-layer evaporation was also considered important, but its contribution was assumed to be not decisive to heat removal rates. The modification was the consideration of the convective instead of conductive effects in this area: stagnation phenomena and presence of eddies generated by the bubble wake after departure were considered responsible for the high heat transfer rates. At the beginning of the bubble cycle, the thermal layer was supposed to grow in transient conduction until the unsteady-state convection became relevant and asymptotically reached the steady-state in stagnation flow conditions. The clear dependence of the heat flux on the liquid Prandtl number in the suggested correlation highlights the importance of the convective effect, neglected in Mikic and Rohsenow (1969). A similar conclusion only based on analysis of Particle Image Velocimetry for growing bubbles was also derived by Basic et al. (2006).

Stephan and Abdelsalam (1980) focused their efforts in trying to find a general formulation valid for most of the experimental data available at that time. A different correlation was obtained for each of the following fluids: water, hydrocarbons, cryogenic fluids and refrigerants (with mean absolute errors respectively equal to 11.3%, 12.2%, 14.3% and 10.57%), and a general correlation given in Equation 2.36, applicable to all liquids with a mean absolute error equal to 22.3%. The accuracy of the general correlation was said to be not adequate, and the individual correlations should

be preferred. The analysis was not meant to be conclusive but needed to be completed once a sufficient number of new experimental data had become available.

$$\frac{\dot{q}D_b}{\Delta T \cdot k_L} = 0.23\left(\frac{\dot{q}D_b}{k_L T_{sat}}\right)^{0.674}\left(\frac{\rho_V}{\rho_L}\right)^{0.297}\left(\frac{H_{fg}D_b^2}{\alpha_L^2}\right)^{0.371}\left(\frac{\rho_L-\rho_V}{\rho_L}\right)^{-1.73}\left(\frac{\alpha_L^2\rho_L}{\sigma D_b}\right)^{0.35} \quad \textbf{(2.36)}$$

The analysis of the data was dealt with using a linear and non-linear regression analysis and applied only to data concerning pool boiling on horizontal surface in the range of fully established nucleate boiling at different pressures under the effect of gravity for different materials of the wall. Roughness and contact angle were assumed equal to average values if not directly specified in the experiments. Data that significantly deviated from the results of a first run of the regression analysis considering all the data were neglected. The regression analysis aimed first to identify the dimensionless groups that could have played a relevant role during experiments, and then to evaluate their relevance. It was pointed out after analysis of the individual correlations that the properties of the heater are relevant only for cryogenic fluids.

Cooper (1984) suggested a different approach, based on the use of few reduced variables, intended as the properties scaled by their corresponding critical values. The selected variables were intended to take into account the different operating conditions and to eliminate redundant properties. The starting formulation was as in Equation 2.37, where p_r and T_r are respectively the reduced pressure and temperature, and C_E, A, B and C are constants derived from experiments by using a least squares analysis. Equation 2.37 was then simplified into Equation 2.38 by omitting T_r (supposed to have the least effect on variations in the correlation) and reducing the term $(1-T_r)^C$ to $(-\log_{10} p_r)^D$, since both the terms go to zero when approaching the critical point. D was also assumed constant.

$$\frac{h}{(\dot{q})^m} = p_r^A \cdot T_r^B (1-T_r)^C C_E \quad \textbf{(2.37)}$$

$$\frac{h}{(\dot{q})^m} = p_r^A \cdot (-\log_{10} p_r)^D C_E \quad \textbf{(2.38)}$$

The constant C_E was determined on the basis of the characteristics of the fluid, summarised by the molecular weight (M), the characteristics of the heaters and particularly the roughness (R_p, supposed to vary with the pressure, as $p_r^{B'\log_{10} R_p}$), shape and material. Equation 2.39 was derived; in addition, a multiplicative factor equal to 1.7 to be used in case of horizontal copper cylinders (to account the increase in heat transfer coefficient with respect to horizontal flat plates). The same author highlighted the modesty in accuracy of results, and particularly the large scatter between the experimental results, in spite of the advantage of the simple formulation.

$$\frac{h}{(\dot{q})^{0.67}} = 55 p_r^{0.12-0.2\log_{10} R_p} \cdot (-\log_{10} p_r)^{-0.55} M^{-0.5} \qquad \textbf{(2.39)}$$

Recently, Pioro et al. (2004) analysed seven different correlations all using similar formulations with dimensionless groups related by specific coefficients and power exponents. Two groups were distinguished, depending on the used approach. For the first approach, fixed coefficients and power exponents were defined, interpolating the available data for different liquids and heater materials in one general correlation. This method presents the great advantage of applicability to a very wide number of conditions, but introduces a significantly high loss of accuracy. The second approach was based on the choice of specific coefficients and power exponents for each liquid-heater couple, with a very high precision in prevision inside the range of applicability, but requiring experimental results for each prevision, with a consequent loss of generalization.

2.10. Numerical models

A valid alternative solution to empirical correlations and mechanistic models may be found in numerical models, based on the simulation of the physical and thermal-hydraulic phenomena occurring in the liquid and in the solid substrate. Unfortunately, the complete solution would require too high computational power if applied to a large population of nucleation sites, so that simplified versions are studied. Several approaches have been presented, each one presenting advantages and disadvantages. Amongst them, the most common approaches are:

- Hybrid models. This approach aims to simulate a large number of nucleation sites, as in the models suggested by Pasamehmetoglu and Nelson (1991) or

Golobič et al. (2004). The focus is on simulation of the time-dependent 3-dimensional temperature field in the solid substrate. In the liquid side most of phenomena are replaced by semi-empirical simplified models in order to reduce the computational time. This model may offer a valid contribution to study site interactions, but it is limited by the correlations used to describe phenomena in the liquid side, which depend on the experimental conditions.

- Simulation assuming constant wall temperature. The complete solution of Navier-Stokes equations for the fluid side is developed, but the assumption of a constant wall temperature makes this model unrealistic, as demonstrated by Kenning and Yan (1996).
- Simulation of one isolated bubble. This group of models completely solve the time-dependent 2 (axial-symmetric) or 3-dimensional equations for both the liquid and the solid. The total heat flux from the surface is calculated assuming a larger distribution of nucleation sites all acting with similar behaviour. The advantage of this method is the precision and accuracy in description of the physical phenomena, with the drawback of limitation of applicability only to low heat fluxes, so that the nucleation sites have low interactions with each other. Examples of this model are presented by Stephan et al. (2009) and Dhir (2006).
- Simulation of stems. An example of this model is presented by Son and Dhir (2008): it assumes close-spaced nucleation sites forming vapour stems with a micro-layer formation in between the nucleation sites.

One of the first attempts to numerically simulate a large number of nucleation sites interacting with each other was developed by Pasamehmetoglu and Nelson (1991). The effect of site distribution on several variables of nucleate boiling (e.g. waiting and growth times, maximum, minimum and average superheat and bubble flux ratio, defined as the "number of bubbles growing on the surface divided by the number of active cavities") was studied. The model aimed to solve the temperature field on the solid substrate, horizontally positioned, via a 3-dimensional implicit-explicit analysis. The substrate was divided in finite volumes, called cells (octagonal or square cylinders shaped) and the conduction equation was solved for each of them. One cavity with a fixed cavity radius was associated to each cell; the horizontal dimension was imposed by the maximum bubble departure diameter and the height by the thickness of the

substrate. A local heat transfer coefficient, variable with the position and the activation of the nucleation site, was associated to the top surface of each cell at each time step. Single-phase natural convection was assumed in the region far from the growing bubbles, while for the region in proximity or underneath the bubble, the quasi-state conduction theory in the micro-layer was applied. The transient conduction equation was imposed for the thermal boundary layer during the waiting time. For the first time step after bubble departure the quench heat transfer model was applied. If one of the cavity radii is in the range of most favourable cavity radius defined by Han and Griffith (1965a), the nucleation site was supposed to activate. The bubble then grows according to the criterion established by Stralen et al. (1975), combining isobaric and isothermal bubble growth. The departure of the bubble occurs when the computed diameter reaches its maximum value, called bubble departure diameter, obtained from literature correlations. Several cavity distributions were studied, in order to evaluate the non-uniformity effects. The results showed significant variations in waiting time when the cavity distribution was not uniform, as well as perturbation on minimum, maximum and surface-averaged superheats and deviations from periodic behaviour for the bubble flux ratio. A strong indication of non-linear phenomena was then deduced. In a following paper Sadasivan et al. (1993) aimed to study the effect of variation of the following variables on the boiling curve:

- Cavity shape and dimensions: the cavities were all assumed conical with cavity radius R_{cav}. The cavity radius distribution is obtained by a probability density function. A reduction of the cavity radius led to a shift to the right of the boiling curve.
- The number of cavities: in some of the considered cases, more than one cavity per cell was allowed by using a normal distribution, all located very close to the centre of the cell. The cavity with the largest cavity radius was assumed to nucleate. An increase in number of cavities per cell implied a shift to the left of the boiling curve, particularly evident for low cavity radii (an increase in the number of cavities per cells implied a higher probability to have a cavity with a large radius).
- Contact angle: a reduction of this parameter led to a shift to the right of the boiling curve, with particularly marked effect for low number of cavities per cell.

A variant of this model was developed by Golobič et al. (1996), suitable to study either a single bubble growth or many vapour chimneys. A 2-dimensional axial-symmetric model was used to solve the temperature equation in the solid thin plate, Equation 2.40, with $\xi = 1$ in case of uniform volumetric heat source (as for an electrical heat generation), and $\xi = 0$ otherwise.

$$\frac{\partial T}{\partial t} = \frac{k_H}{\rho_H c_H}\left[\frac{\partial^2 T}{\partial x_r^{\,2}} + \frac{1}{x_r}\frac{\partial T}{\partial x_r} + \frac{\partial^2 T}{\partial z^2}\right] + \xi\frac{Q_{vol}}{\rho c_H} \qquad \textbf{(2.40)}$$

The bubble was supposed to grow as a truncated sphere with fixed apparent contact angle during the entire bubble growth (equal to 30° for this case). For each nucleation site five areas with specific different heat transfer coefficients between the plate and the liquid were identified, see Figure 2-25. A fixed heat transfer coefficient between the back of the plate and the surrounding air, and a zero lateral heat flux at the boundary of the area of influence ($r = r_{\inf l}$) were imposed. For the inner part of the contact area ($r \le r_i$) a fixed heat transfer coefficient (specifically zero for the presented case) was imposed. In the circular area framed between r_i and r_s a small fixed heat transfer coefficient, due to the adsorbed film was accounted. A large heat transfer coefficient was associated to the triple contact line area of width θ_{le}, assuming pure

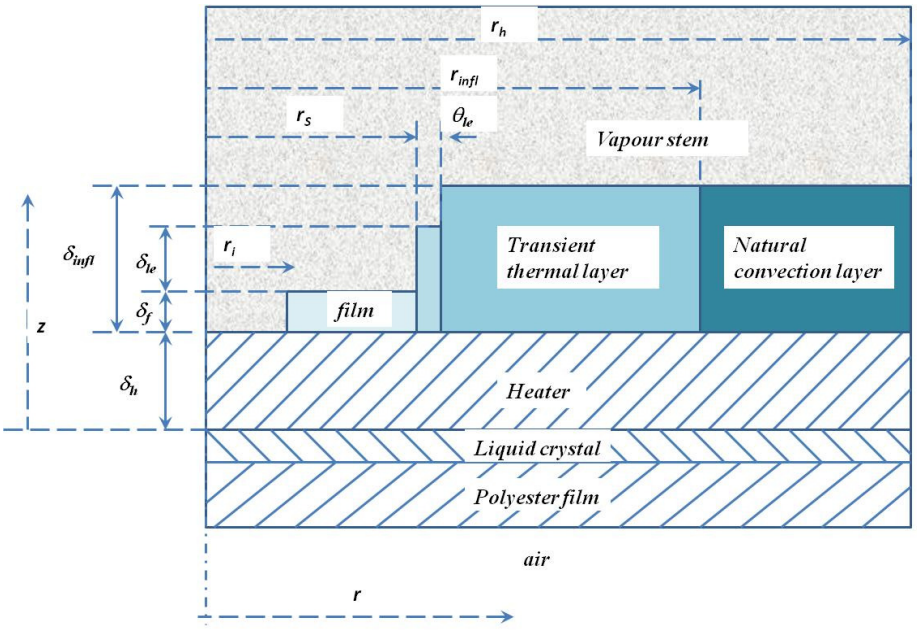

Figure 2-25: Heat transfer coefficient areas (Golobič et al., 1996)

conduction through the micro-layer of total thickness $\delta_f + \delta_{le}$. In the area immediately outside the contact area, (area of influence, for $r_s + \delta_{le} \le r \le r_{\inf l}$) the transient conduction equation was used, and the convection effect was neglected. In the external region ($r \ge r_{\inf l}$), natural convection was accounted. The results of simulations for temperature were compared to experimental data (Kenning and Yan, 1996) for an uninterrupted series of bubbles growing at an isolated nucleation site, from a thin stainless steel plate (0.13 mm thick) immersed in water, with input heat fluxes of 51 and 102 kW/m^2. The temperature variations were measured on the back of the plate by liquid crystal thermography: nevertheless, it was pointed out that the sensitivity of measurements is not high enough to confirm the model and a thinner plate or a material with higher thermal diffusivity would be required to improve it. A modified version was later proposed by Golobič et al (2004), and compared again to the experiments for a stainless steel plate of Kenning and Yan (1996), by using the NEF results obtained by McSharry et al. (2002) and Hardenberg et al. (2002, 2004). In fact, the model requires the definition of the position of the potential nucleation sites' activation temperature and bubble departure radius as obtained, e.g. by NEF analysis. The bubble is assumed to grow as a truncated sphere (in this case with a fixed apparent contact angle equal to 32°). Activation of a cavity is supposed to depend only on the activation temperature, and hydrodynamic effects of seeding or inhibition are not considered. Bubble departure occurs in the model when the bubble reaches a fixed diameter (bubble departure diameter). A high heat transfer rate is assumed in correspondence with the triple contact line; a much lower (but not zero) heat transfer rate is attributed to the inner contact area. Natural convection is imposed outside the bubble contact area. Three simulations were run, varying the number of potential nucleation sites, depending on the number of activations per site identified by the NEF analysis: the considered cases were for 1505 sites (all the sites activated at least once during the time slot considered by NEF), for 414 sites (activated at least twice) and for 66 sites (activated at least 6 times). A general strong overestimation of the total number of activations in simulations was observed, increasing with the number of potential activation sites. Bubble coalescence was not considered in the simulations. A more detailed description of the model is provided in the next chapter.

One of the first examples of models focusing on a single bubble growth was proposed by Stephan and Hammer (1994). Temperature, heat flux and bubble growth distributions were evaluated by using only two parameters (obtained either from experiments or correlations), and exactly the bubble site density and the departure radius for a single bubble, other than the thermodynamic properties of liquid and heater. The wall temperature is considered variable, with a fixed value on the bottom surface (T_{out}) and the vapour is assumed to be at constant pressure. A finite element method is used to generate the mesh distribution. This time dependent 2-dimensional axial-symmetrical model supposes the bubble to grow as a truncated sphere and it is based on the existence of a thin micro-layer under the bubble base. The space around a growing bubble is divided into two regions, micro-region and macro-region, as shown in Figure 2-26 and described below:

- The micro-region, see Figure 2-27, is defined as the region where the variation of the curvature of the liquid-vapour interface, the adhesion forces and the interfacial thermal resistance are strongly influencing the heat transfer. This

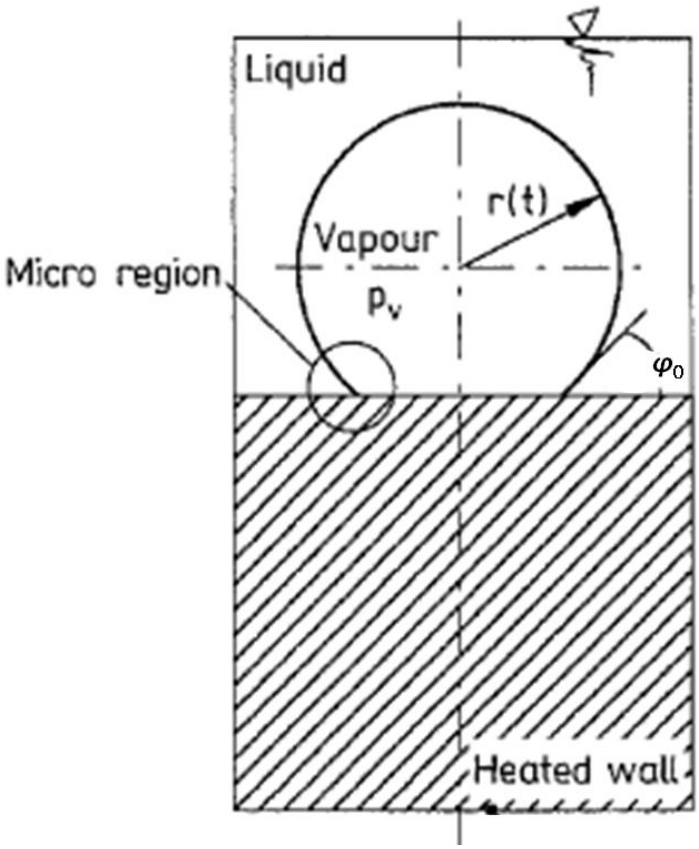

Figure 2-26: Micro- and macro-regions (Stephan and Hammer, 1994)

region is in correspondence of the triple contact line, called meniscus, i.e. the area when the bubble curvature K_{bubble} undergoes a strong variation, from the dome to the centre of the base of the bubble. A strong evaporation was supposed to occur in this area and determine a loss in liquid that is replaced by a continuous transverse liquid flow from the macro-region outside the bubble towards the centre of the base of the bubble. The evaporation heat was used to calculate the mass evaporation rate, and then the radius of the bubble at the new time step.

- The macro-region is defined as the region adjacent to the micro-region and the wall. Here, the two-dimensional conduction equations were numerically solved, and coupled with the differential equations of the micro-region.

Simulations were run for R-114 on a copper plate (0.5 mm thick), with a superheat of 3.5 K, and bubble departure radius of 0.125 mm for an isolated bubble, with apparent contact angle of 27°. Analysis of the heat flux profile along the radius showed a large

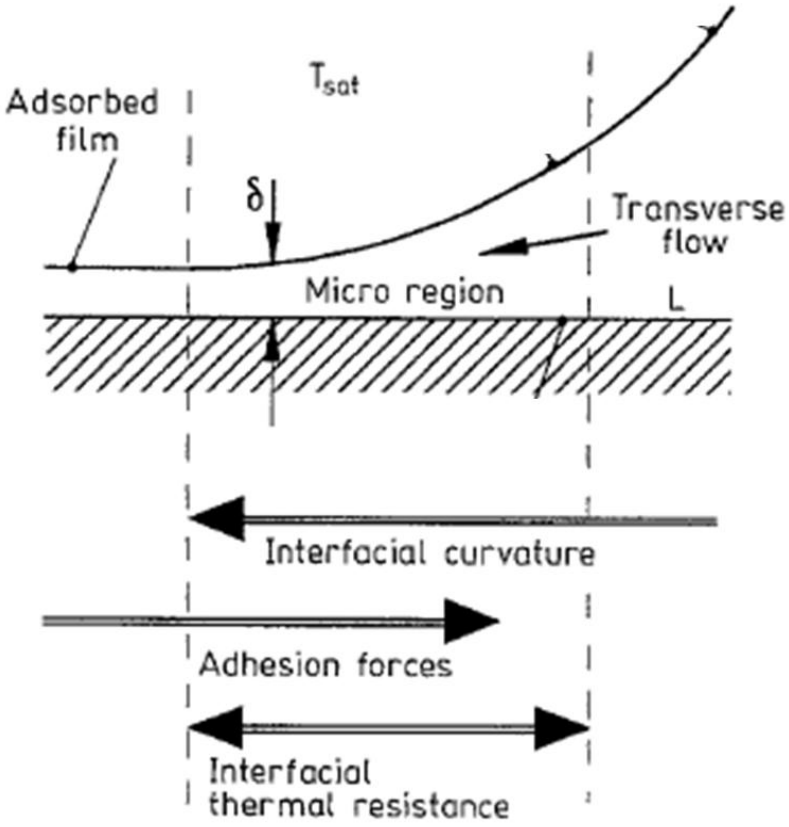

Figure 2-27: Micro-region (Stephan and Hammer, 1994)

peak in correspondence of the meniscus, much larger than the burn-out values. The fraction of heat flux in the micro-region was shown to play a relevant role in the bubble growth, and it significantly increased with increasing wall superheat. The bubble radius exhibited a square root dependence on time, as described before for previous mechanistic correlations. The results for the heat transfer coefficient versus the mean heat flux were compared (after being averaged) with experimental results showing a good agreement. The model was successively extended to the study of binary mixtures (Kern and Stephan, 2003). In a successive study Stephan and Fuchs (2006) improved the previous model developing a fully transient simulation of the whole period between two growing bubbles, i.e. bubble growth, detachment and rise. The new model, usable for either imposed heat flux or temperature on the back of the plate, requires only two input parameters, i.e. the waiting time and the bubble site density. The heat fluxes at the back of the plate, at the dome of the bubble and at the triple contact line were compared. In particular, the wall heat storage (defined as the difference between the input and removed heat fluxes) was shown to be negative during the bubble growth, implying that more heat was contributing to evaporation than to increase of the temperature in the plate. After detachment of the bubble, the wall heat storage became positive. Contributions at the dome of the bubble and at the triple contact line were both found to be relevant for the bubble growth. Heat transfer in the plate was considered essential for a correct study of nucleate boiling. Analysis of temperature variations for two different plate materials (copper and steel) with very different thermal conductivity showed that for steel (lower conductivity) the variations are definitely more marked, with higher temperature gradients across the plate. In a recent study for FC-84 (Stephan et al., 2009) the importance of micro-layer evaporation for the bubble growth was confirmed, with very high heat flux rates during the first stage of the bubble growth (up to 250 kW/m^2).

Another model based on single bubble growth was developed by Mei et al. (1995a): numerical simulations solved the 2-dimensional axial-symmetric temperature field in the solid and in the micro-layer, for bubble growth in heterogeneous boiling and isolated bubble regime. The hydrodynamic of the fluid and the heat transferred at the dome of the bubble were neglected in order to study temperature variations in the substrate through a time-dependent 2-dimensional (axial-symmetric) model. The micro-layer is supposed to have a wedge shape, with small wedge angle. Two possible heat sources were accounted: heat flux at the bottom surface of the substrate and internal approximately uniform volumetric heat source. Only two empirical parameters were

used, one to take into account the deviation from a perfect sphere of the bubble and a second to describe the wedge angle. This parameter was determined empirically, supposing the viscosity to play an almost negligible role in it. Four dimensionless parameters were identified as fundamental through a dimensional analysis and simplification, i.e. the Jacob Number ($Ja = \frac{\rho_L c_L \Delta T_{sat}}{\rho_V H_{fg}}$), Fourier number ($Fo = \frac{\alpha_H t_d}{\delta_H^{\,2}}$), the liquid-to-solid thermal conductivity ratio ($\kappa = \frac{k_L}{k_H}$) and the liquid-to-solid thermal diffusivity ratio ($\alpha = \frac{\alpha_L}{\alpha_H}$). Particularly, the Jacob number was considered to have an important effect on the shape: for high values, the bubble tended to resemble a hemisphere while for low values it resembled a perfect sphere. A detailed analysis of the effect of the four parameters is developed in a companion paper Mei et al. (1995b): in particular, an increase of *Ja* or α, or alternatively a decrease of *Fo* or κ, led to larger dimensionless radius (scaled with the bubble radius if constant wall temperature was assumed). It was also noticed that a large *Ja* strongly affected the temperature variations in the substrate, while a large *Fo* implied a small thickness, and then a small thermal capacity of the substrate, with complete penetration of the temperature variations in the vertical direction. On the contrary for small *Fo* the back of the plate was approximately independent on the temperature variations on the upper surface, so that measurements on the back could be misleading. An increase of κ led to a larger gradient of temperature in the substrate, while an increase in α led to a stronger effect of thermal interaction in the vertical direction to the detriment of the radial direction.

Another model focusing on the single bubble growth was suggested by Son et al. (2002) but assuming constant wall temperature. The space around an active site is divided in micro- and macro-region similarly to the model suggested by Stephan and Hammer (1994). The micro-layer model was solved by applying the lubrication theory and then combined with a complete time dependent axial-symmetric model for conservation of momentum, energy and mass equations for the macro-region. The thickness of the micro-layer below the bubble at the border of the micro-region was of the order of molecular size and specifically in this case equal to 6 x 10^{-10} m. A level set formulation was used to capture the liquid-vapour interface of the macro-region and the disjoining pressure was included to account for the heat transfer through the micro-layer. The numerical simulations were compared with the experimental results for an

isolated bubble growth, focusing on vertical coalescence, i.e. merging of two consecutive bubbles created at the same nucleation site, the first one already detached and lifting up, and the second one still attached to the wall. Previous analyses (Son et al., 1999, Dhir, 2001), based on the same numerical model, investigated the dependence of the bubble departure diameter and bubble growth rates on wall superheat, contact angle, liquid sub-cooling and effect of gravity. The formation of vortexes in the liquid layer, in proximity of the lower part of the bubble dome, was shown. The vortexes appeared to become larger during the shrinking of the contact area. A thin thermal layer was supposed to form after bubble departure, with a higher heat transfer coefficient and leading to a decrease in temperature in the area vacated by the departed bubble. In particular, an increase in wall superheat determined larger bubble departure diameters and bubble growth rates (with a reduction of the total growth time). An increase in contact angle did not significantly affect the growth rates, and led to larger bubbles and consequently larger growth times. On the contrary, a larger sub-cooling reduced the growth rate and slightly reduced the bubble departure diameter; the first effect was due to an increasing importance of condensation on the upper part of the bubble dome. Condensation was considered to be negligible during the initial stages of bubble growth, but to become determinant at departure. Generally, the simulations tended to over-predict the bubble growth time. Later, Dhir (2006) used a numerical model assuming constant wall temperature and simulating hydrodynamic phenomena for artificial sites and imposed waiting time between bubble growth to parametrically investigate the effect of fluids and contact angle. Results for a single bubble growth in water (contact angle equal to 35°) and PF-5060 (contact angle equal to 10°) showed a good agreement with experiments. Analysis of time-integrated and averaged over the whole control area contributions to the heat removal from the surface showed that micro-layer evaporation contributed approximately by 15%. The heat transfer contributing to the bubble growth was shown to start immediately after the waiting time and to have a maximum in correspondence of the maximum contact area. Occurrence of vertical and horizontal coalescence for twin and triple cavities was also analysed.

Nonlinear phenomena were numerically investigated by Sadasivan et al. (1995) for high fluxes, leading to mushroom stem formation. A small sector of plate was studied allowing only one bubble stem mushroom in it. Uniform conditions on the fluid side for all the nucleation sites, randomly located via a Poisson distribution, could be then supposed. Five possible phenomena (but not necessarily the only ones) were

accounted, i.e. activation-deactivation of a nucleation site, macro-layer evaporation, phenomena occurring at the triple contact line area (meniscus), variations in micro-layer thickness and bubble growth and departure. Of those, the activation/deactivation phenomena were object of non-linear study, while the other contributions were linearised, with the assumption that in case the first phenomenon was leading to chaos, nonlinear contribution of the others was not deviating from chaotic behaviour. The final objective of the paper was specifically not to provide a "better prediction" but a "better understanding", via "numerical experimentations", i.e. sensitivity analysis of possible affecting parameters. The 3-dimensional time dependent conservation equation in the solid plate (with possible internal heat generation source) and in liquid macro-layer (with variable thickness and then dynamic domain) were solved. Adiabatic conditions are applied to the edge of the plate with imposed heat flux at the bottom. Three regions are identified at the heater's boiling surface:

- Inner part of the contact area (not including the triple contact area), where adiabatic conditions were imposed.
- Triple contact line area (called meniscus), where evaporation was supposed to occur.
- Region outside the bubble contact area, where macro-layer evaporation conditions were applied. This region occupied all the areas where the sites were not active.

Activation of a nucleation site occurred if the cavity temperature was larger than a fixed value (activation temperature), while activation is inhibited if the temperature dropped below the deactivation value. The numerical code was applied to a square copper heater (5 mm long and 50 μm thick) with input heat flux variable between 0.85 and 1.04 MW/m^2. Analysis of the temperature at the top surface, averaged over the whole surface, showed the site intermittency and periodicity: period equal to the departure time were detected for the lowest heat flux and increasing with it, up to the highest heat flux value, where larger irregularity appeared. Nonlinear dynamic of the process was then deduced, possibly leading to chaotic behaviour. Analysis of activity of all the sites showed that activation of one site may inhibit the surrounding ones and that phenomena of intermittency (leading to a variable number of active sites with time) were possibly due to thermal interactions in the heater. An important comment made was connected to the impossibility of identifying a representative area other than the

whole surface, due to the non uniform behaviour of the sites. Also He et al. (2001) developed a numerical model to study pool boiling for high heat flux during formation of stem vapour caused by multiple coalescences between bubbles, in order to investigate the effects on the boiling curve and on critical heat flux. Pure conduction model is applied in the macro-layer to calculate its time-dependent thickness. Another numerical model for vapour stems was proposed by Son and Dhir (2008): the bubbles were assumed to initially grow independently and then, when coalescence occurred, the presence of a macro-layer trapped in between two coalesced bubbles was simulated. Mass, momentum and energy equations were solved for each phase of the fluid in the macro-region, while the micro-region was solved with lubrication theory and then coupled to the macro-region.

Lately, Mukherjee and Kandlikar (2007) analysed the effect of contact angle via a numerical model that solves the Navier-Stokes equations for the liquid but assumes uniform wall temperature. Axial symmetry is supposed, so that only one quarter of the bubble was studied. The bubble was supposed to grow as a truncated sphere, with either a constant static contact angle or a dynamic contact angle. The contact angle is assumed static for an essential status of rest of the contact area, dynamic otherwise. Two different values were attributed to the dynamic contact angle depending on the fact that the contact area was expanding (receding contact angle) or shrinking (advancing contact angle). Five simulations were run using different contact angles. For the dynamic contact angle simulations, the angle was supposed either dependent on bubble base velocity or equal to two fixed values depending on increasing or decreasing bubble contact area. In the last case, a phenomenon called “slip/stick” was observed: for certain values of the bubble base radius, the base does not continue to grow and sticks to the wall, even though the bubble increases its size, until a sudden acceleration occurs again (slip). In this case, the base growth may show a typical rough history because the contact angle keeps changing value. It was noticed that the slip/stick behaviour was more pronounced for lower wettability. Instead, the use of a continuous variation of the contact angle with the base velocity or a constant static angle generates very smooth contact area growths. At departure, simulations showed the presence of a vortex created near the base of the bubble. The value of contact angle was seen to be relevant also for the intensity of the vortex. In particular, for low wettability, the vortex created is larger and its effect on the thermal boundary layer is more pronounced.

2.11. Chaos in pool nucleate boiling

As already noticed by Sadasivan et al. (1995) an increase in heat flux may lead to a strong component of nonlinear phenomena and possibly to chaos. Specifically, Chai et al. (2000) pointed out that linearization of the processes for nucleate boiling may lead to a mistaken description of the phenomena. Moreover, according to Chai et al. (2000), chaos may occur at high heat fluxes, as highlighted by study of "attractors" during the numerical analysis. An attractor identifies the relationship between the bubble diameter and the average superheat, i.e. the difference between the average surface temperature and the liquid saturation temperature. Shoji and Takagi (2001) provided a detailed analysis and explanation of the procedure used to identify nonlinear phenomena and possible chaotic behaviour. The behaviour of three different shapes for artificial cavities was studied: conical, cylindrical and re-entrant. For conical cavities, which showed long waiting times and intermittent bubbling, an embedding procedure was developed in order to study the trajectory described by the temporal evolution of a variable of the system (in this case the temperature). The coordinates of the points of the trajectory were defined by the value of the variable at successive specific time steps and plotted in phase maps, as shown in Figure 2-28. At low heat fluxes (a), two different behaviours were clearly identifiable, i.e. on one hand large triangles corresponding to long term variation and long waiting time and on the other hand ball-like trajectories corresponding to short-term phenomena, indicated by an arrow in figure. At higher heat fluxes the trajectories became much more complicated so that the two behaviours were not clearly distinguishable anymore. For cylindrical and re-entrant cavities return maps were constructed on the base of successive departure times used as 2-D coordinates in the map. If the points lie close to the bisector, periodic behaviour is identifiable, as it occurred at low heat fluxes. On the other side, if the points lie in clusters, related phenomena are present (such as dependence of the bubble size and temperature drop for a second bubble growing after a long waiting time on the previous one); this situation occurred for intermediate heat fluxes. If the points are completely scattered, not correlated, chaotic behaviour can be supposed. At high heat fluxes, partial scattering was shown, identifying possibility of deterministic chaos. Despite that, for both types of cavities, a larger number of points were required to clearly state the presence of chaos.

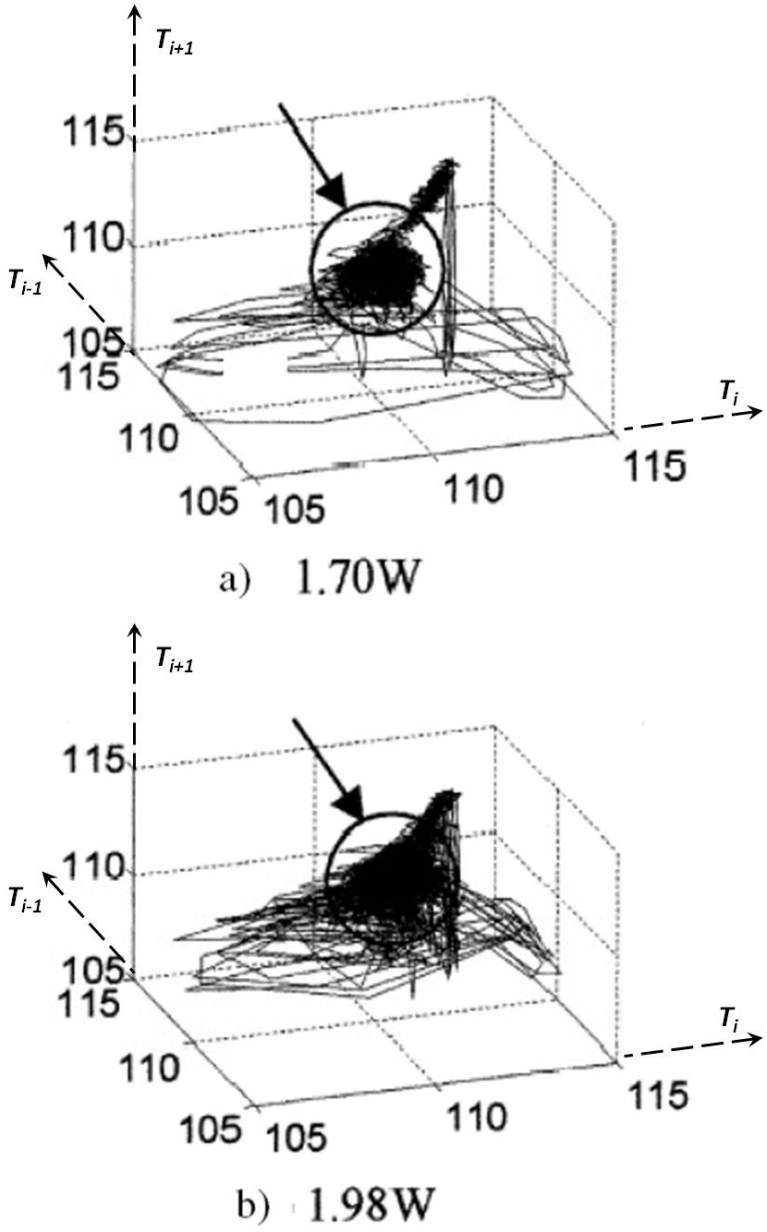

Figure 2-28: Phase maps (Shoji and Takagi, 2001)

Successively, Mosdorf and Shoji (2004, 2006) experimentally analysed chaotic behaviour for single, twin and triple cavities (10 μm in diameter and 80 μm in depth). The system was set in order not to have waiting times between growing bubbles. Analysis of 3-dimensional attractors for a single bubble showed that chaotic thermal oscillations were present. The behaviour of attractors was studied via the number of points characterising them and attributing a "dimension" per each number of points. Analysis of the "dimension spectrum" provided an estimation of the degrees of freedom of the system. Instead, analysis of the Lyapunov exponents, see Mosdorf and Shoji (2004), and in particular of the largest exponents (related to the bubble departure frequency) showed that the loss of stability occurred in a time similar to the single bubble growth: in this case, chaotic behaviour could possibly occur. Investigation on twin cavities at variable spacing highlighted a more complex behaviour of the 3-dimensional attractors. Two contributions could be accounted to have a strong effect in modifying the shape of the attractors in this case in the region between $0.3 < S/D < 1.2$. The first was attributed to temperature changes occurring with low amplitude and similar to single nucleation site behaviour. The second, implying higher temperature variations and occurring at lower frequencies, was attributed to the presence of neighbour nucleation sites. The dependence of the largest Lyapunov exponent L (and its inverse value, i.e. the period of long time memory for the system) and the average bubble growth on the dimensionless spacing S/D was derived, as shown in Figure 2-29. If the long time memory of the system $1/L$ increased, a higher predictability of the process could be supposed: at low spacing, the long time memory increased because two very close-spaced bubbles merged and acted as a single bubble. For increasing distance, the predictability decreased, until it reached a minimum for $S/D = 1.5$ the coalescence effect became negligible while the hydrodynamic interaction played a more important role, so that the dynamic of the bubble growth may change because of modifications at neighbouring sites. The analysis of the temperature-induced variations for twin and triple cavities was carried out via use of the dimensions of the attractors for a low density of points. At low spacing (thermal interaction), for triple cavities a complexity lower than for twin cavities showed. Instead, at higher spacing (hydrodynamic interaction) the complexity for the triple cavity case increased showing a single peak for a dimensionless spacing between 1.5 and 2 (depending on the heat flux). However, the nonlinearity of the system and the presence of chaos were not

completely understood. Moreover Gerasimov et al. (2006) pointed out that false chaos may occur in nucleate boiling. The necessity of carefully analysing experimental data was particularly stressed out, because an incorrect choice of the "embedding" dimension or the presence of noise could lead to false chaos interpretation.

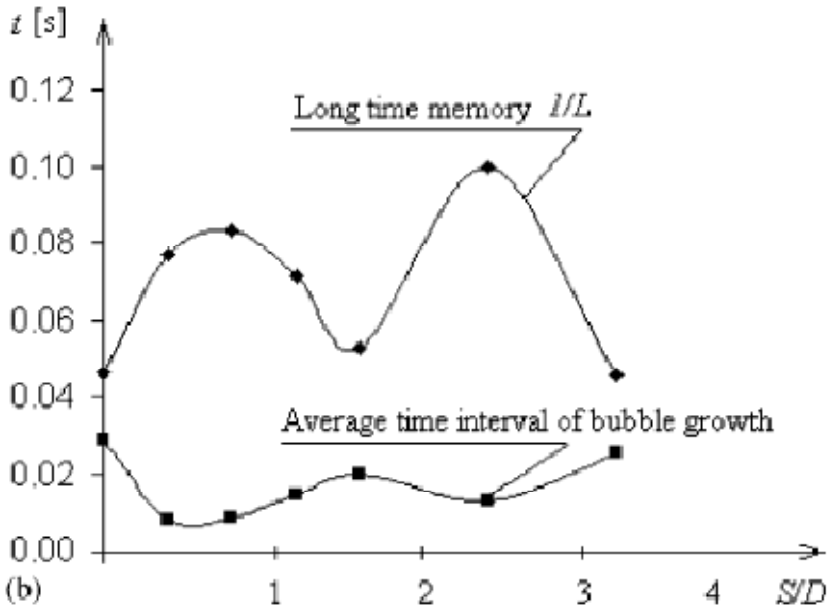

Figure 2-29: Long time memory and average time interval of bubble growth dependence on dimensionless distance (Mosdorf and Shoji, 2004)

2.12. Conclusions

This study aimed to identify the possible phenomena and mechanisms that play a fundamental role during nucleate boiling heat transfer. These will be used in the development and improvement of a numerical code based on a hybrid approach (analysed in the following chapter), i.e. combining the solutions of the temperature field on the substrate with semi-empirical models based on experimental and theoretical studies for heat transfer conditions and for bubble nucleation and growth, interactions and coalescence. This approach is different to other numerical codes that may focus on the complete solution of macro- and micro-scale phenomena both in the substrate and liquid fields. The first presents a substantial drawback of a partial loss of details in the description of particular phenomena as the perfect shape of the bubble or the fluid movement around it, but it offers the important advantage of being applicable to a much larger number of nucleation sites possibly strongly interacting with each other. The assumption of no-interactions between nucleation sites can constitute a severe limitation

when applied to real experimental conditions outside the boundaries of research facilities: in fact, the effect of the site distribution is accredited to have a strong effect on the temperature variations in the substrate, and then on the potential critical heat flux. Consideration of these aspects are of fundamental importance if the numerical code is aimed, as it is in this case, to be used as a tool for the design of new test sections with micro-fabricated cavities with optimization of the heat transfer coefficient conditions.

The choice of which models are to be included in the numerical code is made difficult by the absence of sufficient evidence supporting any of them in the whole range of possible conditions simulated. For this reason, the code has been studied in order to make simulations sufficiently flexible to accommodate different models and rely on experimental evidence to select one or the other. From the analysis of the different models for the growth of a single bubble, two main contributions have been identified: one at the dome of the bubble and one at the base. Both of them have now been taken into account in the code, although by simplified models. The first is based on the boundary thermal layer theory, assuming that a liquid layer constantly surrounds the bubble dome during its growth. The instantaneous heat contribution is therefore related to the size of the bubble itself and depends on the time elapsed from nucleation. This is numerically combined at each time step to the heat contribution at the base of the bubble, based either on the micro-layer or the contact line evaporation models although the code is easily modifiable to include different models as they may be identified in the future (provided that the suggested models have a central symmetry with respect to the nucleation site). Both the contact line and micro-layer models have been experimentally observed and debate on their applicability is still open. It may be possible that both of them are plausible and the choice depends on the particular experimental conditions.

Similarly, for the bubble nucleation and departure, the lack of a clear understanding of the processes involved makes the implementation of simple and general conditions very complicated. Nucleation of a new bubble was found generally connected to the thermal layer superheat, although strongly dependent also on the cavity radius and surface treatment used before the experiments. The waiting time would be consequently derived by the time necessary for the thermal layer to reach again the activation superheat after departure of a bubble, although theoretical studies suggested values significantly smaller than those reported in experiments. The complete analysis of departure of a bubble is theoretically also more complicated because this phenomenon involves the bubble shape deformation and balance of forces and, so far, is

not completely understood. However, the departure conditions are often connected to the final bubble size.

This section showed also that the analysis of the growth of an isolated bubble by itself cannot provide the description of the heat transfer mechanisms for a generic surface. The concept of influence area of a growing bubble was introduced, highlighting that close spaced sites may not act independently and their total effect cannot be generally considered as the sum of their single independent contributions. Interactions were found to be strongly connected to the surface characteristics, which affect the nucleation sites density. Moreover, the process can be complicated by possible seeding and inhibitory effects, intended as the capability of one active site to increase or reduce (and possibly stop) the site activity of surrounding ones. A strong dependence of these phenomena on the mutual distance between sites with respect to the bubble size was generally observed, although experimental results did not completely agree on the range of distances to which the different effects apply. Interactions were also observed to occur between bubbles already growing, both across the substrate and fluid (respectively identified as thermal or hydrodynamic), leading in some cases to coalescence. This is a macroscopic phenomenon involving deformation of the shape and consequent merging of two or more bubbles and it may involve also bubbles already departed from the wall.

The strong dependence and non-linearity of all these aspects show the necessity to have a numerical model that takes into account most of them when simulating a large number of potential nucleation sites. Moreover, a model focusing on the interactions may provide an insight of occurrence of chaos, which has recently become of high interest in boiling phenomena, although the need to use simplified models may conflict with the sensitivity of chaotic systems to small influences.

3. Numerical model

The numerical code was initially developed at Los Alamos National Laboratory (Pasamehmetoglu and Nelson, 1991) and successively modified at the University of Ljubljana (Golobič et al., 1996). The modified version of the code (Golobič et al., 2004) was acquired by Brunel University in 2006. As described before in Section 2.10, the numerical code simulates the temperature field in a solid substrate with an applied heat source horizontally immersed in a liquid. The heat is removed from the upper surface of the substrate by nucleate boiling processes at fixed locations simulating the nucleation sites. The code is based on a hybrid approach, combining the explicit exact solution of the temperature field in the solid substrate with semi-empirical models for the heat transfer on the upper surface, for bubble growth and for interactions between adjacent sites. The final objective of the code is the simulation of a substrate with a large number of interacting nucleation sites in reasonable computation times on normal computer workstations (i.e. a simulation time of 24 hours on a dual processor, 4 core per processor, workstation for approximately 100 interacting sites with a consistent number of activations per site). This way, the code can be used as a tool to design new substrates with a specified distribution of artificial cavities acting as nucleation sites.

The analysis will start with the description of the original version of the code, followed by the explanation of the necessity of changes from both the physical and numerical points of view, with a detailed analysis of improvements introduced so far.

3.1. Original version of the code

The original version of the code was structured in a single FORTRAN file (containing all the instructions) and several input files (including most of the input data and details relative to size and arrangement of the cells). The main instruction file contained the main body (including most of the physics) and several sub-routines located at the end of it. A sub-routine is a procedure (series of instructions) called during the execution of the code inserted separately in order to make the code more readable.

The logic used in the original version of the code is presented in Figure 3-1. The code uses experimental values from the bubble growth and nucleation site position as input data. For instance, in the case presented in Golobič et al. (2004), the code is used to reproduce experimental results on a stainless steel plate (SS, 125 µm thick) cooled by water at atmospheric pressure with imposed volumetric heat source in the substrate (electric heat generation) with temperatures on the rear of the plate and measured by liquid crystal thermography. The measured data are then processed by using a NEF analysis (developed by McSharry et al., 2002, and analysed in Section 2.7) that allows the determination of the position ($\bar{x}$, $\bar{y}$) of the nucleation sites that activated at least once during the examined time. On the base of those, the position of the nucleation sites ($x_{NS,i}$, $y_{NS,i}$), the activation temperature ($T_{act,i}$) and the bubble departure radius ($r_{bd,i}$) to be used in the numerical code are derived for each individuated site *i*. A 3-dimensional, time dependent numerical analysis of the temperature field in the solid substrate is then carried out and the results compared with the experimental data. A non-uniform mesh distribution adaptable to the activation/deactivation of the sites is used. The distribution is coarser in correspondence of the natural convection area and more refined (smaller cell dimensions) with a circular symmetry distribution otherwise. The bubble is modelled to grow as a truncated sphere with fixed apparent contact angle supposing that

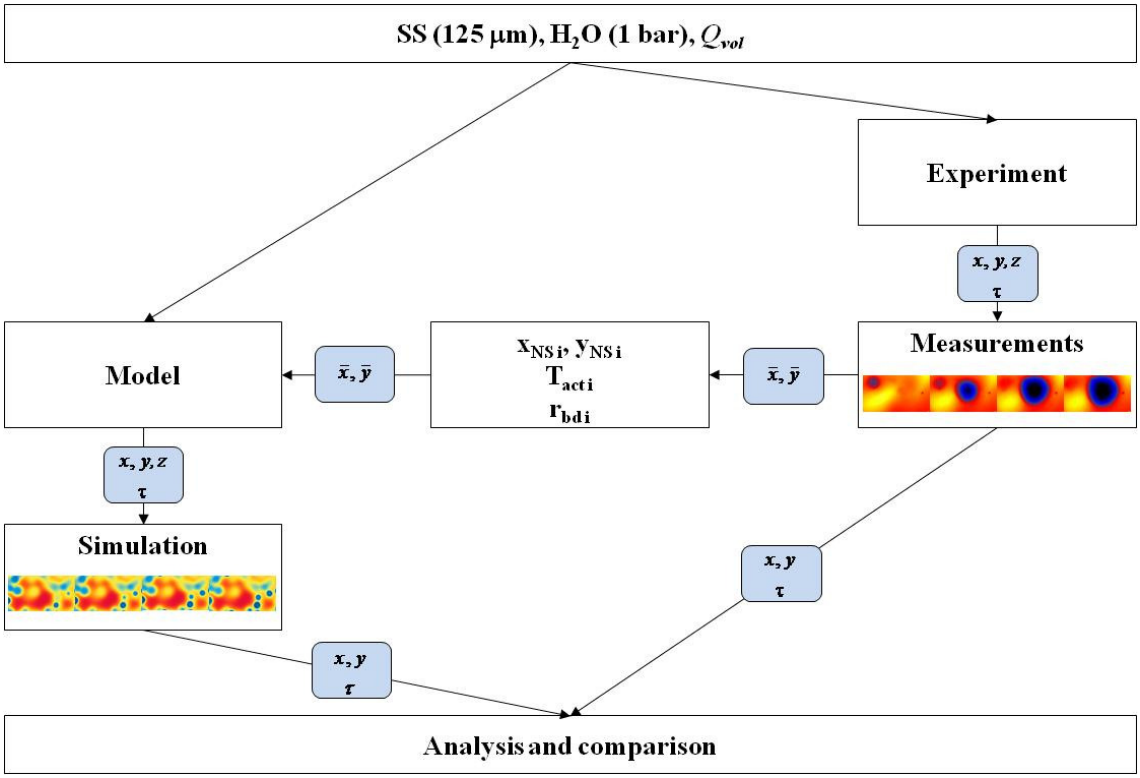

Figure 3-1: Logic of the code

the only contribution to the bubble growth is the vapour volume generated by evaporation of liquid at the bubble contact area.

3.1.1. Input data

The dependence of simulation results on experimental data requires a detailed analysis of the input data required by the code, as described here:

- Simulated time t_{sim} represents the period of time that is meant to be simulated and that is imposed by the user: it must be long enough to guarantee that the transitory period has finished and that the most active sites have been activated a sufficient number of times to allow good statistics.
- Time step Δt strongly depends on the characteristic of the mesh and on temperature variations on the substrate. A too large time step may generate numerical accumulation of errors or instability of simulations that may lead to false reproduction of physical phenomena. On the other hand, a too small time step leads to unreasonably slow simulations.
- Mesh distribution: the code uses an adaptable mesh distribution in the horizontal direction. Once a nucleation site becomes active, the code automatically replaces the initial coarse cell distribution with a refined distribution in the area of radius r_m (mesh radius) around the site itself. The mesh radius is imposed slightly larger than the maximum contact area radius for the specific site. The coarse mesh distribution is then restored at departure of the bubble. The coarse cells may have either a regular (square cells aligned along a Cartesian grid) or irregular distribution. By contrast, the cells in the refined areas have the shape of prisms regularly arranged in rings all centred in the nucleation site. Moreover, the substrate is vertically divided in equidistant layers, each of them having the same mesh distribution as the top one, and undergoing the same modifications at activation and deactivation of the sites. A more detailed analysis of the procedures involved will be provided in the following section.
- Mesh dimensions: the minimum and maximum dimensions of the cells are strictly connected to the time step. In the case of regular distribution of square coarse cells, they are identified by the width w_{xy}, constant for all the cells but the ones located at the edges of the substrate. By contrast, the refined cells have approximately the shape of sectors of circular rings. Their area is automatically

calculated by the code for each cell. Another important parameter is the number of vertical layers n_{vL} into which the substrate is divided. It depends on the thickness of the substrate and is connected to the width of the coarse cells. For very thin substrates, only one layer is simulated. The thickness of each layer is called Δz. Care must be taken in definition of the cell size, since the difference in size for adjacent cells (and principally at the interface between coarse and refined areas) may strongly alter the results of the simulations.

- Characteristics of the substrate: the dimensions of the substrate (and particularly its thickness δ_H, relevant for the effects of thermal disturbance in the vertical direction), conductivity (k_H), density (ρ_H), specific heat (c_H), initial temperature (T_{in}) and boundary conditions are to be defined at the beginning of each simulation.
- Characteristics of the fluid: saturation temperature (T_{sat}), latent heat (H_{fg}), density of vapour (ρ_V) and density (ρ_L), specific heat (c_L) and conductivity (k_L) of the liquid are also required.
- Heat transfer data: volumetric heat source ($\dot{q}$), heated area, heat transfer coefficients (*HTC*) in the different areas (i.e. for natural convection and nucleate boiling areas), enhancing factor for convection heat transfer (f_{enh}) need also to be introduced as input data.
- Bubble growth model: number and position of the potential activation sites (x_{NS}, y_{NS}), bubble departure radius (r_{bd}), activation temperature (T_{act}), and apparent contact angle (φ_0) are obtained from experiments or literature.

3.1.2. Mesh management

At the beginning of simulations, the substrate is horizontally divided into an initial distribution of coarse cells, identically repeated for each of the vertical layers in which the substrate is divided. Each cell is identified by two parameters, k and z. The parameter k identifies the progressive number of the cell and it is modified during the simulations. The parameter z identifies the position across the vertical direction in the substrate: 0 for the lowest surface of the cells in the bottom layer, 1 for the top surface of the cells in the bottom layer and coincident with the bottom surface of cells on the second layer from the bottom, and so on). The cells have the shape of a prism with either a triangular (irregular cell distribution) or rectangular (regular cell distribution)

base. An example of the mesh distribution for the case of cells with triangular base is shown in Figure 3-2 (a), for cells with an irregular distribution. If a nucleation site becomes active (according to the criterion defined in section 3.1.3), the cells located in a circular area around the nucleation site are removed (Figure 3-2, b) and then replaced (during the entire bubble growth) with a cell distribution with circular symmetry around the nucleation site with significantly smaller cell size (Figure 3-2, c).

The replaced area has a radius r_m slightly larger than the maximum contact area $r_{c,max}$ (reached at bubble departure since the apparent contact angle has a fixed value, so that $r_{c,\max} = r_{bd} \cdot \sin(\varphi_0)$); its value may vary from site to site. When the site becomes inactive again, the original coarse cell distribution is restored. A similar trend is shown in Figure 3-3 for a regular distribution of square cells. In both cases, the location of the nucleation sites is independent on the coarse mesh distribution. A drawback of this procedure is the limitation on the minimum distance (S) imposed to adjacent sites (i and j) active at the same time, as in Equation 3.1 (where w_{xy} is the width of the coarse cells and r_m is the mesh radius, corresponding in this case to the maximum contact area radius as specified before). All the variables are indicated in Figure 3-4.

$$S > 1.2\left(r_{mi} + r_{mj}\right) + 1.0 w_{xy} \qquad \textbf{(3.1)}$$

This numerical condition is inserted in order to avoid overlapping of refined cells: in fact, the code is unable to correctly reconnect refined cells belonging to different nucleation sites once one of the sites deactivates. In this case, some of the previously connecting cells may be linked to no longer existing cells. A row of coarse unrefined

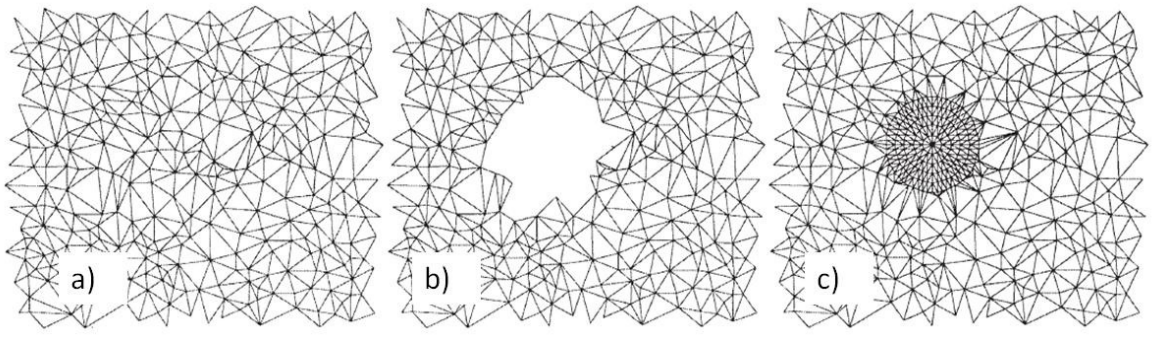

Figure 3-2: Mesh distribution for cells with triangular base – irregular distribution (Golobič et al., 2004)

cells is then always required to lie in between refined cells belonging to different nucleation sites. This numerical constraint constitutes an important limitation in investigation of site interactions because it fixes a minimum distance at which two sites can become active that may not exist in reality.

Important parameters to be accounted in the refinement process are the number of vertical layers (n_{vL}), the number of rings that constitute the refined area (n_R) and the number of cells in the first ring (n_{cR}), which defines the final number of refined cells per nucleation site and the level of detail in the angular direction assigned for each ring. The number of cells for different rings is not constant; it is increased with a fixed value per ring ($n_{R,incr}$, usually either 4 or 8 to maintain circular symmetry) in order to keep a similar area for all the refined cells. In Figure 3-4, n_R is equal to 8 for site 1 and to 4 for site 2, n_{cR} is equal to 4 and so is $n_{R,incr}$.

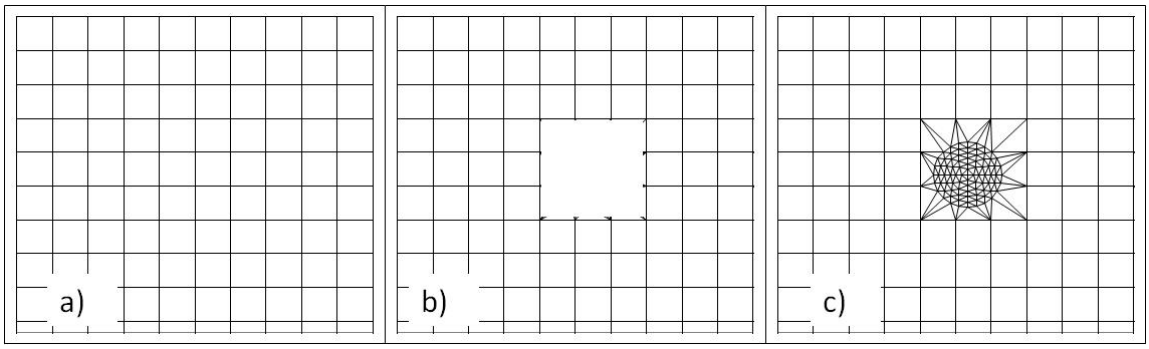

Figure 3-3: Mesh distribution for cells with square base – regular distribution

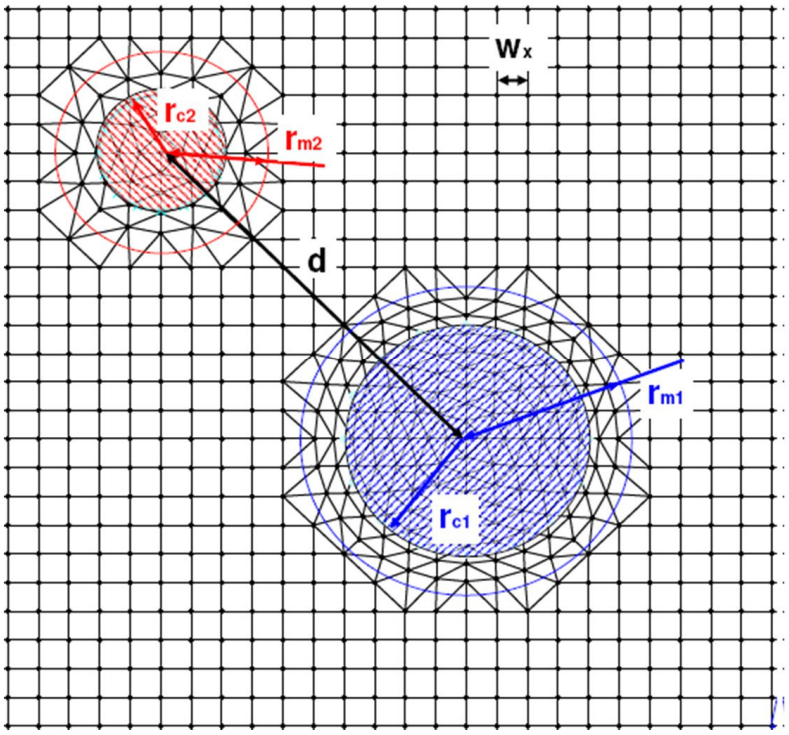

Figure 3-4: Minimum distance between active sites

3.1.3. Physics of the model

Solution of the energy equation on the solid plate

The main objective of the original version of the code is the study of the temperature field in the solid substrate. This is achieved by explicitly solving the time-dependent 3-dimensional temperature equation for temperature with volumetric heat source, Equation 3.2, discretised as expressed in Equation 3.3 with the symbols as in Figure 3-5. The dots in the figure represent the centres of the cells (supposed hexagonal with a square base in this example). The equation is numerically solved by using an explicit method for advancing in calculations: the temperature at the time step $\bar{t} + \Delta t$ and at a specific cell (identified with k) and corresponding to a specific layer (z) is directly calculated from the temperature distribution at the previous time step $\bar{t}$, taking into account the contributions (as heat flux through the cell surface) from all the adjacent cells in both the vertical and horizontal direction as well as the possible volumetric heat generation (Q_{vol}). The second-order accurate finite volume method has been used to evaluate the partial differential equations in the form of algebraic equations.

$$\frac{\partial T}{\partial t} = \frac{k_H}{\rho_H c_H}\left(\frac{\partial^2 T}{\partial x^2} + \frac{\partial^2 T}{\partial y^2} + \frac{\partial^2 T}{\partial z^2}\right) + \frac{Q_{vol}}{\rho_H c_H} \quad \textbf{(3.2)}$$

$$T(\bar{t} + \Delta t; k, z) = T(\bar{t}; k, z) + \frac{Q\Delta t}{A_{v,i}\Delta z \rho_H c_H} \quad \textbf{(3.3)}$$

Equation 3.3 represents the variation of the temperature in the generic cell k for the vertical position z due to the sum of heat contributions (q_1) during the time interval Δt in the cell volume $A_{v,i}\Delta z$. The different contributions to q_1 are expressed in Equation 3.4: the first term on the right represents the contribution of the volumetric heat source $\dot{q}$; the second term the conduction across the layer in the vertical direction; the third term the sum of contributions from each of the adjacent cells (j) in the horizontal direction. The code automatically calculates the area of the base of the cell $A_{v,k}$, the interface area $A_{h\ k,j}$ between cell k and the generic adjacent cell j and the distance $S_{k,j}$ between the centres of the cells k and j.

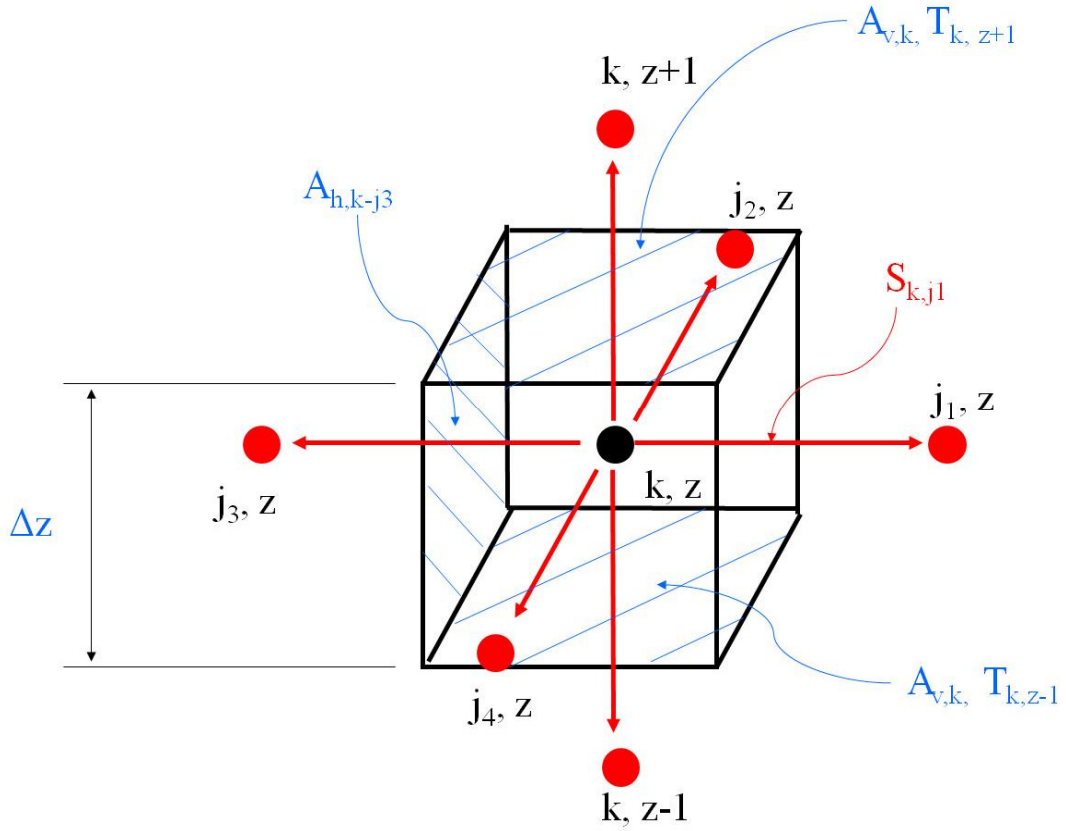

Figure 3-5: Geometry of a cell

$$Q = \dot{q}A_{v,k}\Delta z + A_{v,k}\frac{k_H}{\Delta z}\left[T(\bar{t};k,z-1) - 2T(\bar{t};k,z) + T(\bar{t};k,z+1)\right] + \\ + \sum_j A_{h,k-j}\frac{k_H \Delta z}{S_{k,j}}\left[T(\bar{t};k,z) - T(\bar{t};j,z)\right] \quad \textbf{(3.4)}$$

Two temperature values are associated to each cell, i.e. the values at the centres of the lower and upper surface (so that in presence of only one layer simulating the substrate, the temperature drop across it can be accounted). A different equation is used for the bottom and top layer, considering only half of the thickness of the cell. If not differently specified, the variable *T* will indicate the temperature for the generic cell *k* at the top surface of the substrate.

Boundary and initial conditions

The original version of the code assumes that the temperature at the lateral edges of the substrate is equal to the saturation temperature, as expressed in Equation 3.5, with the symbols as in Figure 3-6. For the bottom surface ($z = 0$), natural convection with the surrounding area is supposed, as expressed in Equation 3.6, with α_{air} equal to zero if adiabatic conditions are to be simulated.

$$T\,|_{x=0, x=x_{ca}, y=o, y=y_{ca}; 0\le z\le \delta_H} = T_{sat} \quad \textbf{(3.5)}$$

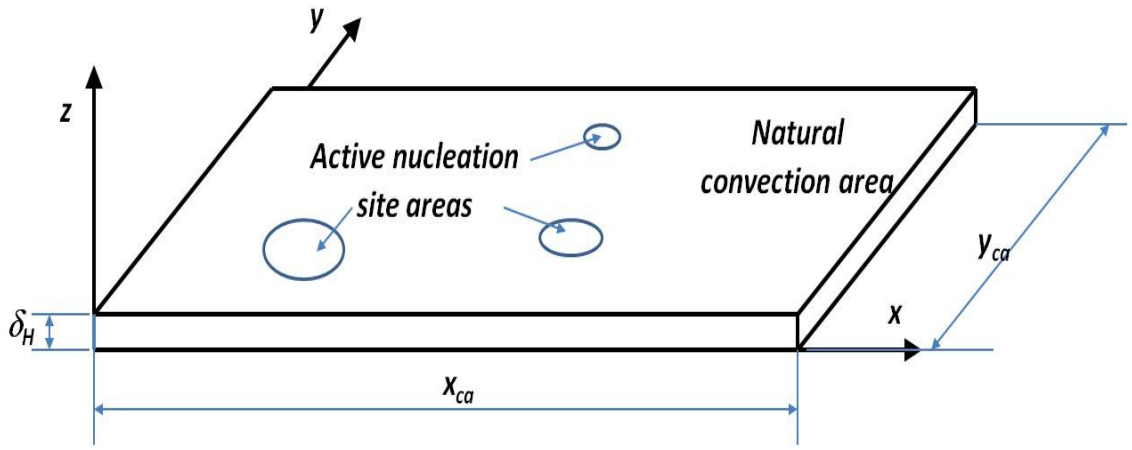

Figure 3-6: Geometry of the substrate (Golobič et al., 2004)

$$\left.\frac{\partial T}{\partial z}\right|_{0\le x\le x_{ca},0\le y\le y_{ca},z=0} = \alpha_{air}(T - T_{air}) \qquad \textbf{(3.6)}$$

At the initial time step ($t = 0\ s$) the temperature for all the cells and all layers is set equal to a fixed value (T_{in}), either equal to the saturation temperature or higher.

Heat transfer mechanisms

For each cell in the upper surface of the substrate, at each time step, a heat transfer coefficient (*HTC*) uniform in the cell itself is assigned depending on the relative distance of the cell from the centre of active nucleation sites and on the size of the bubbles. Three different areas are identified (Figure 3-7):

1. A natural convection area, corresponding to the area outside the bubble contact areas. A heat transfer coefficient for natural convection (HTC_{NC}, as in Equation 3.7 specific to the case of a stainless steel plate immersed in water at atmospheric pressure as in Golobič et al., 2004) is here applied. The enhancing factor f_{enh} is introduced to account for a possible uniform increase of the heat transfer coefficient caused by agitation of the bubbles and derived from experimental results. The equation can be easily replaced with any explicit correlation.

$$HTC_{NC} = f_{enh} \cdot 0.14\rho_L c_L \left[\frac{\gamma_{vol} g}{\upsilon_L}\left(\frac{k_L}{\rho_L c_{pL}}\right)^2 (T - T_{sat})\right] \qquad \textbf{(3.7)}$$

2. A triple contact line area, corresponding to the circular perimeter of the contact area of radius $r_c(t) = r_b(t)\sin\varphi$. Here, a high heat transfer coefficient (HTC_{CL}, as in Equation 3.8) is applied. In this area pure conduction in the liquid micro-layer of thickness δ_{ML}. The thickness of the micro-layer as also defined as input data by the user at the beginning of simulations, so that the heat transfer coefficient in this area is indirectly imposed. The width of the contact line area corresponds to the width of the refined cells in the radial direction (dependent on the bubble size at departure and number of rings used for the refined mesh area). It is generally much larger than the theoretical contact line area, so that the heat

transfer coefficient values are required to be scaled to obtain the correct heat flux from the area.

$$HTC_{CL} = \frac{k_L}{\delta_{ML}} \tag{3.8}$$

3. The inner area of the contact area, i.e. the area enclosed by the triple contact area, where a low but not zero heat transfer coefficient (HTC_{in}) is assigned. This contribution takes into account possible residuals of liquid in the dry spot below the bubble, in the inner part of the contact area, considered as adsorbed film, by the use of a empirical correlation with a central peak and decreasing towards the contact line region.

The code automatically calculates to which of these areas each cell belongs, and on the base of that, a heat transfer coefficient is assigned. The mesh management process refines the cell distribution in the regions corresponding to an area slightly bigger than the contact line area, so that the heat transfer may undergo rapid and significant variations in this area. By contrast, for the natural convection area, involving mostly (but not exclusively) coarse cells, a more uniform heat transfer coefficient distribution will be normally observed.

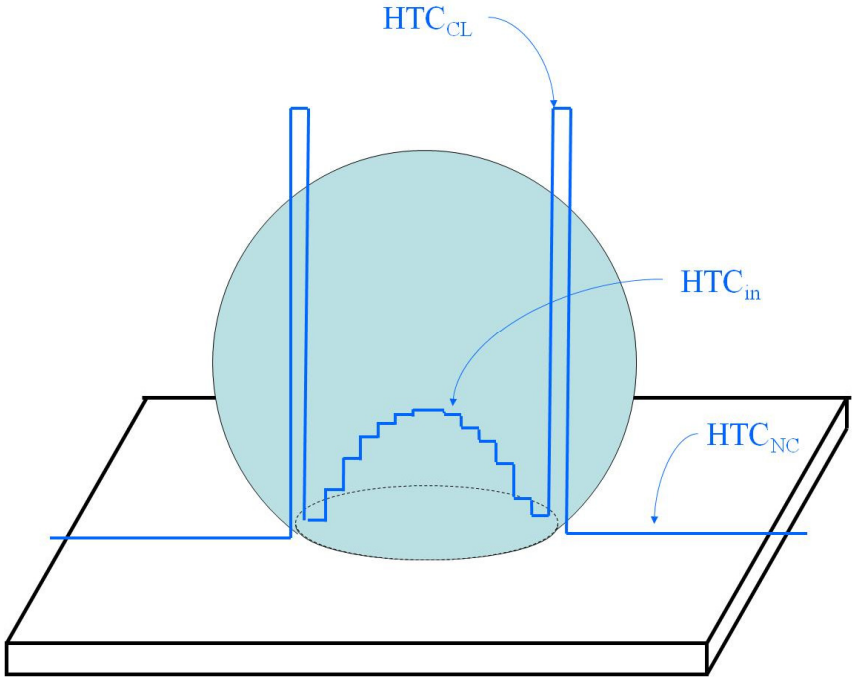

Figure 3-7: Heat transfer coefficients distribution around a growing bubble (original model OR)

Activation and deactivation of a nucleation site

For each nucleation site *i*, an activation temperature, $T_{act,i}$, is assigned; for each of the inactive sites, at each time step, the code checks the temperature for the cell $\bar{k}$ corresponding to its centre. If the value exceeds the activation temperature, see Equation 3.9, and if the not-overlapping mesh condition is satisfied (Equation 3.1), activation of the site occurs, and the mesh distribution is locally refined as described before. The bubble grows until departure that occurs when the equivalent bubble radius $r_{eq,i}(t)$ reaches a maximum value, called bubble departure radius $r_{bd,i}$, Equation 3.10, specified by the user for each nucleation site on the base of experimental or literature data.

$$T(t,\bar{k},z_{\delta_H}) \geq T_{act,i} \tag{3.9}$$

$$r_{be,i}(t) \geq r_{bd,i} \tag{3.10}$$

Bubble growth model

At activation (occurring for instance at $t = t_0$) the bubble starts from a zero bubble radius, $r_{b,i}(t_0) = 0$, so that the initial nucleus radius is neglected. From the following time step, the bubble grows as a truncated sphere with a fixed apparent contact angle from nucleation to departure $\varphi = \varphi_0$. Evaporation occurs only at the contact area (i.e. the region enclosed by the triple contact line) according to Equation 3.11. The term on the left side represents the cumulative heat due to evaporation at the considered time step; the first term on the right side represents the cumulative heat at the previous time step; the second term accounts for evaporation in the inner area (with heat transfer coefficient HTC_{in}) excluding the contact line area itself and the last term the evaporation at the triple contact line area (HTC_{CL}). Evaporation at the dome of the bubble is neglected. The equivalent bubble radius is calculated according to Equation 3.12, assuming a truncated sphere shape for the bubble.

The contact area radius is then calculated, $r_c(t) = r_b(t)\sin\varphi$. Figure 3-8 shows the fundamental bubble growth parameters for advancing triple contact line.

$$Q_{b,i}(\bar{t}+\Delta t)=Q_{b,i}(\bar{t})+\sum_{\substack{(x_j,y_j)\in \\ inner\ area}} A_{v,j}HTC_{in,j}\left[T(\bar{t};j,\delta_H)-T_{sat}\right]\Delta t+$$
$$+\sum_{\substack{(x_j,y_j)\in \\ triple\ cont \\ area}} A_{v,j}HTC_{CL,j}\left[T(\bar{t};j,\delta_H)-T_{sat}\right]\Delta t \qquad \textbf{(3.11)}$$

$$r_{eq,i}(\bar{t}+\Delta t)=\sqrt[3]{\frac{3Q_{b,i}(\bar{t}+\Delta t)}{4\pi\rho_L H_{fg}}} \qquad \textbf{(3.12)}$$

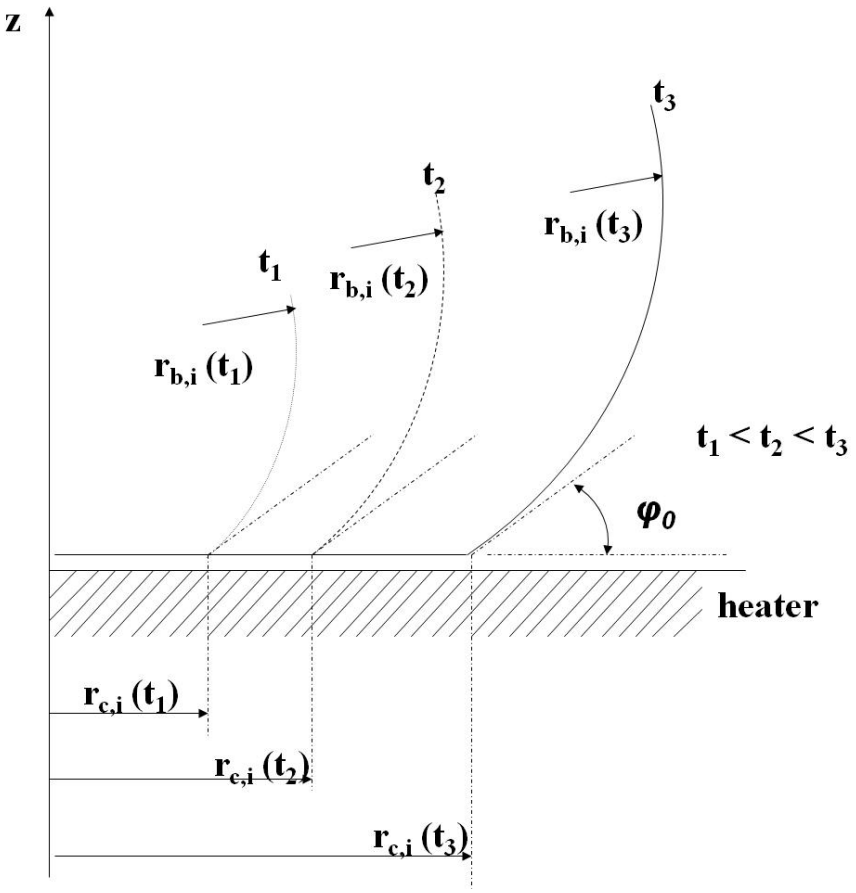

Figure 3-8: Advancing triple contact line

Interactions between nucleation sites

Referring to the interactions between a nucleation site and the surrounding regions and between different nucleation sites described in Section 2.2, this version of the code models only the thermal interaction between the substrate and the bubble. However, the thermal interaction between adjacent nucleation sites is indirectly accounted (if existing) because of the complete solution of the temperature field in the substrate itself. Hydrodynamic interactions (between a bubble and the surrounding liquid and between different bubbles) are completely neglected, since the fluid-dynamics of the process in the liquid side is not simulated. This condition, even though very simplistic, allows relatively small computational times, and consequently the study of thermal interactions for a large number of nucleation sites.

3.1.4. Output data

The original version of the code focuses on the study of a large number of nucleation sites with no individual attention to any site. The most important output data generated are then related to the analysis of both the mean value of the temperature (averaged on the surface) and its distribution on the surface itself. In particular, the fluctuations of the temperature around the nominal value were studied and then compared to experimental results.

The following data were the main explicit output data:

- Activation of the nucleation sites: for each nucleation site, the number and activation times were recorded in order to study the possible distribution in clusters of the most active sites.
- History of the mean value of temperature averaged over the central area, in order to evaluate the fluctuations due to boiling phenomena.

- History of the number of nucleation sites active at the same moment.
- History of the fractions of the surface affected by nucleate boiling and by natural convection with respect to the whole surface.
- Surface distribution of temperature at fixed time steps, used for graphical visualisation of the hottest and coldest areas. An example is shown in Figure 3-9 for an asymmetric temperature distribution for two close-spaced sites. The data

refer to one of the cases considered in the next chapter and shows two craters due to the cooling effect of the high heat transfer in the contact area region.

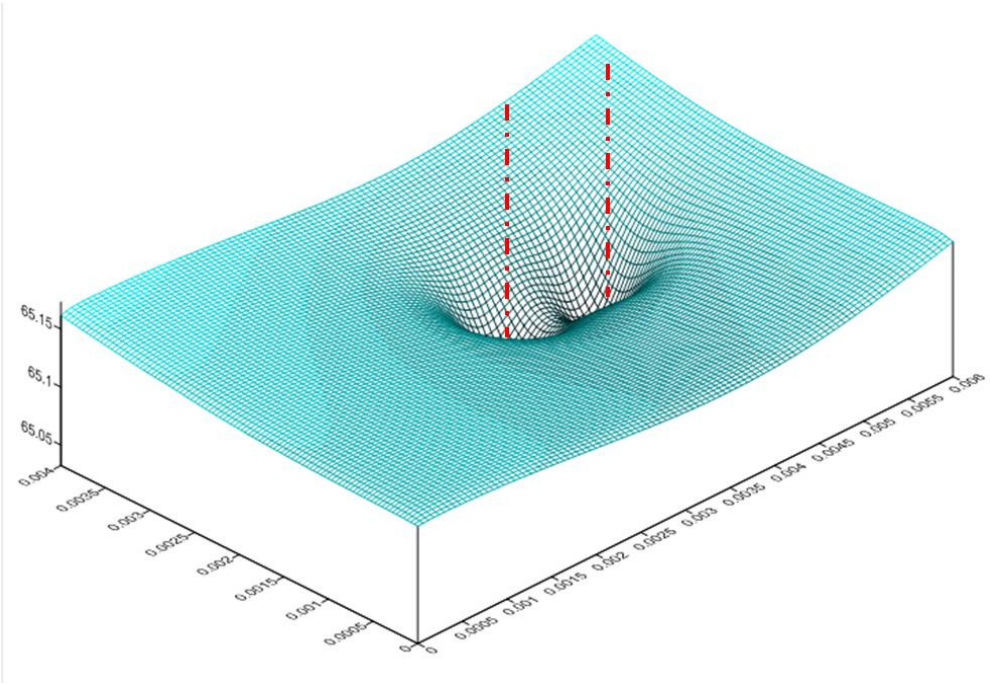

Figure 3-9: Temperature surface distribution

3.1.5. Critical analysis and necessity of improvements

This version of the code, even though it is a very powerful instrument for the analysis of thermal interactions between active nucleation sites randomly located on a surface, still presents some drawbacks. First at all, as mentioned before, interactions and phenomena on the liquid side, including coalescence, are completely neglected. However, the choice of not simulating phenomena in the liquid side (that are at the moment used only as boundary conditions for heat removal from the substrate) is justifiable by the consequent reduction of the computational time.

A second problem is related to the mesh refinement and unrefinement processes, and in particular the limitation imposed by Equation 3.1: under particular conditions, the phenomenon of numerical alternating growth or inhibition in activation of adjacent sites may occur (because the sites are too close together, only one of the two is allowed to be active at a given time) may be generated and the results may be incorrectly interpreted as due to physical effects (e.g. site seeding or inhibition) if not carefully analysed.

Moreover, the choice of particular physical approximations, such as neglecting of the heat transfer at the dome of the bubble, or the choice of a fixed apparent contact

angle, leads to unrealistic physical processes, (as a contact area maximum at departure) and makes the code still unsuitable to be used as a design tool to investigate a large number of situations. However, these approximations are attributable more to this being an early and unrefined version of the code than to strategic choices.

Some of the needed improvements have been analysed and partially solved during this PhD project in Brunel University, even though the code still needs further improvements from both the numerical and physical point of view. In the following sections an analysis of the suggested modifications will be presented. The effects of these modifications on the bubble growth and temperature variations will be presented in the next chapter.

3.2.New version of the code

The new version of the code is specifically studied to deal with experimental results obtained at University of Edinburgh that use a silicon wafer (0.38 mm thick) with artificial micro-fabricated cavities located on the top surface. The wafer is completely immersed in FC-72 at saturation conditions, with variable pressure. A more detailed analysis of the experimental facilities and results will be provided in the following chapter. However, the code can be easily modified to be applied to a wider range of substrate materials and liquids.

3.2.1. Numerical improvements

Parallelisation

The restructuring of the code was developed in collaboration with R.A. Nelson at Los Alamos National Laboratory (USA); in particular, the creation of independent files for each procedure and the organisation in a Visual Studio project allowed the parallelisation process. Two options are now available to run the code: the first option (debug mode) allows the user to suspend the simulations while checking the values of the variables at that particular instant; the second option (release mode) allows a better performance and shorter simulation times. The quality of performance in release mode depends on some optimisation parameters that must be tuned to provide the fastest solution. The concept behind parallelisation is related to the execution of operations by different cores of the processors at the same time. Great care must be used in applying this approach, since an inappropriate management of the variable may lead to an

incorrect solution. The difference in simulation time between using the two run modes may be as large as 4 times.

Restructuring of the numerical code

A second objective of restructuring of the code was to make it more accessible for modifications and improvements. The first step in reorganization involved the splitting of the single instruction file in different files: each subroutine has been associated with an independent file, leaving in the main file only the main body with most of the instructions related to the physical processes. A rearrangement of the variables was also carried out: variables used in more than one routine that were previously declared in the main body and then shared are now organised in independent files, so that their replacement or elimination are facilitate. All the necessary files have been grouped in four directories:

- //_Source_files containing the files with all the instructions of the code including the main body and all the sub-routines.
- //_Header_files containing the files with the declaration of all the shared variables and the parameters (a parameter differs from a variable because its value cannot be modified during simulations).
- //_Input containing the files with the main input data for procedures, physical processes and mesh creation and management.
- //_Output_gen containing the general output files related to error messages.

Four extra directories are created for the output files, as listed here:

- //Out_m containing the general output files for the mesh distribution. These files are optional since they occupy a large storing space.
- //Out_s containing the surface distribution files, with data for temperature, heat flux and temperature at different time steps. Also these files are optional.
- //Out_t containing data files used during the mesh refinement process.
- //Output containing the output files plotted as time histories. Here are stored the files for activation, temperature, bubble radius, heat contribution, coalescence and so on per each site, as described below.

The most important procedures contained in "_Source_files" are listed here in alphabetical order:

- Bubbles_vA.f constitutes the main body of the code and contains the main instructions, including the initialization of some variables, plotting of some output files and recalling of most of the subroutines listed below.
- Coalescence.f is a short subroutine that defines simple semi-empirical rules to account for coalescence.
- Deactivation.f deals with the problems following deactivation of a nucleation site, including recalling sub-routines for mesh management and re-initialisation of the variables involved in the bubble growth.
- Dodajmrezo.f generates the position of the refined cells following activation of a new site.
- Dolocialfo.f assigns the correct heat transfer coefficient to each of the cells on the top layer (both coarse and refined), depending on the area to which it belongs (according to Figure 3-7) and to the distance from the nucleation site.
- Growth_ref.f calculates the bubble volume, shape and radius from the heat contributions.
- Input_read.f deals with reading data from the input files at the beginning of each simulation.
- Mesh_creation.f generates the files used during the simulations for mesh management during the refinement and unrefinement processes. The same files were to be generated separately in the original version of the code. This new procedure is particularly convenient in case of multiple simulations with different mesh characteristics.
- Plot_results.f deals with plotting of results along a line, as described later.
- Plot_surf_res.f creates optional output files specifying for each cell located on the top surface of the substrate the value of one variable. At present the code is set to generate plots of temperature, heat flux and heat transfer coefficients, so that surface distributions may be successively generated.
- T_in_rec.f is optionally used to elaborate output files from previous simulations (using a similar mesh distribution) in order to have a non-uniform temperature field as initial condition for a new simulation.

Control variables

Several variables have been recently introduced in the code to detect the presence of possible errors, monitoring the variables the most subject to numerical inconsistencies. Three control variables have been inserted, evaluating errors on the minimum time step, on the mesh refinement process and on the heat production.

- The first variable verifies that the minimum time step satisfies Equation 3.13 for the minimum size of the cell (evaluated at each time step); in the formulation, $A_{v,min}$ represents the minimum cell area in the horizontal direction and Δz gives an estimate of the thickness of the layer in the substrate (see Figure 3-5 for details on symbols).

$$\Delta t < 0.3 \min\left\{A_{v,\min}, \Delta z^2\right\} \frac{k_H}{\rho_H c_H} \tag{3.13}$$

- The mesh refinement process is monitored by a variable that verifies that the total area of the substrate is approximately equal to the sum of all the cells. In fact, it may occur that either because of an erroneous choice of the coarse and refined cell sizes or because of numerical errors, the code links the new cells created after refinement to non-existent or no longer existing cells. In this case, the sum of the surface area of the cells becomes significantly bigger than the area of the whole substrate. If the limit for the tolerance of this parameter is exceeded, the code displays a warning message asking for confirmation before continuing with the simulations.
- Another control variable is related to the heat flux: if adiabatic conditions are applied to the edge and bottom of the substrate, the total heat removed from the top surface must be equal, in steady state conditions, to the heat source (applied as heat flux or volumetric heat generation). A plot of the history of this variable is always generated by the code to allow future checks. The error is generally small, but not zero, if the calculations take into account the ideal surface area of the substrate, slightly different from the sum of the areas of each cell, also without mesh refinement. However, the error is generally smaller than 1%. Moreover, if the error exceeds a specific percentage value, a warning message

appears during the simulations specifying the error entity and asking the user whether to continue. This variable is an instrument to check the conservation of energy during and after the simulations. A future improvement to the code could be the inclusion of the heat dispersion at the lateral edge of the substrate (currently not accounted, since in most of the simulations the edges have been supposed adiabatic).

3.2.2. Input data

Proceeding with the reorganisation of the numerical code, important improvements were made for the input data. The first main improvement was the creation of a unique input file per simulation, containing all the input data and parameters so that a new user can easily change them without knowing the details of the logic of the code. However, particular care should be used in the insertion of the data since some of them may generate instability, as for instance an incorrect use of the mesh parameters. This file contains now also a unique identifier (a four digits combination of letters, numbers and symbols, here indicated by xxxx) chosen by the user and present both in the name of the file and inside it. The input file contains the instructions for creation of files of data to be used for mesh generation and management (previously inserted separately as input files) and now contained in a dedicated directory called "Input_xxxx". The use of an identifier allows several simulations for the same project avoiding over-writing or elimination of previous output files, as it can happen using the original version of the code. An important improvement connected to this aspect is the introduction of a new routine that allows sequential simulations, so that the user will not be required anymore to wait until the end of a simulation to start a second one.

Additional input data

Additional input data are now inserted to define the precision and frequency required in plotting output files. The user can now decide for some outputs to skip plotting them or to limit the results to a narrower time interval; in particular this is important for the series of output data related to the surface and mesh distribution that can occupy a large storage space.

Moreover, the fluctuations of some input data detected during experiments may now be taken into account in the new version of the model by inserting an uncertainty

parameter for the bubble departure radius and for the activation superheat (equal to the difference between the activation temperature and the saturation temperature). The uncertainty represents the maximum variation from the nominal value allowed: for each parameter, the code independently chooses, per each bubble growth and per each site, a positive or negative random value in the indicated range to be added to the nominal value. The uncertainty may also be set equal to zero, as it is in most of the sensitivity analysis, in order to develop a completely deterministic analysis. The uncertainty parameters become instead relevant for long-term simulations.

3.2.3. Mesh management

An important innovation from the numerical point of view is the use of a new procedure for mesh management. The original version of the code locally refined the mesh distribution around a nucleation site only once per bubble growth, i.e. once the site has become active. Immediately after departure and deactivation, the previous distribution of coarse cells was restored. The use of a fixed mesh radius may lead to unrealistic phenomena of alternating bubble growth or inhibition at close spaced nucleation site (as analysed in Section 3.1.2). In fact, if one site was active, all the others located at a close distance were numerically inhibited to activate. This effect is more evident with increasing size of the coarse cells. Unfortunately, the size of the coarse cells cannot be reduced indefinitely, because a size reduction implies an increase in the total number of cells and then of the computational time.

Two strategies to limit the occurrence of numerical alternating bubble growth and inhibition have been suggested and implemented, described below. These models (*a* and *b*) are based on intermediate mesh refinement procedures that use a mesh radius that varies stepwise with the contact area radius. This solution increases the computational time but it is able to temporarily reduce the refinement area allowing bubble growth at the same time for close-spaced sites in particular conditions. The differences between the two models are explained here for different time steps ($t_1 < t_2$).

- Model *a* uses a fixed number of refined cells per nucleation site, with consequent stepwise variable size of the refined cells.
- Model *b* uses a fixed size of refined cells per site, with variable number of circular rings and number of refined cells per site. This strategy can be interpreted as the introduction (for increasing contact area radius) or removal

(for decreasing contact area radius) of the external ring of refined cells when required by the mesh radius, with no variation of position of the inner refined cells during the bubble growth.

Figure 3-10 shows a comparison of the mesh distribution (the black lines identify the connections between the centres of the cells, indicated by the small black dots) for the two models: the refined area is clearly related to the contact area, in red. For model *a*, the number of rings is always 6 but the size of all the refined cells is clearly larger at t_2 than at t_1, while for model *b* the number of rings increases from 5 to 6 (and consequently the number of cells), while maintaining the size of the past 5 rings. The drawback associated to model *a* is the variation in size and position of the refined cells, so that the position of the cell is changing at each intermediate mesh refinement process. This condition generates a partial loss of information in the temperature distribution before the refinement. The same problem would be present also for solution *b*: however, fixed positions of the cells allow the use of a new procedure (file: temp_rest.f) able to

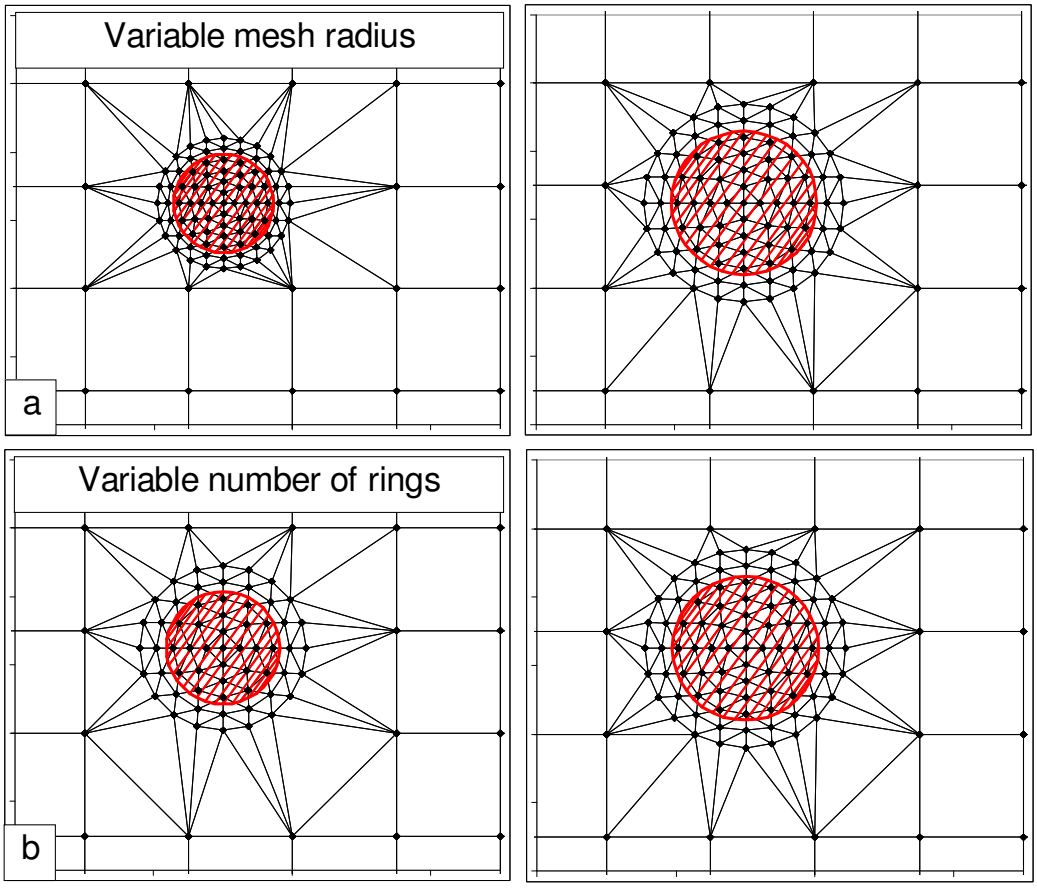

Figure 3-10: Refinement methods.
a) Variable mesh radius. b) Variable number of rings

completely restore the temperature distribution after the refinement as it was before it, except in the added or removed external ring. Moreover, the application of model *a* involves the use of a denser cell distribution with smaller cells for small contact area radii (i.e. during the initial and final stage of bubble growth). The small size of the cells may also generate numerical instability problems if the time step is not sufficiently reduced, and a more complicated mesh refinement process due to the imbalance in cell size.

Both processes involve a large increase in the required computational time, but they are not completely able to remove the effect of alternating bubble growth: in practice, the temporary refinement process requires verification of Equation 3.1 after each refinement. If the equation is not satisfied, the growth of the two bubbles is not allowed at the same time. For this reason, the bubble connected to the area that the code is attempting to refine is forced to immediately depart (without any necking process) and the coarse mesh distribution is restored in the emptied area.

Figure 3-11 shows the effect of numerical inhibition of nucleation site 5 located at a close distance in the middle of 4 active nucleation sites. The central site is inhibited from activation in case *a* (the intermediate mesh refinement process is not applied in this case) due to limitation for adjacent sites imposed by Equation 3.1. The site in the middle of the substrate is not able to activate during the simulated time, even though the condition on the temperature is always satisfied. By contrast, in case *b*, the activation of all the sites at the same time occurs several times, actually more than when the site was

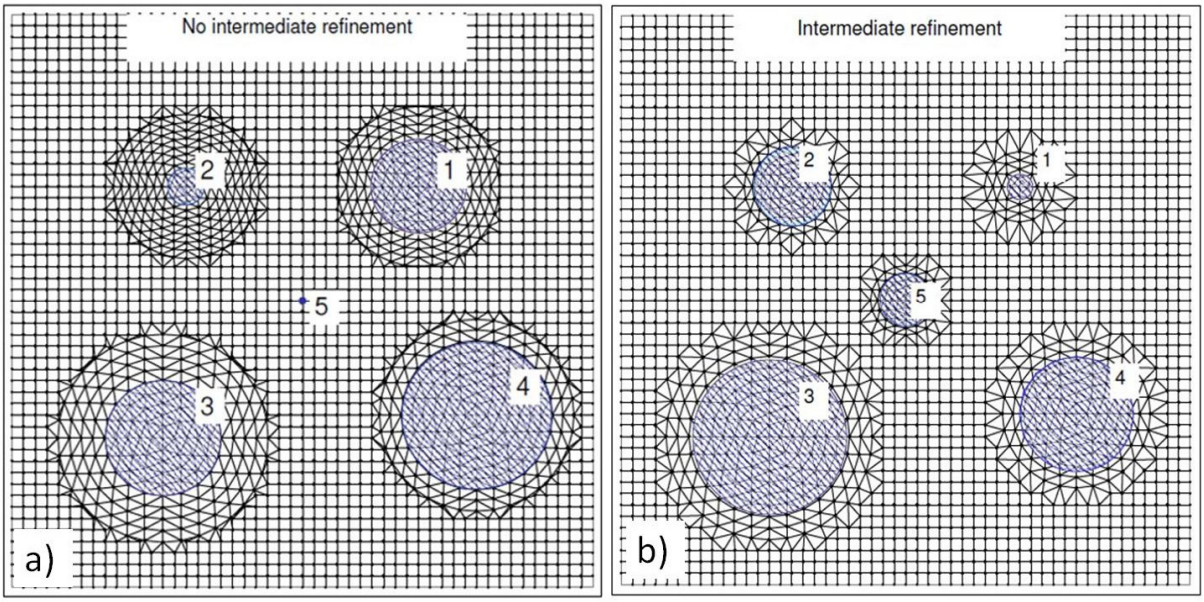

Figure 3-11: Numerical inhibitory effect

isolated. This occurs because the bubble growth for the central site may not reach its final size, since the intermediate refinement process may be still inhibited for large mesh radii. It is important to specify that in this case, the central site had the largest sequence number *i* (i.e. the sites were numbered from 1 to 5, and the central site was identified with the number 5). A complete different behaviour of the sites has been observed when a lower sequence number for central site was used with no intermediate refinement process. When it was identified with the number 1, the four surrounding sites were completely and continuously inhibited from activation. However, a correct coalescence model could be able to limit the problem, mostly for bubbles with a contact angle not very close to 90°, where the contact radius substantially differs from the bubble radius.

The difference in the inhibitory effect that generates alternating bubble growth is visible if the bubble radii and the contact area radii are compared for two sites located at close distance, as in simulations for which the results are shown in Figure 3-12 and Figure 3-13. The simulations differ only in the number of intermediate mesh refinements used in the two cases (0 for the first one and 5 for the second one). The alternating effect is clearly visible for the 0 intermediate refinements case, see Figure 3-12, so that the site 1 is becoming active only when site 2 deactivates and vice versa. By contrast, for the 5 intermediate refinements case, depicted in Figure 3-13, the process allows the bubbles to grow at the same time, even though not for the whole bubble growth. In fact, when both the areas are at maximum, the bubble at site 2 is

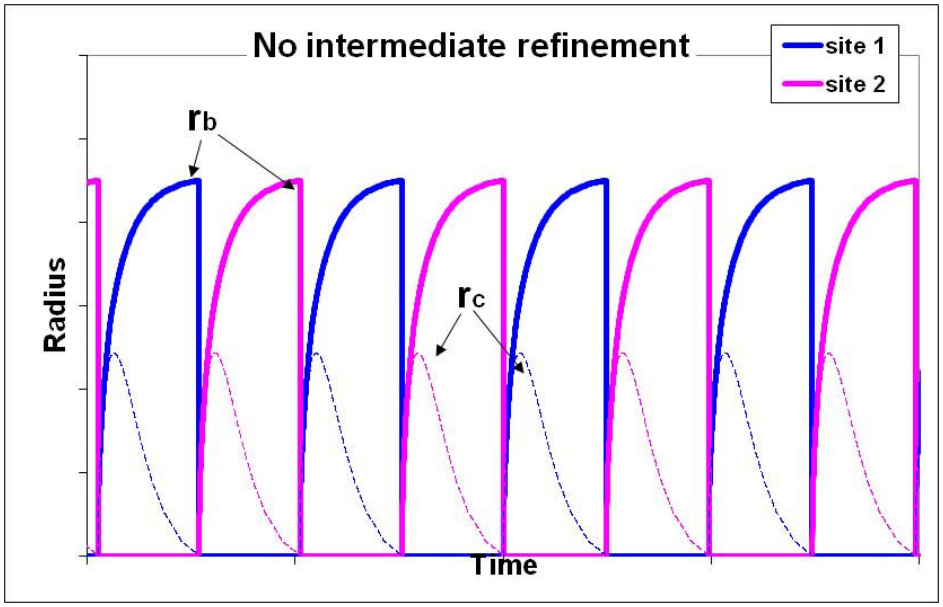

Figure 3-12: Alternate effect with no intermediate mesh refinement

forced to immediately depart before the radius has reached its maximum size, as it occurs three times during the presented time slot (and indicated by ↓ in Figure 3-13). A more detailed analysis of the effects of both the sequence order for the sites and the alternating growth will be provided in the following chapter, since the phenomena are strongly influenced by several factors (e.g. the activation temperature, the average temperature and the initial apparent contact angle).

Alternative approaches have been evaluated to speed up simulations, such as the use of a fixed distribution of fine cells with no temporary refinement, or the use of a refined cell distribution not modifiable during the simulations. The first approach is not recommended since the position of the nucleation sites is limited by the cell distribution. The second solution would not allow bubbles to grow at very close-spaced nucleation sites, limiting the choice of the location of the sites themselves. A third compromise is described in the next section and it is based on the division of the nucleation sites in two groups, standard sites and unrefined nucleation sites.

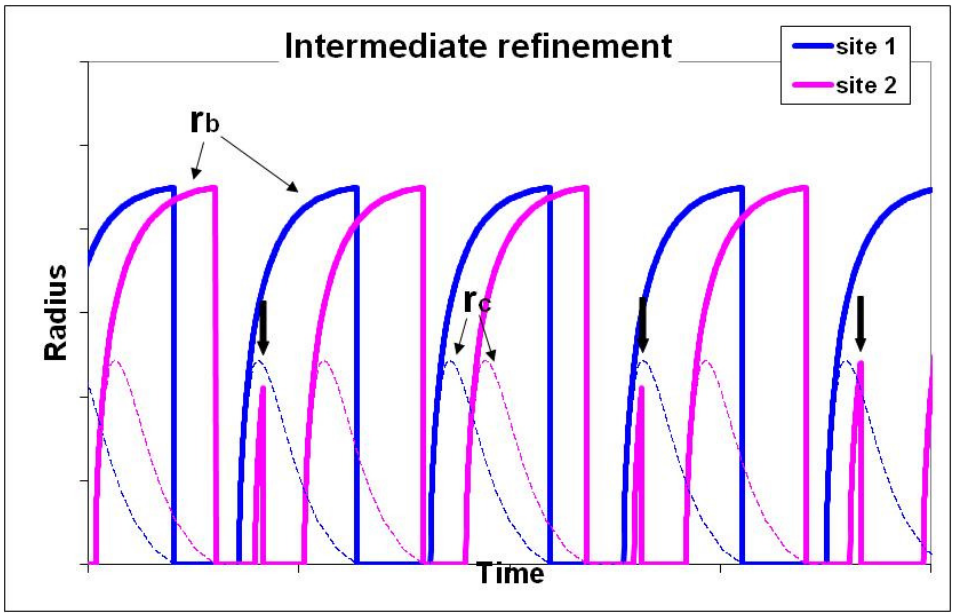

Figure 3-13: Reduction of the alternate bubble growth effect using the intermediate mesh refinement

Standard and unrefined nucleation sites

The final objective of using the code as a design tool requires simulations to be run on high-speed commercial workstations (for instance with dual processors, four cores per processor) for approximately 24 hours, for 100 potential nucleation sites and simulated time allowing at least 30-40 activations for the most active sites. The use of the standard procedure of mesh refinement (either original or modified) for all the sites makes the code unsuitable for such requirements. To overcome this problem, a simplified solution has been studied: the whole population of nucleation sites was divided in two groups, called standard sites and unrefined sites.

- The standard sites coincide with the original nucleation sites (that supposes the local mesh refinement around them once activated, as described before); in a simulation of 100 sites the standard sites are limited in number to 20, in order to achieve the time constraints. The limitation corresponds to the number of sites active at the same time, while the general number may be significantly increased.
- The unrefined sites are dealt with a new procedure that modifies only the heat transfer coefficients for the cells located in a pseudo circular area around the nucleation site (aiming to simulate a coarse contact area) with no local modification of the mesh distribution. The use of unrefined sites strongly reduces the computational time, even though the physics around these sites is less detailed (mostly for large coarse cells). However, the number of unrefined sites cannot be indefinitely increased and so far it has been limited to 80.

The comparison of the cell distribution and the computational triple contact line area for standard and unrefined sites is shown in blue in Figure 3-14. Comparison of the coarse cell size in Figure 3-10 and Figure 3-14 suggests that the size may significantly affect the representation of the pseudo contact area for unrefined sites when the maximum contact area is of the same order of or slightly bigger than the coarse cell size. In this case, the pseudo contact area cannot properly simulate local variations but can only provide an approximate average value for the heat transfer in that area.

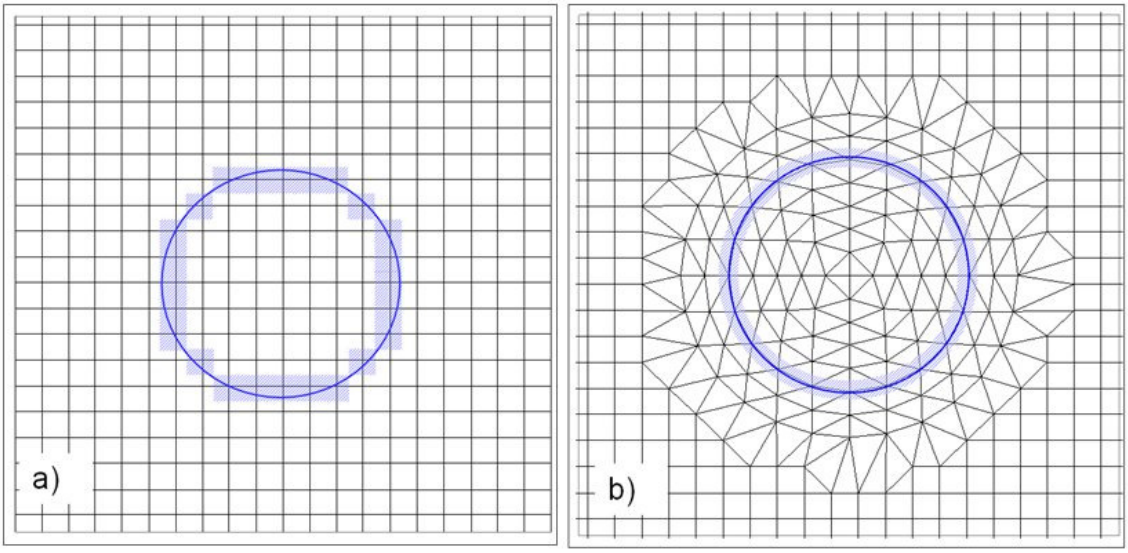

Figure 3-14: Simulation of the triple contact line area:
a) Unrefined sites. b) Refined sites

Tuning of the heat transfer coefficients on experimental data

Another option has been inserted in the code in order to make it more flexible. In the original version of the code, the heat transfer coefficient for the triple contact area was defined according to Equation 3.8, so that the thickness of the micro-layer was the direct input datum. In the new version, the heat transfer coefficients for both standard and unrefined sites must be specified. However, an option is available to automatically (and independently) tune these values for the first standard and unrefined sites according to bubble growth period and bubble departure radius. The option is very helpful in cases where these data are available from experiments: a preliminary simulation can be run to identify the correct heat transfer coefficient, which will be assumed valid also for other situations and applied to a larger or different site distribution.

3.2.4. Improvements to the physical model

Heat source

Several innovations have been introduced in the physics of the models: some of them involve only few significant changes, while some others are based on a new approach in the model. A first simple but important modification is related to the introduction of a heat flux source applied to the back of the substrate that may replace or coexist with the volumetric heat source implemented in the original version of the

model. In particular, while the volumetric heat source is meant to reproduce electric heat generation for metal substrates, the heat flux source simulates the behaviour of a laser or of a very thin metal layer, electrically heated and located on the back of the substrate. The difference in heat source becomes significant for relatively thin or poorly conductive substrates, where thermal variations in the substrate itself become important.

Activation conditions

A second important change is related to the process used to calculate the activation superheat and then the activation temperature that at the moment constitutes the only criterion for determining the activation of a site. In Golobič et al. (2004) the activation temperature was derived from a NEF analysis applied to experimental results. At present, if experimental data are not available, the activation superheat ΔT_{act} can be calculated as in Equation 3.14, supposing that the activation temperature is the minimum temperature necessary for a nucleus of radius equal to the cavity radius to start growing.

$$\begin{cases} \Delta p = 2\sigma / r_{cav} & \text{(a)} \\ \log_{10} p(Pa) = 9.729 - 1562 / T(K) & \text{(b)} \end{cases} \qquad \textbf{(3.14)}$$

For a cavity of fixed cavity mouth radius (r_{cav}) and surface tension (σ), the minimum overpressure (Δp) needed for the bubble to start growing is defined by the equation (a). From equation (b), specific for FC-72 (based on 3M Fluorinert Electronic Liquid FC-72 data, 2006), the saturation temperature at experimental conditions and the temperature at a pressure equal to the experimental value plus the overpressure may be calculated. The activation superheat can be then derived. Alternative criteria may be studied and easily introduced in the code, based for instance on variations of the superheat instead of its absolute value. Moreover, a modifiable uncertainty parameter has been recently added to the nominal activation superheat to simulate the uncertainty of data from experimental results.

Heat transfer models

The correlation for the natural convection heat transfer coefficient for water on stainless steel described in Equation 3.7 has been replaced by Equation 3.15 for FC-72

on silicon (Parker and El-Genk, 2005), liquid used in the latest experiments developed at the University of Edinburgh. However, the correlations may be easily replaced in the subroutine Dolocialfo.f (see Section 3.2.1 for further details).

$$HTC_{NC}(t;k) = f_{enh} \cdot 314 \cdot [T(t;k,z) - T_{sat}]^{0.2} \quad \textbf{(3.15)}$$

The heat transfer model applied to the upper surface used in the original version of the code (*OR,* Section 3.1.3) assumes a very high heat transfer coefficient in correspondence to the triple contact line, a not-zero heat transfer with a central peak coefficient in the inner part of the contact area and natural convection outside the bubble contact area (Figure 3-7). This model is in contrast with both the micro-layer model (ML) supported by recent experimental results of Golobič et al. (2009) and the contact line model (*CL*) supported by Stephan (Stephan and Hammer, 1994, and Stephan and Fuchs, 2006).

The first assumes that a thin film of liquid (micro-layer) is trapped between the bubble and the substrate: pure conduction is assumed in it, so that $HTC = \frac{k_L}{\delta_{ML}}$. A peak for the heat transfer coefficient is assumed at the centre of the contact area (i.e. the micro-layer is supposed to have its minimum thickness) and a radial decrease, with no increase near the triple contact line; the maximum does not change with increasing contact area. The latter model assumes a strong evaporation in a very narrow area (triple contact line) and a very small or zero heat transfer coefficient in the inner part. In both cases, the maximum heat transfer coefficients are either directly imposed by the user at the beginning of simulations or automatically tuned by the code during simulations to match the experimental values for bubble growth period and bubble departure radius. Moreover, in the ring immediately outside the contact area, the heat transfer coefficient has been changed; an enhancing factor ($f_{enh,turb}$) equal to 2 has been imposed in order to account for the turbulence effect generated by the bubble growth. The two models (*ML* and *CL*) are compared in Figure 3-15.

The application of the micro-layer model produces a local temperature drop at the centre, at maximum when the contact area is at maximum (due to conduction in the lateral direction). Instead, the application of the contact line model leads to a temperature drop in the substrate at the contact line itself; the centre of the contact area experiences an initial drop, when the contact area is very narrow, a successive recovery

during the bubble growth and a new reduction close to departure. The entities of temperature drops and recovery strongly depend on the characteristics of the substrate and in particular on its thermal capacity and the effect will be numerically analysed in the following chapter.

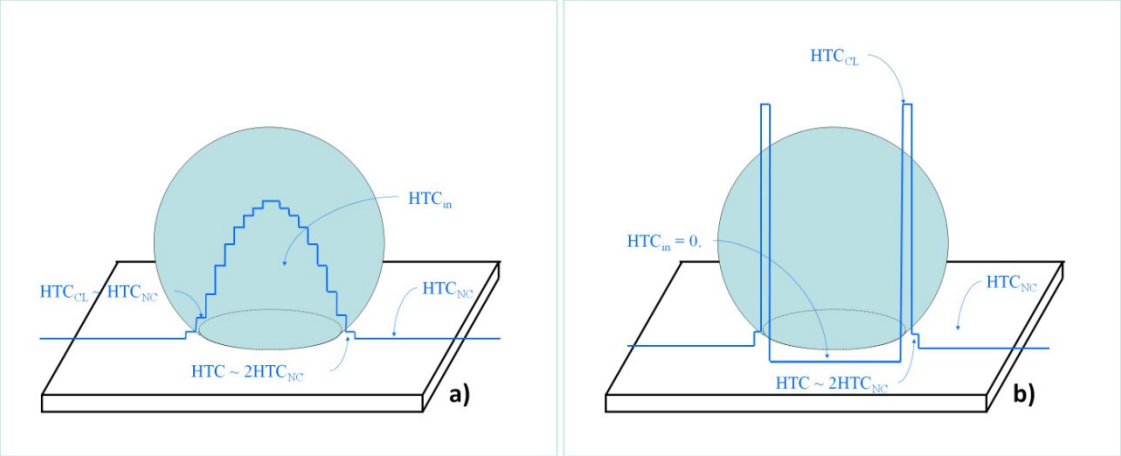

Figure 3-15: Heat transfer coefficients models: a) Micro-layer model (*ML*); b) Contact-Line model (*CL*).

Heat transfer at the dome of the bubble

The original model assumed no evaporation at the dome of the bubble. This model strongly disagrees with the theoretical models based on the thermal layer theory, for which in some cases almost the total vapour volume can be attributed to evaporation at the dome of the bubble, as analysed in Section 2.3. For this reason a simple evaporation model has been implemented based on Equation 3.16: $Q_{D,i}$ represents for site i the cumulative heat contribution through the dome of the bubble from the activation time $t_{act,i}$ to the generic instant t when the bubble has an effective radius $r_{b,i}(t)$; $f_{D,i}$ is a constant parameter, generally equal either to 0 or 1 (but it in principle may assume whichever positive value) to adjust the evaporation contribution at the dome; $f_{S,i}(t)$ is a time-dependant geometrical shape factor introduced to take into account the truncated sphere shape. $T_{eff,i}$ in Equation 3.17, depends on the activation temperature defined for each site; it is defined by assuming that the external part of the liquid thermal layer around the bubble dome stays at a temperature equal to the activation temperature $T_{act,i}$ throughout the whole bubble growth.

$$Q_{D,i} = f_D\left[4\pi r_{b,i}^2 f_{S,i}(t)\right]\cdot\left[k_l \frac{\left(T_{eff,i} - T_{sat}\right)}{\sqrt{\pi\alpha_L\left(t - t_{act,i}\right)}}\right]\Delta t \qquad \textbf{(3.16)}$$

$$T_{eff,i} = \frac{T_{act,i} + T_{sat}}{2} \qquad \textbf{(3.17)}$$

The effect of this contribution is particularly relevant for large bubbles or for very thin or poorly conductive substrates, as showed in the next sections during the analysis of numerical results.

Variable contact angle and decreasing contact area radius

A very important improvement implemented during this PhD project is related to the shape of the bubble. The original solution, assuming a constant apparent contact angle, was judged inadequate to realistically describe the bubble growth. Several solutions have been attempted: all of them have in common the choice of an initial stage where the bubble is supposed to grow as a truncated sphere with a constant apparent contact angle φ_0. When the bubble radius reaches a fixed fraction of the bubble departure radius (f_{decr}, empirically defined by the user) a second phase starts: here the contact angle is gradually decreased from the initial value to zero. Three angle decrease modes have been implemented to replace the original one, as listed below in chronological order:

a) Fixed linear angle decrease rate ($u_\varphi = u_{\varphi 0}$), as in Equation 3.18. This model uses a fixed linear angle decrease imposed by the user at the beginning of simulations. In this case, $u_{\varphi 0}$ must be manually tuned in order to obtain the correct growth time depending on $f_{\varphi,decr}$. This solution was considered impractical because a series of preliminary simulations was required to adjust the value of $u_{\varphi 0}$.

$$\varphi_i(t - t_{act,i}) = \begin{cases} \varphi_0 & \text{if} \quad r_{b,i}(t - t_{act}) < f_{\varphi,decr} r_{bd,i} \\ \varphi_0[1 - u_{\varphi 0,i}(t - t_{act,i})] & \text{if} \quad r_{b,i}(t - t_{act}) > f_{\varphi,decr} r_{bd,i} \end{cases} \qquad \textbf{(3.18)}$$

b) Apparent contact angle rate linearly decreasing with increasing bubble radius. A first alternative to the previous solution was represented by the choice of an angle decrease rate depending on the bubble radius, according to Equation 3.19. This choice allowed the elimination of the tuning process, since the contact angle becomes zero exactly when the bubble radius reaches its departure value.

$$\varphi_i(t-t_{act}) = \begin{cases} \varphi_0 & \text{if} \quad r_{b,i}(t-t_{act}) < f_{\varphi,decr} r_{bd,i} \\ \varphi_0 \dfrac{1}{1-f_{\varphi,decr}} \left[1 - \dfrac{r_{b,i}(t-t_{act})}{r_{bd,i}} \right] & \text{if} \quad r_{b,i}(t-t_{act}) > f_{\varphi,decr} r_{bd,i} \end{cases} \tag{3.19}$$

c) Apparent contact angle rate linearly decreasing with increasing bubble volume. This solution, as formulated in Equation 3.20 and currently used in the code, allows a smoother decrease of the contact angle (in the passage from a constant to a decreasing value) and consecutively of the contact area radius. Moreover, the concept of using the bubble volume instead of the radius as driving parameter in bubble deformation (and then modification of the contact angle) was considered closer to reality, since the volume is the driving parameter in the force balance at departure (when the contact area starts shrinking).

$$\varphi_i(t-t_{act}) = \begin{cases} \varphi_0 & \text{if} \quad r_{b,i}(t-t_{act}) < f_{\varphi,decr} r_{bd,i} \\ \varphi_0 \dfrac{1}{1-f_{\varphi,decr}^3} \left[1 - \dfrac{r_{b,i}^3(t-t_{act})}{r_{bd,i}^3} \right] & \text{if} \quad r_{b,i}(t-t_{act}) > f_{\varphi,decr} r_{bd,i} \end{cases} \tag{3.20}$$

Coalescence

Coalescence phenomena were not taken into account in the original version of the code. However, different studies attribute an important role to these aspects. In Section 2.8 three kinds of coalescence were identified: horizontal, declining and vertical coalescence. According to the conclusion of Shoji et al. (2005), vertical coalescence does not depend on the distance between nucleation sites and on site population. Since the code is created in order to deal with a large number of sites, the process has not been introduced yet. If experimental results prove that vertical coalescence could significantly alter the heat transfer coefficient between the substrate and the liquid or the temperature distribution in the substrate, the model should be revised to account for this phenomenon. On the other hand, horizontal coalescence is considered to have a very

large influence on the heat transfer between the substrate and the liquid and to possibly induce significant temperature variations. For this reason, a very simplified model for horizontal coalescence has been introduced for two bubbles growing in close proximity so that their domes may come in contact while the contact areas are still separate (so that the limitation on mesh distribution is satisfied). At the moment, the procedure is implemented so that coalescence occurs when the domes come in contact. Two situations, both of them observed in Golobič et al. (2006), are considered at present, as shown in Figure 3-16:

a) If the bubbles have similar sizes they are assumed to continue growing as two independent isolated bubbles (with truncated sphere shape), with interfering domes, but with no variations of the heat transfer coefficients between the substrate and the liquid. Deformation of the bubble is not taken into account. The bubbles grow independently until each of them departs when the defined bubble departure radius is reached. An improvement to this model may be implemented by introducing an enhancing heat transfer coefficient (HTC_C) in the area below the interfering domes: this would take into account the strong evaporation in the new contact area of the elongated shape of the bubble.

b) If the sizes of the two bubbles are significantly different (at present, if the bubble radii ratio is equal or larger than 2.0) the smaller bubble (2) is assumed to be instantaneously absorbed by the larger bubble (1), and then completely disappear. Bubble (1) instead undergoes a sudden increase in volume. The bubble departure radius is then increased according to Equation 3.21 by a factor accounting for the inclusion of the smaller bubble volume into the bigger bubble. The subscripts BC and AC refer respectively to the time before and after coalescence. This solution avoids the possibility for the bigger bubble to disappear immediately after inclusion by exceeding the maximum bubble size (this could happen if coalescence occurs when the bigger bubble is close to its maximum size). Moreover, it allows simulation of multiple coalescence, as may happen when a large bubble sequentially absorbs several smaller bubbles. A further improvement may be included in this model, by assuming a fast detachment phase of the small bubble after coalescence instead of instantaneous inclusion and disappearance.

$$r_{bd,1}(t_{AC}) = 1.005\left[1+\frac{V_2(t_{BC})}{V_{bd,1}}\right]^{1/3} r_{bd,1}(t_{BC}) \qquad \textbf{(3.21)}$$

The model does not consider coalescence between an attached bubble and a detached bubble from adjacent sites (declining coalescence), so that a review would be necessary if this type of coalescence was found to have a strong influence, principally on the basis of future experimental results that will help in clarifying the involved processes.

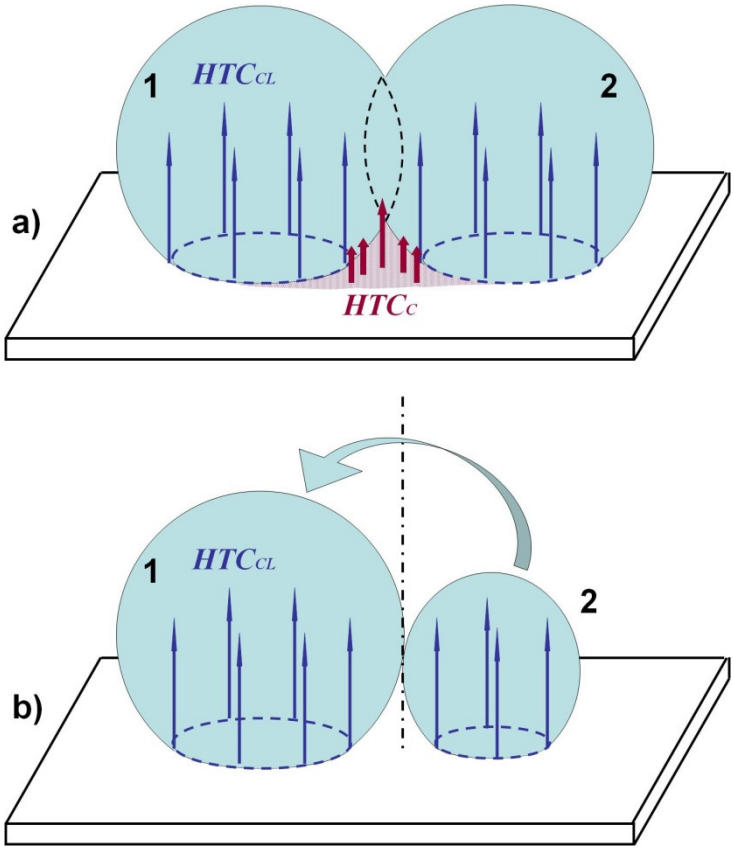

Figure 3-16: Coalescence models

3.2.5. Output data

Bubble growth data

A first improvement for the output files is the use of the same identifier defined for the input files (Section 3.2.2): sequential running of simulations is then allowed without overwriting of data. The output files are now grouped in four directories. The original output data (as specified in Section 3.1.4) have been maintained, although rearranged in order to make them more readable. However, many new output data and files, which were present in the original version of the code as variables, but not as outputs, have been made explicit. Most of them are necessary to make the bubble growth and local interactions for selected nucleation sites more similar to experimental observations. The new outputs related to the bubble growth (shown in Figure 3-17) are listed below:

- Bubble radius, $r_b(t)$, intended as the effective radius of the truncated sphere (different from the equivalent bubble radius, i.e. the radius of a perfect sphere having the same volume of the truncated sphere).
- Apparent contact angle, $\varphi(t)$, i.e. the angle that the truncated sphere forms with the substrate in correspondence to the triple contact line.
- Contact area radius, $r_c(t)$, calculated on the base of the bubble radius and the apparent contact angle, according to $r_c(t) = r_b(t)\ sin\ \varphi(t)$.
- Volume, $V_b(t)$, i.e. the effective volume of the bubble intended as a truncated sphere. The effective volume is related to the volume of a truncated sphere with the same radius by a shape factor $f_{Vol}(t)$ depending on the apparent contact angle and then indirectly on time.
- The variation of temperature at the nucleation site at the top and bottom surfaces of the substrate (respectively $T_{NS,top}(t)$ and $T_{NS,bottom}(t)$).
- The variation of temperature in a fixed square area around the nucleation site, generally larger than the contact area and representing the area of the temperature sensors in experiments, on the top surface of the substrate, $T_{SEN,b}(t)$.
- The cumulative heat contributions for the bubble growth, at the dome of the bubble, $Q_D(t)$, and through the contact area, $Q_c(t)$.
- The occurrence of coalescence as simulated in the simple models described in Section 3.2.4.

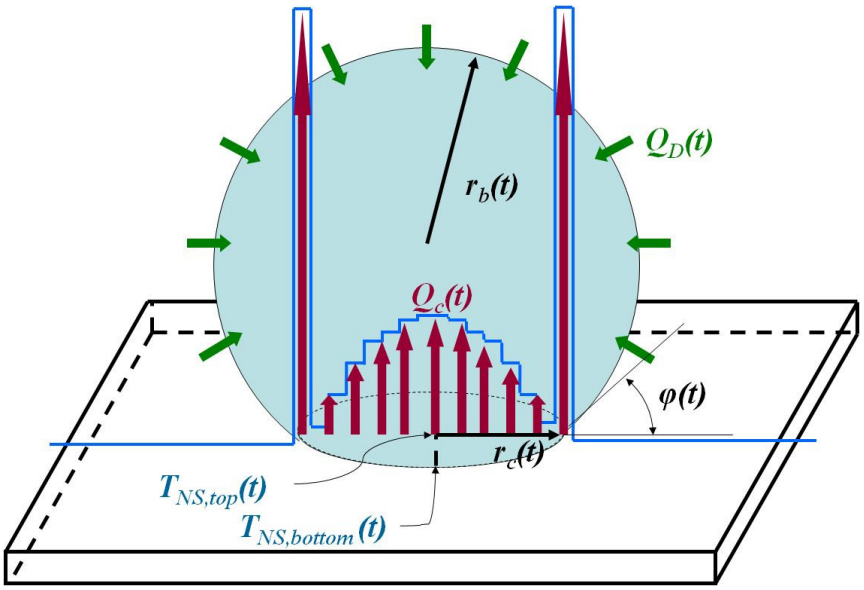

Figure 3-17: Bubble growth parameters

Additional outputs

Another important series of output data is now accessible, i.e. plots of specific variables (in particular temperature, heat flux and heat transfer coefficient) along lines passing through selected nucleation sites at fixed time steps. These outputs are particularly important to visually detect and then quantify the temperature drop in the proximity of the nucleation site, or to measure the same variations at different time steps so that an analysis of the temporal evolution of the process is possible. Most of the output files must be successively elaborated (using for instance Microsoft Excel) to be visualized: some extra routines and files have been already created to facilitate this procedure.

3.3.Summary

The original version of this hybrid code was studied in order to provide an analysis of thermal variations across a solid surface immersed in a saturated liquid, with potential activation sites distributed on the upper surface at specific locations, simulating random distributions of sites from experimental results. However, the numerical results were found in partial disagreement with experiments, with a general overestimation of the nucleation site activity. Moreover, the sub-models used to describe the physics of the processes involved were retained imprecise in some cases. From here the necessity to introduce modifications to the physics to make the code

models closer to experimental results. During this PhD project, more focus was put on the physics of the single bubble growth and also to make the code more flexible to simulate a wider range of experimental conditions. A simplified model to account for the heat transfer at the dome of the bubble, previously neglected, was introduced. Also, the heat transfer model at the base of the bubble was modified to reproduce either the contact line or micro-layer model, both experimentally observed, although the original combined model still represents an alternative option. An important modification is the introduction of an increasing-decreasing contact area to replace the only increasing model used in the original version of the model, which was leading to the unrealistic result of a bubble departing when the contact area was at maximum. Several models were implemented for the contact area decrease, all connected to the reduction of apparent contact angle value, so that the bubble is now departing, under normal conditions, with the shape of a perfect sphere. A very crude model for coalescence was also introduced, with distinction between two possible situations. For bubbles coalescing with similar radii, coalescence is not supposed to alter the bubble growth at the moment, although its occurrence is accounted and a sub-model could be introduced to modify the heat transfer conditions in the area around the involved nucleation sites. For bubble with dissimilar radii, instantaneous merging of the small bubble into the large one is supposed, with sudden disappearance of the small one and an increase in volume for the large one. The code was also modified to be used to simulated both volumetric and superficial (applied to the back of the substrate) heat sources, and the activation criteria have been reviewed.

The code has also been rearranged from the numerical point of view in collaboration with Dr Nelson at Los Alamos National Laboratory, in order to make it suitable for parallel computing, so that the computational speed could be increased. Also, the input and output data have been reorganised to be more user-friendly, and control variables have been introduced to detect the presence of numerical errors during computations. Important changes have been made also in the mesh management processes. The original method of local replacement of the coarse mesh distribution around a nucleation site only at its activation (with a finer distribution with central symmetry) and deactivation (by restoration of the coarse cells) was replaced because possibly leading, in case of close spaced sites, to numerical alternate growth of bubbles due to overlapping of the refined mesh. The new model cannot completely eliminate the alternating effect, but can reduce its occurrence by using intermediate refinements with

an increasing-decreasing area for the refined mesh distribution so that the possibility for the mesh to overlap was reduced. This new approach allows bubbles to grow at the same time at closer distances, although this is not applicable when both the bubbles are closer to departure.

To increase the computational speed a new concept of nucleation sites (called unrefined sites) has been studied to be used to simulate the sites located in marginal areas and in order to provide better boundary conditions. The unrefined sites provide a less detailed description of the bubble growth phenomena, since the mesh refinement process does not involve them, but are able to reproduce the superheat variations across the surface.

The use of these numerical improvements allowed simulations to match the original objective of the project to reproduce the behaviour of a large number of sites (of the order of 100 standard sites) in reasonable computational times (of the order of days). The code can be then used as a tool for the design of new test sections. Moreover, the improved physics of the processes is able to better reproduce the experimental evidence.

4. Analysis of the influence of the input data

4.1. Introduction

The main objective of this chapter is the identification of the effect of variation of the main input parameters. The analysis will start with the definition of a base case with an isolated nucleation site on a silicon wafer based on experimental results produced at the University of Edinburgh. For the input parameters needed for simulations and not provided by experimental results, first guess values will be assumed. Their influence on simulation results will then be investigated in the second part of this chapter. For that reason, a sensitivity analysis will be developed, with variation of the values of the main input parameters: this aims to evaluate which of them are likely to have the highest influence when tuning the code to match experimental data. The study will also include a direct comparison of the new models introduced in the modified versions of the code. The analysis will proceed with the evaluation of the effect of the distance between two, three and four nucleation sites on superheat and bubble frequency. Finally, a larger distribution of nucleation sites arranged either in square or triangular distributions will be studied.

This study will provide the leading guide for the definition of the parameters to be used on one hand on the Validation process against experimental data produced at University of Edinburgh and on the other hand on the process of design of a new test section.

4.2. Definition of the base case

A direct comparison of the original and modified versions of the code including each time only one of the improvements discussed in the previous chapter would be very difficult because of the numerical re-arrangements that make the two codes completely different. Instead, a reference case (base case) will be created and the effects of the changes and improvements will be evaluated with respect to this case.

4.2.1. *Experimental facilities*

Three test sections have been designed and used at the University of Edinburgh. While the first test section was mainly used for the commissioning of the experimental setup, the second and third generation test sections were used for the actual experiments. The last two used integrated temperature micro-sensors, located in correspondence to micro-fabricated nucleation sites. The second generation test section (19 x 39.5 mm^2, 0.38 mm thick) has five sensors located on the bold of the wafer, with the arrangement shown in Figure 4-1 (a) representing only the central part of the test section. The five cavities have diameter equal to 2 µm (S1), 5 µm (S2), 10 µm (S3), 20 µm (S4) and 50 µm (S5) and three different test sections from the same chip were produced with three cavities etched to different depths of 40, 80 and 100 µm. Sensors and heaters were located on the same side of the silicon wafer.

The third generation test section differs from the previous one mainly because the sensors are located on the top bold around the nucleation site. Each sensor covers an area of 0.84 x 0.84 mm^2, with a sensitivity of ±0.5 K while the heater is still located on the back of the silicon wafer. The chip size was 50 x 50 mm^2 and 0.38 mm thick, with a central heated area of 40 x 37 mm^2, which allows a variable heat flux. 16 cavities were

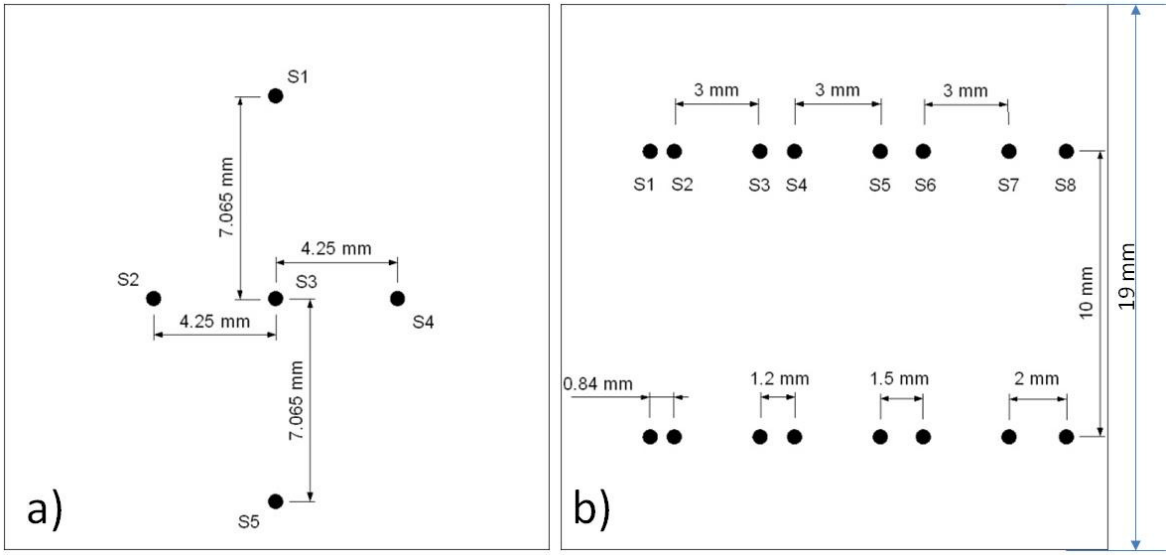

Figure 4-1: Arrangement of the micro-fabricated cavities for the second generation (left) and third generation (right) test sections

micro-fabricated (80 µm deep) and located at the centre of each sensor, with the arrangement shown in Figure 4-1 (b) for the central part of the test section. The cavities are arranged in two lines in pairs with variable inter-distance; the distance between each pair on the same line is 0.84, 1.2, 1.5 and 2 mm, while the distance between the lines is 10 mm. In each line, all the cavities have the same mouth diameter (10 µm and 3 µm) and are supposed to act as artificial nucleation sites.

The test section is horizontally immersed in a boiling chamber filled with degassed FC-72 at variable pressure. The boiling chamber has four windows for optical access so that the experiments can be monitored and recorded with a high-speed camera (IDT Nanosense MkIII), set to acquire 1000 frames per second (fps). A scheme of the experimental facilities is shown in Figure 4-2. A detailed description of the facilities can be found in Hutter (2009).

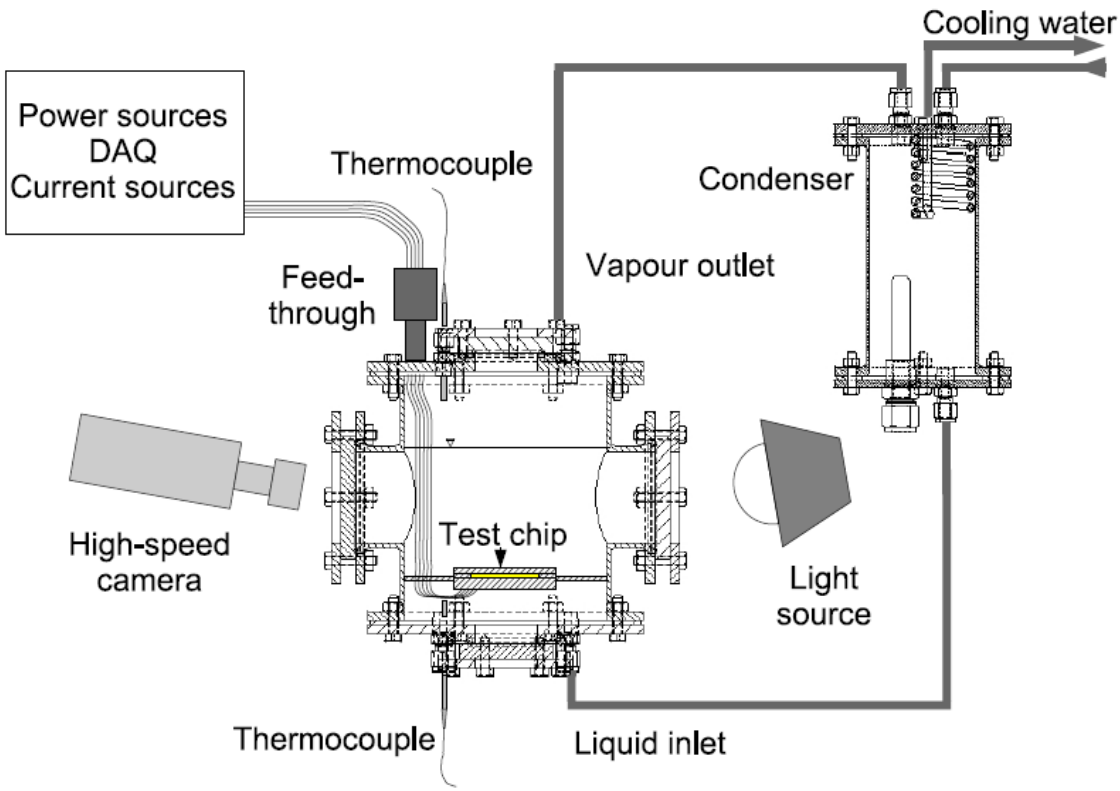

Figure 4-2: Experimental setup

4.2.2. Experimental input data for simulations

The base case refers to the experimental results developed on the third generation test section. During the considered experiments, the section was completely immersed

in FC-72 at atmospheric pressure and saturation conditions; a fixed input heat flux equal to 4.480 $\frac{kW}{m^2}$, was applied to the back of plate. The results refer to bubbles growing from an isolated nucleation site, S7 (the closest nucleation site is located at 2 mm from it) and no coalescence was observed during experiments. The bubble departure radius (r_{bd}), calculated averaging the values for eight bubble growths, was equal to 0.33 mm for a growth time (t_g) of 21 ms. The measured wall superheat (ΔT_{SEN}, difference between the temperature spatially averaged over an area corresponding to the sensor size, i.e. 0.84x0.84 mm^2 on the top surface and saturation temperature) was approximately 8.1 K during a detection period much longer (approximately 220 ms) than the bubble growth time. A summary of the experimental conditions is provided in Table 1.

Table 1: Experimental conditions and results

Conditions		*Results*		
$\dot{q}$	r_c	r_{bd}	t_g	ΔT_{SEN}
4.48 kW/m^2	5 µm	0.33 mm	21.0 ms	8.1 K

In this case, the measured wall superheat is much greater than the theoretical triggering superheat value specified in simulations based on the cavity radius of 5 µm (i.e. the activation superheat, which will range for the case of FC-72 on silicon between 0.94 and 4.49 K in the sensitivity analysis described later in Section 0). The minimum sensor size was dictated by the available micro-fabrication methods, leading to dimensions rather larger than the contact area so that the radial temperature variations in the immediate vicinity of nucleation sites cannot be measured. The measured superheat may therefore not correspond to the superheat at the nucleation site. However, the results of simulations that will be presented in the next section for silicon in FC-72 suggest that the superheat differences between the area outside the contact area and at the nucleation site are small. Consequently, when the superheat is significantly larger than the theoretical value the waiting time before nucleation of the next bubble should be zero, as also experimentally observed in this case. Also, the activation conditions are not expected to have a large effect on simulations. By contrast, for lower measured superheats (but still larger than the theoretical activation value) waiting times in experiments could be present and simulations may be not able to reproduce them. Examples of this behaviour for silicon on FC-72 are shown later in Section 5.3.1. For

other materials, such as thin metal foils, there may be waiting times also in simulations because the superheat falls below the activation superheat during the final stage of the bubble growth.

4.2.3. Numerical input data

The properties of liquid and substrate used during the simulations are summarised in Table 2.

Table 2: Physical properties used as input data for simulations

Substrate [Silicon] 18 x 18 mm	δ_H 0.38 mm	ρ_H 2340 $\frac{kg}{m^3}$	c_H 750 $\frac{J}{kgK}$	k_H 110 $\frac{W}{mK}$	
Liquid [FC-72] 1 Atm	T_{sat} 57.17 °C	ρ_v 12.76 $\frac{kg}{m^3}$	ρ_L 1611 $\frac{kg}{m^3}$	c_L 1088 $\frac{J}{kgK}$	k_L 0.054 $\frac{W}{mK}$

For simulations related to the base case, the following numerical assumptions (summarised in Table 3) have been made:

- The original horizontal dimensions of the substrate (40 x 36 mm^2 for the heated area) have been reduced to a 18.1 x 18.1 mm^2 square in order to reduce the computational time. However, the original thickness (0.38 mm) has been retained.
- Numerical data: the time step (Δt) for this simulation has been set equal to 0.5 µs, for a simulated time t_{sim} of 0.5 s (guaranteeing a good compromise between stability and steady conditions for the simulations and computational time). The substrate has been divided into 6 vertical layers (n_{vL}); the size of coarse cells (w_{xy}) has been set equal to 0.1 mm.
- Standard nucleation sites: the normal mesh refinement process (with no intermediate steps) with 7 circular rings (n_R), 4 cells per ring (n_{cR}), 4 cells of difference between adjacent rings ($n_{R,incr}$) has been used.

Table 3: Simulations data

Substrate data	*Length* 18.1 mm	*Width* 18.1 mm	δ_H 0.38 mm	
Numerical data	Δt 0.5 µs	t_{sim} 0.5 s	w_{xy} 0.1 mm	n_{vL} 6
Standard site	n_R 7	n_{cR} 4	$n_{R,incr}$ 4	

The same input data will be used for all the simulations cases in this chapter if not differently stated.

One single nucleation site (input data: r_{bd} = 0.33 mm, τ_g = 21.0 ms) has been located at the centre of the substrate for simulations. The assumption is justified by the large distance (2 mm) between the two cavities, with respect to the measured average bubble departure diameter (0.66 mm), leading to a distance to bubble departure diameter ratio approximately equal to 3. According to Zhang and Shoji (2003) and to the similar experimental results developed at University of Edinburgh (Hutter et al., 2009), thermal and fluid-dynamic influence is not relevant at such distance.

Moreover, the following assumptions from the physical point of view have been made, referring to the improvements described in Section 3.2.4:

- Boundary conditions: the edges of the substrate have been kept at adiabatic conditions.
- Heat source: a uniform heat flux ($\dot{q}$) equal to 4.480 $\frac{kW}{m^2}$ has been applied to the whole surface (18.1 x 18.1 mm^2) on the back of the substrate.
- Activation conditions: The activation temperature (T_{act}) has been assumed equal to 58.15 °C, corresponding to an activation superheat ($\Delta T_{act} = T_{act} - T_{sat}$) of 0.94 K (approximated to 1 K) calculated according to Equation 3.14 for a cavity mouth radius of 5 µm.
- Heat transfer coefficients: the contact line heat transfer mode, with a high heat transfer in the contact line region and a zero heat flux in the inner part of the contact area, has been imposed. For the natural convection area, the correlation expressed in Equation 3.15 has been applied. An enhancing natural convection factor (f_{enh}) equal to 1.16 has been imposed to match the superheat as measured by the sensor and averaged over the detection time (ΔT = 8.1 K).

- Variable contact angle and decreasing contact area radius: the third mode of contact angle decrease has been imposed (decrease with the inverse of the volume of the bubble, V_b). The following bubble growth guess input data have been assumed: initial contact angle (φ_0) equal to 30° and angle decrease factor (f_{decr}) equal to 0.6.
- Heat transfer at the dome of the bubble: the heat transfer at the dome of the bubble has been fully accounted according to Equation 3.16 with $f_D = 1.0$.
- Standard nucleation sites: no intermediate refinement process has been assumed. No unrefined sites have been simulated.
- Coalescence: only one nucleation site has been assumed, so that coalescence does not occur.

The assumptions above are summarized in Table 4. The sensitivity analysis will study the effect of variation of each of the listed parameters.

Table 4: Base case physical input data

Heat source	**Activation conditions**		***HTC* model**	**Contact angle variation**			**Dome contr.**	**Natural Convection**
$\dot{q}$	T_{act}	ΔT_{act}	CL	Decrease with	φ_0	f_{decr}	f_D	f_{enh}
4.48 kW/m^2	58.15 °C	1.0 K		$1/V_b$ - Model 3	30°	0.6	1.0	1.16

4.2.4. Bubble growth

The time-histories for the most important output data related to the bubble growth are shown in Figure 4-3. Starting from the bottom of the figure, the contact area radius (r_c), the effective bubble radius (r_b) and the apparent contact angle (φ_0) are shown, Figure 4-3 (d) and (c); then the cumulative heat contributions for the bubble growth (at the dome, Q_{dome}, at the base, Q_{base}, and total, $Q_{tot} = Q_{base} + Q_{dome}$), Figure 4-3 (b) and finally the superheat variations at the nucleation site at the top ($\Delta T_{NS,top}$) and bottom ($\Delta T_{NS,bottom}$) surfaces, and averaged over an area corresponding to the sensor area in the experiments (ΔT_{SEN}), Figure 4-3 (a). The superheat variations will be analysed in the next section. During the sensitivity analysis, care must be taken in the analysis of the superheat variations in the graphs usually showing the variations at the nucleation site at the top surface ($\Delta T_{NS,top}$). This is because they are significantly greater than ΔT_{SEN}, due

to the large area of the sensors used at the University of Edinburgh (Hutter, 2009). The sensors' spatial resolution in the experiments is much worse than in simulations, and also less than the resolution in some other experiments, as highlighted in Kenning (2009).

The comparison of the simulated bubble growth with the experimental data shows that the exact growth time period can be reproduced by simulations. As discussed in Section 3.2, the inputs to the model could be set to force the final bubble radius and the

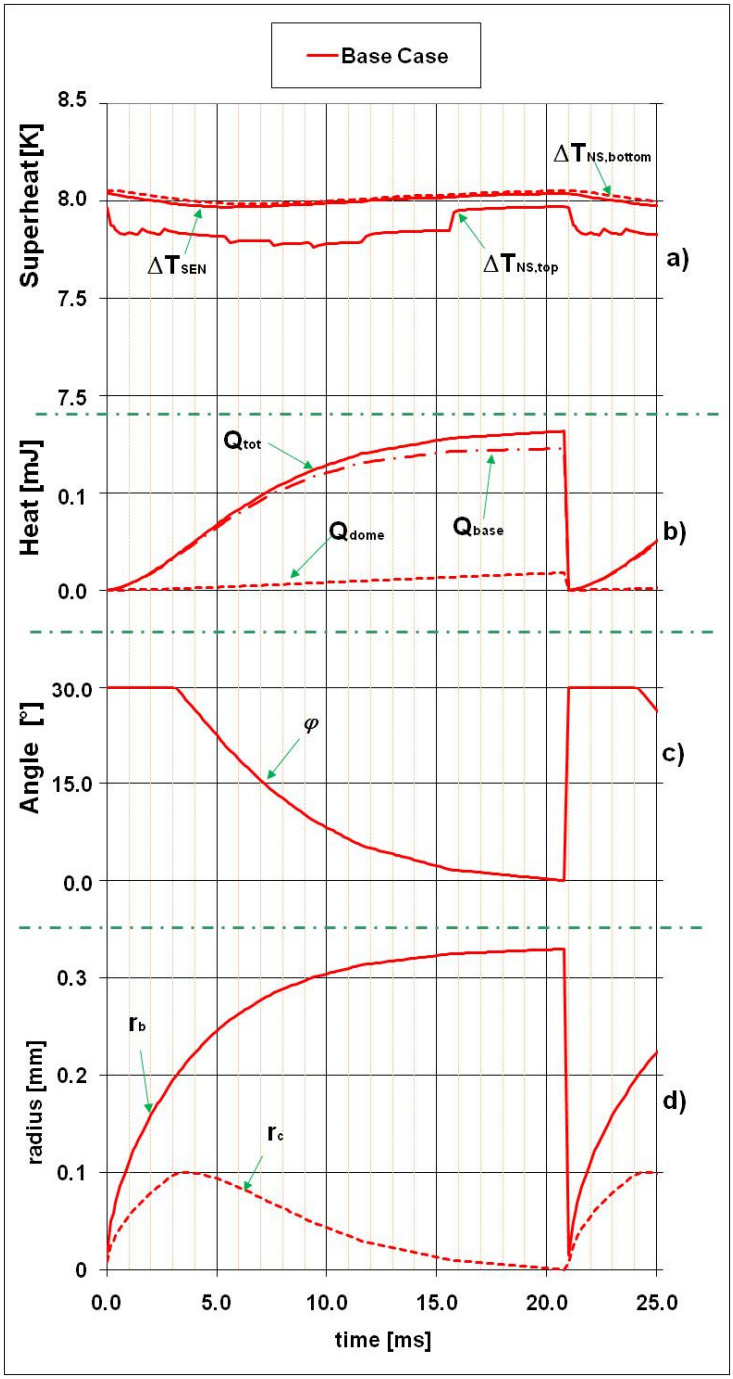

Figure 4-3: Base case: bubble growth and superheat simulation results

departure time to be correct. This approach is generally used when studying the bubble growth for an isolated nucleation site in the preliminary design phase. The heat transfer coefficient data obtained here will be then used as input data for the analysis of distributions with a larger number of nucleation sites. In this case, the growth time will not generally match the experimentally measured value, due to the interaction between nucleation sites. From analysis of the simulated contact area radius in Figure 4-3 (d): it is clear that when the bubble radius reaches the 60% of its maximum value (i.e. f_{decr} = 0.6, r_b ~ 0.2 mm) at ~ 3.5 ms, the apparent contact angle starts decreasing with a corresponding decrease in the contact area radius. The maximum contact area radius is approximately 0.1 mm ($r_{c,max} = f_{decr} \cdot r_{bd} \cdot sin\varphi_0$) and the initial stage of the bubble growth (t < 3.5 ms, increasing contact area) is much faster than the second stage (~ 17.5 ms, shrinking contact area, 3.5 < t < 21.0 ms).

From the analysis of the heat contributions, it is possible to establish that, according to the numerical model used, the heat contribution at the dome of the bubble is significantly smaller than evaporation at the contact area (approximately 8 times at bubble departure). However, while the dome contribution rate increases with time (and then with the bubble radius), the contribution rate at the base varies with the contact area radius, so that the initial fast increase is followed by a second phase where the rate gradually decreases to zero, leading to a flatter heat transfer contribution. Before the introduction of the heat contribution at the dome, this phenomenon could lead to bubbles hovering attached to the substrate wall for a very long time: in fact, the heat contribution at the contact area (reduced to the central cell simulating the nucleation site) might not be enough to complete the bubble growth.

4.2.5. Superheat variations

The analysis of the simulated superheat history over an area reproducing the sensor area (T_{SEN} in Figure 4-3) shows an average value of 8.0 K, only slightly smaller than the experimentally measured superheat (8.1 K). Very small variations (±0.05 K) are observed during the bubble growth (and always smaller than the sensor sensitivity). This makes it impossible to determine the experimental activation and deactivation times only from the measured superheat histories (i.e. independently of the visual observation of the bubble growth). The superheat in correspondence with the nucleation site simulated on the back of the substrate ($\Delta T_{NS,bottom}$, dashed line in Figure 4-3)

presents values very similar ΔT_{SEN}, with the two curves almost overlapping. By contrast, superheat variations at the nucleation site on the top surface ($\Delta T_{NS,top}$) are much larger (~ 0.12 K) than ΔT_{SEN} or $\Delta T_{NS,bottom}$. The difference is probably due to the high heat capacity of the substrate. For $\Delta T_{NS,bottom}$, local thermal disturbance on the top surface propagates but cannot be detected on the back due to the relatively large thickness of the substrate. Similarly, variations on the top surface are much smaller than the sensor sensitivity if averaged over the sensor area, relatively larger than the maximum contact area. $\Delta T_{NS,top}$ also shows a stepwise variation (clearly visible for instance between 16 and 21 ms): as a matter of fact, when the contact line changes so that a different mesh ring is involved, the simulated contact line area is significanlty modified and so the instantaneous heat removal at the triple contact line region is. Consequently the dome contribution varies because of the indirect effect of change in bubble radius rate.

The superheat distributions at the bottom and top surfaces along a line passing through the nucleation site and restricted to the central area of the substrate (6 mm < x < 12 mm) are shown Figure 4-4 at two different time steps (t = +3 and +20 ms). The two time steps correspond respectively to the initial and final stage of the bubble growth, as shown by the schematic bubble representation on the top part of the figure. The

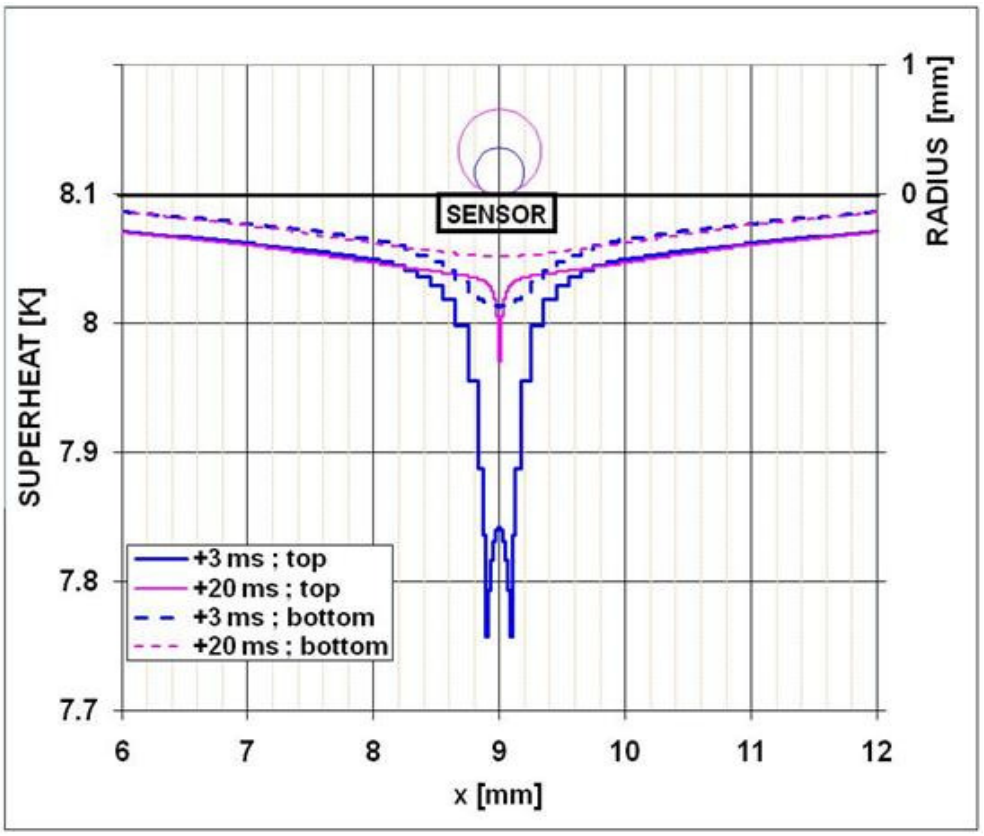

Figure 4-4: Base case: Superheat distribution along a line

superheat around the contact line on the top surface experiences a significant drop, mostly at the initial stage of the bubble growth (+3 ms), when the contact area is larger. However, the high conductance in the lateral direction in the substrate leads to large modifications at the centre of the contact area too, despite the applied zero *HTC*. The maximum superheat variation occurs in proximity of the contact line for +3 ms and it is significantly larger (~ 0.4 K) than the maximum variation at the nucleation site (~ 0.25 K) and definitely larger than any average value over an area equal to the sensor area. It is also evident the attenuation effect across the substrate in the vertical direction when superheat at the top and bottom of the surface are compared. For that reason, the solution of locating the sensor on the back of the substrate (previously adopted during experiments) was abandoned in favour of location on the top surface. However, the large size of the sensor (0.84 mm wide) with respect to the maximum bubble size (r_{bd} = 0.33 mm) and in particular to the maximum contact area ($r_{c,max}$ ~ 0.1 mm), make the sensor equally unsuitable to meet the original objectives. Figure 4-4 shows also the superheat distribution in the area around the nucleation site: for a distance larger than 1.0 mm from the centre of the contact area the superheat is not directly affected by the superheat variations at the nucleation sites anymore, but only by its activity. Figure 4-4 also allows explaining the variations in $\Delta T_{NS,top}$ shown in Figure 4-3. In fact, the superheat at the nucleation site would be expected to decrease immediately after activation, while the contact area is small (due to a high *HTC* only in correspondence of the cell containing the nucleation site) and then partially recovering due to the zero *HTC* during the bubble growth. During the last phase, when the contact area is small again and a high *HTC* is applied to this area, the superheat would be expected to decrease as well. By contrast, Figure 4-4 shows that, even if the superheat at the nucleation site has a local depression, its bold type value (obtained averaging the distribution over an area equivalent to the sensor size) is significantly higher during the initial stage of the bubble growth. The figure also shows that the superheat at the bottom surface (ΔT_{bottom}) undergoes a drop of ~ 0.05 K between the unaffected area (i.e. x = 8 mm) and the centre (x = 9 mm) and even larger if the edges of the substrate are considered. Considering that $\Delta T_{NS,bottom}$ values are very similar in simulations to ΔT_{SEN} in Figure 4-3, it can be assumed that the variations at the bottom of the plate have a similar character to those measured by the sensor. If so, the superheat drop between natural convection and boiling areas would justify the difference in superheat between the experimental and simulated ΔT_{SEN}. However, in the following analysis the factor f_{enh} will be always

calculated from the superheat as measured by the sensor, with no corrections due to the mentioned drop. According to these results, it may be concluded that the sensors now available for the Edinburgh experiments are not able to achieve the required sensitivity and spatial resolution. Development of improved sensors was not possible during this project due to time constraints, but further studies in this area would require greatly smaller dimensions for the sensors, at least for the current size of the bubbles (less than 1 mm in diameter). Larger bubbles could be detected for experiments on silicon at lower pressures or on metal foils cooled by water (compare for instance Golobič et al., 2006 and 2009). However, also in the case of average bubble departure radii of 3 mm, the maximum contact area would be approximately 1 mm, of the same order of the sensor size (0.84 mm long). It would be then impossible to detect local superheat variations.

Figure 4-5 shows the 2-dimensional superheat distribution at t = 3 ms over an area passing through the nucleation site and 1 mm long. The distribution highlights the concentrated cooling effect in the area corresponding to the triple contact line, clearly identifiable for x ~ 8.9 and 9.1 mm (corresponding in figure to x ~ 0.0089 and 0.0091 m).

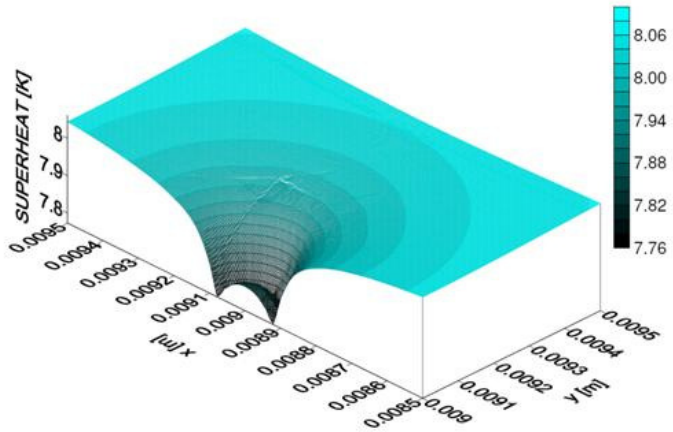

Figure 4-5: Base case: 2-dimensional superheat distribution

4.2.6. Heat Flux and HTC distributions

The variation of the instantaneous heat flux and the *HTC* distributions along a line passing through the centre of the bubble (located at x = 9 mm) for the central part of the substrate (i.e. for 8 mm < x < 10 mm) together with the effective (simulated) bubble sizes, are shown in Figure 4-6 (respectively *a* and *b*).

The figure shows the distributions at two time steps (+ 3 ms and + 20 ms, similarly to Figure 4-4). For the distributions relative to the beginning of the bubble growth (+3 ms) the triple contact line and the inner contact areas at x ~ 8.9 and 9.1 mm (equivalent to a contact area radius of ~ 0.1 mm) are clearly identifiable, where both the heat flux and the *HTC* have a maximum, respectively of ~ 1300 $\frac{kW}{m^2}$ and ~ 170 $\frac{kW}{m^2K}$. The peak values are applied over a ring area of width $w_{cl,sim}$ ~ 20 µm, much larger than the theoretical width, where strong evaporation is supposed. If a theoretical contact line width $w_{cl,theor}$ = 0.1 µm is assumed, the calculated heat flux and *HTC* can be scaled (Figure 4-7), so that $\dot{q}_{cl,scal} = \dot{q}_{cl,sim} \frac{w_{cl,sim}}{w_{cl,theor}}$ and $HTC_{cl,scal} = HTC_{cl,sim} \frac{w_{cl,sim}}{w_{cl,theor}}$, obtaining respectively $\dot{q}_{cl,scal}$ ~ 260000 $\frac{kW}{m^2}$ and $HTC_{cl,scal}$ ~ 34000 $\frac{kW}{m^2K}$. The heat flux can be compared with results from the simulation developed by Stephan and Hammer (1994) and Kern and Stephan (2003) reporting heat fluxes respectively equal to 7000 $\frac{kW}{m^2}$ and 30000 $\frac{kW}{m^2}$. The heat flux would then be approximately 40 to 20 times larger. However, the simulated conditions are essentially different (R114 on copper for Stephan and Hammer and a binary mixture propane/*n*-butane on copper for Kern and Stephan, 2003). In the following sections, an analysis of the effect of some variables on the *HTC* and consequently on the heat flux will be analysed.

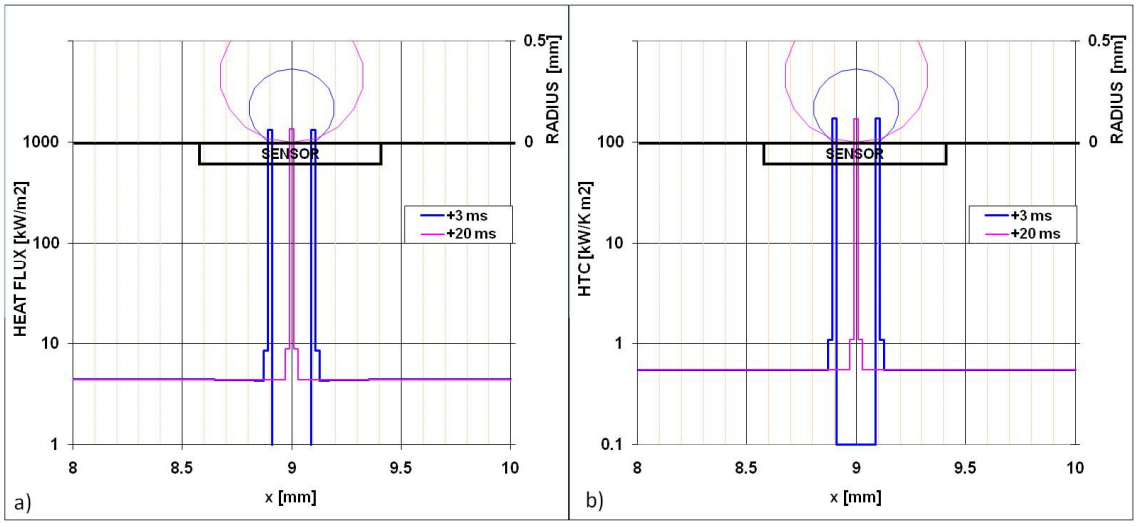

Figure 4-6: Base case: Instantaneous heat flux (a) and *HTC* (b) along a line

The plots also show that the heat transfer coefficient for natural convection outside the contact area is approximately constant (the small variations due to the dependence of the heat transfer coefficient on the superheat), except for the ring immediately outside the triple contact line region, where the enhancing natural convection heat transfer coefficient ($f_{enh,NC}$ = 2) was imposed. Although the *HTC* is constant outside this area, a small depression over a larger area in the heat flux is visible in Figure 4-6 (for 8.65 < x < 8.85 mm and 9.15 < x < 9.35 mm): this is due to the temperature reduction caused by the high lateral conductance on the substrate.

The 2-dimensional distributions of the heat flux and *HTC* on the top surface for half of the central area of the substrate are shown in Figure 4-8. For these variables, a clear local depression in the proximity of the contact area, and high peaks for the contact line area are evident.

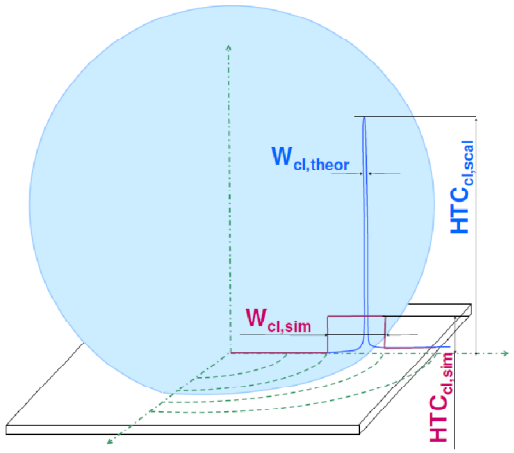

Figure 4-7: Scaled and theoretical contact line regions

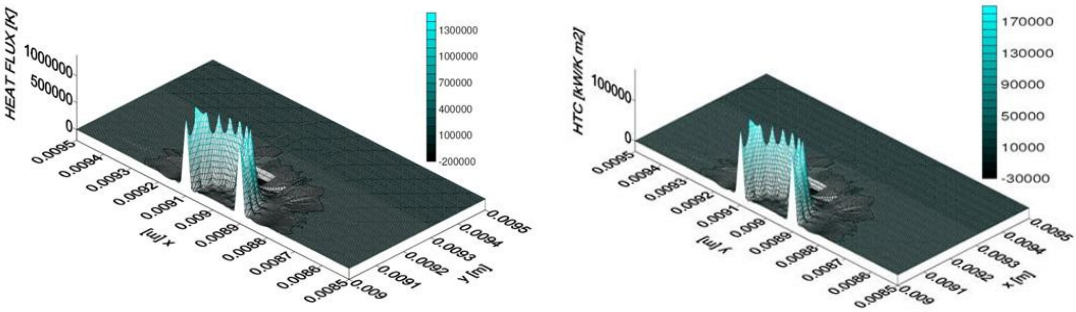

Figure 4-8: Base case: Heat flux and HTC 2-dimensional distribution

4.3.Sensitivity analysis

The sensitivity analysis will start with the investigation of the effects of the boundary conditions applied to the edge of the substrate (either adiabatic or imposed temperature) and with the analysis of the two possible heat sources available in the present version of the code. The two sources, corresponding either to a volumetric heat source (to simulate for instance direct electric heating in metal substrates) or surface heat flux applied on the back of the substrate (to simulate thin film heaters); the two heat sources could be ideally combined in simulations, although this solution is unlikely in reality. The analysis will proceed with the investigation of the effect of the activation superheat on the bubble growth. A study of the different effects of the contact area shrinking (including the comparison between the models for the apparent contact angle decrease, the variation of the initial apparent contact angle and contact angle decrease factor) will be then developed. It will be followed by a study of the effects of the heat evaporation at the dome of the bubble and the application of different models for heat transfer at the base of the bubble. The investigation will conclude with a comparative analysis of the effects of the use of standard and unrefined sites. Afterwards, the effect of the thickness of the substrate with particular focus on the wall superheat will be developed. All these cases will be compared with results from the base case, with particular attention to their effects on bubble growth rate, superheat variations in the area around the nucleation sites and on the heat transfer coefficients (*HTC*) to be applied to obtain the bubble growth that matches the experimental results.

4.3.1. Boundary conditions

The first analysis aims to evaluate the effect of the boundary conditions at the edge of the substrate. The comparison of the use of adiabatic conditions (used for the base case) with a fixed temperature condition equal to 65.25 °C, equivalent to an average superheat of 8.1 K, is illustrated in Figure 4-9. The figure shows the superheat variation along a line passing through the centre of the nucleation site for half of the surface, i.e. from the nucleation site located at x = 9 mm to the edge (x = 18.1 mm), calculated both at the top and bottom surfaces of the substrate, during the first stage of the bubble growth (+3 ms). The bubble size is also shown in the upper part on the right. It is clear that the effect of variation of the boundary conditions affects only the external region of the surface, i.e. the one closer to the edges for x > 16 mm, for both top and bottom surfaces. It is also possible to see that for the constant temperature condition, the superheat at the edge (x = 18.1 mm) both the top and bottom distributions converge to the same superheat (ΔT = 8.1 K), while for the other case the difference between the two surfaces is approximately constant in the regions away from the nucleation site.

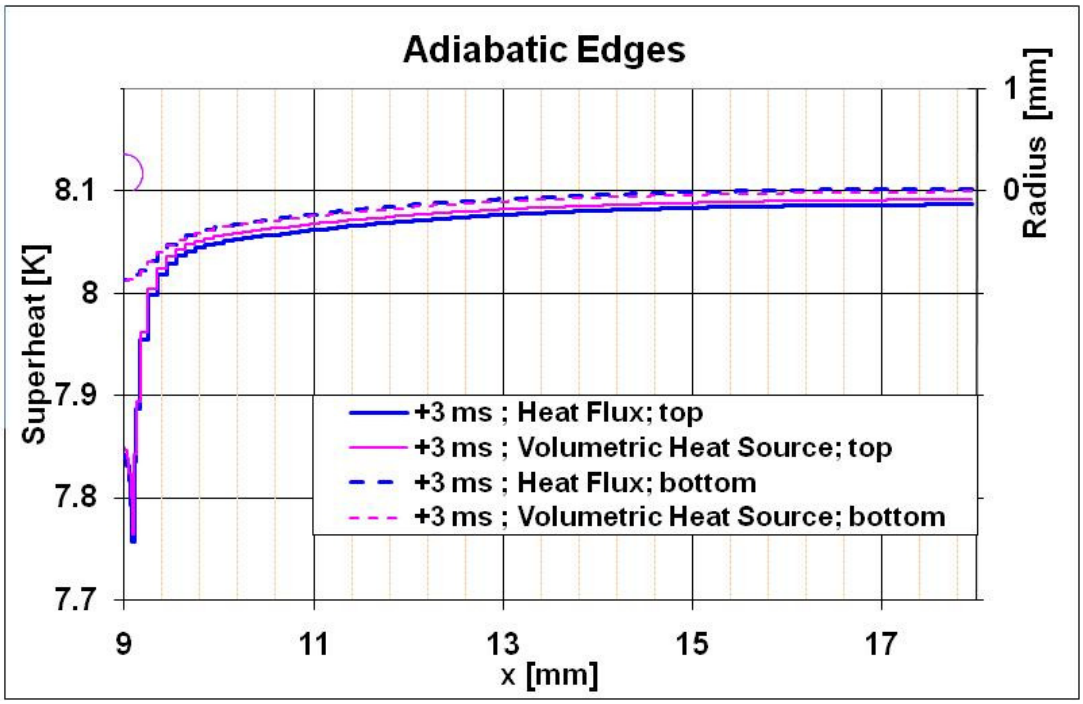

Figure 4-9: Effect of the variation of the boundary conditions on superheat distribution along a line on the top and bottom of the substrate

4.3.2. *Heat source*

The second case analyses the variation of the heat source: the heat flux applied to the back of the substrate (in the base case) is replaced here by a volumetric heat source of equivalent entity, so that the total heat provided in the given time interval to the substrate is maintained. Adiabatic edges are assumed as boundary conditions. Figure 4-10 shows the superheat variations similarly to the previous case. It is apparent that the for the volumetric heat distribution, the difference between the superheat values at the bottom and top surfaces is smaller than for the imposed heat flux case, caused by the smaller drop across the substrate because of conduction. However, the value at the surface is approximately the same because of the same heat removal at the top surface. From analysis of the superheat distribution around the nucleation site for both the cases, it is clear that the superheat in this area is approximately not affected by the variation of conditions, so that the bubble growth rates and bubble departure frequencies do not vary.

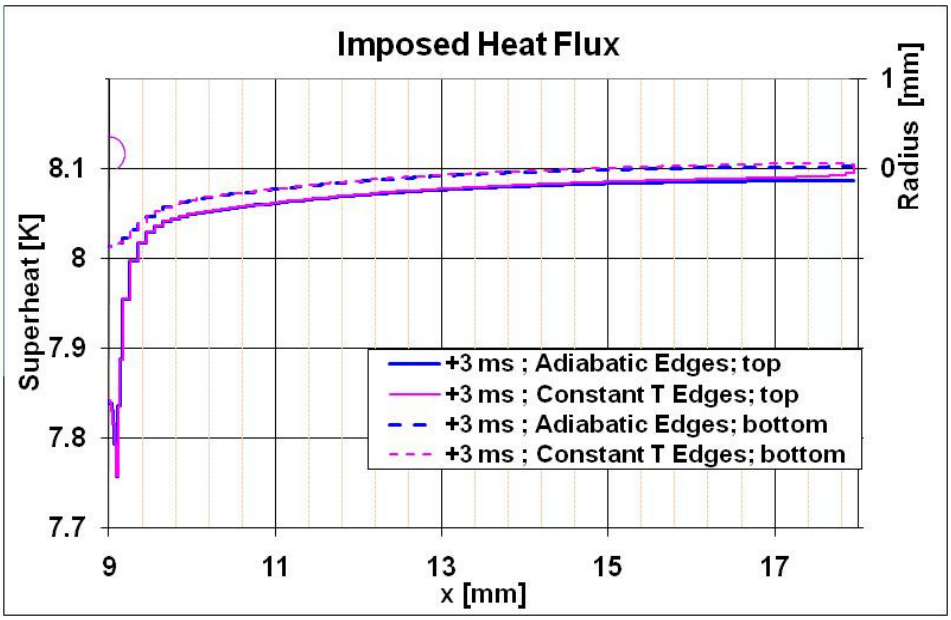

Figure 4-10: Effect of the variation of heat sources on superheat distribution along a line on the top and bottom of the substrate

4.3.3. Activation superheat

The variation of activation superheat has been investigated here in order to understand its effect on superheat distribution and bubble growth. The activation superheat is calculated on the base of the cavity mouth radius according to Equation 3.14: several activation superheats (and consequently cavity mouth radii) have been simulated, as summarised in Table 5, together with the activation temperatures. The cavity radius ranges from 5 to 1 µm, including the base case, which assumes an activation temperature of 58.15 °C (in red in the table).

Table 5: Activation temperatures

r_{cav} (µm)	5.0	4.7	4.0	3.0	2.0	1.55	1.0
ΔT_{act} (K)	0.94	1.0	1.18	1.56	2.31	2.96	4.49
T_{act} (°C)	58.09	58.15	58.33	58.71	59.46	60.11	61.64

For all the cases analysed in this section, representing different cavity sizes, experiments could not provide evidence of the measured activation superheats. However, for all of them, the bubble departure radius and growth time will be assumed equal to the value for the base case (respectively 0.33 mm and 21 ms). Also, the same average measured superheat at the wall used for the base case (8.1 K) will be imposed. No waiting times are expected because the superheat at the nucleation site (approximately 8 K) is always larger than the higher superheat required (corresponding to the case for $r_{cav} = 1\ \mu m$). For all these reasons, the comparison shown here must be intended as a mere exercise constructed on an arbitrary basis.

Comparison of the base case (ΔT_{act} = 1.0 K) and the case for ΔT_{act} = 4.49 K (corresponding to r_{cav} = 1 µm) is shown in Figure 4-11. The figure shows that the heat contribution at the dome of the bubble is significantly larger for the larger cavity radius, causing the contribution at the base of the bubble to decrease (in order to maintain the same total heat contribution at departure, necessary to provide the total evaporated volume). This leads to a lower growth rate during the first stage of the growth, so that the contact area radius and the apparent contact angle start to decrease later than for the base case. The contribution at the dome of the bubble is larger because of the larger activation temperature, which determines the temperature of the thermal layer covering the bubble dome during the growth. The difference in contributions leads also to a

superheat at the nucleation site which is less variable for the larger activation superheat case.

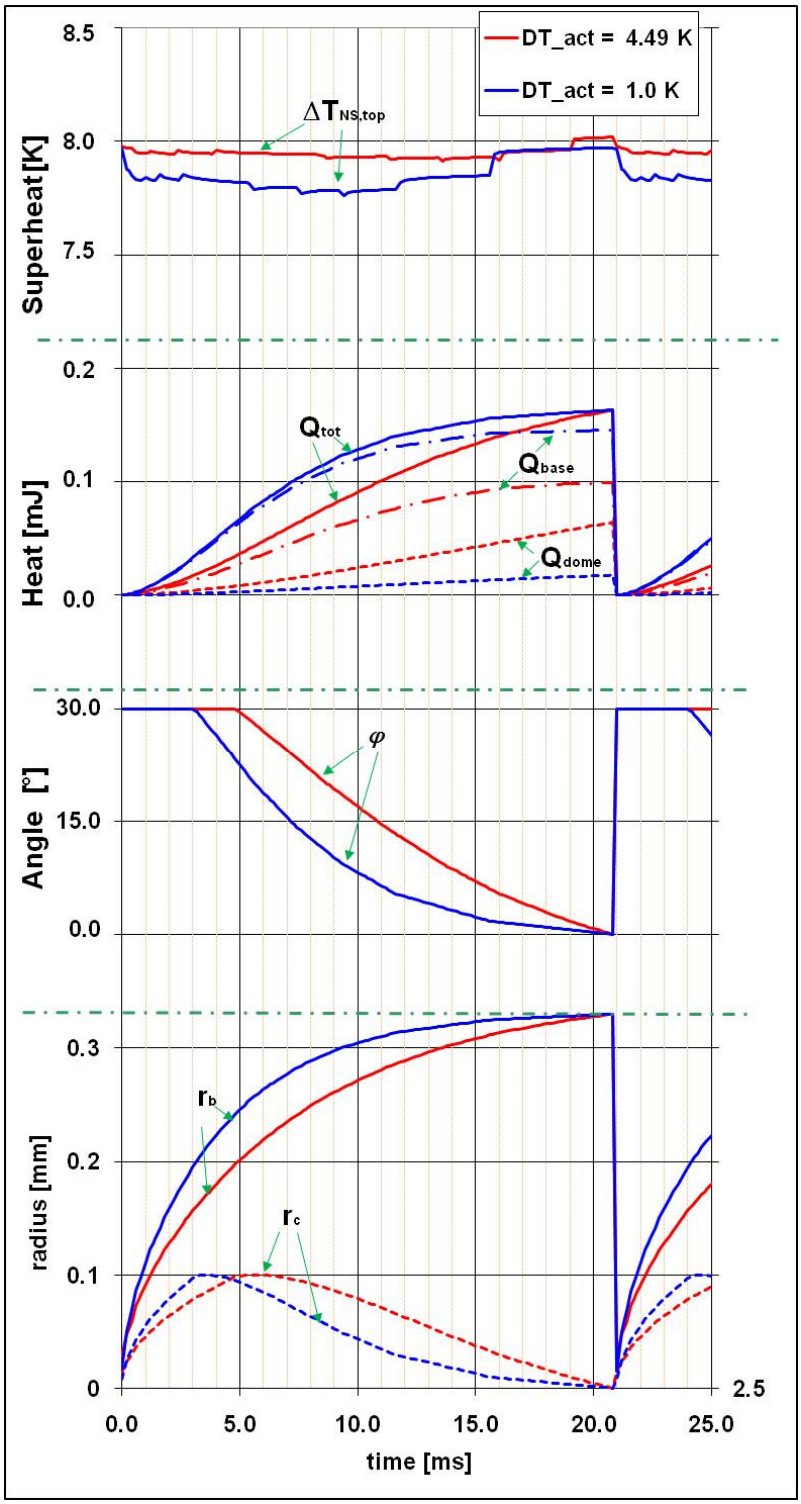

Figure 4-11: Effect of activation superheat on bubble growth and superheat

The analysis of Figure 4-12 shows the effect of the cavity radius and of activation superheat on the scaled heat transfer coefficient ($HTC_{cl,scal}$) imposed for the cells belonging to the contact line region. The $HTC_{cl,sim}$ values, obtained on the basis of the imposed bubble growth time from experiments, have been scaled as described in Section 4.2.6 by assuming a theoretical triple contact line width $w_{cl,theor}$ equal to 0.1 µm. The scaled heat transfer coefficient is seen to drop from ~ 35000 $\frac{kW}{m^2 K}$ to ~ 15000 $\frac{kW}{m^2 K}$, for a variation of the cavity radius from 1 µm to 5 µm (corresponding to a superheat variation from 4.49 K to 0.94 K). Assuming that the average superheat approximately is equal to 8 K (from analysis of Figure 4-11), the heat flux is seen to drop from 280000 to 120000 $\frac{kW}{m^2}$.

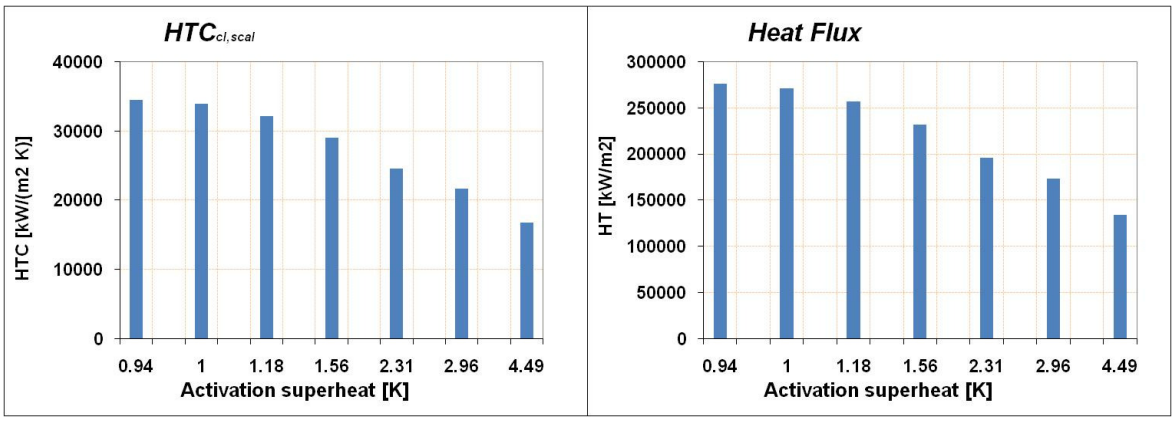

Figure 4-12: Effect of the activation superheat and cavity radius on $HTC_{cl,scal}$ and Heat Flux

4.3.4. Shrinking of the contact area

Three different analyses will be developed to study the effect of shrinking of the contact area, not included in the original version of the model. The first analysis focuses on the different contact angle decrease modes introduced. An analysis of the contact angle decrease factor will be then developed to conclude with the analysis of the effects of the variation of the initial apparent contact angle.

Contact angle decrease modes

The first test is related to the analysis of the contact angle decrease mode as described in Section 3.2.4, with an initial apparent contact angle (φ_0) equal to 30°:

0. No contact angle variation: the contact area continuously increases until departure, when the contact area radius reaches its maximum.
1. Constant angle decrease rate: the contact angle monotonically decreases after the bubble radius reaches a fixed fraction of the bubble departure radius ($r_b(t) > f_{decr} \cdot r_{bd}$) with a fixed angle decrease rate.
2. Variation with the inverse of the bubble radius: the contact angle decreases to zero with the inverse of the radius of the bubble radius after the bubble radius reaches a fixed fraction of the bubble departure radius ($r_b(t) > f_{decr}\, r_{bd}$).
3. Variation with the inverse of the bubble volume: the contact angle decreases to zero with the inverse of the volume of the bubble (imposed for the base case), after the bubble radius reaches a fixed fraction of the bubble departure radius ($r_b(t) > f_{decr}\, r_{bd}$).

The four modes (0, 1, 2 and 3) can significantly affect the bubble growth and temperature variations at the nucleation site, as shown in Figure 4-13. The apparent contact angle variation severely influences the bubble growth, almost linear for mode *0*, and severely more arched (with a faster initial bubble growth and slower next to departure) for mode *2*. Also, the contact area radius, which is maximum at departure for mode *0* ($r_{c,max} = r_{bd} \cdot sin\varphi_0$) and $r_{c,max} = f_{decr} \cdot r_{bd} \cdot sin\varphi_0$ for the other cases, reflects this distribution, with a clear shift to the left for reaching of the maximum in case *2*. The superheat at the nucleation site (ΔT_{NS}) is approximately constant for mode *0*, due to the fact that the nucleation site is always subject to a zero heat flux except for the very initial stage of the bubble growth (where it is possible to identify a very small decrease with respect to the average value). By contrast, for the other cases, the superheat has a minimum when the contact area approximately reaches its maximum. The heat contribution through the base of the bubble presents an opposite history for mode *0* with respect to the other modes, with an initial heat contribution lower than during the late stage of the bubble growth. A refinement of the angle decrease model should be implemented once more experimental data of the variations of the contact area are available.

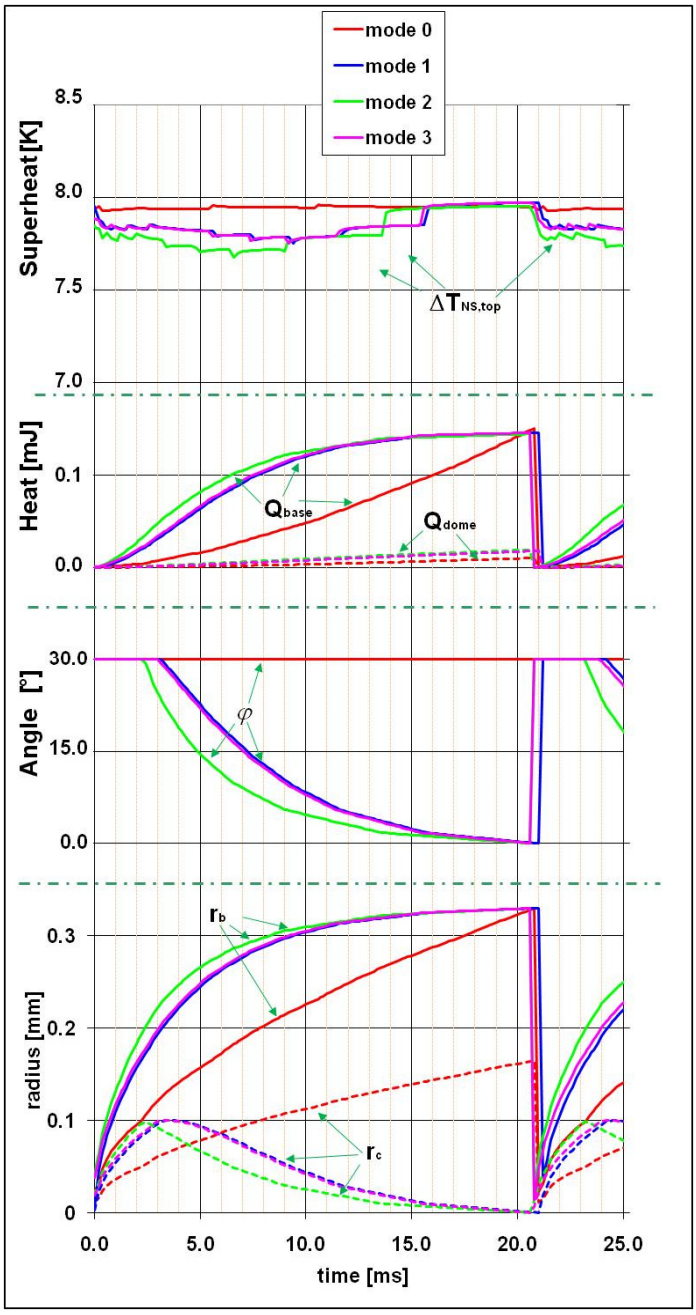

Figure 4-13: Effect of the contact angle decrease modes on bubble growth and superheat

Variation of the contact angle decrease factor

The effects of variation of the contact angle decrease factor (f_{decr}) are studied here. As for the base case, the apparent contact angle decrease mode depending on the volume of the bubble (mode *3*) and the heat transfer at the dome of the bubble (f_D = 1) are assumed. The initial apparent contact angle value (φ_0) has been assumed equal to 30°. The simulated values of the decrease fraction f_{decr} are listed in Table 6 and range from 0.4 to 1.0, i.e. the contact area is supposed to start shrinking when the bubble

radius reaches between 40% and 100% of the bubble departure radius. The base case corresponds to f_{decr} = 0.6 (in red in the table).

Table 6: Apparent contact angle decrease fraction values

f_{decr}	0.4	0.5	0.6	0.7	0.8	0.9	0.95	1.0

Four of the listed cases (f_{decr} = 0.4, 0.6, 0.8 and 0.95) are presented in Figure 4-14: from analysis of the apparent contact angle histories, it is clear when the contact area starts shrinking, with a decreasing period generally much smaller than the increasing one. Moreover, the heat contribution rates during the last phase were very limited. This phenomenon is particularly evident for f_{decr} = 0.95, i.e. when the area reduction occurs very close to departure. For this case, analysis of the superheat history shows an almost constant superheat during the whole bubble growth (similar to the case with no reduction of the contact area). Only a small reduction with respect to the average value is visible during the last stage indicating that the cooling effect at low contact area radii is relevant. For the other cases the superheat presents a history similar to the base case, with the only difference of a shifting on the right of the minimum superheat for f_{decr} = 0.8, representing an intermediate case between the base case and the case with no decrease of the contact area. From analysis of the bubble radius histories, the case with f_{decr} = 0.95 (i.e. if the contact area is supposed to start shrinking only during the very last stage of the bubble growth) has the most constant bubble growth rate, with less arched bubble radius history; in this case, a sharp variation of the contact area radius from increasing to decreasing contact area can be observed. By contrast, for lower angle decrease fractions, the effect on the contact area radius is smoother, because a continuous detachment process could be associated to this case, with a gradual variation between increasing and decreasing contact area. For high angle decrease fractions, the sudden variation in contact area radius suggests a more violent phenomenon, with forced breaking of the force balance resulting in a sudden detachment of the bubble. The comparison of the scaled heat transfer coefficients ($HTC_{cl,scal}$) is analysed in Figure 4-15.The *HTC* are scaled supposing a contact line width of 0.1 µm. An approximate linear effect can be observed, due to the proportionality between the angle decrease fraction and the maximum contact area (determining the mesh radius, and consecutively

the cell size). The $HTC_{cl,scal}$ decreases from ~ 40000 to ~ 12000 $\frac{kW}{m^2 K}$ for angle decrease fraction increasing from 0.4 to 1.0. If an average superheat equal to 8 K is assumed, a heat flux decrease from ~ 320000 to ~ 100000 $\frac{kW}{m^2}$ can be associated.

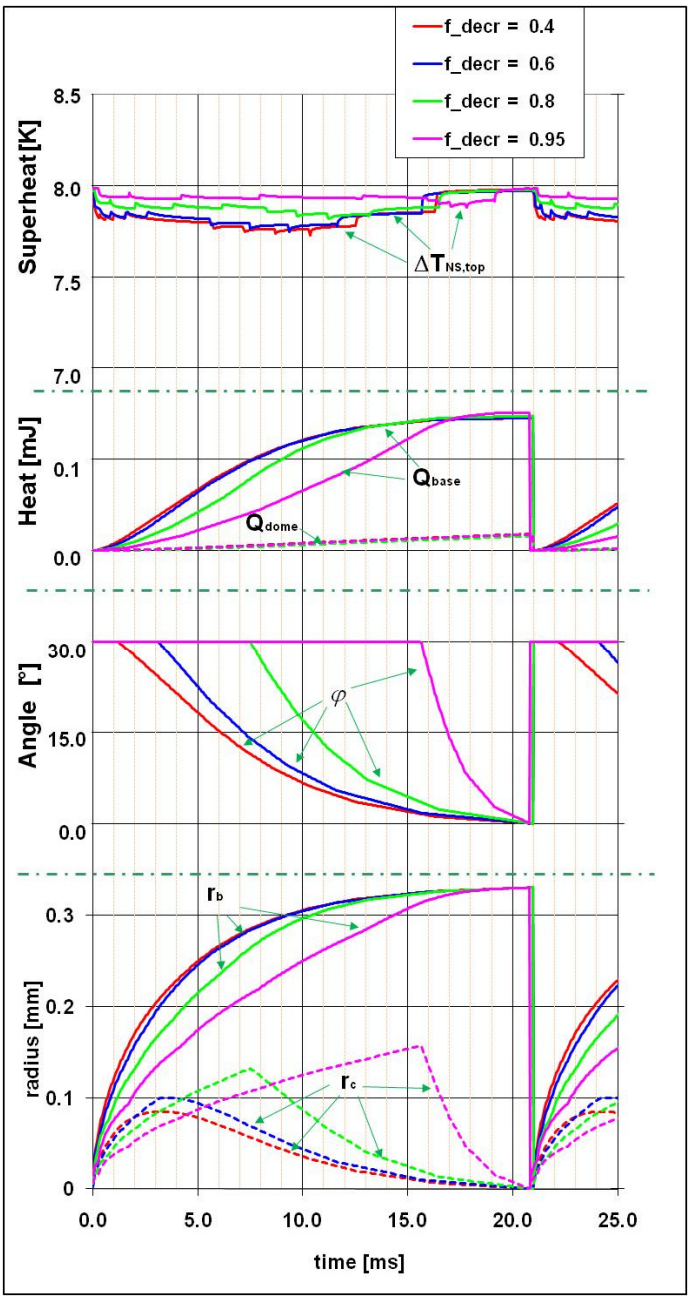

Figure 4-14: Effects of the angle decrease fraction on bubble growth and superheat

Variation of the initial value of the apparent contact angle

The effect of variation of the initial value of the apparent contact angle will be analysed here. Eight cases, listed in Table 7 (including the base case, highlighted in red, φ_0 = *30°*), have been simulated. The values range from 15° (when the bubble grows almost as a perfect sphere with a very small initial apparent contact angle, and then a very small contact area) to 90° (when the bubble initially grows as a hemisphere).

Table 7: Apparent contact angle values

φ_o	15°	20°	30°	45°	60°	75°	85°	90°

Two series of results will be presented here, corresponding to two fixed angle decrease fraction values equal to 0.6 and 0.9. The comparisons of the main bubble growth parameters for four cases (φ_o = 15°, 30°, 60° and 90°) for the two series are shown in Figure 4-16.

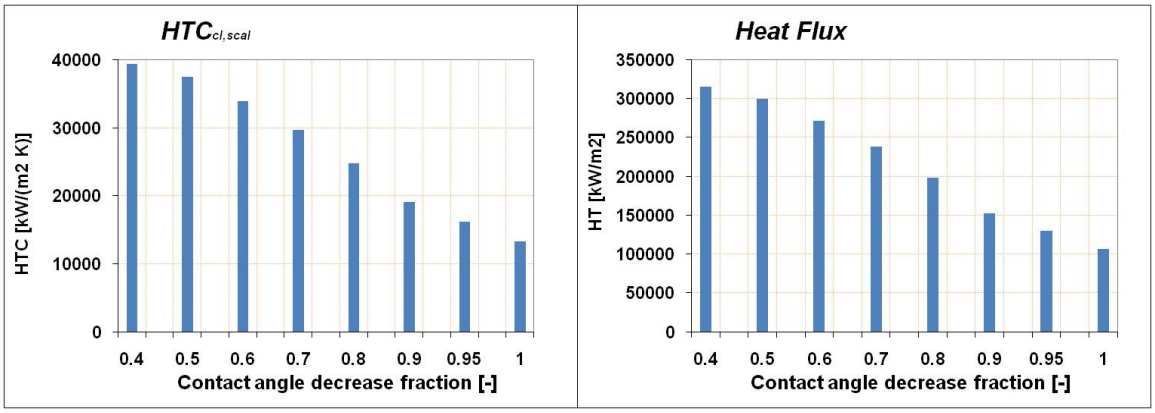

Figure 4-15: Effect of contact angle decrease fraction on $HTC_{cl,scal}$ and Heat Flux

For f_{decr} = 0.6, the angle decrease starts approximately at the same time for all the cases, generating bubble radius histories that are very similar for all the cases. The bubble radius rate is larger than for the experimental results during the initial stage of the bubble growth, and smaller towards the end. Also no difference can be noticed in the heat contributions for all the cases. However, the maximum contact area radius significanlty increases for decreasing initial contact angles. This causes larger superheat variations at the nucleation site for smaller angles, due to the smaller value of the average contact area, and then more marked effects at the centre of the contact area itself in proximity of the nucleation site.

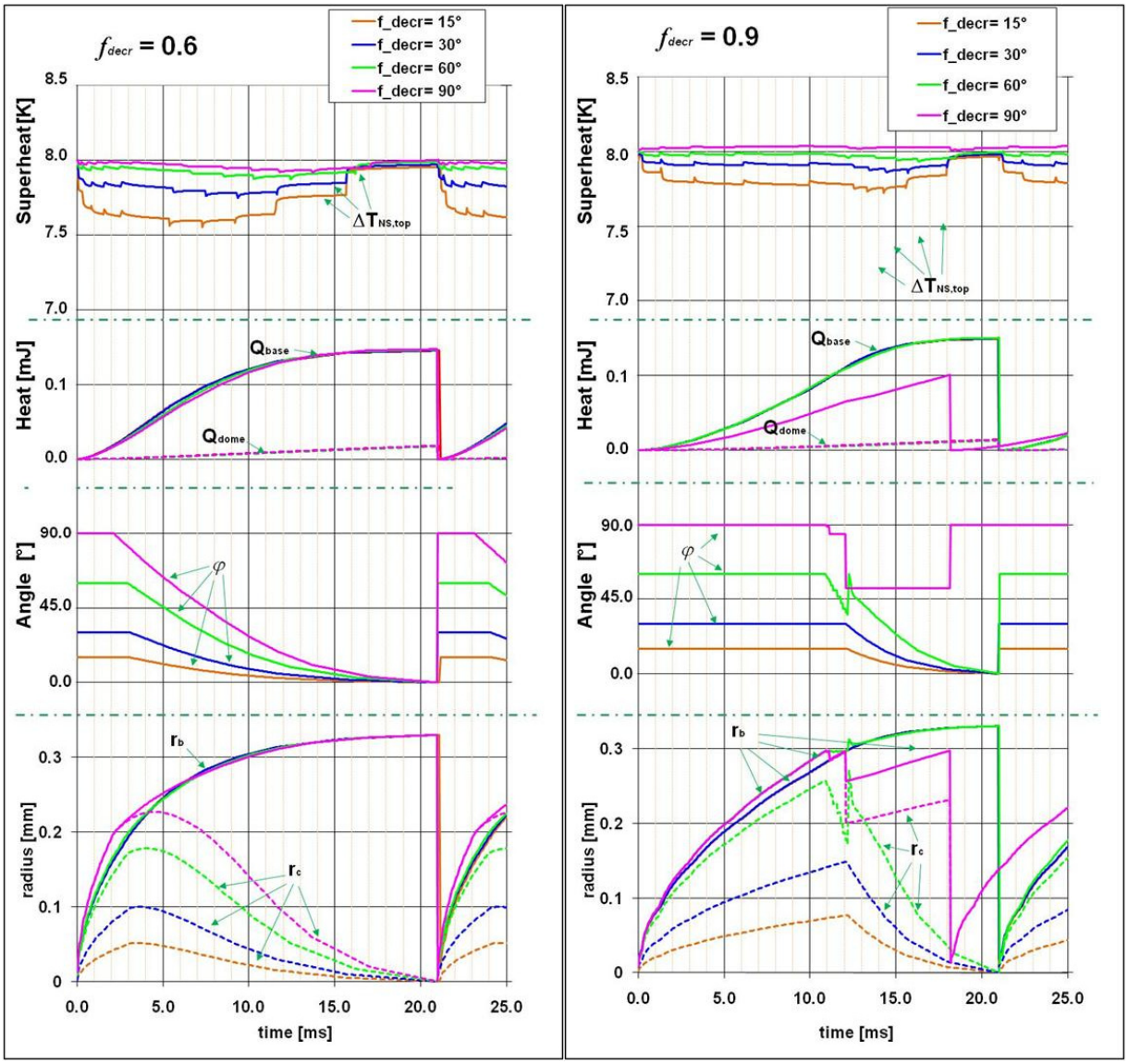

Figure 4-16: Effect of the initial value of the apparent contact angle variation for angle decrease fraction equal to 0.6 (left) and 0.9 (right)

For f_{decr} = 0.9, for initial apparent contact angle equal to 15° or 30° it is possible to observe the previous sharp change between increasing and decreasing contact area previously described for f_{decr} = 0.95. However, a new phenomenon can be observed for φ_0 = 60°: the analysis of the contact area radius shows two oscillations between 11 and 12 ms, during the contact area transition phase. This is due to the application of the contact area decrease condition expressed by Equation 3.20. This condition imposes that the angle starts to decrease when the third power of the ratio of the instantaneous radius and the bubble departure radius is larger than a specified fraction of the departure volume. When the initial contact angle is not close to 90°, the third power of the instantaneous radius represents a good approximation of the volume, so that the ratio approximately represents the ratio between the instantaneous volumes. However, for large values of φ_0, the difference in shapes leads to a significant deviation: a sudden decrease of the contact area radius, leads to a readjustment of the instantaneous bubble radius that may undergo a significant reduction. In this case, Equation 3.20 may not be satisfied for the decreasing area condition producing then an initial oscillatory effect. This effect is even more marked for φ_0 = 90°, but in this case an additional phenomenon is present. The contact angle, instead of decreasing to zero as in the previous cases, sets at a fixed value of ~ 50°. This phenomenon suggests that once the shape has readjusted, the volume at transition from increasing to decreasing contact area is not sufficiently larger than the minimum required in satisfying Equation 3.20. Then the contact angle stops decreasing (and so does the contact area radius). This hypothesis is confirmed by the sharp jump of the bubble radius at transition for f_{decr} = 0.9. Because of this phenomenon, a much larger number of iterations are needed for the *HTC* to adjust in order to simulate the bubble growth from experiments. A similar effect can be also seen for φ_0 = 75° and φ_0 = 85°, but in the first of the two, the code is able to match the experimental growth time. Comparison of the superheat histories for the two cases of angle decrease fraction shows that variations are smaller for higher f_{decr}.

The variations of the $HTC_{cl,scal}$ and Heat Flux are shown in Figure 4-17 for both f_{decr} = 0.6 and 0.9. The heat transfer coefficient and heat flux values significantly decrease with increasing apparent contact angle and increasing angle decrease fraction. For f_{decr} = 0.6, $HTC_{cl,scal}$ ranges from ~ 70000 to ~ 15000 $\frac{kW}{m^2 K}$ (corresponding to heat fluxes from 550000 to 100000 $\frac{kW}{m^2}$) while for f_{decr} = 0.9, $HTC_{cl,scal}$ drops from ~ 37000

to ~ 8000 $\frac{kW}{m^2 K}$ (corresponding to heat fluxes from 300000 to 60000 $\frac{kW}{m^2}$). For the last case, only the cases where the experimental growth time was matched were used.

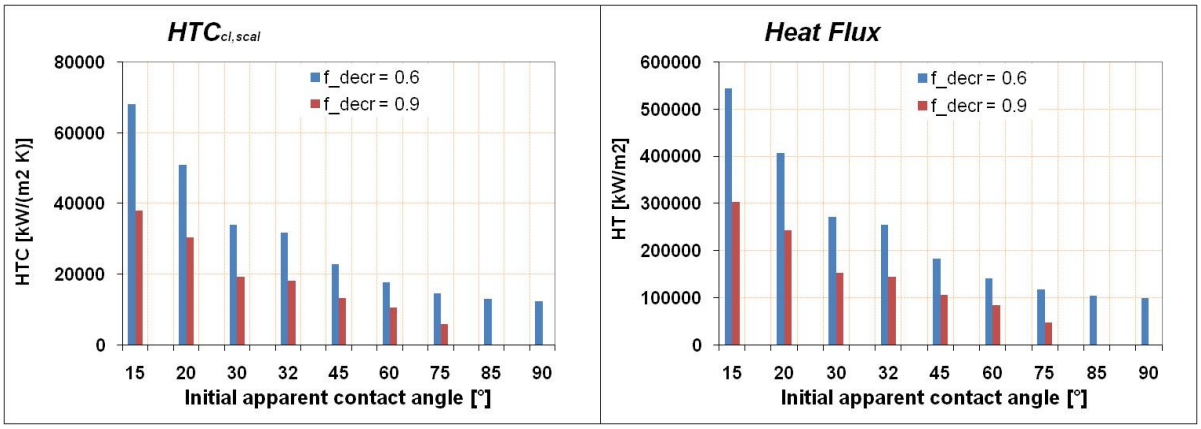

Figure 4-17: Effects of the initial apparent contact angle variation on $HTC_{cl,scal}$ and Heat Flux

4.3.5. Heat transfer at the dome of the bubble

The application of the heat contribution at the dome of the bubble significantly modifies the bubble growth history. In Figure 4-18 three different cases of heat contribution at the dome are presented. The base case assumes a dome heat contribution factor f_D equal to 1.0, so that the heat contribution calculated according to Equation 3.16 is fully considered. The case f_D = 0.0 assumes no contribution at the dome of the bubble so that all the vapour is generated by evaporation at the base of the bubble. Finally, the case f_D = 2.0 assumes a heat contribution at the dome of the bubble double with respect to the base case. The effect of the dome heat contribution factor is evident if the heat contributions are analysed. Since the total heat (from the dome and from the base) provided to the bubble must be constant (the final bubble volume is fixed), an increase in f_D increases the dome heat contribution and consequently reduces the heat contribution at the base of the bubble. Moreover, it decreases the bubble growth rate during the initial stage of the bubble growth, determining a shift to the right of the time when the contact radius reaches its maximum: the bubble growth history is consequently less arched. This suggests that the dome heat contribution may play an important role in the bubble growth and its contribution should not be neglected (as it was in the original version of the code). Therefore, the model used should be improved on the basis of more detailed results (either from experiments or from independent

numerical simulations) in the future. The effect of reduction of the heat contribution at the base of the bubble with increasing f_D determines also smaller superheat variations at the nucleation site: the maximum superheat variation is approximately 0.22 K for the base case, 0.2 K for f_D = 2.0 and 0.35 K for no heat contribution at the bubble dome. Figure 4-19 compares the $HTC_{cl,scal}$ and heat flux variation for increasing angle

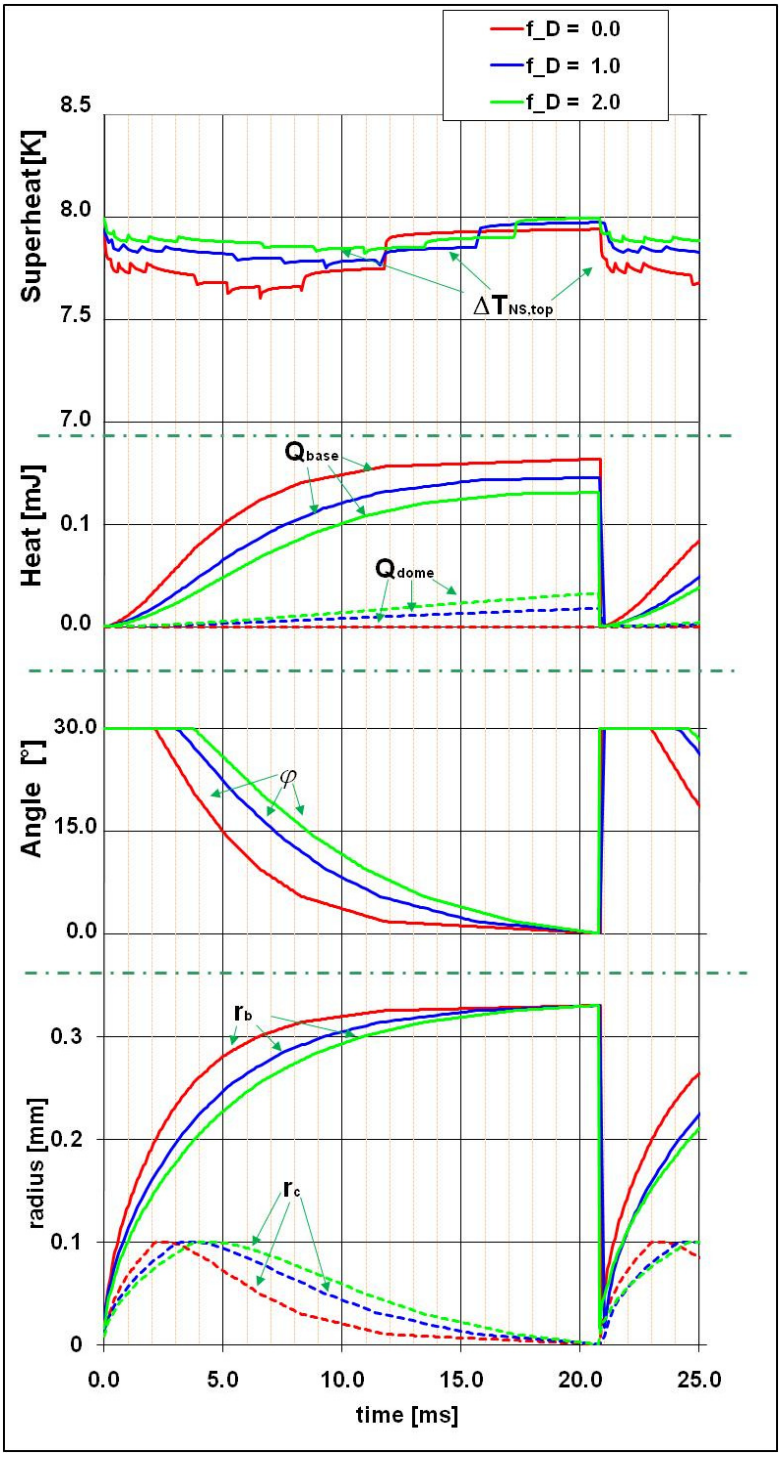

Figure 4-18: Effect of dome heat contribution factor on superheat and bubble growth

decreasing fraction in the two cases of f_D = 0.0 and f_D = 1.0 (base case). The elimination of the contribution at the dome of the bubble strongly increases the $HTC_{cl,scal}$ and heat flux of approximately a factor 3 to 4. The $HTC_{cl,scal}$ is approximately 160000 $\frac{kW}{m^2 K}$ for an angle decrease fraction f_{decr} equal to 0.4 and ~ 40000 $\frac{kW}{m^2 K}$ for f_{decr} = 1.0. Similarly, the heat flux drops from $1.2 \cdot 10^6$ to $0.4 \cdot 10^6$ $\frac{kW}{m^2}$.

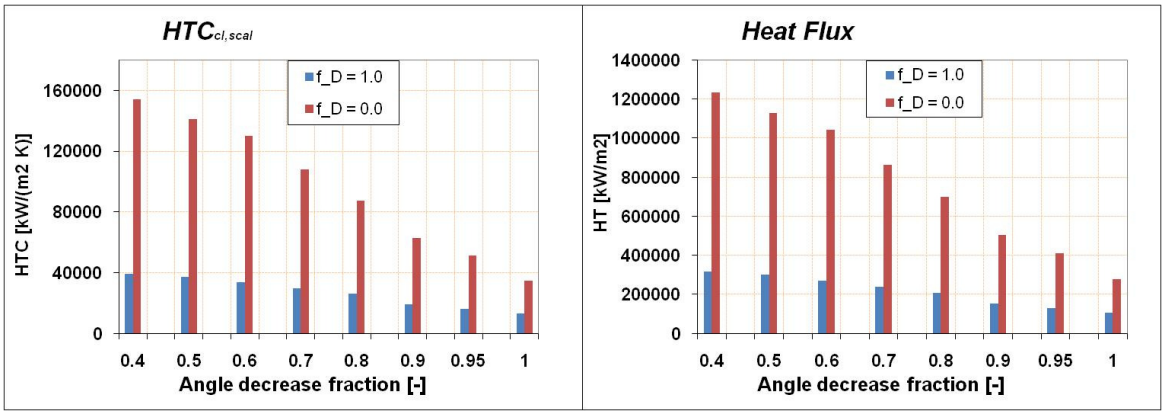

Figure 4-19: Effect of the dome heat contribution factor and angle decrease fraction on $HTC_{cl,scaled}$ and Heat flux

4.3.6. Heat transfer evaporation models

Two different heat transfer evaporation models at the base of the bubble have been used to simulate the heat transfer between the solid substrate and the bubble through the contact area, as described in Section 3.2.4. The comparative superheat and *HTC* distributions along a line passing through the centre of the nucleation site for the central part of the substrate are shown in Figure 4-20 for f_{decr} = 0.6 and for t ~ +3 ms from activation of the nucleation site.

- The contact line model (*CL*, used in the base case, in red in the figure) assumes a high *HTC* peak for cells crossing the triple contact line formed between the bubble base and the substrate and dividing the liquid from the vapour inside the bubble. A zero *HTC* is imposed for the inner region of the contact area.
- The micro-layer model (*ML*, in blue in the figure) assumes a film of liquid trapped below the bubble during the whole bubble growth. It generates a *HTC* distribution with a central peak and gradually decreasing towards the triple

contact line region to the value for natural convection. The central peak corresponds to the region where the micro-layer is thinner.

The contact area radius corresponding to the examined time is approximately at maximum (~ 0.1 mm) for both the models. However, the bubble radii slightly differ because of the different heat input from the base of the bubble as it can be seen also in Figure 4-21. Consequentially, the superheat distribution for the *CL* model (in red, Figure 4-20, left) shows a depression at the contact line and a partial recovery in the centre of the contact area due to the zero heat transfer coefficient. By contrast, the superheat distribution for the *ML* model (in blue, Figure 4-20, left) shows a continuous decrease towards the centre of the contact area, due to the constant high heat transfer coefficient in this region. The maximum *HTC* for the *ML* model is significantly smaller than for the *CL* model since the heat contribution is spread over an area larger than the simulated contact line area. However, the difference is not very marked because the high *HTC* in *ML* is applied only to a small area. Analysis of Figure 4-21 for f_{decr} = 0.6 shows that while contact and bubble radii, contact angle and heat contributions are very similar, the superheat variations at the nucleation site are much larger for the *ML* model, due to the constant cooling of the nucleation site itself, with variations during the bubble growth period larger than 0.5 K and occurring when the contact radius is at maximum. However, since the maximum variation occurs when the contact area radius is at

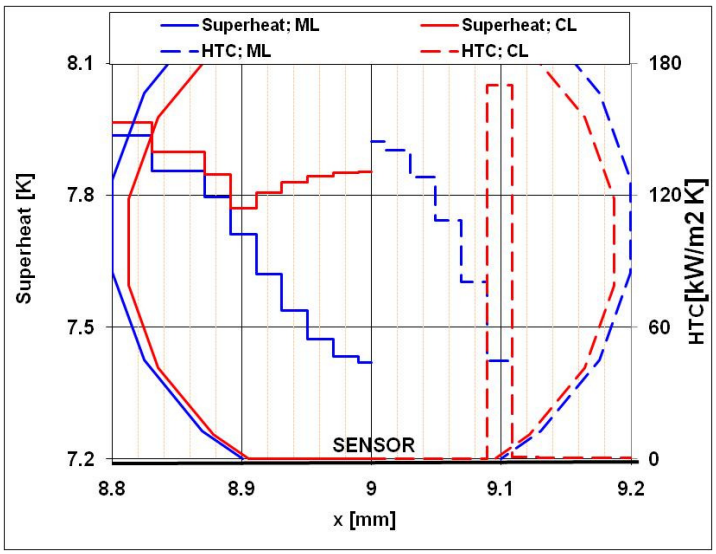

Figure 4-20: Superheat and HTC distributions along a line in the region around the nucleation site for micro-layer (*ML*) and contact line (*CL*) models

maximum, the superheat variation is not useful in indicating whether a nucleation site has become active. Comparison of the superheat variations for two different angle decrease fractions (f_{decr} = 0.6 in Figure 4-21, left and f_{decr} = 0.9 in Figure 4-21, right) shows that variations become smaller for larger values of this parameter. This is probably due to the smaller value of the *HTC* for larger maximum contact radius (and then for larger f_{decr}).

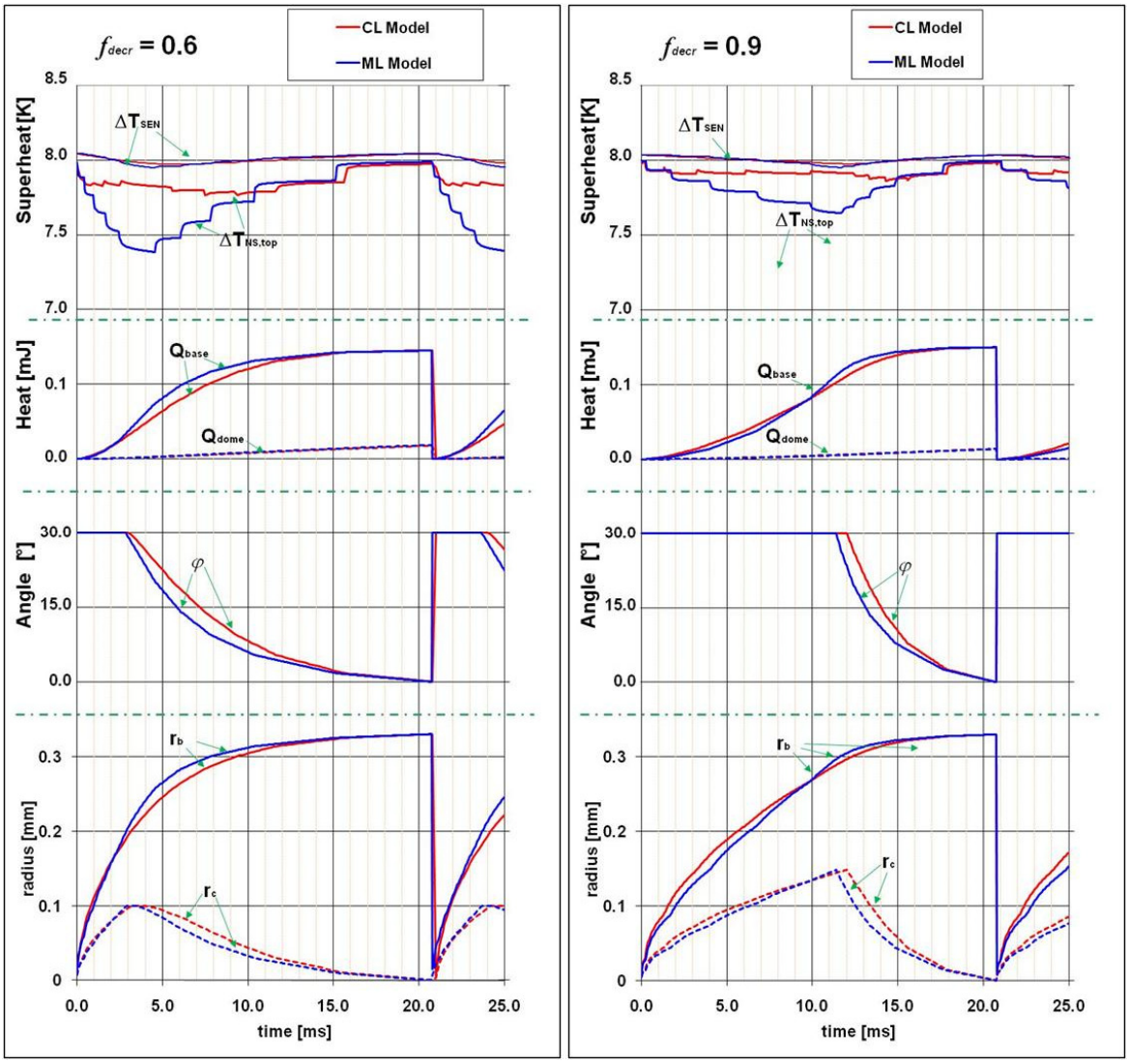

Figure 4-21: Effects of the heat transfer evaporation models at the base of the bubble for f_{decr} = 0.6 and f_{decr} = 0.9 on superheat and bubble growth

4.3.7. *Standard and unrefined nucleation sites*

The use of unrefined sites has been introduced to reduce the computational time so that a larger number of nucleation sites could be simulated. This process, as described in Section 3.2.3, reduced the use of the mesh refinement procedure (very time consuming), although the computational time also increases with the number of unrefined sites.

The process approximates the contact line area with a pseudo circular distribution of cells around the nucleation site, possibly degenerating into the whole cell if the maximum contact area is much smaller than the coarse mesh size (compare Figure 4-22 for this specific case). Square coarse cells with cell width w_{xy} = 0.1 mm are used in these simulations. However, while for the base case (i.e. where the refinement process takes place) the average cell width around a nucleation site is approximately 0.02 mm (blue area in Figure 4-22, a), for the unrefined site the cell width is ~ 0.1 mm (blue area in Figure 4-22, b), approximately five times larger. In both cases, the cell width corresponds to the triple contact line width.

The mesh distribution strongly affects the pseudo-contact area for unrefined sites as it can be seen in Figure 4-23, showing the superheat distribution along a line passing through the centre of the nucleation site at two different time steps (+7.8 and +14.2 ms from activation of the nucleation site) during the bubble growth. It is evident that although the unrefined site mesh distribution is not able to properly reproduce the contact line area and to follow the contact radius increase (the maximum contact radius is approximately of the same order of magnitude of the coarse cell width), the maximum

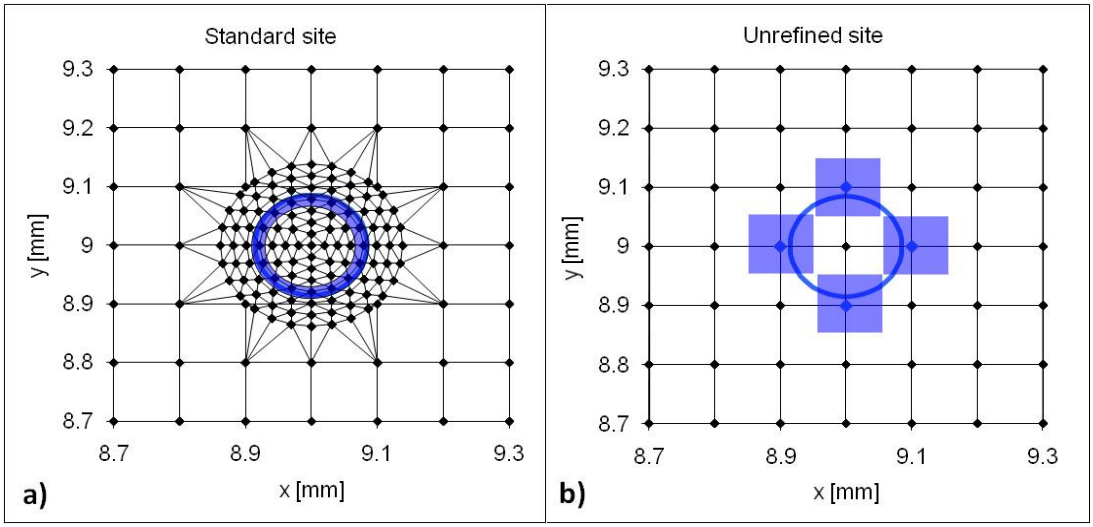

Figure 4-22: Mesh distribution and contact line area for standard (a) and unrefined (b) sites

difference in superheat is less than 0.1 K. The difference decreases with increasing distance from the nucleation site and becomes smaller than 0.02 K at a distance larger than 3 mm.

The use of unrefined sites strongly limits the level of detail of local variation in superheat, mostly in the angular direction along the triple contact line. Simulations predict superheat variations at the nucleation site generally smaller than 0.5 K and even smaller if averaged over the sensor area. The simulated superheat variations at the nucleation site and then bubble growth variables during the bubble growth are compared in Figure 4-24 for a standard site and three simulations using different coarse mesh width, and consequently different unrefined sites contact line width. The value averaged over the sensor area is not available for unrefined sites, but the presented value almost represents it due to the size of the coarse cells. It is clear that for the unrefined site the superheat variations are less precise than for the standard case, but they still well represent the same range.

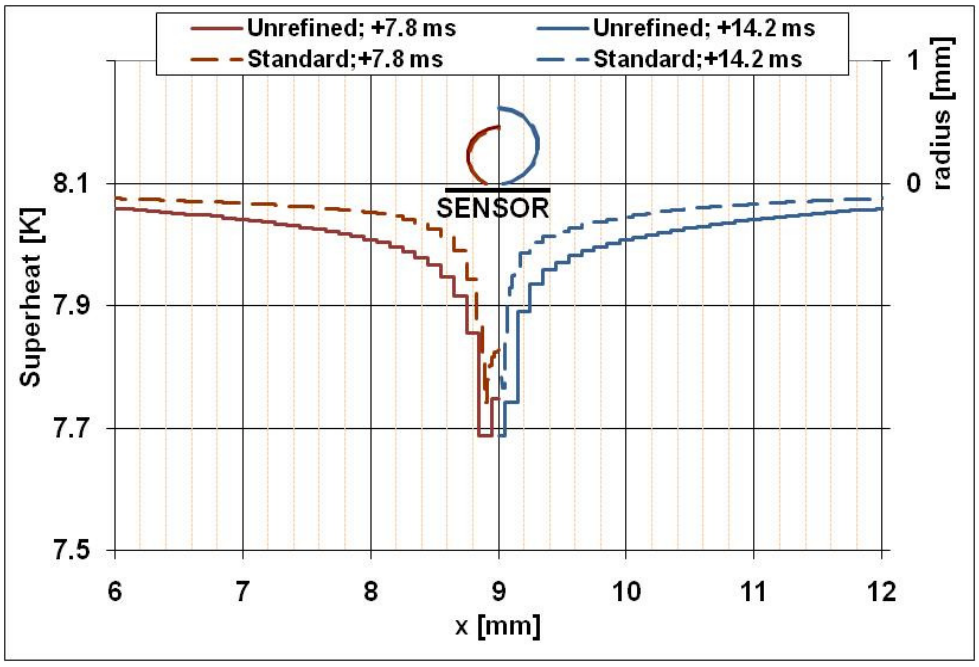

Figure 4-23: Superheat distribution along a line for standard and unrefined sites

The long periods during which the superheat is approximately constant (i.e. for t less than 1 ms and for t between 10 and 22 ms for w_{xy} = 0.1 mm) are due to the persistency of the high heat transfer rate applied to the single cell containing the nucleation site. In fact, during these periods, the contact radius is smaller than half of the coarse mesh size, so that a high *HTC* is applied only to the central cell. All the other variables (bubble and contact angle radii, apparent contact angle and heat contributions)

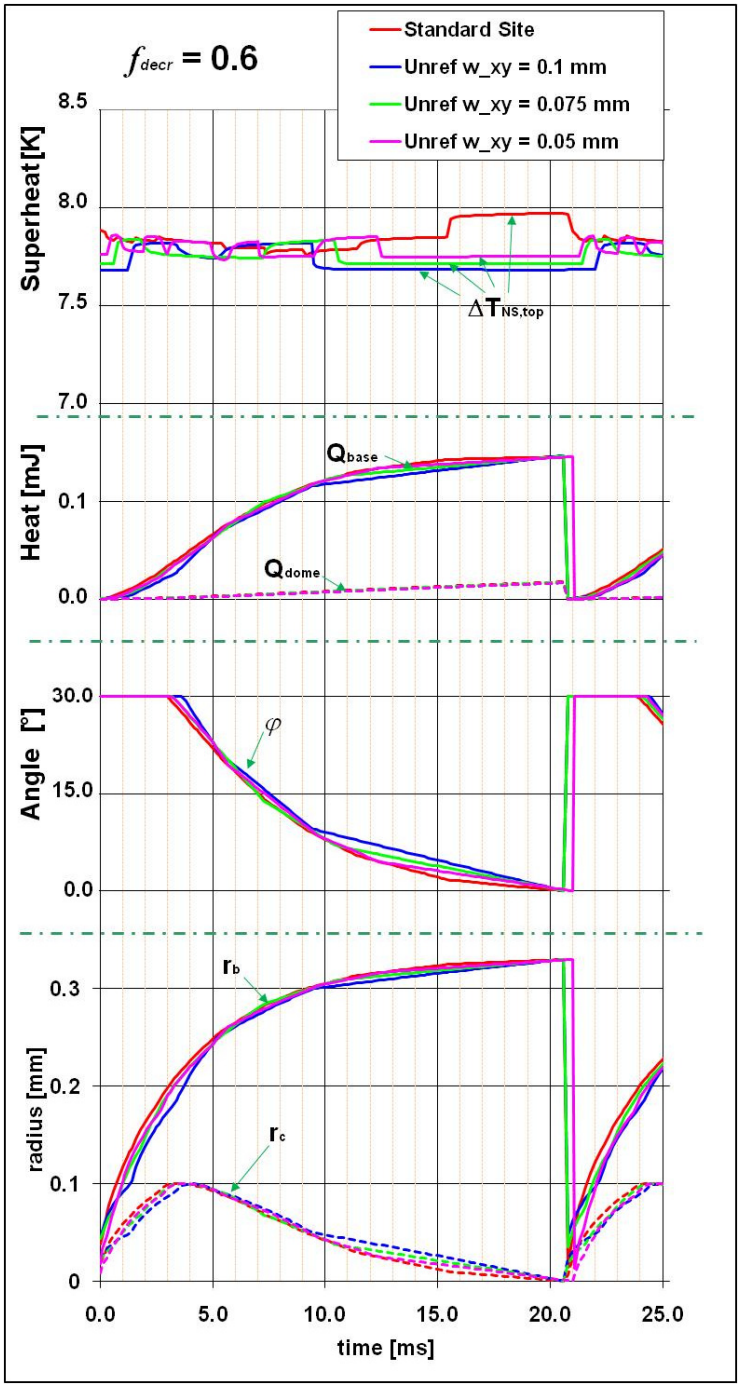

Figure 4-24: Bubble growth and superheat variation for standard and unrefined sites

are very similar for standard and unrefined sites, even though for the unrefined case the variations are rougher due to the sudden variation of the number of cells to which the high *HTC* is applied. The effect of the cell size on $HTC_{cl,scal}$ and heat flux is shown in Figure 4-25: however, for the unrefined sites case the two variables have not been scaled only over the simulated to theoretical contact line ratio as in the base case but over the coarse to refined cells width.

This double scaling was necessary in order to take into account that the square cells can only barely approximate the contact line area. This is the reason why for the unrefined sites case the variation is significant and the heat transfer coefficient and heat flux considerably differ from the standard sites case. The different *HTC* and heat flux values for the three cases with unrefined cases depend also on the use of the pseudo-circular area, which cannot be accounted for by the double scaling factor. A further reduction in the size of the Cartesian cells would be expected to show an asymptotic behaviour, since the triple contact line area would be better simulated.

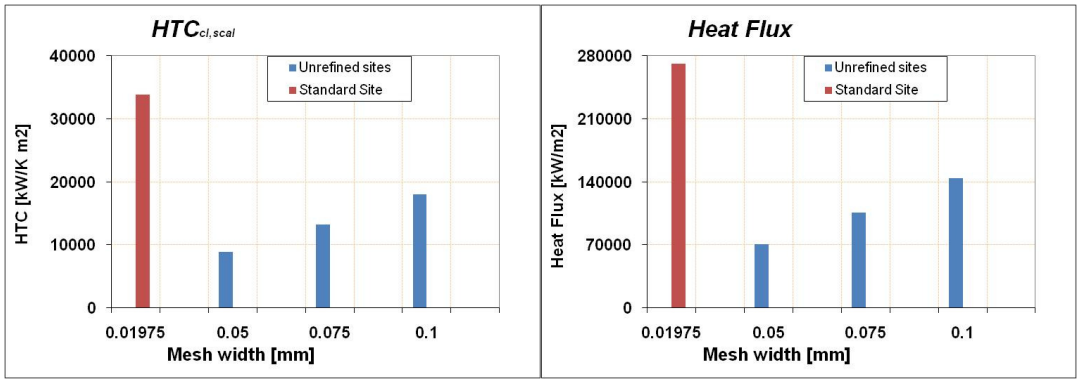

Figure 4-25: Effects of the mesh size on $HTC_{cl,scaled}$ and heat flux

4.3.8. Variation of the thickness of the substrate

The thickness of the substrate is a very important parameter to take into account in designing a new test section. For Silicon, its minimum value may be limited by fabrication constraints; however, the study of its effect on superheat variations via numerical simulations may be very important in order to define how much effort should be put in trying to reduce the thickness. One of the main advantages of having a small thickness could be the possibility of observing the superheat variations on the back of the substrate, so that techniques alternative to temperature sensors may be used in measuring them (e.g. infrared camera). Figure 4-26 shows the results for numerical simulations using 4 different values of the thickness: 0.380 (the base case), 0.285, 0.190

and 0.095 mm. The *HTC* has not being tuned during these simulations as during the sensitivity analysis. The bubble growth and superheat variations on the top surface highlight that for the first three cases the modification of the thickness does not produce significant changes. By contrast, for Δz = 0.095 mm some slight changes occur, both on the growth time and on superheat at the nucleation site. The growth time is slightly larger than for the other cases, due to the superheat at the contact area, significantly lower (between 0.2 and 0.4 K) for this case. From analysis of the superheat variations at the bottom of the substrate, it is apparent that the variations increase during the bubble growth with decreasing thickness, due to the lower attenuation factor from the top to the bottom surface. For the first two cases (Δz = 0.380 and 0.275 mm), superheat variations on the upper surface are hardly recognisable on the back of the substrate, also because of the small entity of the variations themselves. For Δz = 0.190 mm the minimum and maximum in superheat are better identifiable for both top and bottom surface with the same variation entity: however, small superheat variations on the top surface do not propagate to the back surface. For the smallest thickness, variations on the back and top surfaces are very similar mostly on the first stage of the bubble growth, and with no

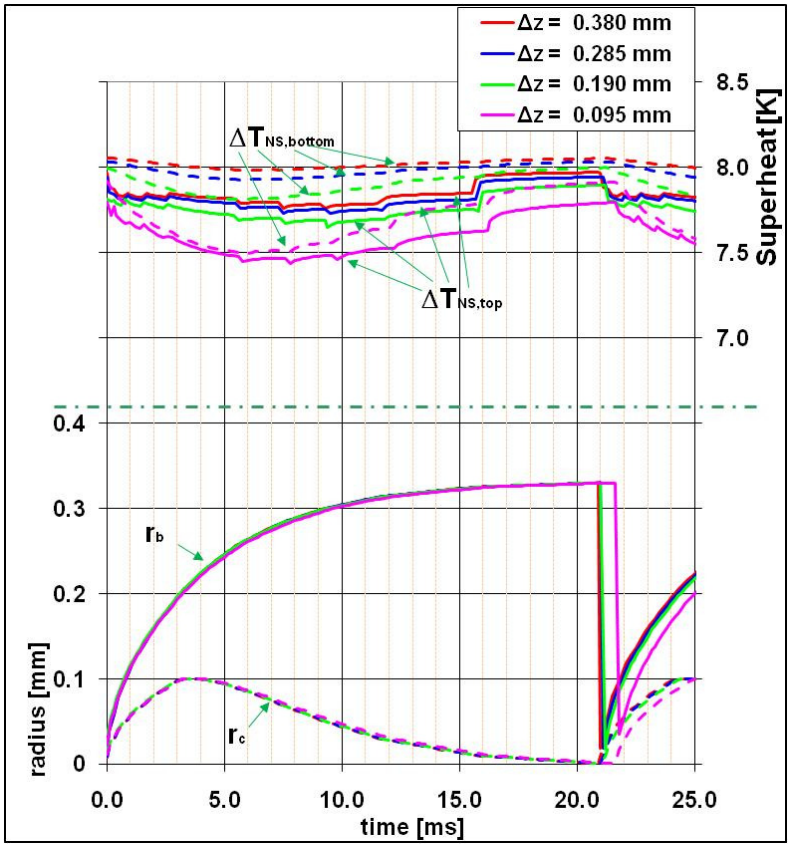

Figure 4-26: Effect of the substrate thickness on superheat variations

time delay. During the last stage of the bubble growth, the difference in superheat is more marked, probably due to the slower variation rate. Moreover, for smaller thicknesses, the superheat variations are generally more marked with a lower average value that determines a slightly longer growth time (~ 1 ms longer).

4.4. Conclusions

The sensitivity analysis on one hand showed the importance of variations of input data related to the simulated physics of the process, and on the other the difference in applied *HTC* and heat flux necessary to reproduce the experimental bubble growth and superheat used for the base case. None of the parameters significantly modified the superheat distribution (averaged over the equivalent of the sensor area). However, the effects on bubble growth could be relevant. The parameters that are most likely to affect the bubble growth via altering the bubble growth rate in simulations were found to be:

- The activation superheat: an increase of this parameter (involving a reduction of the cavity mouth radius according to the used model) leads to a more uniform bubble growth rate.
- The contact area decrease mode and contact angle decrease fraction. The use of a model with continuously increasing bubble contact area, with no final decrease before departure would lead to more constant bubble growth rate. However, the assumption of no reduction of the contact area is unrealistic from the physical point of view. Instead, the use of very large contact angle decrease fractions (i.e. the contact area starts decreasing very close to the departure) leads to similar results. Therefore, an improved model should be developed as soon as more data related to the bubble growth are available.
- The evaporation at the dome of the bubble. Consideration or not of this contribution to the bubble growth leads to significantly different bubble growth rates, with higher values during the initial stage of the growth and slower close to departure if it is neglected.

By contrast, variations of the initial value of the apparent contact angle, the heat transfer at the base of the bubble and the use of standard or unrefined sites do not significantly alter the bubble growth. The superheat at the nucleation site and the tuned *HTC* needed to match the bubble growth from experimental data may be significantly modified but the consequent variations in superheat are very small (not more than ±0.5

K). Such small superheat variations are of the same order of precision of current measurements from the sensors used at the University of Edinburgh (Hutter, 2009), implying that the sensors are unable to detect superheat variations during the bubble growth for silicon on FC-72. More precise or smaller sensors should be used, but some changes should be applied either to the experimental setup (such as the use of different liquid-substrate coupling or smaller thickness of the substrate) or to the operating conditions (such as lower pressure or higher imposed heat fluxes).

The advantage of including temperature variations in the substrate may appear at a first sight counter-productive compared to a simple model assuming an isothermal surface, because the much longer computational times predict only very small superheat variations, not detectable by the current sensors. However, the temperature field analysis in the substrate is necessary if variations between groups of sites are to be studied. Even if an isolated site does not produce large superheat variations around the site itself, a group of close spaced sites may significantly lower the average superheat in the area covered by the sites themselves (as observed in Sections 6.1.3 and 6.2), due to the high thermal capacity of silicon and the substrate thickness in this case. Moreover, the code is not restricted to the study of silicon immersed in FC-72, but can be applied to every combination of liquid-substrate, as long as some experimental input data (and in particular the heat transfer coefficient for the natural convection regime, and the bubble growth and wall average superheat data) are provided.

5. Verification and Validation

5.1. Introduction

A complete process of Verification and Validation (V&V) of a code is generally necessary to guarantee that a numerical code is providing a solution that is correct and can represent experimental results. The Verification process aims to establish whether the code is providing the expected numerical solution. The Validation process aims to determine the ability of the code to reproduce the physical processes in a specific range of conditions.

The main objective of this project (developed in collaboration between Brunel University, University of Edinburgh, University of Ljubljana and Los Alamos National Laboratory) was the study of pool nucleate boiling heat transfer on solid substrates horizontally immersed in a liquid from both the numerical and experimental points of view. In particular, the research group at Brunel University had the objective of improving a pre-existing numerical code in order to make it suitable to simulate in reasonable computational times approximately 100 nucleation sites with a normal computer power-station (see Section 3.2 for further details). On the other hand, the University of Edinburgh developed the experimental study on a Silicon substrate with micro-fabricated cavities acting as nucleation sites and fully immersed in FC-72, necessary to complete the Validation process. The experimental results were intended to provide information on bubble activation, growth and departure from optical visualization and on superheat variations measured by temperature sensors located around the nucleation site. However, the superheat measurements are not able to achieve the original objective of clearly identifying activation and deactivation of a nucleation site independently from the optical access because the detected values are lower than the sensitivity of the sensors. For this reason, only a preliminary Validation process can be provided here.

The analysis in this chapter will start with the Verification process by comparison of simulations with theoretical models. A similar process should be run every time a new version of the code is released (one-time Verification) and it aims at verifying that the code is simulating the physics of the problem as intended by the user. Finally, a

preliminary Validation process on the base of available experimental results and on the base of the numerical relevant results obtained in the previous section from the sensitivity analysis will be presented.

5.2. Verification of the code

The verification process is very important to highlight the possible presence of numerical errors in the application of the approximate model for the physics or in the use of the different routines. The numerical results for a series of tests applied to different conditions will be compared with theoretical models. The analysis will start with the verification of the conduction model in the substrate when a uniform natural convection heat transfer coefficient is applied on the upper surface. Tests will be carried out now including the mesh refinement process, in order to evaluate the response of the code to mesh modifications. The analysis will continue with the investigation of the mesh refinement process when boiling occurs, and the results will be compared to the base case previously analysed (Section 4.2), when either the coarse or refined cells are modified. In particular, the effects on the *HTC* necessary to match the experimental bubble growth will be compared.

5.2.1. Verification of the conduction model

The first test evaluates the response of the code when applied to a horizontally positioned Silicon substrate cooled on the upper surface by FC-72 at atmospheric pressure; the numerical input data used for FORTRAN simulations and the physical properties of the substrate and liquid are listed respectively in Table 8 and Table 9.

Table 8: Numerical input data for FORTRAN simulations

Numerical	Δt	t_{sim}	w_{xy}	n_{vL}	T_{in}	*N. cells*
data	1.0 µs	0.5 s	0.1 mm	1 or 6	65.25 °C	181x181

Table 9: Physical properties used as input data for FORTRAN simulations

Substrate [Silicon] 18.1 x 18.1 mm	δ_H 0.38 mm	ρ_H 2340. $\frac{kg}{m^3}$	c_H 750. $\frac{J}{kgK}$	k_H 110. $\frac{W}{mK}$	
Liquid [FC-72] 1 Atm	T_{sat} 57.17 °C	ρ_V 12.76 $\frac{kg}{m^3}$	ρ_L 1611. $\frac{kg}{m^3}$	c_L 1088. $\frac{J}{kgK}$	k_L 0.054 $\frac{W}{mK}$

During these simulations, the natural convection heat transfer model has been imposed to all the cells: the activation temperature for the nucleation sites has been increased to very high values in order to manually prevent activation of the sites. Under these conditions, no mesh refinement may take place. Two different heat sources, applied one at a time, are assumed:

- Heat flux applied to the back of the substrate ($\dot{q}_{bottom} = 4.480 \frac{kW}{m^2}$), with adiabatic conditions imposed at the edges. The imposed heat flux corresponds to the heat source applied during the experiments described in the previous chapter for the base case (Section 4.2).
- Volumetric heat source ($Q_{vol} = 11789.5 \frac{kW}{m^3}$) with adiabatic conditions applied to the back and edges of the plate. The heat source has been derived from the previous case in order to maintain the same total heat generation.

Two cases assuming 1 and 6 vertical layers (keeping the total substrate thickness and varying the thickness of each layer) have been simulated. A square substrate 18.1 mm long (with a cell width equal to 0.1 mm) and 0.38 mm thick has been assumed. The transient time t_{trans} (i.e. the time elapsed between the beginning of simulations and the simulated time when temperature reaches its steady state temperature, T_{trans}, i.e. when the difference between the temperature and the steady-state value in the central cell of the substrate on the top surface is lower than $1.0 \cdot 10^{-3}$ K) and the steady state superheat ($\Delta T_{trans} = T_{trans} - T_{sat}$, i.e. the value reached once the transient period is completed) will be analysed. The results for ΔT_{trans} are summarised in Table 10.

Table 10: ΔT_{trans} for FORTRAN simulations

	ΔT_{trans}
Heat flux (back)	8.095 K
Volumetric Source	8.1276 K

No significant difference is predicted for ΔT_{trans} (the difference is smaller than 0.05 K) between the cases of heat flux applied to the back of the substrate and volumetric heat source. The modification from 1 to 6 layers does not affect the steady state superheat significantly. For the case with volumetric source, the results for the transient time t_{trans} are qualitatively compared in Figure **5-1** with theoretical results. These were obtained by imposing the heat balance to a thin plate (supposing no superheat variation across the thickness), as expressed in Equation 5.1 for the generic time t in the differential form. Using the initial condition that $T(t = 0\ s) = T_0$, the rearrangement of Equation 5.1 leads to Equation 5.2.

$$\rho_H \delta_H c_H dT = Q_{vol} \delta_H dt - HTC(T - T_{sat})dt \tag{5.1}$$

$$T - T_{sat} = \frac{q''}{HTC} - \frac{q'' - HTC(T_0 - T_f)}{HTC} \exp\left(-\frac{HTC}{\rho_H c_H \delta_H} t\right) \tag{5.2}$$

According to the theoretical model, ΔT_{trans} is ~ 8.1453 K, slightly higher than for FORTRAN simulations due to the fact that the theoretical solution does not take into account the heat dispersion in the lateral direction and that the *HTC* has been supposed constant (instead of varying with *T*) and equal to its average value.

The case of imposed heat flux applied to the back of the substrate does not present an easy explicit solution due to the presence at the same time of the imposed heat flux and of the convective heat removal on the top surface. However, the order of magnitude of t_{trans} found with the previous balance should be maintained (since the heat balance is the same, provided that the volumetric source is replaced by the heat flux). ΔT_{trans} on the top surface can be derived for the steady-state case to be ~ 8.0954 K from the balance

expressed in Equation 5.3, with *HTC* as defined in Equation 3.15. The factor f_{enh} = 1.16 is the same used during simulations.

$$q'' = 1.16 \cdot HTC(T - T_{sat}) \tag{5.3}$$

The results for the superheat temporal variation for the case of imposed heat flux are shown in Figure 5-2. It can be noted that the transient time is shorter than in the previous case due to a smaller total variation of the superheat.

The superheat distribution along a line passing through the centre of the substrate is shown in Figure 5-3. It can be noted that the presence of the volumetric source determines an asymmetry in the superheat distribution. This phenomenon depends numerically on the explicit approach used in the code to calculate the temperature field in the substrate. In fact, at each time step, the code derives the new temperature values in each cell, starting from the one with lower numbering (and then with lower *x* and *y* coordinates) and located in the upper layer, as described in Section 3.1.3. The asymmetry disappears for the heat flux case. In both cases the superheat is ~ 8.1 K, but while for the heat flux case its value is approximately constant along the line, for the case of volumetric source on the left side of the substrate, the superheat has a value slightly higher than average (~ 8.16 K) which continuously decreases until the right side (~ 8.13 K).

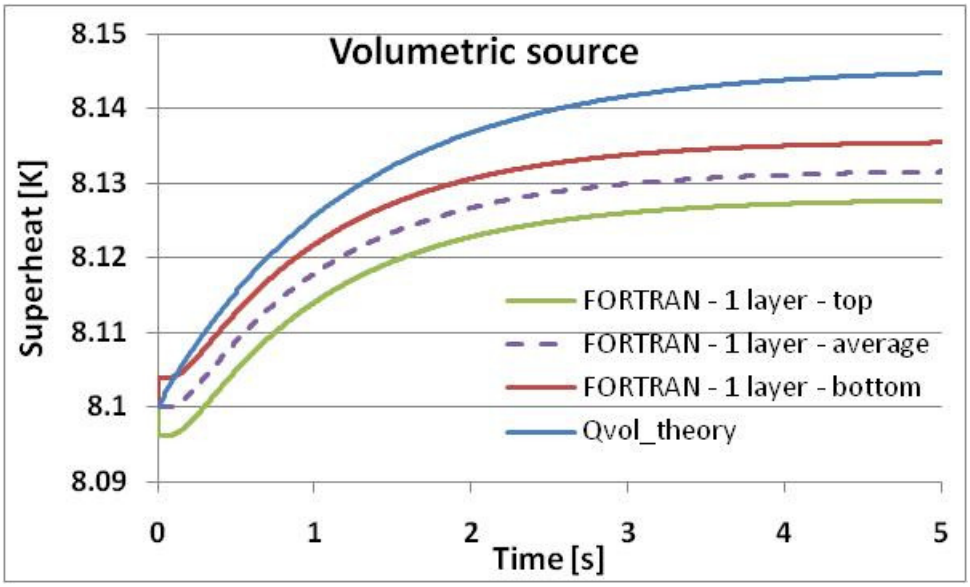

Figure 5-1: Comparison of theoretical and simulation (FORTRAN) results for the superheat temporal variation in the case of volumetric source

The considered case, which assumes 6 vertical layers with no mesh refinement, heat flux applied to the back of the substrate ($\dot{q}_{bottom} = 4.480 \frac{kW}{m^2}$) and natural convection applied to all the cells, will be identified as Vu0.

The temperature drop across the substrate in the vertical direction obtained from FORTRAN simulations assuming 6 vertical layers is ΔT_{trans} = -0.01547 K. It is compared with the theoretical value obtained in the ideal case of steady state temperature in an infinite substrate and imposed heat flux applied to the back surface. According to Equation 5.4, if a heat flux equal to 4.480 $\frac{kW}{m^2}$ is imposed, the theoretical superheat drops to -0.015476 K (under the specified conditions), which is in very good agreement with simulated results.

$$\dot{q} = -k_H \frac{dT}{dz} \quad \Rightarrow \quad \Delta T = -\frac{\dot{q}\Delta z}{k_H} \sim -0.015476K \tag{5.4}$$

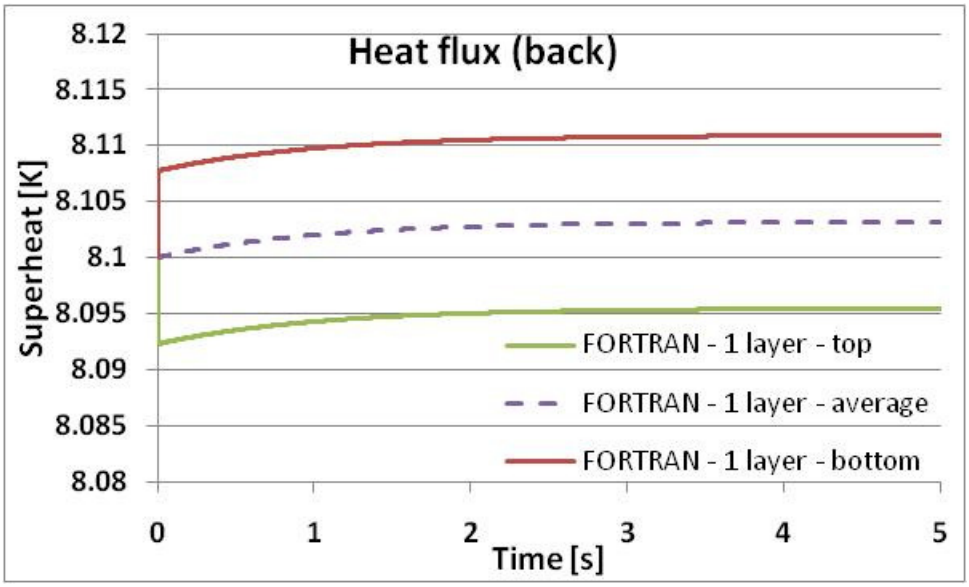

Figure 5-2: Comparison of theoretical and simulation (FORTRAN) results for the superheat temporal variation in the case of heat flux applied to the back

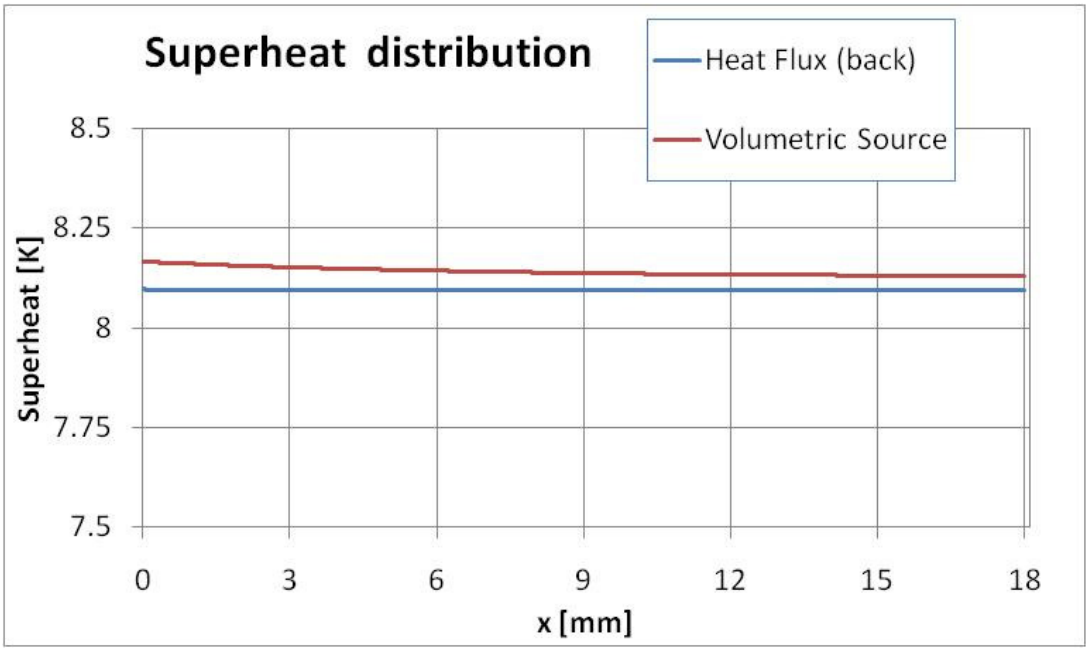

Figure 5-3: Comparison of the heat source effect along a line passing through the centre of the substrate

5.2.2. Verification of the mesh refinement process without boiling

The second test aims to evaluate the correctness of the mesh refinement process. In this case, the sites will be activated regularly when the activation temperature is exceeded, i.e. $T > T_{act}$ = 58.15 °C in this case, corresponding to an activation superheat of ~ 1 K. The heat flux on the top surface will not be locally modified to account for evaporation, but will be maintained at natural convection conditions for all the cells, regardless whether the nucleation site is active and the local distribution of mesh refined occurred or not. The bubble will grow normally, assuming that all the heat flux generated at the contact area together with the contribution at the dome of the bubble will contribute to the evaporated volume. The growth time will be not analysed here. The characteristics of the liquid and substrate are the same described in Section 4.2. Two nucleation standard sites located in the central area of the substrate at a distance equal to 1 mm will be assumed. The case assuming 6 vertical layers with mesh refinement, heat flux applied to the back of the substrate ($\dot{q}_{bottom}$ = 4.480 $\frac{kW}{m^2}$) and natural convection applied to all the cells will be identified as Case Vr0. Superheat results show a very similar behaviour if compared with the case with no mesh refinement (Case Vu0), with a difference in superheat less than $1.0 \cdot 10^{-6}$ and a maximum

error in the heat control variable (Section 3.2.1) lower than 1%. Case Vr0 is also compared with some verification cases aiming to test the capabilities of the code.

The first comparison test (Vr1) evaluates the effect of a different coarse mesh size: w_{xy} was increased from 0.1 mm to 0.2 mm. Superheat results showed very small differences after a simulated time of 0.25 s (error in temperature at the nucleation site lower than $1.0 \cdot 10^{-5}$ K). The error increases with time: the difference may be caused by the not perfect correspondence of the position of the cells in the two cases when the refined cells are introduced.

The second test (Vr2) increases the number of refined cells in the first ring around a nucleation site from 4 to 8. This implies that the dimension of the cells in the angular direction is reduced to half for all refined cells. Analysis of the superheat at the nucleation site shows a very good correspondence between this case and Cases Vr0 and Vr1 with a variable error always lower than $1.0 \cdot 10^{-5}$ K.

The third test (Vr3) introduces three intermediate mesh refinement processes (Section 3.2.3) with fixed cell size. Also in this case, the maximum error in superheat is lower than $1.0 \cdot 10^{-5}$ K.

All the tests show a good stability of the mesh refinement process.

5.2.3. Verification of the mesh refinement process during boiling

Variation of the number of the rings

This section investigates the effect of the number of rings (n_R, and consequently the size of refined cells) on the scaled *HTC*: four different values (n_R = 5, 6, 8, 10) have been evaluated other than the base case (n_R = 7). The simulations have been run in order to find the *HTC* and heat flux matching the experimental bubble growth as for the base case. Figure 5-4 shows that the $HTC_{cl,scal}$ (and consequently the scaled heat flux) has only a very slight dependence on n_R. This result confirms that the bubble growth does not depend on the mesh distribution, but only on the input data, i.e. bubble growth time, bubble departure radius and heat flux conditions. Analysis of the temperature variations at the nucleation site shows only very small variations, mostly during the last stage of the bubble growth, but always smaller than 0.1 K.

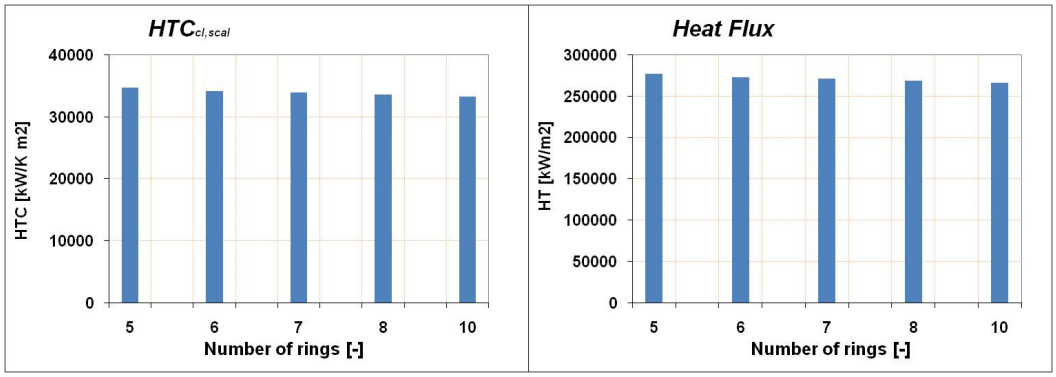

Figure 5-4: Effect of n_R on the $HTC_{cl,scal}$ and Heat Flux

Intermediate refinement process

A similar analysis has been developed to verify the intermediate refinement process: the number of refinement steps in the process was varied from 0 for the base case to 2, 3, 4 and 5. Also in this case it is possible to verify that this process is only slightly affecting the scaled *HTC* and heat flux necessary to guarantee the correct bubble growth time, as shown in Figure 5-5.

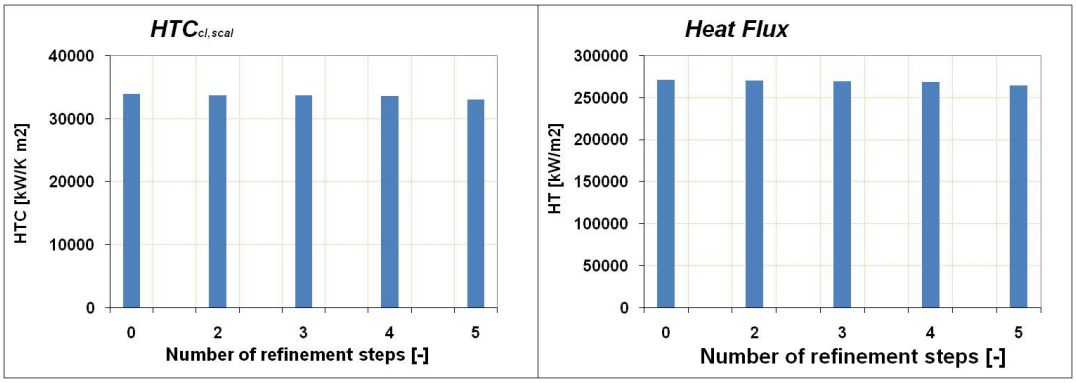

Figure 5-5: Effect of the number of intermediate refinements steps

5.2.4. Summary of the verification process

The verification process was initially developed for the physical problem of a substrate with imposed heat source cooled by natural convection. The results with no mesh modification and with different heat sources showed a good agreement between simulations and theoretical models for the case of an infinite substrate.

Analysis of the effect of the mesh modification process assuming a uniform natural convection heat transfer coefficient on the upper surface, using different mesh size for both coarse and refined cells, showed a good stability of the code. Comparison

of the results with previous results with regular distribution of coarse mesh not modified during the simulations, showed also a very good agreement.

Comparison of the *HTC*, necessary to match the experimental bubble growth defined in the base case, shows only a little dependence on the mesh distribution and refinement process when nucleate boiling occurs.

5.3. Validation of the code

A complete process of Validation of the code would require a consistent amount of experimental data in order to provide a comparison with the numerical model in a wide range of situations. The original aim of validating the code against data of bubble radius histories and superheat variations experimentally produced at the University of Edinburgh has not been completely achieved. Two strong limitations arose during the experiments. Firstly the size of the sensors was too large (0.84x0.84 mm^2) with respect to the bubble size (maximum measured bubble departure diameter smaller than 1.0 mm, so that the maximum contact area could be significantly smaller), as already analysed in Section 4.2. The local superheat variations corresponding to the contact line were then impossible to detect. Secondly, the minimum sensitivity of the sensor (0.5 K), is significantly higher or of the same order of the superheat variations over the measured area and anyway just comparable to local superheat variations obtained during simulations. The validation process will be then limited here to two studies. The first one will focus on the capabilities of the code to reproduce the bubble growth: 5 different cases will be considered, obtained by varying the applied heat flux and determining the resulting wall superheat. The second analysis will develop a long term investigation of the superheat fluctuation of one isolated site at sub-atmospheric conditions.

5.3.1. Bubble growth analysis

For the first part of the validation, the results from five experiments developed at the University of Edinburgh will be analysed, summarised in Table 11. The first three cases (1-3) refer to the third generation test section described in Section 4.2.1, while cases 4 and 5 refer to the second generation. In the first case, the temperature sensors were located on the top surface around the nucleation site, while for the other at the back of the substrate. The input heat flux applied to the back of the substrate was different for each case ranging from 0.46 to 13.4 kW/m^2. This led to variable wall superheat measured by the sensors ranging from 1.4 to 10.1 K. For the second

generation test section, results refer to cavity S3 (compare Section 4.2.1 and Hutter, 2009), while for the third generation all results refer to the artificial cavity S7, shown in Figure 4-1 (b) in Section 4.2. For all the considered cases, neither occurrence of vertical or horizontal coalescence nor activity of the other sites was detected. Significant waiting times were detected only for the cases with low measured superheats, i.e. cases 2 and 3. However, for cases 1-3, only the sites adjacent to S7 were directly monitored visually during the examined period. However, the others were located at such distance from S7 that their effect would not have been relevant. The sites with lower mouth cavity radius (S8-S16, as shown in Figure 4-1 (b) and described in Section 4.2) required higher activation superheat and were not generally showing any activity. Vertical bubble coalescence was not simulated here: however, recent studies from Hutter et al. (2009) showed that this phenomenon may affect the bubble volume at departure, which would imply a variation in the final evaporation heat as input datum in simulations. Would this phenomenon found to be relevant on the heat transfer on the upper surface, a new model simulating it should be implemented in the future. The measured bubble departure radii (always very small) and growth times (averaged over 8 bubble growths for cases 1 to 3 and over 3 growths for cases 4 and 5) were used as main input data for simulations and then compared with the measured bubble growth histories. The measured data for the bubble growths and their average values for the different cases are shown in Figure 5-6.

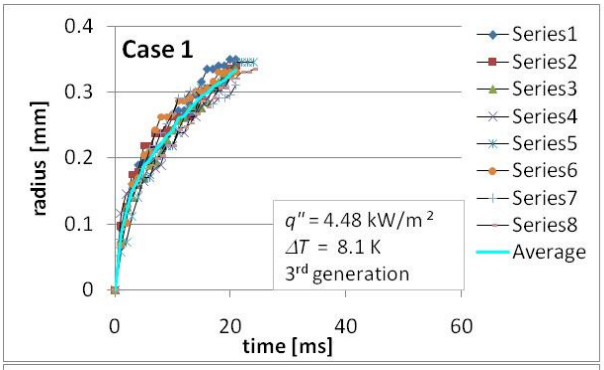

Table 11: Summary of experimental results

Case	*Test section*	q'' [kW/m^2]	ΔT_W [K]	f_{enh}	r_{bd} [mm]	τ_g [ms]
1	3rd	4.48	8.1	1.16	0.33	21.0
2	3rd	2.36	4.8	1.14	0.22	18.0
3	3rd	0.46	1.4	0.98	0.19	27.0
4	2nd	0.85	1.4	1.97	0.16	59.0
5	2nd	13.4	10.1	2.66	0.35	24.0

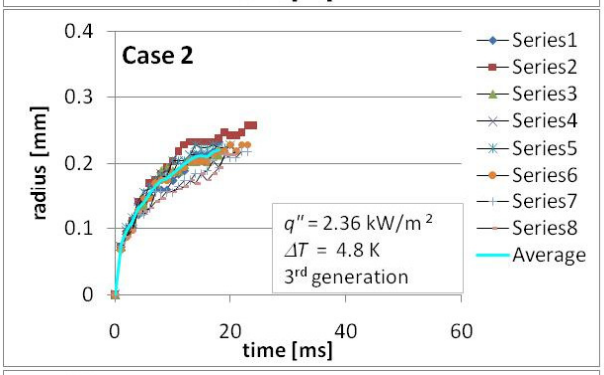

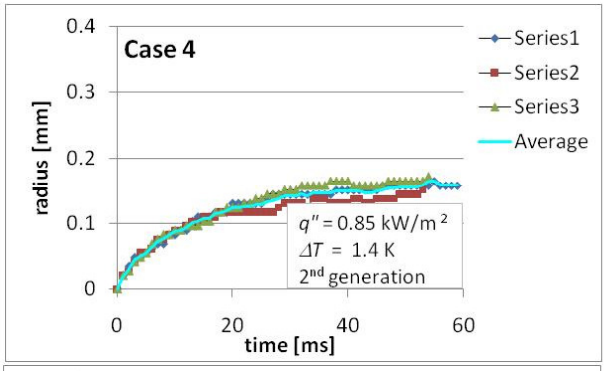

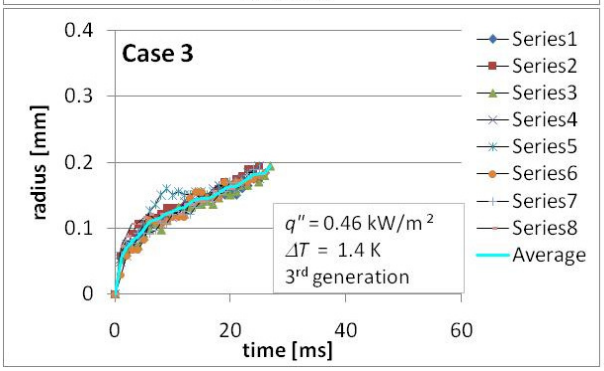

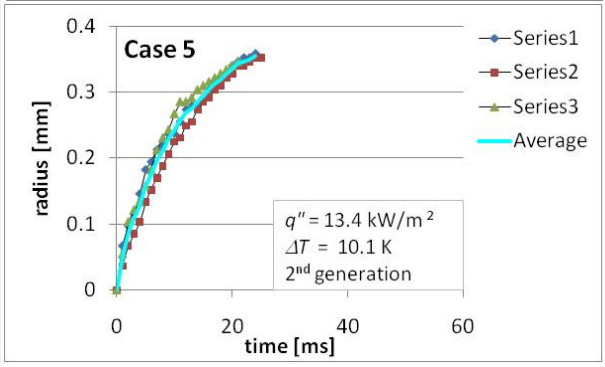

Figure 5-6: Experimental bubble growths

The comparisons between the experimental and simulated dimensionless bubble growth for the five cases under the two conditions of f_{decr} = 0.6 and 0.9 are respectively shown in Figure 5-7 (a) and (b). The input data for the liquid and substrate properties were the same of the base case, apart from the natural convection enhancement factor f_{enh}, modified in each case in order to match the experimental superheat. The time has been made dimensionless by dividing it by the average growth time (t/t_g), while the dimensionless bubble radius has been obtained by dividing the bubble radius by the bubble departure radius (r_b/r_{bd}). The figure shows that the code is able to reproduce well the bubble growth histories under different conditions and that all the bubbles growing similarly if the dimensionless values are considered. For f_{decr} = 0.6, the simulated bubble growth rate is less uniform, and partially disagree with the experimental cases apart

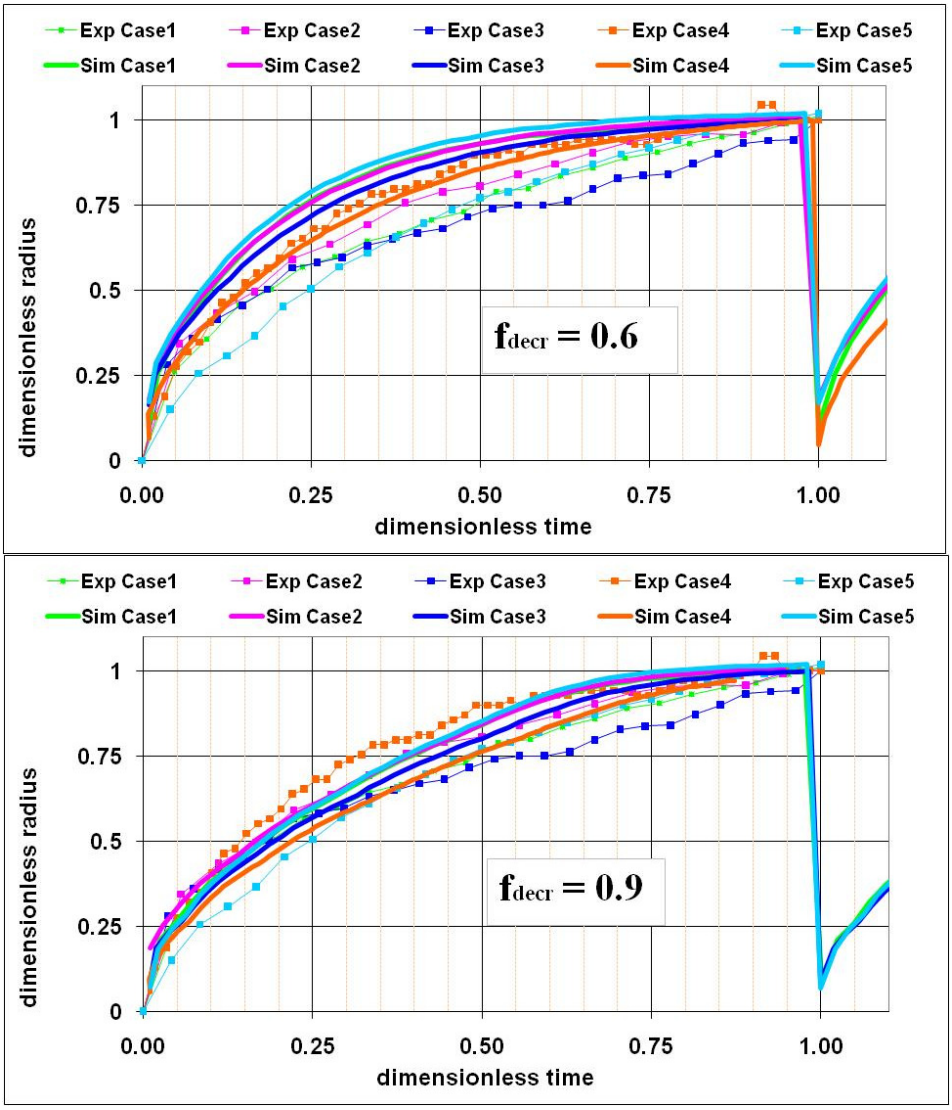

Figure 5-7: Comparison of experimental and simulated dimensionless bubble growths. a) f_{decr} = 0.6; b) f_{decr} = 0.9

from case 4. By contrast, f_{decr} = 0.9 seems to generally have a better agreement. For case 3 none of the two decrease factors were able to reproduce the bubble growth rate during the final stage of the growth, although for f_{decr} = 0.9 the first stage of the bubble growth is similar. However, the impossibility to validate the code against the superheat histories makes this process incomplete. From the analysis of long term bubble growth histories, it must be pointed out that significantly long waiting times have been detected for the cases with applied low heat fluxes (and consequently low wall superheat), cases 3 and 4. The code was unable to reproduce any waiting time, due to the fact that during the simulations the superheat at the top surface was always higher than the activation superheat (depending in simulations on the cavity mouth radius and pressure of the liquid). This could suggest that the condition that the activation depends exclusively on the punctual superheat values (as it is for simulations) could be restrictive. Also, the waiting time can be attributed to hydro-dynamic effects in the liquid side, as for instance agitation and wake effects after the departure of the bubble. A new model for the variation of the liquid thermal layer thickness could be introduced in the code in order to take into account the liquid superheat variation close to the heated wall and the induced waiting time. For the cases with high applied heat fluxes no waiting time has been experimentally detected. In both cases 3 and 4 the bubble growth during the initial phase is smaller than the other cases, and the bubble departure radius is significantly smaller. Moreover, for case 4, the growth time is much longer than in all the other cases (two or three times).

More experimental data are needed to complete the validation process and to identify (if indeed it does exist) a dependence between bubble departure radius, bubble growth time and superheat.

The analysis of the tuned $HTC_{cl,scal}$ and Heat Flux needed to match the experimental bubble growth time and bubble departure radius, Figure 5-8, do not show any apparent correlation between the imposed heat flux $\dot{q}$ and $HTC_{cl,scal}$. However, the number of data is too limited to draw any conclusion.

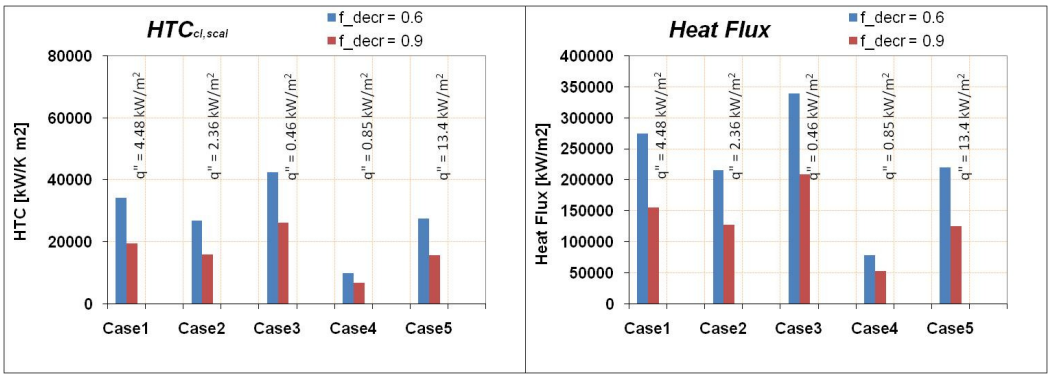

Figure 5-8: $HTC_{cl,scal}$ and Heat Flux derived from simulations for the validations cases

5.3.2. Comparison of the base case: bubble growth and superheat variations

A combined analysis of the temperature history (detected by the sensors) and the bubble radius history (via camera recording) was provided for Case 1. The applied heat flux was 4.480 $\frac{kW}{m^2}$ with a measured superheat of 8.1 K, average bubble departure radius (r_{bd}) equal to 0.33 mm and growth time (t_g) of 21 ms. The properties for liquid and substrate and the input data are the same assumed for the base case (Section 4.2). Also in this case, two contact angle decrease fractions were investigated, f_{decr} = 0.6 and 0.9.

The comparison of the simulated and experimental bubble radius depicted in Figure 5-9 demonstrates that the exact growth time period can be reproduced by both simulations, although the bubble growth rate for f_{decr} = 0.6 is significantly different than for experiments, with a faster simulated initial growth and a slower final phase. For f_{decr} = 0.9 the agreement has much improved, although during the last phase of the bubble growth the bubble growth rate is still different. This would suggest that the simulation with detachment process starting almost at the end of the bubble growth (f_{decr} = 0.9) is the most likely, at least for these experimental conditions.

The analysis of the simulated superheat histories over an area reproducing the sensor area (ΔT_{SEN}) shows a small underestimate with respect to the experimental data with a difference of ~ 0.1 K, anyway smaller than the sensitivity of the sensor itself (±0.5 K). The difference can be explained if considered that the enhancement factor for natural convection (f_{enh} = 1.16) has been imposed to match the measured superheat below a growing bubble. However, as mentioned before in Section 4.2.5, the superheat difference between the values in the natural convection area far from the bubble and below a growing bubble (as measured by the sensor) can be larger than 0.05 K.

The experimental superheat variations are significantly larger than for simulations, although always smaller than the sensitivity of the sensors. Moreover, the variations seem randomly distributed and not related to the different stages of the bubble growth. This makes it impossible to determine the activation and deactivation times only on the base of the temperature histories (i.e. independently on visual observation). The simulated variation is limited to less than ±0.04 K during a single bubble growth.

This case represents a very good match between experimental and simulation results. It proves that the code is able to reproduce the experimental bubble growth and superheat. Still, it strongly depends on experimental data used as input data. The dependence could be partially removed if a larger amount of experimental data were available.

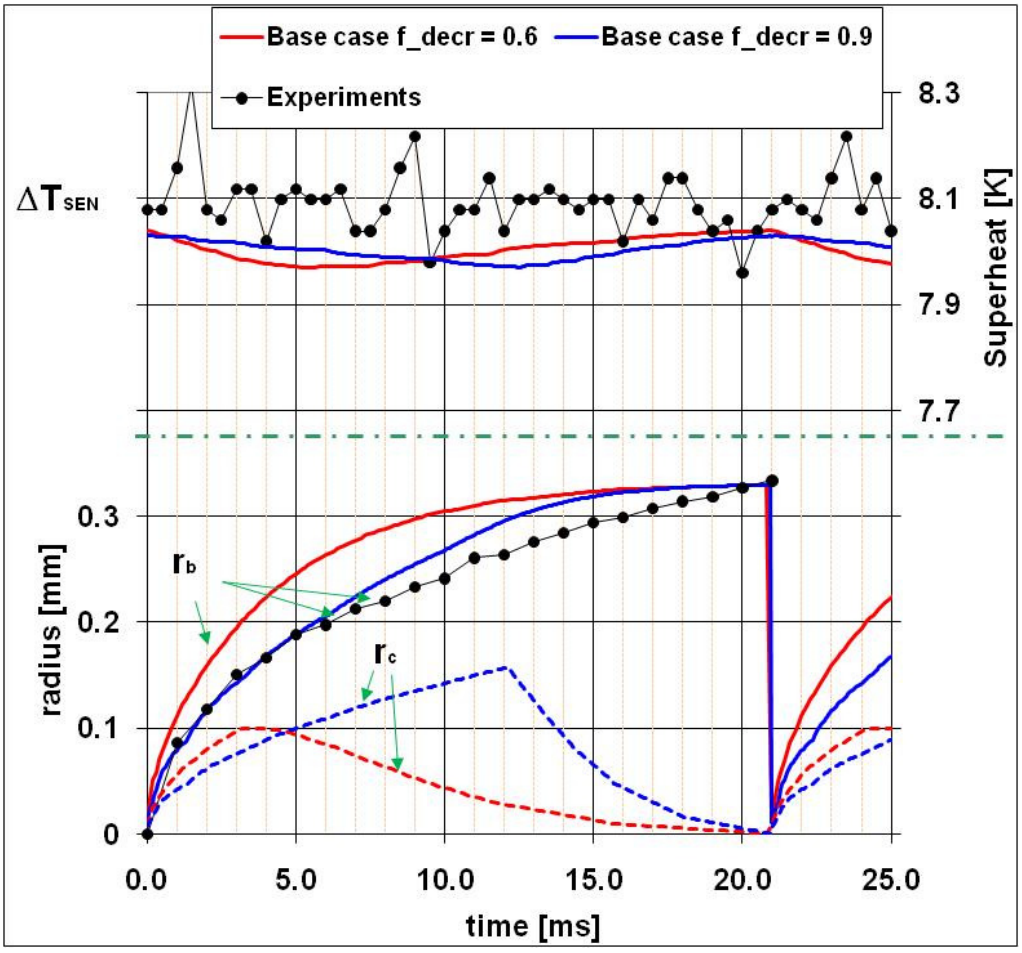

Figure 5-9: Validation for the base case

5.3.3. Long term superheat analysis

The second part of the validation compares numerical data with experimental results developed using the third generation test section at sub-atmospheric pressure

conditions, in order to obtain larger bubble departure radii and consequent larger contact areas. The final aim was to produce larger superheat variations, able to be clearly detected by the sensors. Analysis of the superheat response of the sensor located at S7 over a long period, approximately 4 s (with applied heat flux of 8.6 kW/m^2), is shown in Figure 5-10. The pressure was reduced to 0.0463 MPa, leading to a bubble departure radius r_{bd} ~ 0.45 mm (significantly larger than in the base case) and t_g ~ 10 ms. The uncertainty terms for bubble departure radius and superheat were set here equal to ±10%, in order to reproduce the uncertainty in bubble departure radius and activation superheat.

The cavity experimentally showed large-period intermittent irregularities in activity, which were not predicted by the code. However, the code could be forced to artificially reproduce them by manually changing the activation temperature during the simulations. During the experiments, S7 was the only site over the monitored area to become active; however, should the sites outside the monitored area have been active, their effect would have been negligible due to the large distance.

Two cases were simulated here; one assuming only one potential active site, and one with two potential active sites 2 mm apart (as for S7 and S8 in the third generation test section), with the same imposed activity periods. For both cases, the activation superheat has been assumed equal to 2.14 K (according to Equation 3.14). Comparison

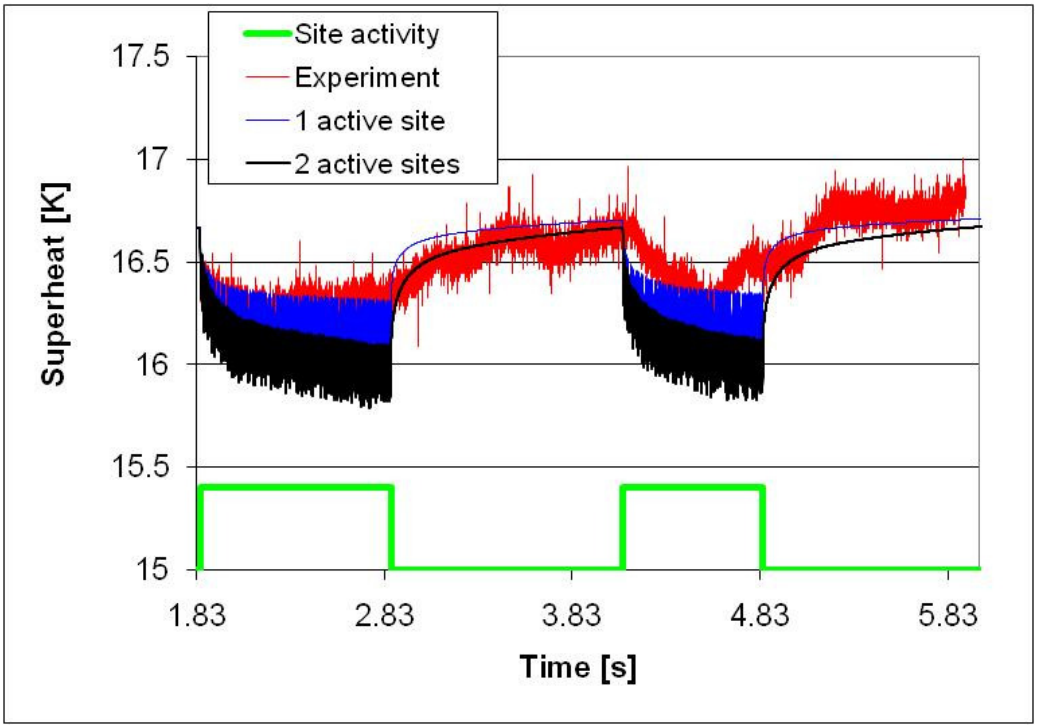

Figure 5-10: Long term superheat variations

of the numerical and experimental results (Figure 5-10) shows a general good agreement for both cases, although variations in the case of only 1 active nucleation site are more similar to the experimental results. For the case with two active nucleation sites, the combined cooling effect of the sites significantly reduced the wall superheat during the activity periods. When the site becomes inactive, the variations in the simulations are faster and larger than in experiments. This effect could be related to hydro-dynamic effects in the liquid that are not modelled by the code or to possible hysteresis phenomena, which could also cause the inhibition of the site after long period of regular activity.

5.3.4. Validation against experiments on thin metal foils

The last part of the validation process is carried out against experimental data on thin metal foils immersed in water developed at the University of Ljubljana by the team led by Prof. Golobič, who has also actively collaborated to this PhD project. Two series of results will be analysed, the first on Titanium, 25 µm thick, with an applied heat flux of 50 kW/m^2 (Golobič et al., 2006) and the second on Platinum, 6 µm thick, with an applied heat flux of 100 kW/m^2 (Golobič et al., 2009). In both cases, the temperature variations were measured on the back of the foil with an infrared (IR) camera.

Experiments on Titanium, $\dot{q} = 50 \frac{kW}{m^2}$

The experimental results refer to the growth of an isolated bubble on Titanium (25 µm thick) refrigerated with water at saturation conditions (T_{sat} = 100 °C, p = 1 atm) with applied heat flux of 50 kW/m^2. A more detailed description of the experimental setup and of the properties of the foil and liquid are provided in Golobič et al. (2006). It must be noted that the characteristics of the substrate may be subject to uncertainties due to their sensibility to its exact composition, leading to a possible over-estimate of the input heat flux, Kenning et al. (2009). However, the input data used during numerical simulations are listed in Table 12.

The values explicitly provided in Golobič et al. (2006) related to the bubble growth, heat transfer coefficients and heat flux distributions were only the time when the bubble reaches its maximum contact area radius (t = 6 ms) and the departure time (t = 18 ms). However, the contact area radii (r_c) and the superheat at the nucleation site (ΔT_{NS}, in the centre of the contact area) at different time steps were obtained from the

graph showing the analysis of the temperature distribution along a line passing through the centre of the site. The bubble radius values (r_b) at different time steps were obtained from analysis of the bubble growth sequence, as average of the vertical and horizontal dimensions, when the bubble appeared to be not spherical. Those data are listed in Table 13: however, their values may be subject to errors or uncertainties due to the quality of the figures themselves.

Table 12: Input data for thin metal foil validation (Golobič et al., 2006)

Substrate [Titanium] 16.1 x 21.9 mm²		δ_H 25 µm	ρ_H 4500 $\frac{kg}{m^3}$	c_H 523 $\frac{J}{kgK}$	k_H 21.9 $\frac{W}{mK}$	$\dot{q}$ = 50 $\frac{kW}{m^2}$
Liquid [Water] 1 Atm, 100 °C		ρ_v 0.5974 $\frac{kg}{m^3}$	ρ_L 958 $\frac{kg}{m^3}$	c_L 4216 $\frac{J}{kgK}$	k_L 0.677 $\frac{W}{mK}$	H_{fg} 2257300 $\frac{J}{kg}$
Bubble growth and Heat Transfer	**Exper**	t_g 18.0 ms	r_{bd} 2.665 mm	ΔT_{act} 15.5 K	f_{decr} 0.6	
	Numer	HT model *ML*	HTC_{max} 54 $\frac{kW}{m^2}$	f_D 1.84	φ_0 45°	Natural convection Eq. 3.7, f_{enh} = 1.42
Numerical data		Δt 1.0 µs	w_{xy} 0.5 mm	n_{vL} 2	n_R 14	

Table 13: Bubble growth data and superheat values at the nucleation site (Golobič et al., 2006)

t [ms]	0	1	2	4	6	10	14	18
r_b [mm]	0	~ 0.40	~ 1.17	~ 1.63	~ 1.90	~ 2.17	~ 2.44	~ 2.67
r_c [mm]	0	~ 0.26	~ 0.76	~ 1.14	~ 1.40	~ 1.34	~ 0.60	~ 0
ΔT_{NS} [K]	~ 12.5	~ 7.5	~ 4.0	~ 2.3	~ 2.2	~ 2.2	~ 2.5	~ 4.8
HTC_{max} [kW/m²]	~ 5	~ 38	~ 54	~ 30	NA	~ 25	~ 14	~ 5

The approximate values for the initial apparent contact angle, φ_0 = 45°, and the angle decrease factor, f_{decr} = 0.6, were derived from the bubble growth sequence. For both the bubble contact radius and the apparent contact angle, the values are subjected

to strong uncertainties in getting them from the images. Moreover, for the apparent contact angle, further simplifications due to the simplified time-dependence and the assumption of having a perfect truncated sphere were introduced. The activation superheat, ΔT_{act} = 15.5 K, is the same used in simulations developed by Golobič et al. (2004) referring to similar experiments on metal foils in water (Kenning and Yan, 1996, for a stainless steel plate, 125 µm thick). Similarly, the correlation for heat transfer in the natural convection area is the one provided in Equation 3.7 from Golobič et al. (2004). The enhancing factor due to boiling used here, f_{enh} = 1.42, has been derived in order to maintain a superheat value in the region unaffected by boiling outside the contact area (at a distance from the nucleation centre of ~ 2.5 mm) equal to ~ 17 K. The heat transfer model at the contact area used in this case is the micro-layer model (*ML*, see Section 3.2.4), assuming a central peak at the nucleation site. The peak values (HTC_{max}) during the bubble growth, supposed to occur at the nucleation site, were imposed and not tuned (as it was in the simulations for Silicon with FC-72) according to the 2-dimensional heat transfer coefficient distributions also provided in Golobič et al. (2006) and to additional data provided by private correspondence with Prof. Golobič and in Kenning et al. (2009). Analysis of these values and comparison with similar experiments described in Golobič et al. (2009) showed that the peak value is not constant during the bubble growth. An increasing-decreasing history can be observed

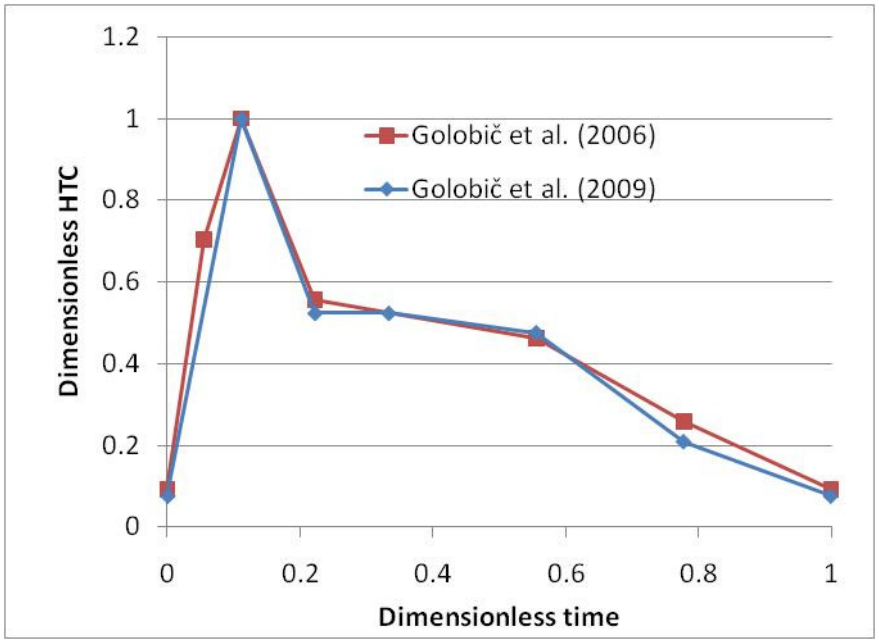

Figure 5-11: Dimensionless HTC_{max} versus dimensionless time

from analysis of the dimensionless heat transfer coefficient versus dimensionless time, scaled respectively to the maximum HTC_{max} and to the growth time and shown for the two cases (Golobič et al., 2006 and 2009) in Figure 5-11. It is interesting to note the strong similarity between the cases, despite the differences in conditions. For the case with Titanium considered here, the maximum (occurring at a dimensionless time ~ 0.1) was equal to 54 kW/m^2. During simulations, an increase was imposed to occur in the early stage of the bubble growth (i.e. when $r_b(t) < 0.5\, f_{decr}\, r_{bd}$), followed by a decrease until departure, as shown in Figure 5-12.

A sensitivity analysis was also developed in this case to evaluate the mutual influence of the heat contributions at the dome and at the base of the bubble, showing that the main contribution was predicted to be attributable to the evaporation at the dome. For this reason, its influence, represented by f_D, has been tuned during this simulations (in order to match the experimental values for bubble departure radius and growth time), and its value found equal to ~ 1.84. Moreover, 9 nucleation sites were simulated in total, distributed with a 3x3 square arrangement with distance between adjacent sites of 5 mm (equal to the length of the area observed in the experiments), in

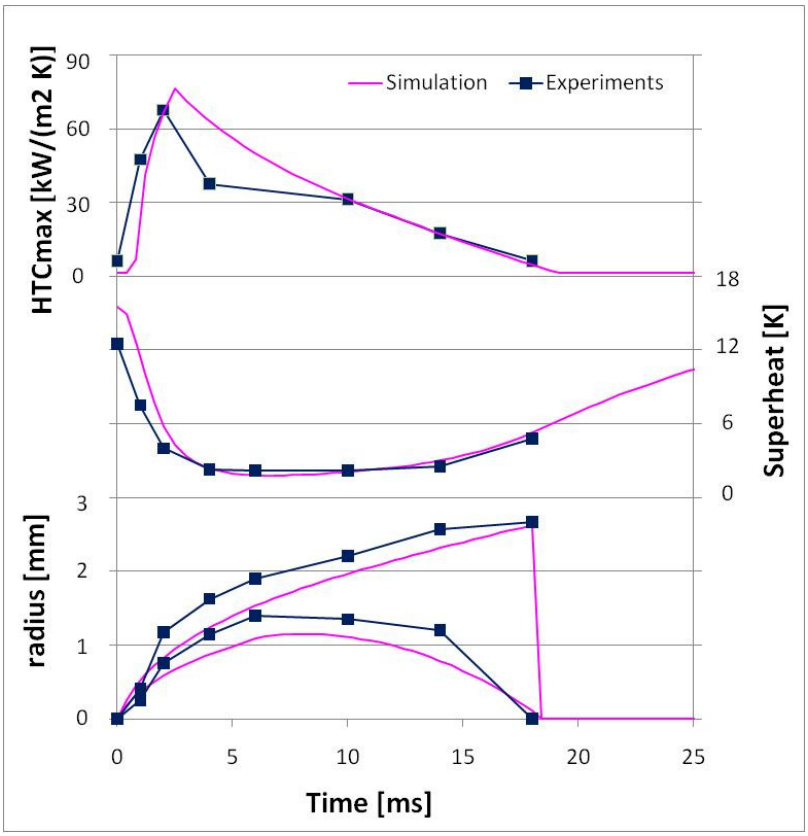

Figure 5-12: Comparison between experimental (Golobič et al., 2006) and simulation results for bubble and contact radii, superheat and HTC_{max}

order to reduce the edge effects. The results shown in the following discussion refer to the nucleation site located in the centre of the plate (x = 20 mm, y = 18 mm). The choice of the mesh size for unrefined cells (w_{xy} = 0.5 mm, significantly larger than the case with Silicon and FC-72, where w_{xy} = 0.1 mm) was due to the larger bubble departure radius in this case. The time step Δt was increased accordingly. The number of vertical layer n_{vL} was reduced to 2 due to the very small thickness of the foil.

The results for the bubble radius, contact radius, superheat at the nucleation site and HTC_{max} histories are shown in Figure 5-12 (the values for experimental data are those listed in Table 13). The superheat history shows a very good agreement between experimental and numerical data during the bubble growth, confirming that the code is able to predict the superheat variations if the correct heat transfer conditions are applied (although a not perfect agreement is shown for HTC_{max} during the intermediate stage of the bubble growth). Analysis of the simulated contact and bubble radii shows a general underestimation with respect to the experimental values apart during the very early and final stages. The simulated contribution at the dome of the bubble (calculated at departure) was found to be approximately 20 times the one at the base of the bubble. This behaviour significantly differs from what was found for simulations with Silicon and FC-72, as described in Section 4.2, where the heat contribution at the dome was significantly smaller than at the base. However, in both cases it was possible to conclude that an accurate model for the evaporation at the dome is necessary, although for different reasons. An increase of the dome contribution to f_D = 2 led to significantly shorter growth time (~ 15 ms). A comparison of the bubble growth from visual observation (pictures) and simulation (violet line) profiles is shown in Figure 5-13 for different time steps. This provides a visual confirmation that the code is able to reproduce the bubble growth, although with the differences mentioned above.

Comparison at departure is not easy since the simulated bubble is still very close to the wall, while for experiments it has already slightly lifted. It must be also highlighted that during the last stage of the bubble growth in experiments the bubble seemed to assume a flattened shape in the vertical direction (although it could be only an optical effect) that the code could not reproduce.

An analysis of the superheat distribution along a line passing through the centre of the contact area at different time steps is shown in Figure 5-14, together with the contact area radii, for both experiments (left side) and simulations (right side). The underestimation of the contact radii in simulations leads to an area of influence of

thermal variations in the substrate significantly smaller than for experiments. Also, the simulations were not able to reproduce the small peak in superheat in the region immediately outside the influence area (x ~ 18.4 mm) during the initial stage of the bubble growth (t = 0, 1, 2 ms), probably due in experiments to hydro-dynamic phenomena that are not simulated by the code. For t = 18 ms, the simulated superheat has a coarser distribution, due to the deactivation of the site and replacement of the refined with coarse cells. It must be specified that the superheat distribution in the experiments was not symmetrical with respect to the nucleation site. The superheat measured in the experiments in the area outside the contact area unaffected by the boiling (at ~ 2 mm from the nucleation site) was slightly smaller (~ 1 K less) than in simulations. However, this did not significantly affect the distribution in the central area.

The comparison between the experimental and simulation *HTC* distributions along a line passing through the nucleation site is presented in Figure 5-15. This shows the increasing-decreasing behaviour for the peak at the nucleation site. A good agreement is shown also in this comparison although the code is not able to reproduce the behaviour of the experimental flatter heat transfer coefficient distribution for t = 4 ms, with a less clear identification of the central peak with respect to the other time steps. This distribution will be seen in the following section (for Platinum, 6 μm thick) to be characteristic of the intermediate stage of the bubble growth. A comparison of the heat

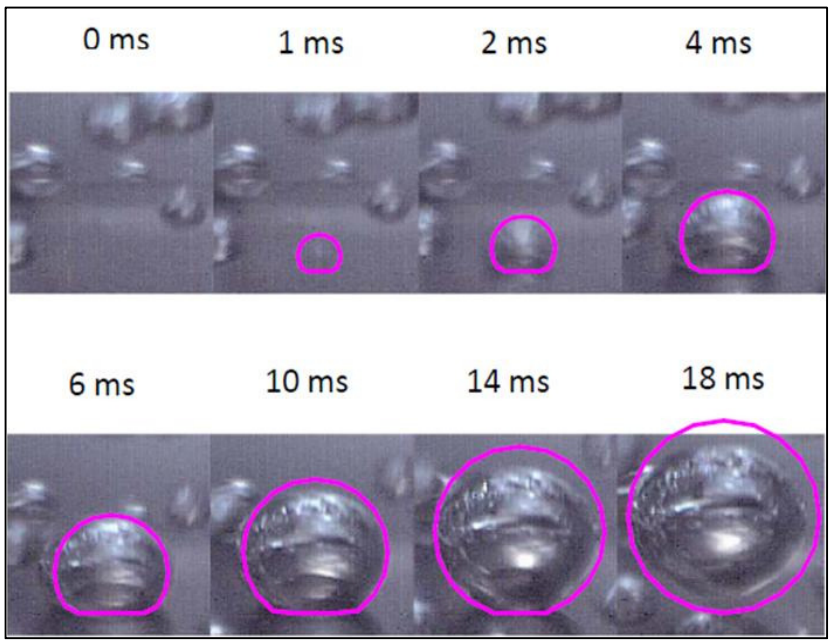

Figure 5-13: Comparison of experimental (Golobič et al., 2006) and simulation results for a bubble growing on a thin metal foil

flux distributions at the upper surface is shown in Figure 5-16. This figure confirms that the code is able, under the imposition of the correct heat transfer coefficient distribution, to predict the experimental heat flux distribution along a line, although the underestimation of the simulated contact area radii (on the top right of the figure) leads to an influence area less that is spread than in experiments. The heat flux distributions present three characteristic trends. (1) During the initial stage of the bubble growth (t = 1 ms), the heat flux has a maximum in proximity of the nucleation centre, due to the high heat transfer coefficient in this area combined with the high superheat values. After that, (2) the drop in superheat in the central area causes a drop in heat flux, while the distribution assumes a crater shape with its maximum at the periphery of the contact area itself, as clearly visible for example for t = 2 and 4 ms. At the same time, the heat flux quickly drops to smaller values, and during the final stage (3) it is reduced to values of the same order of magnitude as the unaffected natural convection area. A circular depression at the periphery of the contact area or immediately outside it where the values are even smaller ($t \geq 10$ ms for experiments and $t \geq 14$ ms for simulations) may be also noted.

This comparisons show that, despite the major simplifications in the simulations to reduce computing time in studies of many sites, the agreement between experimental and numerical results for the local wall superheat during the bubble growth is very impressive.

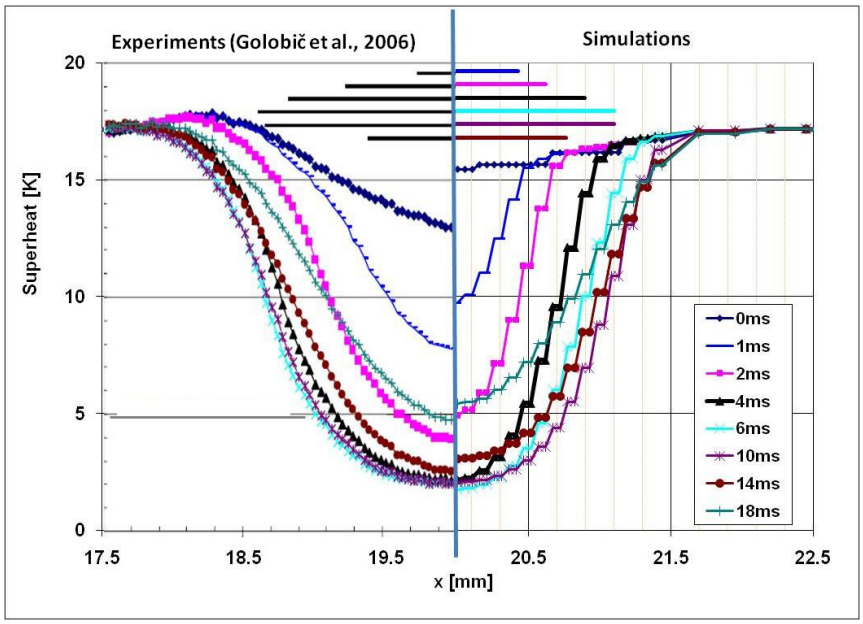

Figure 5-14: Superheat distribution along a line. Comparison of experimental and simulations for Titanium (25 µm)

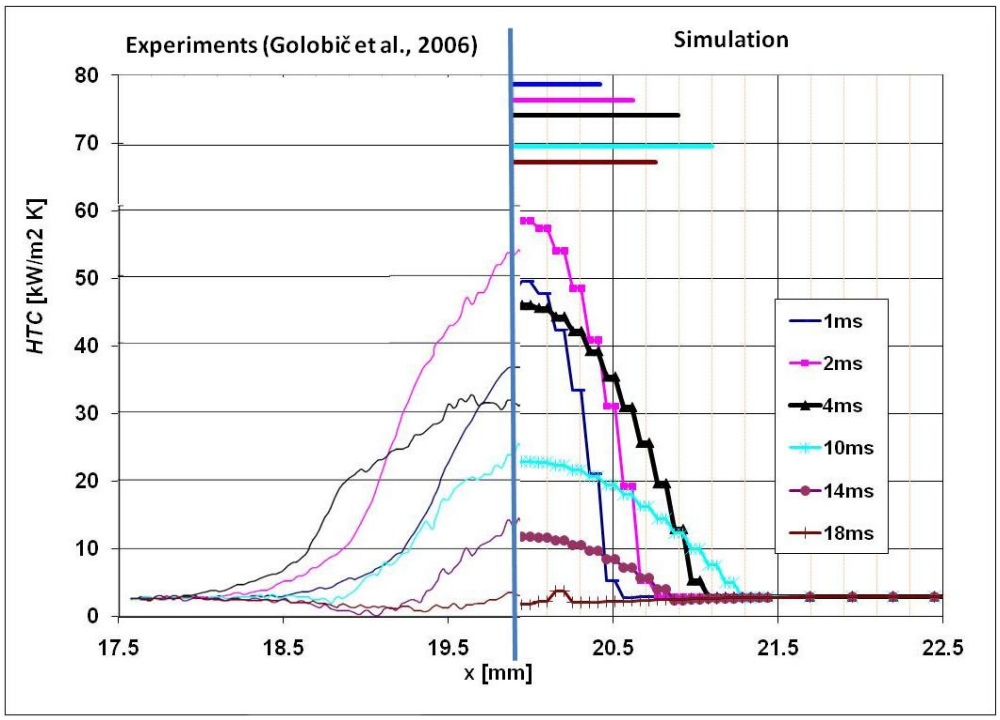

Figure 5-15: *HTC* distribution along a line passing through the nucleation site for Titanium (25 µm)

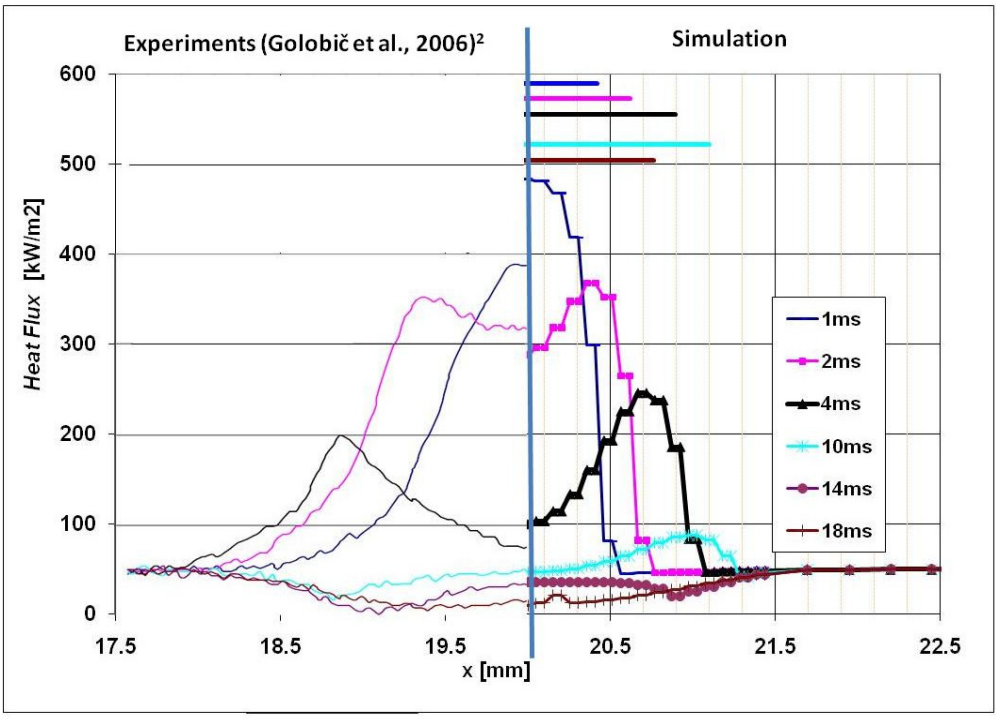

Figure 5-16: Heat flux distribution along a line passing through the nucleation site for Titanium (25 µm)

Experiments on Platinum, $\dot{q} = 100 \frac{kW}{m^2}$

The second set of validation data comes from experimental results using Platinum (6 µm thick) cooled by water at saturation conditions (T_{sat} = 100 °C, p = 1 atm) with applied heat flux of 100 kW/m^2, as described in Golobič et al. (2009). The input data used in the numerical simulations which differ from the previous case are listed in Table 14. In this case, only the contact and bubble radii when the bubble reaches its maximum contact area and size (being respectively 0.775 and 1.1 mm), were specified as experimental results. The growing bubble was intermittently obscured by other bubbles so a sequence of images was not available in this case. The bubble departed 9 ms after nucleation. A sequence of the bubble growth was not available in this case. The superheat and HTC_{max} are extracted from the distributions along a diametric line. Asymmetry in the superheat distributions due to temperature gradient present at the time of nucleation had little effect on the symmetry of the heat flux and heat transfer coefficient distributions. The data are listed in Table 15. The 9 simulated sites were located in this case at a smaller distance (2.25 mm) with respect to the previous case, and f_{enh} has been increased to take into account the higher heat flux. However, the central site is still located in the same position as before.

Table 14: Input data for thin metal foil validation (Golobič et al., 2009)

Substrate [Platinum] 16.1 x 21.9 mm^2		δ_H 6 µm	ρ_H 21400 $\frac{kg}{m^3}$	c_H 133 $\frac{J}{kgK}$	k_H 70 $\frac{W}{mK}$	$\dot{q} = 100 \frac{kW}{m^2}$
Bubble growth and Heat Transfer	**Exper**	t_g 9.0 ms	r_{bd} 1.1 mm	ΔT_{act} 15.5 K	f_{decr} 0.6	
	Numer	HT model *ML*	HTC_{max} 105 $\frac{kW}{m^2}$	f_D 0.97	φ_0 45°	Natural convection Eq. 3.7, f_{enh} = 2.84
Numerical data		Δt 0.1 µs	w_{xy} 0.2 mm	n_{vL} 2	n_R 14	

Table 15: Bubble growth data and superheat values at the nucleation site (Golobič et al., 2009)

t [ms]	0	1	2	3	5	7	9
r_b [mm]	0		~ 1.1				~ 1.1
r_c [mm]	0		~ 0.775				0
ΔT_{NS} [K]	~ 16	~ 2	~ 2	~ 2	~ 2	~ 4	~ 7
HTC_{max} [kW/m^2]	~ 8	~ 105	~ 55	~ 55	~ 50	~ 22	~ 8

The comparison between experiments and simulations for the superheat at the centre, HTC_{max} and contact and bubble radii are shown in Figure 5-17. As in the previous case, the superheat agreement is good, apart from the last stage of bubble growth but the assumed variation of HTC_{max} does match the measured heat transfer coefficient during the intermediate stage of bubble growth. Also in this case, the superheat agreement is good, except during the last stage of the bubble growth, although the HTC_{max} is not able to properly simulate the measured heat transfer coefficient during the intermediate stage of the bubble growth. Tuning of the dome contribution (carried out in the same way as for the platinum foil, i.e. on the basis of the experimental values of bubble departure radius and growth time) led to a dome contribution factor f_D ~ 0.97,

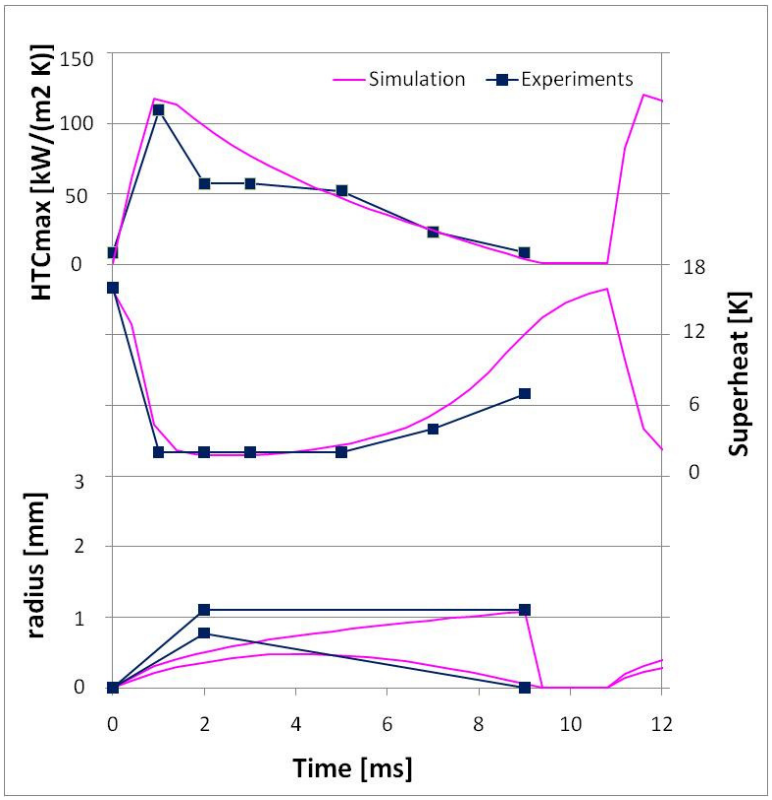

Figure 5-17: Comparison between experimental (Golobič et al., 2009) and simulation results for bubble and contact radii, superheat and HTC_{max} for platinum (6 µm)

approximately half than in the previous case. Comparison of the bubble growth shows a poorer agreement, probably due to the initial quick increase of the bubble radius that the code is not able to reproduce. In addition, there is an important problem connected to the waiting time in this case: the experimental results showed that the nucleation site was inactive for approximately 40 ms, while the predicted value from simulation was much shorter (less than 2 ms). The difference may be due to hydro-dynamic phenomena on the liquid side that the code does not take into account or variability in the activation conditions for this particular site. Further experimental investigation should be undertaken. Would this phenomenon be found to be relevant, an improvement of the code to take into account a heat transfer mechanism different from pure natural convection when the bubble departs should be introduced.

The comparisons of superheat, *HTC* and heat flux distributions along a line passing through the nucleation site are shown respectively in Figure 5-18, Figure 5-19 and Figure 5-20. The figures show that the radius of the area influenced by the bubble is considerably larger than the maximum radius of the contact line reported in the experiments. This cannot be reproduced by the small area of enhancement currently assumed in the simulation. In the experiments, this leads to an area where the superheat is approximately uniform (for instance for t = 3 ms, for a distance from the nucleation

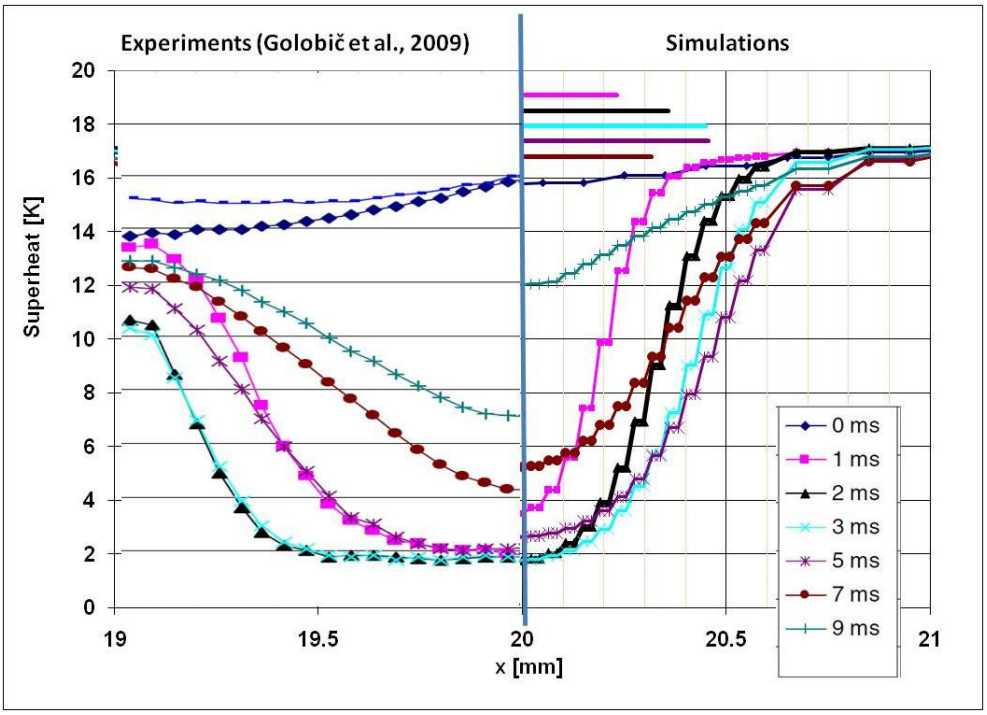

Figure 5-18: Superheat distribution along a line. Comparison of experimental and simulations for Platinum (6 µm)

site less than 0.5 mm) and equal to ~ 2 K. The simulations on the contrary predict a central depression as for the Titanium foil. Regarding the *HTC* and heat flux distributions, the agreement is still qualitatively good, but poorer than for Titanium. In particular, for the initial distribution of heat flux the central peak of the experiments is not predicted for t = 1 ms. Instead, a crater distribution with much smaller maximum value occurs. However, the simulated distribution was much more similar to experiments (with a central peak maximum) for t = 0.5 ms. This may be fortuitous because the method of processing the experimental data acquired at 1 kHz is not accurate at very short times. It can be also noted in Figure 5-19 that the *HTC* has a plateau during the intermediate stage of the bubble growth (t = 2, 3 and partially 5 ms): during this period, the distribution is almost constant.

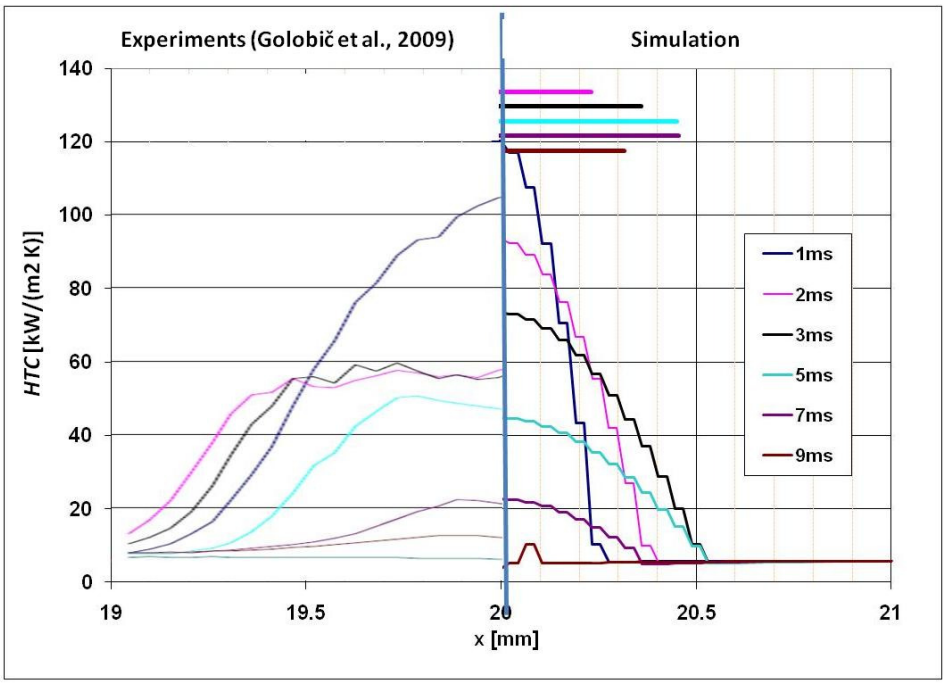

Figure 5-19: *HTC* distribution along a line passing through the nucleation site for Platinum (6 µm)

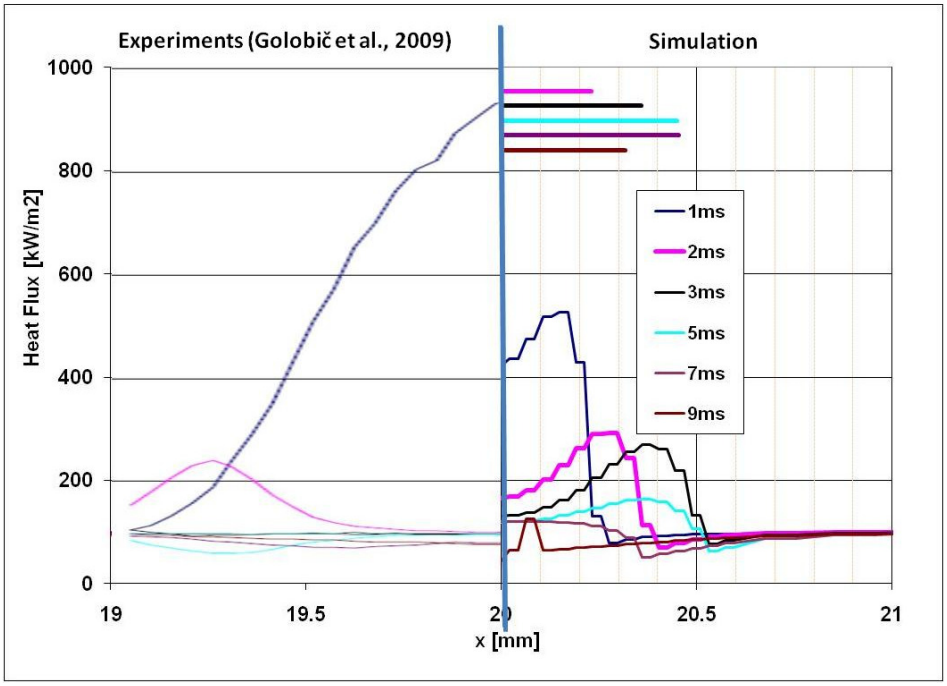

Figure 5-20: Heat flux Heat flux distribution along a line passing through the nucleation site for Titanium (25 µm)

5.4.Summary

The code has been shown to be able to provide the physical answer requested by the user in simple cases of natural convection without boiling during the verification process. In absence of numerical instruments to verify the code during boiling, the numerical results have been compared with experimental results for cases of Silicon immersed in FC-72 and of metal foils (titanium and platinum) immersed in water. For the validation process for silicon in FC-72, the code has been shown to be able to well reproduce the bubble growth at an isolated site for silicon on FC-72 at variable heat fluxes. The experimental average superheat could be also matched, although the correlations used to evaluate the importance of the natural convection in the area outside the bubble contact area were modified. However, analysis of long term superheat variations for an isolated nucleation site showed that the code is able to well reproduce the transient superheat variations when the site switches from a period of regular activity to a period of inhibition and vice versa, although the physical reasons of this phenomenon have been not understood. For this reason, the activity and inactivity periods have been forcedly imposed during the simulations.

Validation of the code against results of bubble growing on thin metal foils showed that the code can reproduce very well the bubble growth and local superheat variations around the nucleation site (which was not isolated during these simulations), if the experimental heat fluxes conditions are imposed, based on the micro-layer heat transfer theory. The choice of the maximum heat transfer coefficients to be applied to the centre of the contact area was determined by the understanding of the very important and surprising similarity for the increasing-decreasing trend for the dimensionless heat transfer coefficient versus the dimensionless growth time for two essentially different cases of thin foils (titanium, 25 μm and platinum 6 μm).

6. Large distributions of sites

This chapter aims to analyse long term simulations on a large distribution of nucleation sites, reproducing either a silicon wafer on FC-72 or a thin metal foil on water. For each of them, a regular and random distribution of sites will be assumed. The dimensions of the substrates will be different for each case, due to the different bubble departure radii. The cases used in the validation process will be used as base case for the analysis. The study will focus in particular on the analysis of the superheat distribution, on the effects of coalescence and on the variations of activity of the sites, with particular attention to the creation of groups of sites acting as clusters. However, the study will start with a preliminary analysis in which the effect of the distance, site arrangement for a small and intermediate number of sites, based on the base case described in Section 4.2. This will create the guidelines for the choice of the site distributions for the large number of sites for the silicon case, and with necessary modifications to the metal foil case.

6.1.Preliminary analysis

6.1.1. Effect of the distance between a pair of sites

Large distance

As described in Section **4.2.1**, the third generation silicon test section used during the experiment at the University of Edinburgh has 16 micro-fabricated cavities, equally divided in two lines (along which they are located). In each line, the cavities are grouped in 4 pairs, each pair with a variable inter-distance S, equal to 2.0, 1.5, 1.2 and 0.84 mm. Five different cases simulating a pair of sites each will be analysed here: the inter-distances S are equal to the ones for the experimental test section, plus one additional case for distance equal to the double of the average bubble departure radius (r_{bd} = 0.33 mm, S = 0.66 mm). Other cases for smaller distances (<0.66 mm) will be analysed in the next sections. A summary of the cases is shown in Table 16, while the arrangement of the pair of sites is shown in Figure 6-1.

Table 16: Values of the inter-distance between large-spaced sites

$S\ [mm]$	2.0	1.5	1.2	0.84	0.66

During simulations, the pair of site is located in the middle of the substrate, along a line passing through the centres of the sites and through the centre of the substrate from which the sites are equidistant. The applied HTC_{cl} is approximately equal to 170 $\frac{kW}{m^2K}$, the value obtained for the base case from simulations of an isolated bubble growth (Section **4.2.6**). Since experimental data for interacting sites were not available at the time of the development of this analysis, it was supposed here that the same heat transfer coefficient conditions could be applied to distributions of nucleation sites as in cases where the sites cannot be considered isolated. The dimensions of the simulated substrate have been reduced to a square 6.1 mm long, in order to allow a reduction of the size of the coarse cells and consequently have a more refined grid. The superheat variations at the centre of the substrate (point A in Figure 6-1) are shown in Figure 6-2. Since the refinement process involves variation of the cell distribution, the position of the cell in which the superheat is calculated (the closest to the centre of the substrate) may vary during simulations and the superheat values appear scattered. In order to reduce the scattering, for each time step the superheat values are averaged over the nearest three time steps. For all the cases it is possible to clearly identify periodic variations with period approximately equal to 18 ms, slightly smaller than the bubble growth period for the isolated bubble (which was 21 ms). The bubble growth for each of the two sites and for each case is shown in blue below the corresponding superheat variation. Coalescence cannot occur because the distance between the sites is larger than the sum of the bubble departure radii for each site, so that each bubble grows independently from the other apart from thermal interactions through the solid substrate. Simulations were run for a simulated time of ~ 1.0 s. The maximum and minimum

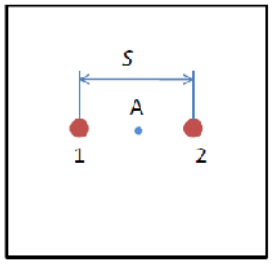

inline

Figure 6-1: Arrangements of a pair of inline sites

superheat values were calculated for each case for one period between 0 and 18 ms, where 0 ms corresponds to ~ 0.9 s of the simulated time. All the calculated values are summarised in Table 17.

Table 17: Superheat variations at variable distance

		S				
		2.0 mm	**1.5 mm**	**1.2 mm**	**0.84 mm**	**0.66 mm**
***ΔT* [K]**	**Maximum**	7.648	7.646	7.640	7.622	7.647
	Average	7.560	7.521	7.484	7.461	7.466
	Minimum	7.485	7.447	7.382	7.379	7.346
	Max Variation	0.162	0.199	0.258	0.243	0.301

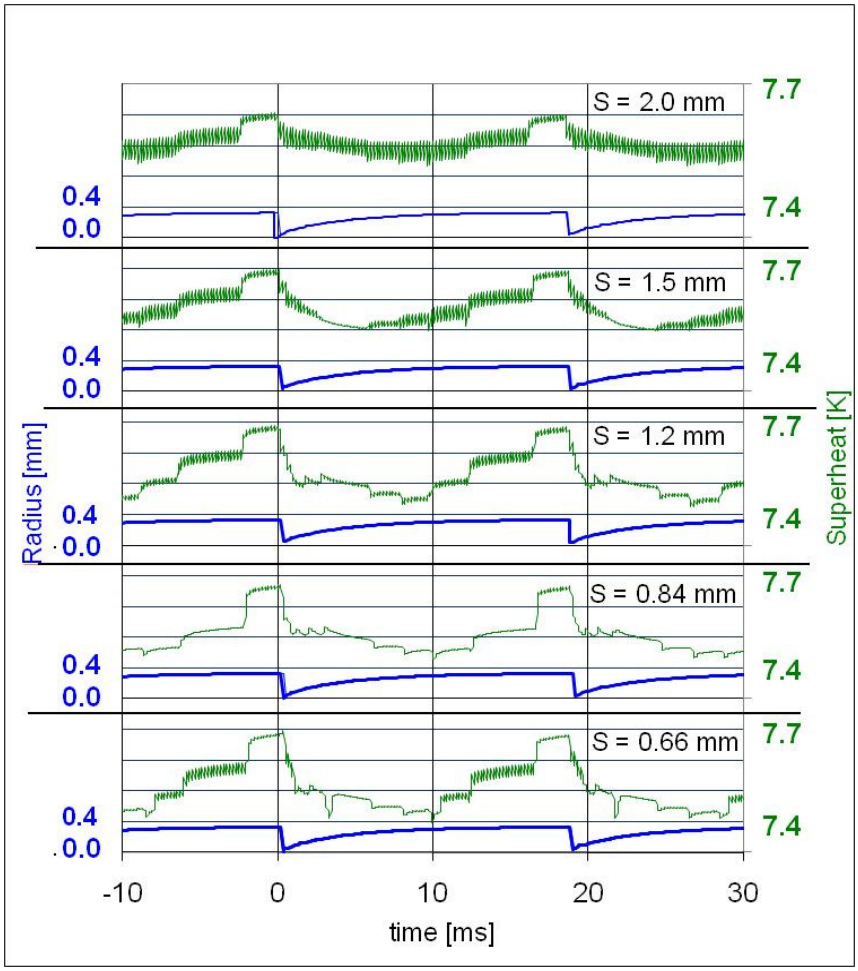

Figure 6-2: Superheat variations for large distance between interacting sites

The maximum value is approximately the same for all the cases (~ 7.64 K), while the minimum value decreases with decreasing distance, from 7.485 K to 7.346 K. The maximum superheat variation (difference between maximum and minimum superheat during the same period) has a minimum for S = 2.0 mm (~ 0.1 K) and then increases with decreasing distance up to its maximum for S = 0.66 mm (~ 0.301 K). This effect is probably due to the thermal interaction between the sites across the substrate, as can be seen in Figure 6-3. This figure shows the superheat distribution along a line passing through the centres of the sites. For large distance (S = 2.0 mm) for two time steps corresponding to the beginning of the period (0 ms when the superheat has a maximum) and to the middle of the period (~ 9 ms when the superheat has a minimum), the sites are too distant to mutually interact. Also the effect in the middle of the sites is not relevant, so that the superheat here is very similar to the value in the unaffected areas far away from the sites (x < 7 mm and x > 11 mm). Reducing the distance between the sites to S = 0.84 and 0.66 mm leads to a larger variation in the area in between the sites, because of the effect of cooling in the lateral direction though the substrate.

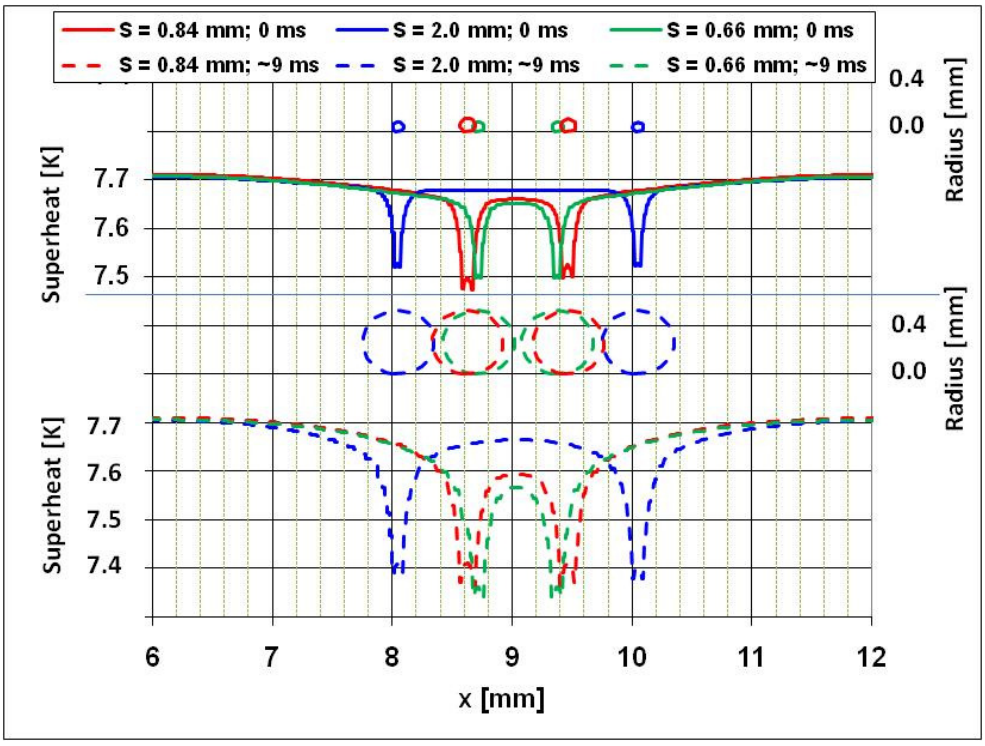

Figure 6-3: Superheat distribution along a line at two different time steps for variable (large) site distance

Short distance and coalescence

This section aims to identify the possibility and effects of occurrence of horizontal coalescence on bubble growth and superheat variations at the nucleation sites. Experimental results developed at Edinburgh University showed no occurrence of horizontal coalescence for the considered pair of nucleation sites with S = 2.0 mm, although vertical coalescence was observed (Hutter et al., 2009). The vertical coalescence model has not been implemented into the code yet. However, if its influence on the heat transfer at the upper surface was found to be relevant for superheat variations, an appropriate model should be introduced to take into account the effects of this phenomenon. For the other pairs of sites (S < 2.0 mm), no results on horizontal coalescence are available yet[3]. These results confirm the theory of Zhang and Shoji (2003) that horizontal coalescence does not occur for a distance to bubble departure diameter ratio (S/D_b) larger than 1.5. According to this hypothesis, the minimum distance S_{min} to have horizontal coalescence would be 1.0 mm for a bubble departure radius of 0.33 mm (as it was in the base case). If the hypothesis of S/D_b < 1.5 was correct, the model would be only partially able to deal with horizontal coalescence, since the numerical assumption limits its occurrence only for the cases where the domes of the bubbles come in contact, so that S/D_b < 1.0. The numerical study will be based only on the comparison of results with the isolated bubble growth parameters at close distance (S = 0.66 mm). Three additional cases will be investigated, with S = 0.495, 0.33 and 0.195 mm, respectively equal to 1.5, 1.0 and 0.5 times the bubble departure radius. The two nucleation sites are located as in the previous case along a horizontal line passing through the middle of the substrate located in the middle of the substrate equidistant from the centre itself. The input data for each nucleation site will be the same used for the base case. The heat transfer coefficient applied to the contact line area corresponds to HTC_{cl} ~ 170 $\frac{kW}{Km^2}$ calculated for the base case to match the experimental growth time (t_g = 21 ms) and bubble departure radius (r_{bd} = 0.33 mm). However, the tuning of HTC_{cl} will not be applied here: the bubble departure radius is then expected to increase if coalescence occurs, according to Equation 3.21.

Two models have been implemented, depending on the ratio of the larger (r_{large}) to the smaller (r_{small}) bubble radii. If the bubbles have similar radii (for 1.0 < r_{large}/r_{small} <

[3] Data related to horizontal coalescence have been made available after the completion of this Section for the pair of nucleation sites with S = 0.84 mm (Hutter, 2009)

2.0, coalescence type C1) the bubbles are assumed to continue to grow independently with interfering domes until departure or until the conditions of non-interfering mesh are both satisfied (Equation 3.1). For different radii (for $r_{large}/r_{small} > 2.0$, coalescence type C2) the large bubble is assumed to incorporate the small one that suddenly disappears while the large one undergoes a volume increase so that the total volume is conserved. The results for the superheat variations for the four values of S, as summarised in Table 18, are shown in Figure 6-4.

Table 18: Values of the inter-distance between close-spaced sites

***S** [mm]*	0.660	0.495	0.330	0.165

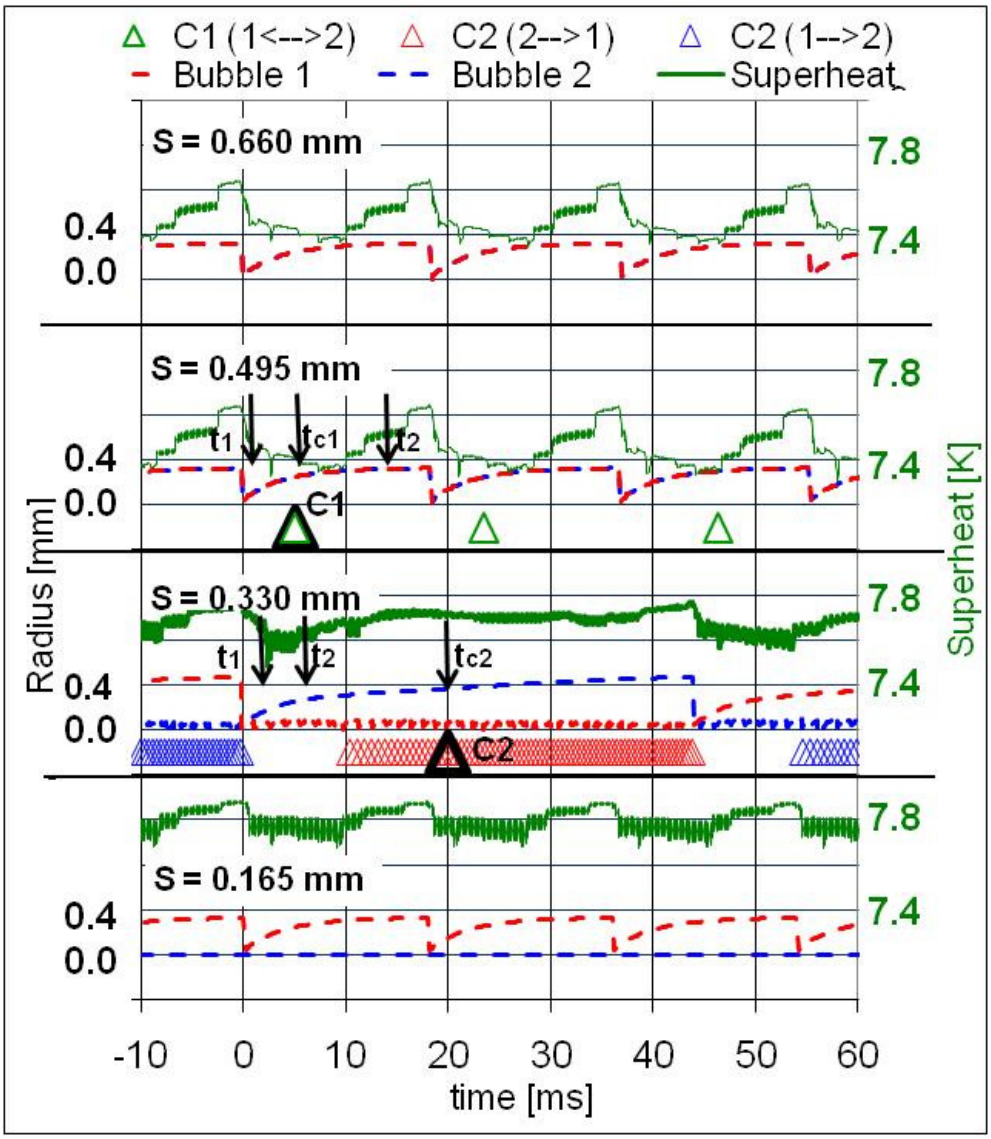

Figure 6-4: Superheat variations for close interacting sites

Also in this case, the time t = 0 ms has been chosen only for convenience and corresponds to a simulated time of approximately 0.9 s. The figure shows the superheat variations and the bubble growth for each of the two sites. Moreover, for the cases in which coalescence occurs (S = 0.495 and 0.330 mm) a triangle below the bubble radii history indicates the time of occurrence.

For S = 0.495 mm, each bubble grows independently on and in phase with the other one (the radii histories overlap in the figure so that only the radius of bubble 1 is visible). Superheat and radii histories are essentially similar to the case S = 0.66 mm, as expected since the coalescence model for similar radii does not alter either the bubble growth or the heat transfer coefficient conditions. Only the minimum superheat is slightly smaller than for S = 0.66 mm. However, coalescence between bubbles with similar radii (C1, with the notation "1<-->2" indicating that the bubbles have similar radii) occurs once per bubble growth (i.e. at ~ 5, ~ 22 and ~ 47 ms). The superheat distribution along the line passing through the centres of the nucleation sites is shown in Figure 6-5 (a) at three different time steps: t_1 ~ 0 ms, t_{c1} ~ 5 ms and t_2 ~ 15 ms. For t_1 ~ 0 ms the bubbles have just appeared and the superheat difference between the nucleation sites and the centre of the substrate (x ~ 9 mm) is small (~ 2 K) and localised to a small area around each nucleation site. At t_{c1} ~ 5 ms, the domes of the bubbles

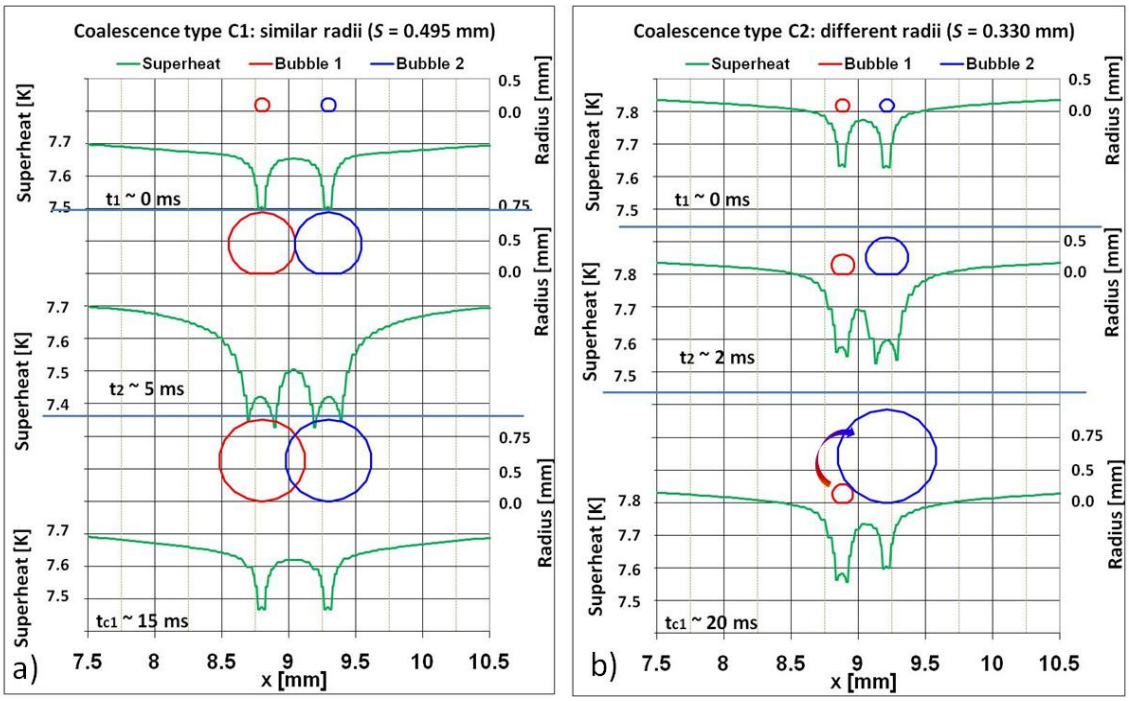

Figure 6-5: Effect of coalescence on superheat distribution along a line passing through the centres of the nucleation sites. a) C1: similar radii (S = 0.495 mm); b) C2: different radii (S = 0.330 mm)

come in contact and coalescence is about to occur. The superheat variation involves a much larger area around the nucleation site with respect to t_1 ~ 0 ms, and also the superheat at x ~ 9 mm is significantly lower at this time step (7.4 K with respect to the 7.55 K at t_1 ~ 0 ms). At t_2 ~ 15 ms, the domes of the bubbles are interfering, and due to the decrease of the contact angle during the final stage of the bubble growth, the superheat variation involves again a small area around each nucleation site and the superheat at x ~ 9 mm increases again.

For S = 0.33 mm a completely different behaviour can be observed in Figure 6-4: the superheat variations are smaller during each period, with a significantly higher average value (~ 7.7 K) at the centre of the substrate (x ~ 9 mm) with respect to the case of S = 0.66 mm (~ 7.5 K). Two factors contribute to produce this effect: the numerical alternating growth effect (and in particular the limitation due to Equation 3.1) and coalescence between bubbles of different radii, C2. From analysis of the bubble radii histories, only one of the two sites is continuously active at the same time, while the other continues to intermittently activate producing very small bubbles (with a bubble radius smaller than 0.1 mm). If the time interval between 0 ms and 44 ms is analysed (i.e. the growth time for bubble 2), the alternating growth effect due to numerical limitations occurs between 0 and ~ 10 ms. At t_1 = 0 ms, the two sites nucleate at the same time and the bubbles seem to have similar radii (Figure 6-5, b): the superheat variations are similar to the correspondent case for C1, seen in Figure 6-5, a), although the average superheat is higher for the case C2. With increasing time (Figure 6-4), site 1 is continuously active with the bubble regularly increasing its radius, while site 2 activates and deactivates with a frequency of ~ 1.43 events/ms. Coalescence during this time cannot occur because the radii are still too small for the domes to interfere (Figure 6-5, b; t_2 = 2 ms). The bubbles have now different radii, and the corresponding superheat variations around each nucleation site involve larger influence areas. At t > 10 ms, coalescence C2 starts to occur regularly, with the bubble at site 1 repetitively incorporated by the bubble at site 2 (1-->2, Figure 6-4) with a frequency of ~ 2.16 events/ms. An example of the superheat distribution and bubble growth just before occurrence of coalescence (C2, 1-->2) is shown in Figure 6-5 (b) for t_{c2} ~ 20 ms. Occurrence of coalescence C2 involves also the variation of the average bubble departure radii. For the small bubble, its value strongly decreases with respect to S = 0.66 mm and it is approximately equal to 0.1 mm during one period. For the large bubble, as it can be seen in Figure 6-4, the bubble does not grow anymore until its

maximum value of 0.33 mm as in the base case, but continues growing according to Equation 3.21. In this case, the bubble at site 2 departs with a final departure radius of ~ 0.469 mm (approximately 1.42 times the base case value) due to multiple coalescence of bubble at site 1 in bubble at site 2. This leads also to a more than double growth time (~ 44 ms, respect to the ~ 21 ms for the base case). For t > 44 ms and t < 0 ms, the role of the two sites is reversed, with the bubble at site 2 repetitively incorporated by bubble at site 1 (2-->1, as shown by blue triangles in Figure 6-4 for t < 0 ms and t > 44 ms). An alternating effect in coalescence between the two cases can be generally observed. From comparison of the superheat distributions for the two cases of coalescence C1 and C2 (Figure 6-4 and Figure 6-5), it is clear that when C2 occurs, the cooling effect on the substrate is less effective, so that the superheat distribution has an average higher value everywhere. The process affects also the activity of the sites, which is strongly increased from 55 activations/s (corresponding to a growth time of 18 ms) for S = 0.66 mm to ~ 440 activations/s (corresponding to an average growth time of 2.27 ms) for S = 0.33 mm. However, most of these activations are due to departure at very small radii.

For S = 0.165 mm (Figure 6-4), only site 1 activates, while site 2 is continuously inhibited by numerical limitation Equation 3.1. The superheat at the centre of the substrate is consequently significantly higher than for S = 0.66 mm.

6.1.2. *Effect of the site arrangement*

This section aims to investigate the effects of the arrangement of the nucleation sites on superheat variations in order to develop a preliminary study for the distribution used in the design process. Two different arrangements (triangular and square) will be compared to the inline distribution used in the previous section on the investigations of the effect of the distance. The three layouts are shown in Figure 6-6. The superheat is always measured in the middle of two close nucleation sites (points A in the figure). For

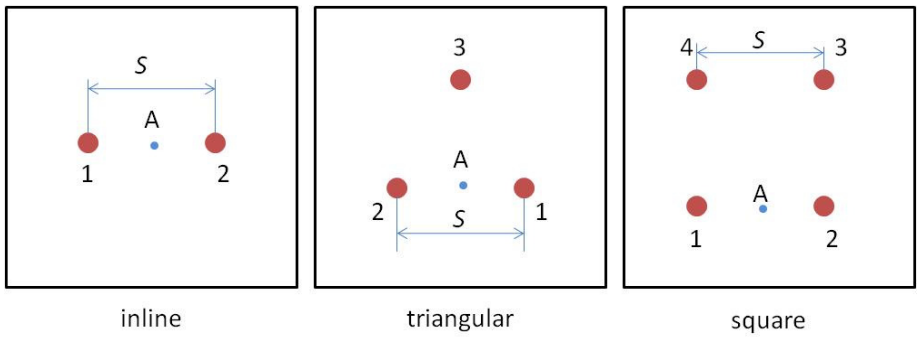

Figure 6-6: Site arrangements: inline (left); triangular (centre); square (right)

each of the two distributions, simulations will be repeated with variable distance *S* between the sites. The values of *S* between the sites are listed in Table 19. Figure 6-7 shows the comparison between the different superheats and bubble growths for the five cases.

Table 19: Values of the inter-distance between sites for square and triangular distributions

***S** [mm]*	0.840	0.660	0.495	0.330	0.165

From analysis of the first three cases (*S* = 0.840, 0.660 and 0.495 mm, which do

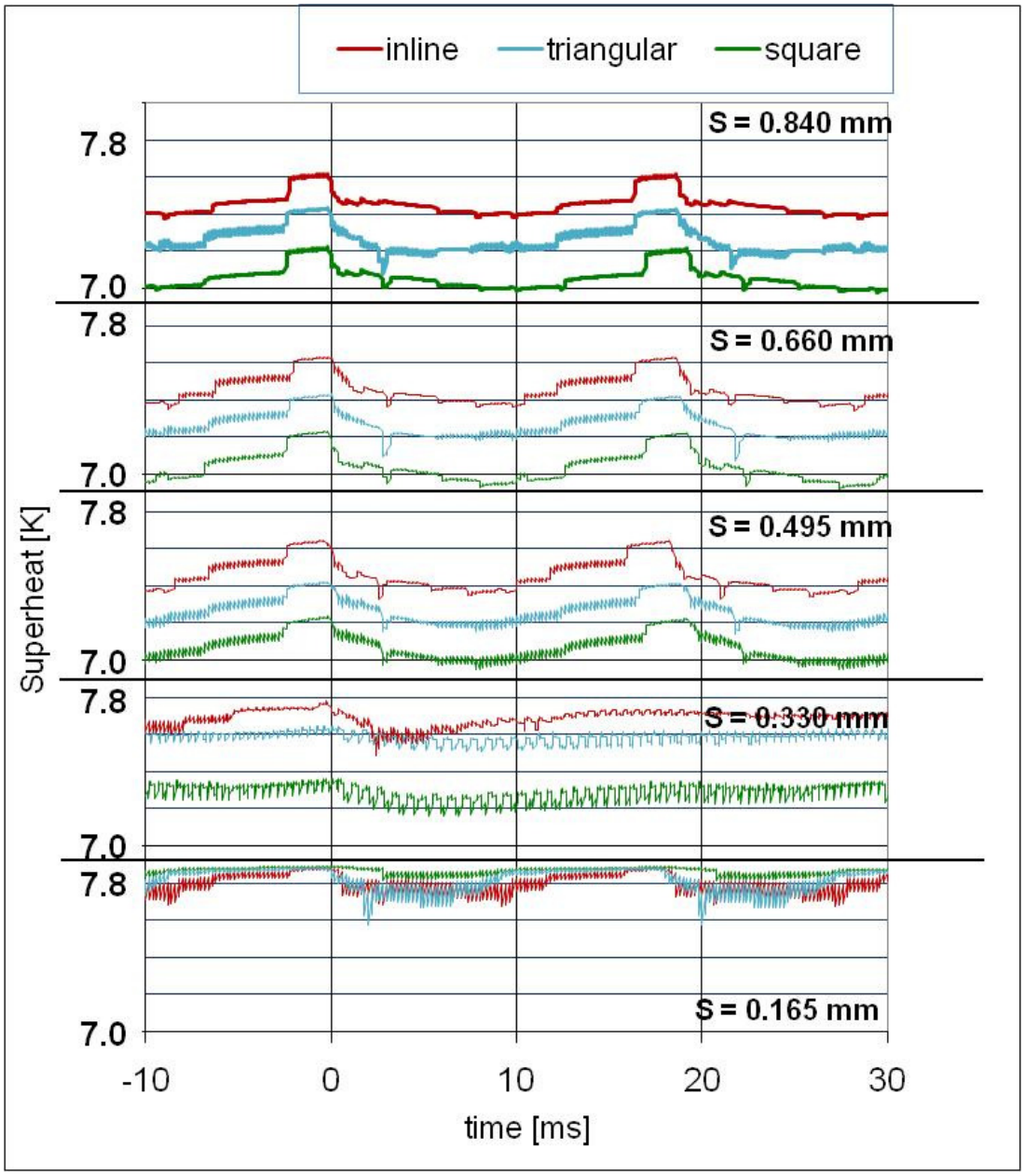

Figure 6-7: Effect of site arrangement on superheat in the midpoint between two adjacent sites

not involve coalescence type C2, the superheat decreases with the number of active sites. The variations during the period are similar for all the arrangements, but with different average values, equal to ~ 7.5 K for the inline arrangement, ~ 7.3 K for the triangular and ~ 7.1 K for the square.

For S = 0.330 mm, while for the inline and square arrangements it is clearly possible to identify a periodic behaviour of the superheat as described before for the inline arrangement, for the triangular arrangement the superheat undergoes only very small variations around the average value, which is significantly higher than for S = 0.660 mm. The effect is caused by multiple coalescences of two bubbles in the third one (generally bubbles at sites 1 and 2 in bubble at site 3 or bubbles at sites 1 and 3 in bubble at site 2) and by deactivation due to the numerical limitations described before. In fact, the bubble radius has an average value of 0.09 mm, approximately 1/3 of the corresponding value for S = 0.840 mm. The site activity for site 1 is approximately 1600 activations/s, ~ 30 times higher than for S = 0.840 mm, and ~ 1.5 times the activity of the other two sites (~ 1100 activations/s per sites 2 and 3). If the only activations leading to a bubble departure radius larger than the base case value are counted (complete growth, which implies that bubbles at the other sites have coalesced into the bubble at the considered site), site 1 activates 4 times, while sites 2 and 3 activate 14 and 13 times respectively in 1 s of simulated time, see Figure 6-8, a). The bubble departure radius is in this case (complete growth) approximately 0.46 mm for a bubble growth time variable between 30 and 35 ms. The effect of lower activity of site 1 with respect to the other two sites (considering the only complete growths) could be assumed to be caused by the sequential order of the sites. However, from analysis of the bubble growth histories for the three sites, complete growth activations do not seem to be directly related to the sequential number, although this may contribute as well. Since the three sites activate at the same time (as for the inline arrangement), the leading bubble (i.e. the bubble that undergoes the complete growth) is the one that first undergoes the mesh change that produces temporary inhibition of the other two sites. From that moment, the bubble continues to grow, while the other two have intermittent activation until the leading bubble departs. This effect is not visible for S = 0.330 mm for the square arrangement, probably because the four sites are not all equidistant in this case. However, also in this case, the average value of the superheat is higher than for S = 0.660 mm, which implies that some of the sites do not regularly activate. From analysis of Figure 6-8 (b) it is clear that sites 2 and 4 never complete their growth but depart

before (either because of the numerical limitation or coalescence type C2), with an average departure radius of ~ 0.1 mm. For sites 1 and 3, three phases are periodically repeated. With reference to site 1, it is possible to identify:

- An enhanced growth period when the bubble incorporates the other bubbles during coalescence type C2. The bubble departs with a radius significantly

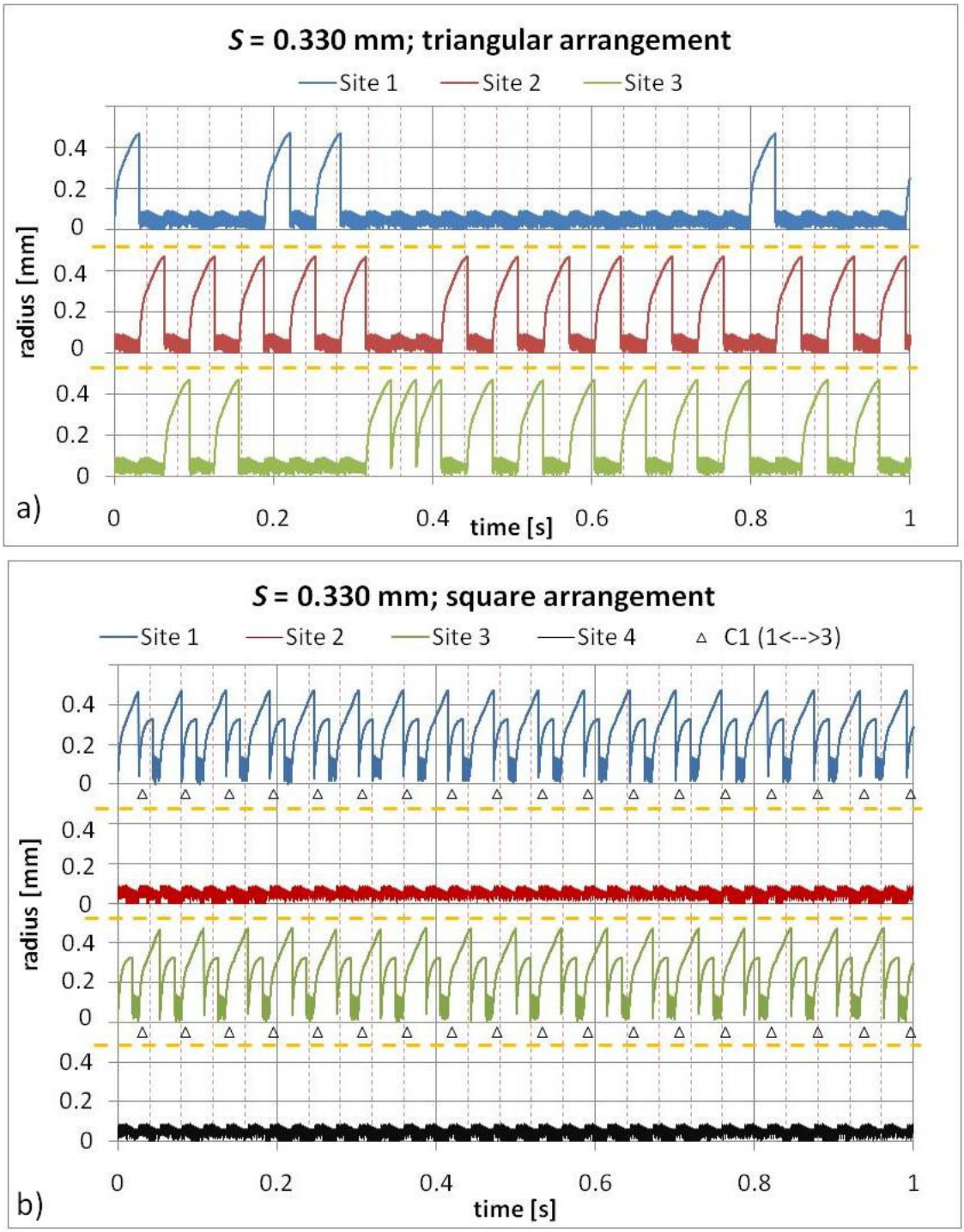

Figure 6-8: Bubble growth for S = 0.330 mm for triangular and square arrangements

larger (~ 0.43 mm) than the average bubble departure radius in the base case (0.33 mm). An example of this case is between 0 and ~ 26 ms.

- A normal growth period, during which the bubble continues to grow essentially undisturbed until departure that occurs with bubble departure radius of 0.33 mm. During this period, cases of coalescence type C1 (1 <-->3), indicated by the black triangles below the bubble histories for sites 1 and 3, occur, as for instance for t ~ 2.16 s. An example of this period is the time interval between 26 and 45 ms.
- A period of intermittent activity, during which the site continuously activates and deactivates, because of either coalescence type C2 into another bubble or numerical limitations on the mesh distribution.

Site 3 presents similar behaviour, but the bubbles at sites 1 and 3 grow out of phase. However, the behaviour is not perfectly similar since coalescence C1 (1<-->2) always occurs during the initial phases of a normal bubble growth for bubble at site 1 and of an enhanced bubble growth for bubble at site 3, although this type of coalescence does not interfere with the growth itself.

Analysis of case S = 0.165 mm in Figure 6-7 shows a significant increase of the average superheat with smaller superheat variations during the period (still identifiable). By contrast with the previous cases, for S = 0.165 mm the site arrangements do not produce significant modifications: in all the cases, only site 1 became active with an activation frequency similar to the isolated bubble case.

6.1.3. Intermediate distribution of nucleation sites

Two comparisons for an intermediate number of nucleation sites (49) will be developed here. In the first case, the comparison between two different arrangements aims to explain the effect of two different arrangements (triangular and square) on superheat. The second will compare the use of standard and unrefined sites with the same site arrangement (square). The objective is to evaluate the effects on superheat of the two methods and if the unrefined sites can replace the standard ones over larger distributions.

Site arrangement: triangular and square

A comparison between the triangular and square distributions has also been developed for an intermediate number of sites (49) distributed as shown in Figure 6-9, with a distance between site S = 0.66 mm for both the cases. The simulated dimensions of the substrate are 6.1x6.1 mm^2 with the centre located at 9.05 mm to facilitate the comparison with data for the base case substrate. The coarse mesh width is 0.05 mm. The sites along the horizontal line for y = 9.05 mm are located on the same position for the two distributions. The superheat variation for the site located in the middle of the substrate shows very similar variations for the two cases. The superheat distribution along the horizontal line passing through the central site (y = 9.05 mm) is shown in Figure 6-10 at two different times (t ~ 1.3 and 2.5 s). The variations are similar in the two cases, although for the square arrangement the cooling effect is slightly less effective (the superheat is slightly higher, mostly at the edges of the substrate). Also in this case, as for the comparison between standard and unrefined sites (Section **4.3.7**), it is possible to notice that the bubbles are growing out of phase. However, the frequency of activation varies only slightly between the sites for the same case (between 21.89 and 22.97 activations/s for the square arrangement and between 23.10 and 23.79 activations/s for the square arrangement, with corresponding growth times of respectively ~ 43 ms and ~ 44.5 ms).

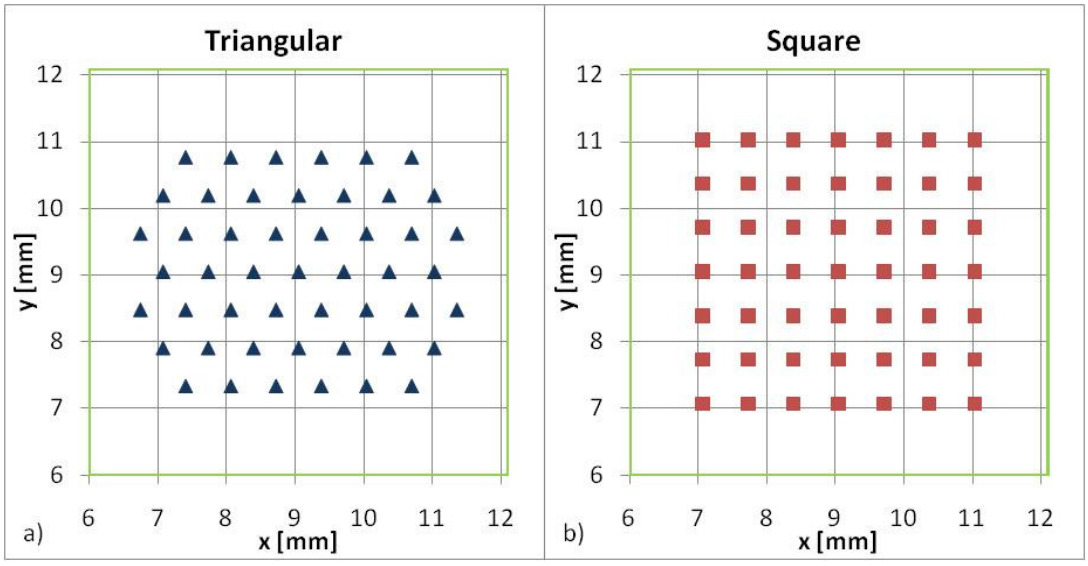

Figure 6-9: Site distribution: a) triangular; b) square

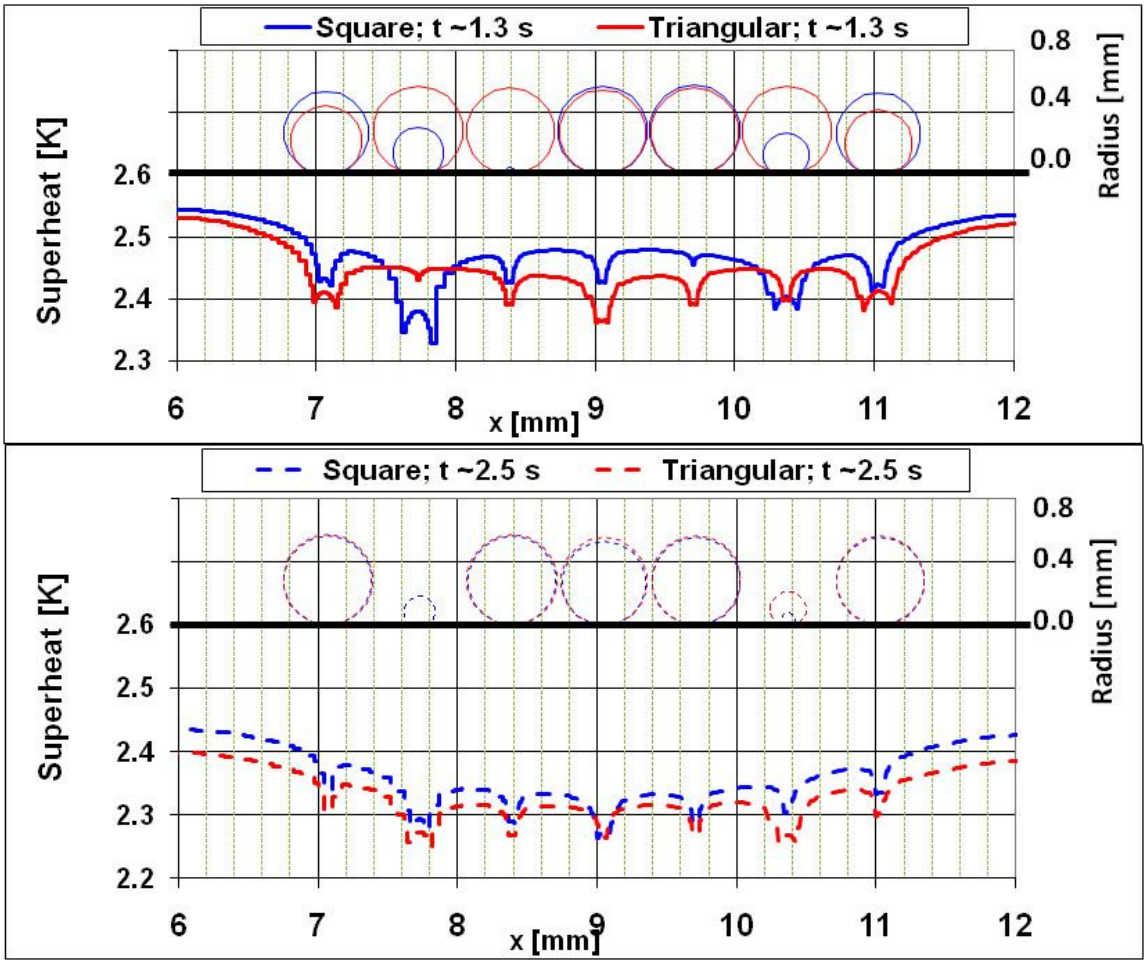

Figure 6-10: Superheat distribution along a line for square and triangular arrangements of the sites

The 2-D superheat distributions for the two site arrangements for half of the simulated substrate are shown in Figure 6-11. It is possible to identify the strong cooling effects around each nucleation site. For several of them it is also visible the local superheat reduction around the triple contact line, with partial increase of superheat in the centre of the contact area where the zero *HTC* is imposed. Moreover, for the triangular arrangement, the superheat at the corners of the substrate is higher than for the square arrangement, because the closest site in the first case is located at a larger distance than in the other case.

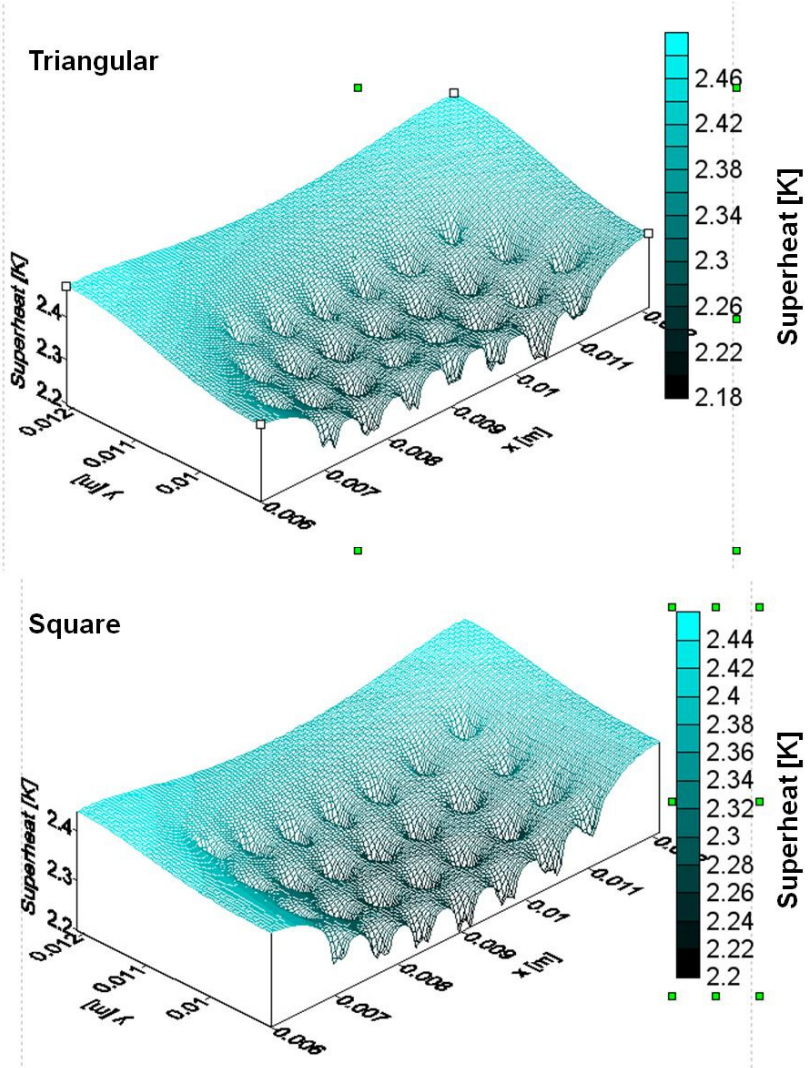

Figure 6-11: 2-dimensional superheat distributions for a large distribution of nucleation sites for triangular and square arrangements

Comparison of standard and unrefined site for an intermediate site distribution

An analysis of the influence of standard and unrefined nucleation sites on the *HTC* was developed also for an intermediate distribution of nucleation sites (49) arranged in a square distribution with distance between the sites equal to the double of the average bubble departure radius (0.66 mm). The site distribution is the same as the previous analysis (Figure 6-9, b). The sites cover approximately the whole surface.

Figure 6-12 a) shows the superheat variation and the bubble radius history for the nucleation site located at the centre of the substrate, referring to the simulated period between 0 and 2.5 s. The transient path for the superheat is very similar for both standard and unrefined site distributions. During the first stage (approximately between 0 and 1.0 s) the superheat undergoes a significant decrease from the initial superheat (7.35 K, lowered according to the previous results for the base case) to approximately 2.0 K. With respect to the base case, the final superheat is much lower due to the cooling effect of the other sites that propagates through the substrate. The bubble radius histories are similar for both unrefined and standard sites, although the bubbles grow out of phase. A more detailed description of the data narrowed over a shorter time period (between 2.0 and 2.5 s) is shown in Figure 6-12 b). The superheat for the distribution of standard sites has a significantly larger average value (2.276 K) with respect to the unrefined sites case with larger superheat variations during the bubble growth (~ 0.16 K and ~ 0.08 K respectively for the standard and unrefined sites). Moreover, it is possible to identify a clearer periodic activity. From the analysis of the bubble growth, it is also possible to notice that the growth time is significantly longer for the unrefined sites, leading to bubble growth times during the last stage of ~ 53 ms for the standard site and of ~ 65 ms for the unrefined site (the central site is here considered). The growth times for both cases are significantly larger for the distribution of 49 nucleation sites with respect to the isolated nucleation site case (~ 21 ms). This is caused by the effect of the decrease in superheat. This phenomenon leads to an increase in activity from 192 to 231 activations/s (if all the events that took place during the simulated time are counted) respectively for the unrefined and standard sites. However, for each case, the mentioned activities are similar for all the sites regardless of the position of the site itself.

A comparison between the superheat distribution along a line passing through the centre of the substrate for standard and unrefined sites is shown in Figure 6-13. Two time steps are analysed: ~ 1.3 s and 2.5 s from the beginning of simulations. The distribution for the unrefined sites case has an average value generally lower (~ 2.25 K at 1.3 s and ~ 2.0 K at 2.5 s) than for the standard sites case (~ 2.48 K at 1.3 s and ~ 2.3 K at 2.5 s). The maximum variation between the centre and the edges of the substrate is approximately less than 0.3 K for all cases. The superheat distribution seems to be approximately symmetrical with respect to the central line (x = 9.05 mm), as also confirmed by the growth of the bubbles shown in the upper part of the figure. Moreover,

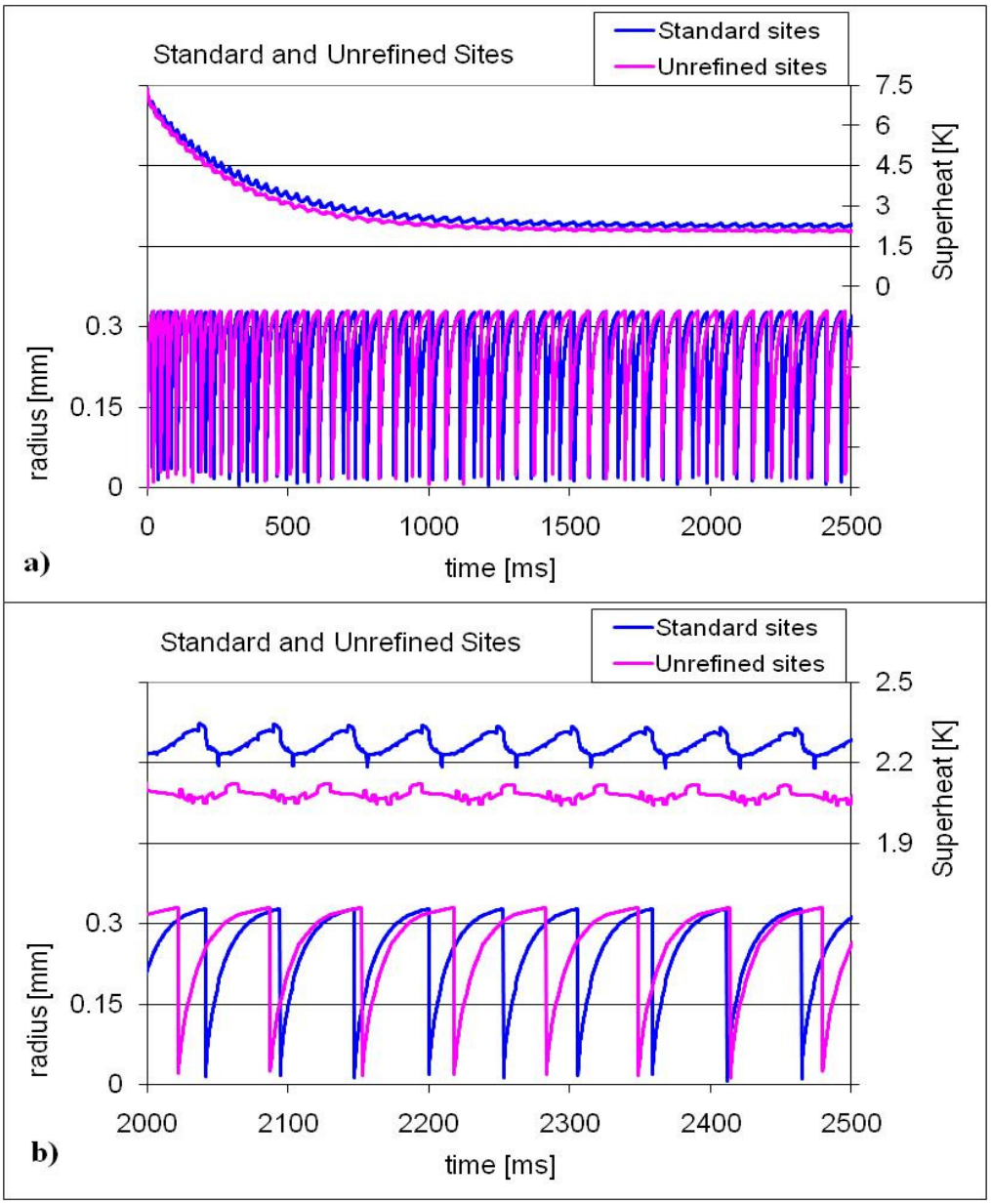

Figure 6-12: Comparison of standard and unrefined sites for a large distribution of nucleation sites. a) whole simulations; b) last stage of simulations

the bubble growths show that some bubbles are growing out of phase. From comparison of the superheat results for unrefined and standard sites, the unrefined sites seem to have a stronger cooling effect with more effective superheat reduction. Unfortunately, the two models cannot be compared at the moment with experimental results in order to decide which of them is more suitable to simulate superheat variations. The difference in superheat in the two cases leads to a significant higher activity for the standard sites (~ 23.5 activations/s) than for the unrefined ones (~ 18.9 activations/s), due to the lower heat flux removal at the upper surface (depending on the superheat). The corresponding growth times are respectively t_g ~ 42 ms and t_g ~ 53 ms, significantly longer than for the isolated bubble simulated in the base case. By contrast, the difference in activity for the same case between the less active sites (located in the central region of the surface) and the most active ones (located towards the edges) is less than 1 activations/s.

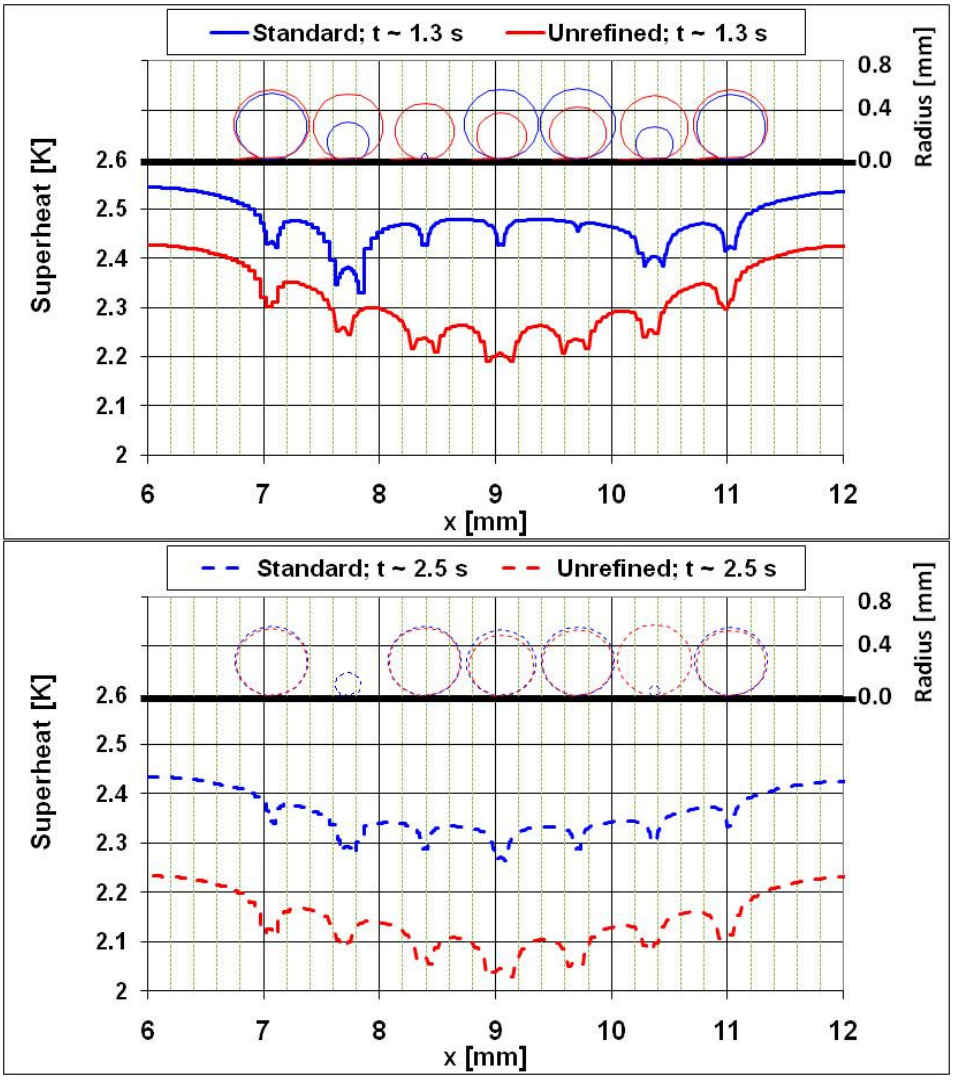

Figure 6-13: Superheat distribution along a line for a large distribution of standard and unrefined sites

6.1.4. Summary of the preliminary analysis

The analysis of the effects of distance between a pair of sites showed that the superheat in the middle of the two sites decreases with decreasing distance (for values larger than or equal to the double of the average bubble departure radius) due to lateral conduction in the substrate. For a distance equal to 1.5 times the bubble departure radius, coalescence between bubbles of approximately the same size is expected to occur, without leading to any significant alteration of the superheat in the middle point with respect to the case with distance equal to 2.0 times the bubble departure radius. For smaller values (equal to the bubble departure radius for the base case) coalescence between bubbles of different size is predicted to occur: this phenomenon leads to a larger bubble departure radius for one of the two bubbles (during the bubble growth period due to inclusion of the small bubble) and a strong reduction in bubble radius for the other one during the same considered period. This produces a less effective heat removal from the surface and then increasing superheat. If the distance is still reduced, only one of the two sites becomes active at the same time, while the other is inhibited because of numerical limitations in the code.

For different site arrangements, similar phenomena can be identified. However, the occurrence strongly depends on the mutual distance between the sites (triangular arrangement) and may lead to inhibition also at distance equal to the bubble departure radius for a square arrangement, where the distance between the sites is not the same for all the sites.

For larger distributions of sites (49, approximately covering the whole surface), the cooling effect is stronger, with a significant reduction (more than 5K) in the central area, due to the high lateral conduction. It was also noted that the triangular arrangement has a stronger cooling effect that the square one, with consequent lower superheats. If standard and unrefined sites models are compared for the square distribution, it is apparent that the superheats do not coincide and differ by ~ 0.15 K, which is not negligible if compared to the average value (~ 2.0 K). As consequence of the reduced superheat, the growth time for all the cases increases with the number of sites leading to lower activation frequencies.

6.2. Large distribution of nucleation sites (100) on Silicon immersed in FC-72

This section focuses on the effects of the application of the base case for a single bubble growth to a large distribution of potential nucleation sites on Silicon immersed in FC-72, of the order of 100 standard nucleation sites, involving the phenomena analysed previously. In particular, it will study the superheat variations across the substrate, activation and occurrence of coalescence, as well as the possibility of inhibition or seeding of sites due to the activity of neighbour nucleation sites. Two studies will be carried out, using either the nominal values for the bubble departure radius and activation superheat or values ranging around the nominal values in order to take into account the presence of possible uncertainties in the measurement. The use of the uncertainty parameters (expressed as percentage value of the nominal value) will modify the two input data by adding at each activation and for each nucleation site a random value in the range imposed by the uncertainty parameters themselves. For the two analysed cases (with and without the use of the uncertainty parameters) it will be assumed that the input data used for the validation process of the code and previously described in the base case (Section 4.2) are applicable. In particular, it will be supposed that the heat transfer mechanisms and the characteristic of the single bubble growth could be maintained and applied to a larger distribution of nucleation sites. The validity of this assumption could not be proved during this PhD project because the comparison with experimental data was not achievable because of time constraints. However, the analysis could be used to have an insight of the phenomena possibly involved and to define some design guidelines. In the future, the comparison of results from the newly designed and fabricated substrates may constitute the basis for the complete validation of the code. The simulated silicon substrate, 0.38 mm thick, is supposedly immersed in FC-72 at saturation conditions at atmospheric pressure. A summary of the data used during the simulations is provided in Table 20.

Table 20: Input data for a large distribution of sites for Silicon

Substrate [Silicon] 6.0 x 6.0 mm²		δ_H 0.38 mm	ρ_H 2340 $\frac{kg}{m^3}$	c_H 750 $\frac{J}{kgK}$	k_H 110 $\frac{W}{mK}$	$\dot{q}$ = 4.48 $\frac{kW}{m^2}$
Liquid [FC-72] 1Atm, 57.15 °C		ρ_v 12.76 $\frac{kg}{m^3}$	ρ_L 1611 $\frac{kg}{m^3}$	c_L 1088 $\frac{J}{kgK}$	k_L 0.054 $\frac{W}{mK}$	H_{fg} 85200 $\frac{J}{kg}$
Bubble growth and Heat Transfer	**Exper**	t_g 21.0 ms	r_{bd} 0.33 mm	ΔT_{act} 1 K	f_{decr} 0.6	ΔT_{IN} 2.25 K
	Numer	HT model *CL*	HTC_{cl} ~ 170 $\frac{kW}{m^2}$	f_D 1.0	φ_0 30°	Natural convection Eq. 3.15, f_{enh} = 1.16
Numerical data		Δt 1.0 µs	w_{xy} 0.1 mm	n_{vL} 2	n_R 7	*Number of sites* 100 standard 96 unrefined

The data for the bubble growth refer to the experimental results developed at the University of Edinburgh (Hutter et al., 2009) and in particular the bubble departure radius r_{bd} = 0.33 mm and the growth time t_g = 21 ms. The choice of the contact line model (*CL*) for the heat transfer at the base of the bubble (with a maximum heat transfer coefficient at the contact line HTC_{cl} ~ 170 $\frac{kW}{m^2}$) instead of the micro-layer (*ML*) model was made with no evident support from experimental results developed at the University of Edinburgh. However, this model was shown during this PhD project to be compatible with the bubble growth history and the superheat variations as measured by the sensors, as seen in Section 4.2. Moreover, Kiger and Moghaddam (2008) and Moghammad and Kiger (2009) experimentally observed for a Silicon substrate (60 µm thick) immersed in FC-72 at atmospheric pressure that the heat transfer coefficient at the contact line appeared to be much larger than in the inner part of the contact area, supporting the use of the contact line model. However, in these cases, the superheat variations are much larger than the ones measured by Hutter (2009) and described in Section 4.2, probably due to the very large average superheat measured in the first case, approximately between 20 and 40 K.

As initial condition during simulations, the imposed superheat was 2.25 K, according to the results found for the distribution of 49 nucleation sites, analysed in Section 6.1.3. The simulated substrate is a square 6 mm long, with centre in x = 20 mm and y = 18 mm. The sites have been arranged in a square distribution with distance between adjacent sites equal to 0.4 mm, equal to approximately 1.21 times the bubble departure radius, in order to have strongly interacting sites (both thermally and via coalescence) but with no interference of the distribution of the refined mesh. The distribution of the sites, distinguishing between the 100 standard sites and the 96 unrefined sites, is shown in Figure 6-14. The dotted lines that connect the sites are purely imaginary and were introduced to visually identify the logic in numbering the sites, so that it was not necessary to label all of them. The site located approximately in the middle of the substrate (x = 20.4 mm and y = 18.2 mm) is site #1, and the site identification number spirally increases towards the edges of the substrate. The 100 standard sites are located in a central area of the substrate (approximately 4 mm long).

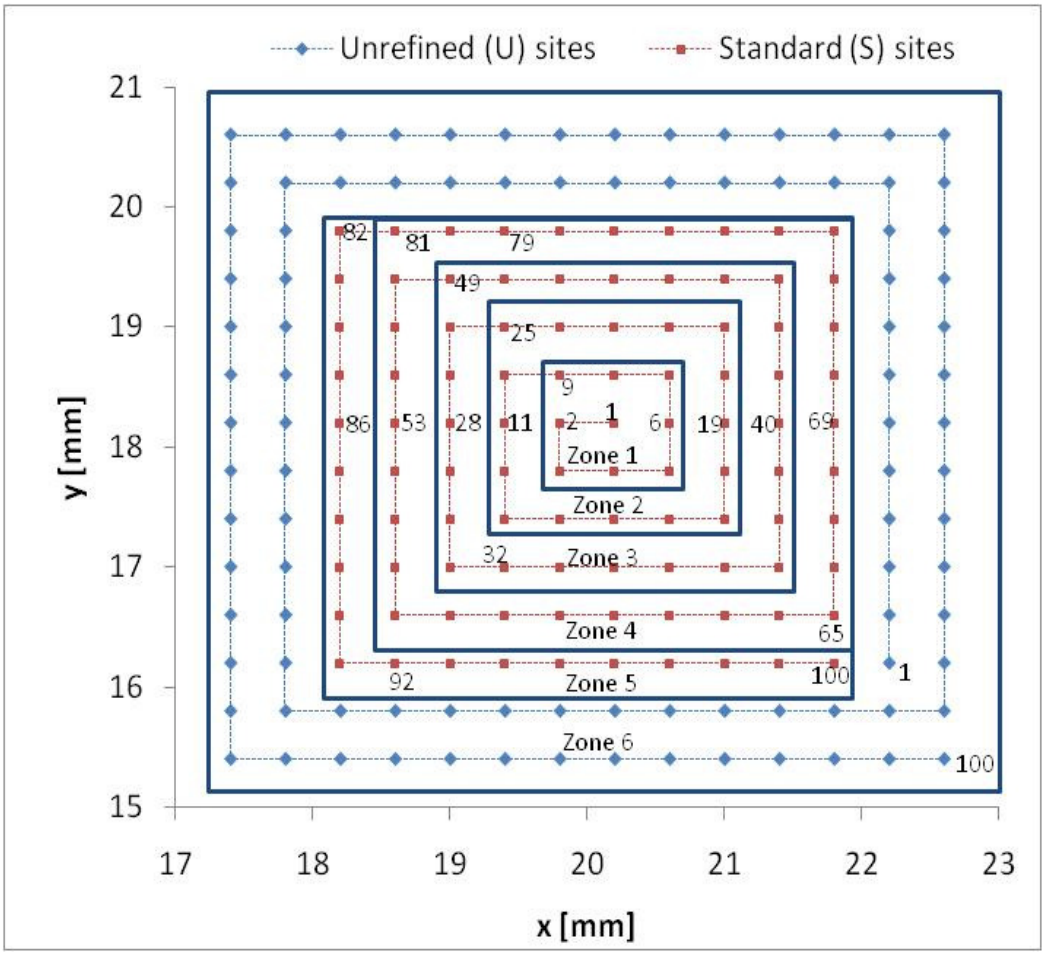

Figure 6-14: Site distribution for Silicon immersed in FC-72 with distance between sites 0.4 mm

Five zones are also identified for this area (Zone 1, sites 1 to 9; Zone 2, sites 10 to 25; Zone 3, sites 26 to 49; Zone 4, sites 50 to 81; Zone 5, sites 82 to 100) to help in identifying the sites in the following graphics. Particular importance in the following analysis will be given to the standard sites located along the horizontal line passing through the standard site #1. The 96 unrefined sites are located in the external area and were simulated in order to reduce the edge effects. For the unrefined sites only one zone (Zone 6) was defined including all the 96 sites, since their activity and superheat variations will not be specifically analysed.

The number of vertical layers in which the thickness of the substrate was divided was reduced from 6 to 2 in order to reduce the computational time. The effect on the superheat variations (negligible for an isolated site) should not be significantly affected by it. The following analysis presents several aspects of the boiling phenomena for the two cases (with and without the use of the uncertainty parameters), with particular focus on the bubble growth and superheat variations, activation of the sites and coalescence effects. Moreover, the presence of irregularities in activation of particular sites, with prediction of groups of sites acting as clusters, or seeding and inhibiting effects will be studied.

6.2.1. Nominal values for activation superheat and bubble departure radius values

The first analysis will focus on the case using the nominal value for bubble departure radius and activation superheat. The simulations were run in order to simulate 5 s. The total computational time was approximately equal to 74 hours, equivalent to ~ 14.8 hours per simulated second. The analysis will start with the effects of the site distribution on the superheat distribution and variations and on the bubble growth. Subsequently, the effects on the activity of the sites and on coalescence will be studied.

Superheat variations and bubble growth

The superheat variations at the nucleation site and the bubble growth histories at four different sites (#1 in Zone 1; #32 in Zone 3; #79 in Zone 4; #100 in Zone 5) are shown for the total length of simulations (i.e. until t = 5 s) in Figure 6-15, a) and for the initial stage (i.e. until t = 1 s) in Figure 6-15, b).

The superheat values regularly oscillate (due to activation of the nucleation sites) between ~ 0.6 and ~ 1 K (equal to the activation superheat) with a maximum superheat variation of ~ 0.4 K, which is smaller than the sensitivity for the sensors currently used for experiments at the University of Edinburgh (Section 4.2). It is clear that after an initial transient period (which lasts approximately 0.5 s), all the four sites have very

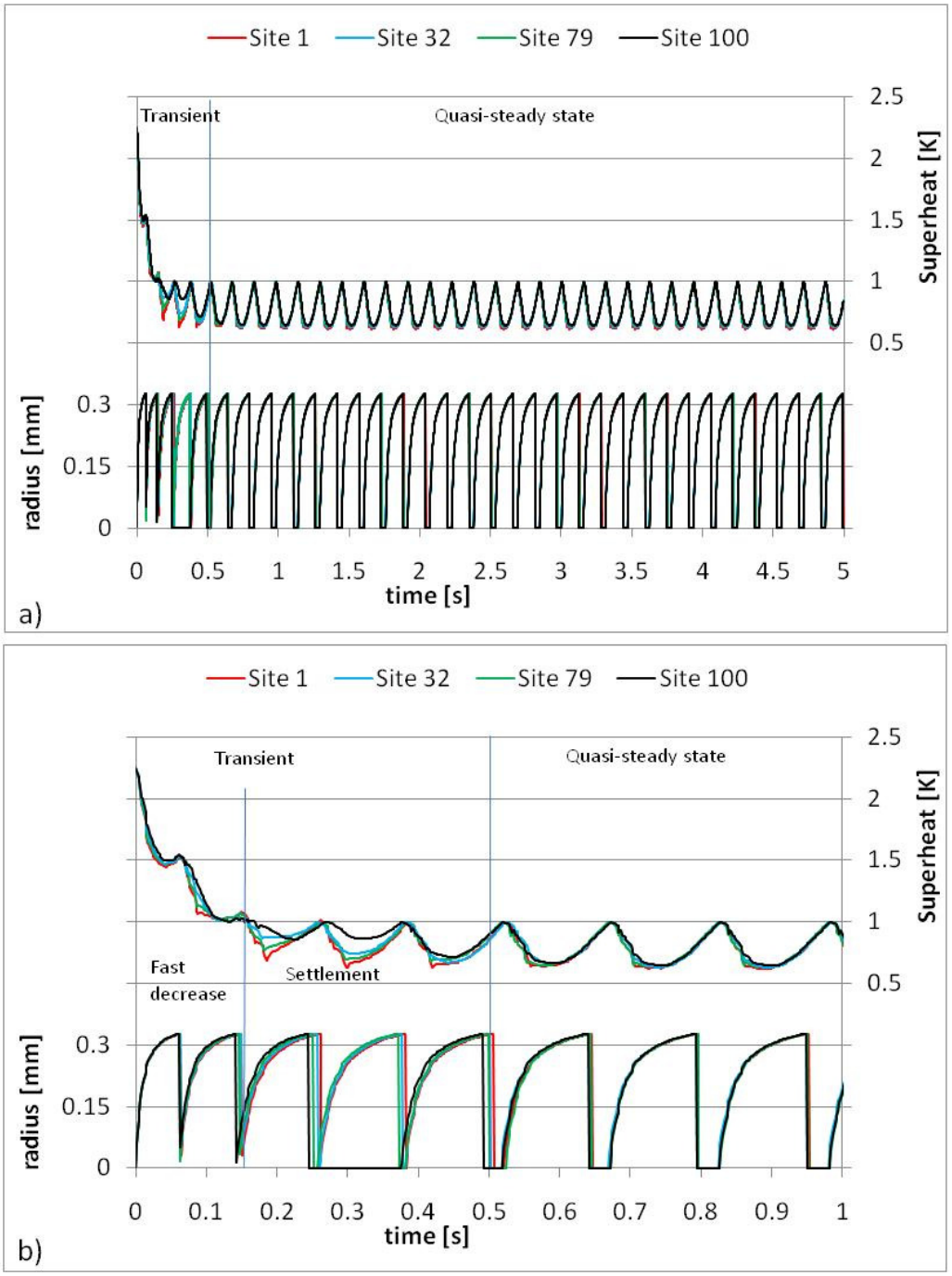

Figure 6-15: Superheat variation at the nucleation site and bubble growth histories for the nucleation sites #1, #32, #79 and #100

similar superheat variations, so that they may all be assumed to activate in phase. The oscillation period is approximately 0.155 s, corresponding to the period of the bubble (including growth time and waiting time, which is not negligible in this case as in the case of a single isolated bubble). The regularity in superheat oscillations suggests a strong thermal interaction between the nucleation sites, due to the high thermal capacity of the substrate. For the initial transient period, two phases can be identified. During the initial fast superheat decrease (t < 0.15 s), the superheat quickly drops from its initial imposed value of 2.25 K to ~ 1 K. This phase is followed by a settlement phase (0.15 s < t < 0.5 s), where the superheat starts to regularly oscillate below its maximum value (1 K). In this case, the maximum superheat variation for each site increases with the site identification number, and consequently with the distance from the centre of the substrate. The sites with lower identification numbers have variations similar to those during the quasi-steady state, while the others are initially more affected by the edge effects.

The 2-dimensional superheat distribution at t = 2.278 s for the entire area (including the area covered by unrefined sites) is shown in Figure 6-16, when the superheat is approximately at minimum for all the sites. There is a strong edge effect. Although the difference in time-averaged superheat between the corners and the centre is only approximately 0.1 K, this is 10% of the activation superheat.

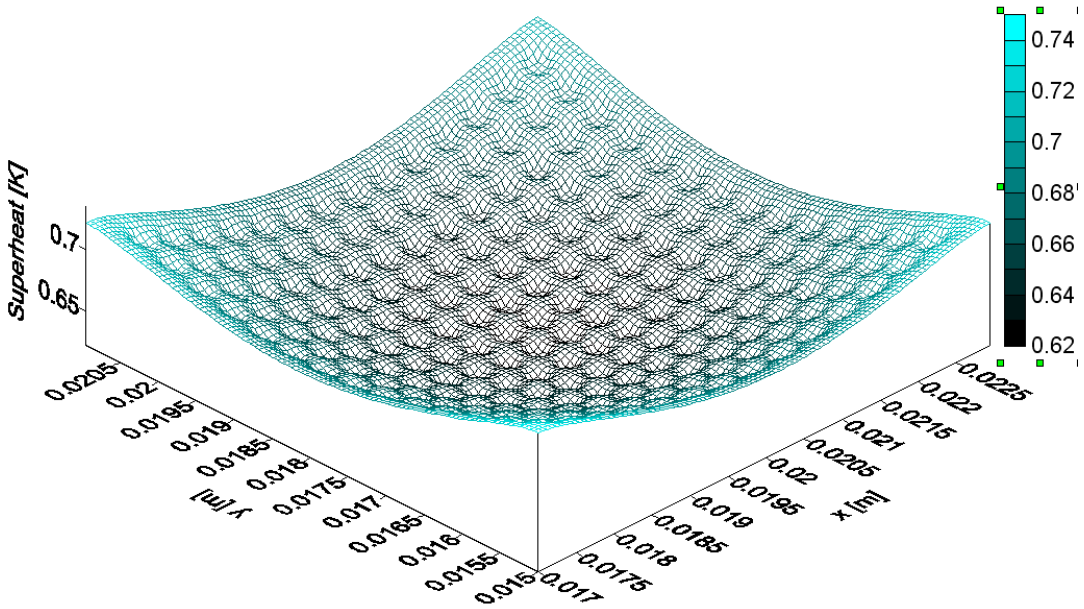

Figure 6-16: 2-dimensional superheat distribution at t = 2.278 s

The bubble growth histories are also shown in Figure 6-15. Site # 100 is the only one that does not become active between 0.25 and 0.36 s. This site, located at the corner of the area covered by standard nucleation sites (surrounded by 3 standard sites and 5 unrefined sites, as it can be seen in Figure 6-14) is more subject to the edge effects, and the average temperature in this area is higher than in the central region, as it can be seen in Figure 6-16. This fact determines the missed activation: however, the superheat continues to oscillate due to the effect of the surrounding sites, so that the site normally activates in phase with the others starting from the following bubble growth cycle. Afterwards, for all the cases, the bubbles grow perfectly in phase.

The superheat variations at different time steps (t = 0.1, 1.8, 3.1 and 4.9 s) along a line passing through the centre of site #1 is shown in Figure 6-17 and compared with the simulated bubble profiles for the bubbles growing at the sites located along this line (#2, #6, #11, #19, #28, #40, #53, #69 and #86, as shown in Figure 6-14). Also in this case, the bubbles appear to grow in-phase. For t = 0.1 s, the superheat ranges from ~ 1.18 K at the edges of the standard sites area (x = 17 and 23 mm) to ~ 1.06 K at the centre of the plate (x = 20 mm), with a distribution similar to the one shown in Figure 6-16. For larger simulated times, the superheat distribution becomes flatter and the superheat stays always below 1 K. For the three remaining cases (t = 1.8, 3.1 and 4.9 s) the average value of superheat and its variations along the line depend on the bubble size: for smaller bubbles, (t = 1.8 s) the difference between the centre and the edges is larger

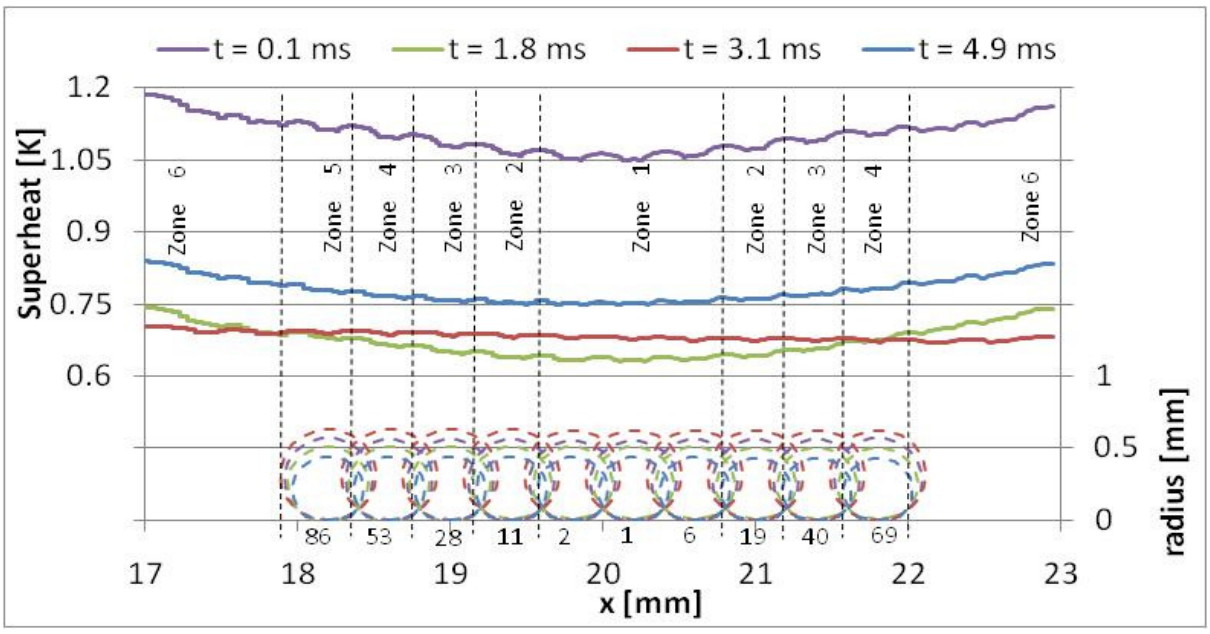

Figure 6-17: Superheat distribution along a line passing through the centre of the plate when the uncertainties parameters are not used

than for the other two cases. Instead, when the radius is close do its departure values (as for t = 4.9 s), the superheat distribution is flatter due to the small contact areas with variations mostly at a very local level due to the high *HTC* at the contact line. These small variations are also visible in the region outside the standard sites region (i.e. in Zone 6), because of the presence of the unrefined sites, although the bubbles growing at the unrefined sites are not shown.

The bubble radii for the standard nucleation sites at different times (t = 0.1, 1.8, 3.1 and 4.9 s) are shown in Figure 6-18, respectively a), b), c) and d). The site #1 is coloured in red in order to be distinguished from the others. Only the area covered by

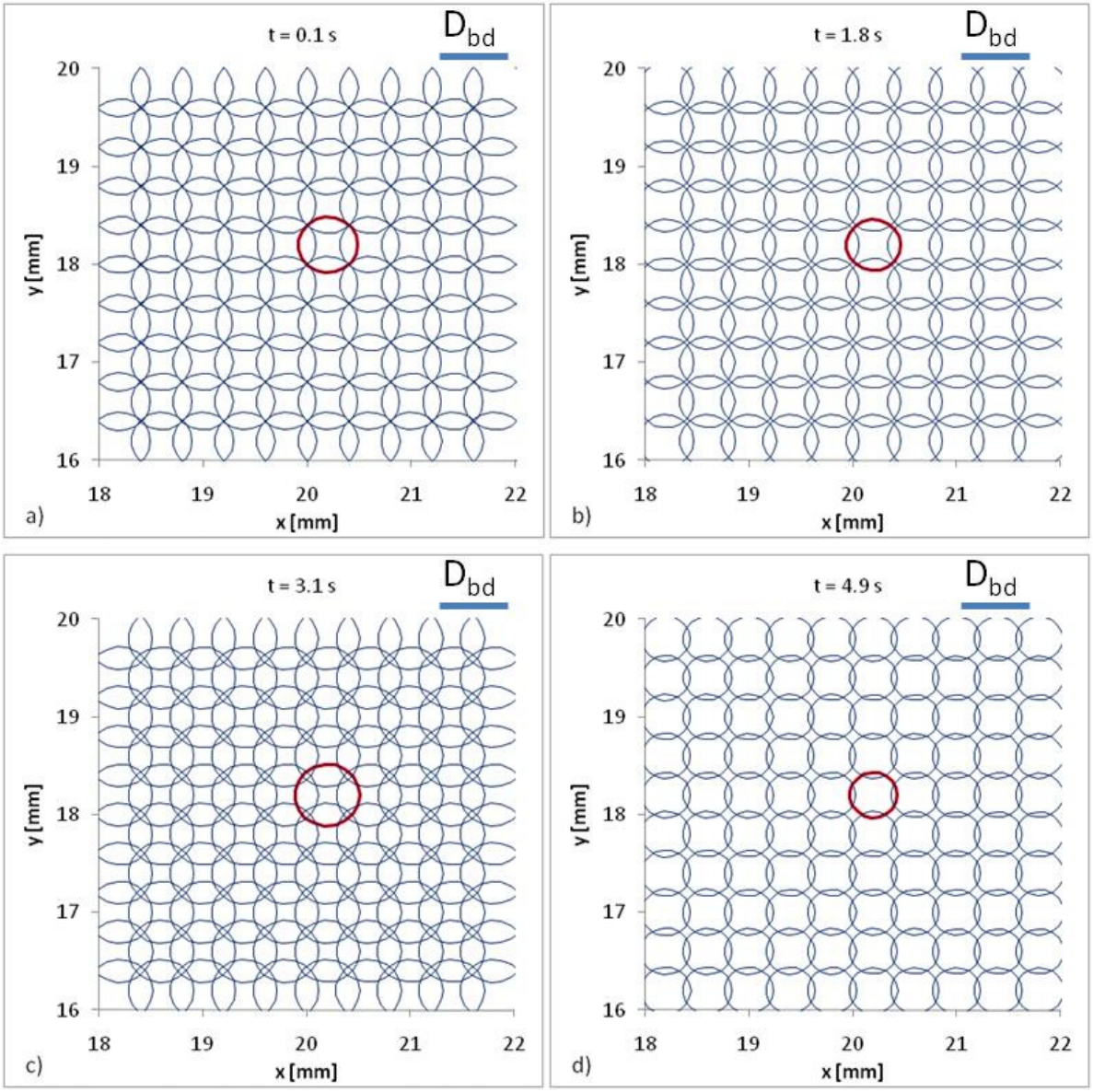

Figure 6-18: Bubble distribution at the standard sites at different time steps when the uncertainty parameters are not used

refined sites is shown. The figure aims to reproduce the distribution of growing bubbles as if seen from above the top surface, so that each circle represents the effective radius at the specified time step.

At t = 0.1 s (a), the bubble radius is ~ 0.28 mm. The domes of the bubbles interfere so that per each site multiple coalescence type C1 occurs (see Section 3.2.4). The analysis of occurrence and frequency of coalescence will be analysed in the following paragraphs. However, since the model for the modification of the heat transfer coefficients between the upper surface of the substrate and the liquid due to coalescence was not included in the code, the coalescence model does not alter the bubble growth. For the bubble growths at the following time steps (Figure 6-18 b, c, d), it is shown that all the sites have approximately the same radius, equal to 0.26 mm for t = 1.0 s, to 0.31 mm for t = 3.1 s and to 0.23 mm for t = 4.9 s. This graphical visualization of the bubble distribution at different time steps will assume particular importance when the uncertainties parameters for the bubble departure radius and activation superheat are introduced (Section 3.2.4). In that case, these parameters will determine a loss of regularity so that a visualization of the bubble growth at different time steps may help in the identification of creation of clusters of sites or of dry patches.

Activity of the sites

From analysis of Figure 6-15, the four sites do not become active the same number of times, as site #100 activated once less during the transient period. The activity of this site is ~ 6.6 activations/s if the entire simulation time is considered and ~ 6.4 activations/s if only the events during the quasi-steady state while are accounted. For the other sites, the activity values in the two cases are respectively ~ 6.8 and ~ 6.4 activations/s. Figure 6-19 graphically visualises the activity of all the sites according to their position. A circle is associated with each nucleation site, with the radius a scaled valued representative of the activity of the site itself. As previously said for Figure 6-18, the importance of this figure increases when irregularities in activation occur. However, in this particular case, the distribution appears very regular, with all the sites having the same circle radius. Also in this case, the central site is indicated in red, and its activity is indicated in the legend.

The bubble period, growth time and waiting time per each site, averaged over the entire simulated time (t > 0 s) and over the quasi-steady phase, i.e. after the transient time (t > 0.5 s), are shown in Figure 6-20. The growth time considering the whole simulation time ranges from ~ 123 ms for site #1 to ~ 119 ms for site #100, with its minimum value equal to ~ 117 ms for site #91. When only the quasi-steady state phase is considered, the values are generally increased of ~ 3-4 ms. The increase effect is due to the larger superheat during the initial phase, which determines a higher heat transfer rate at the base of the bubble and consequently a faster bubble growth. The growth time is seen to have a general decrease with the identification number of the site, and then with the zone to which the nucleation site belongs (then approximately with the distance from the centre). However, per each zone, the growth time slightly changes with the position, with a minimum at the corners of the zone itself. The waiting time has an opposite variation with the site position, with a general increase with the identification number (and then with the zone) and local maximum at the corners. The waiting time ranges from ~ 24 ms fro site #1 to ~ 30 ms for site #100, when the whole simulated time is considered. Only four sites located at the corners of zone 5 and close to the unrefined

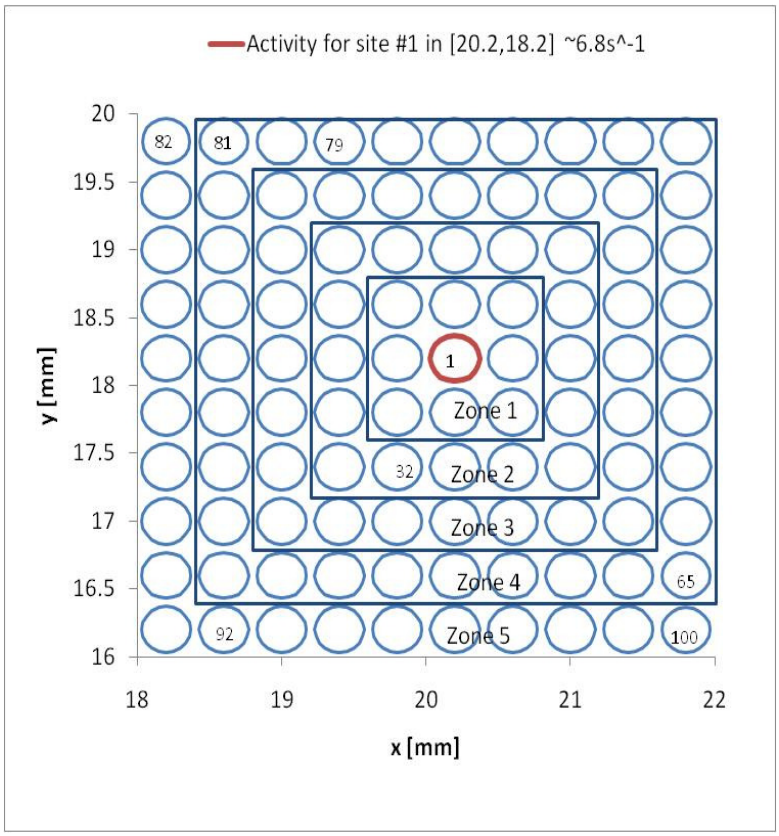

Figure 6-19: Activity of the nucleation sites over the whole simulated time

sites area (#65, #81, #82 and #100, compare Figure 6-14 for their position) present a much larger waiting time, due to the skipping of one activation cycle as previously shown for site #100 in Figure 6-15. However, when the transient time is not considered, the average waiting time increases by ~ 4 ms, and the irregularity shown by the four mentioned sites disappears.

For all the sites, the total period is constant for both the whole simulation (~ 147 ms) and the quasi-steady phase (~ 155 ms), with the exception of the four sites mentioned before when considering the whole simulation, for which the same irregularity shown for the waiting time is present.

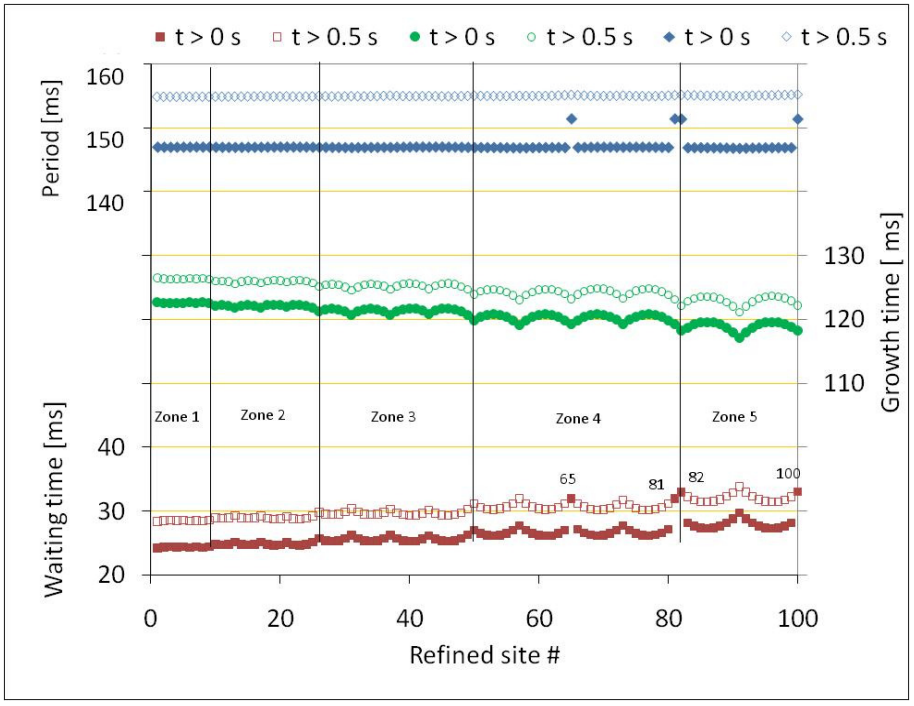

Figure 6-20: Average growth time and waiting time per each nucleation site

Horizontal coalescence

The occurrence of the type C1 of coalescence (i.e. the one involving bubbles of similar radii) is graphically shown in Figure 6-21. The circles are only representative and do not correspond to any particular instant of the simulations, but they are used only to more clearly identify the sites. Each line connecting two sites represents the frequency of coalescence. In this case, all the sites have a very similar coalescence occurrence. For the central sites (i.e. those with identification number lower than 65), each site coalesces with all the eight surrounding sites at each bubble growth. Sites #73, #82, #91 and #100 coalesce only with the three standard sites located around them (coalescence between standard and unrefined sites is not included in the model), while all the others coalesce with five sites. Also in this case, the utility of the figure increases with the loss of regularity as it occurs in the next case when the uncertainties parameters for the bubble departure radius and the superheat activation are introduced.

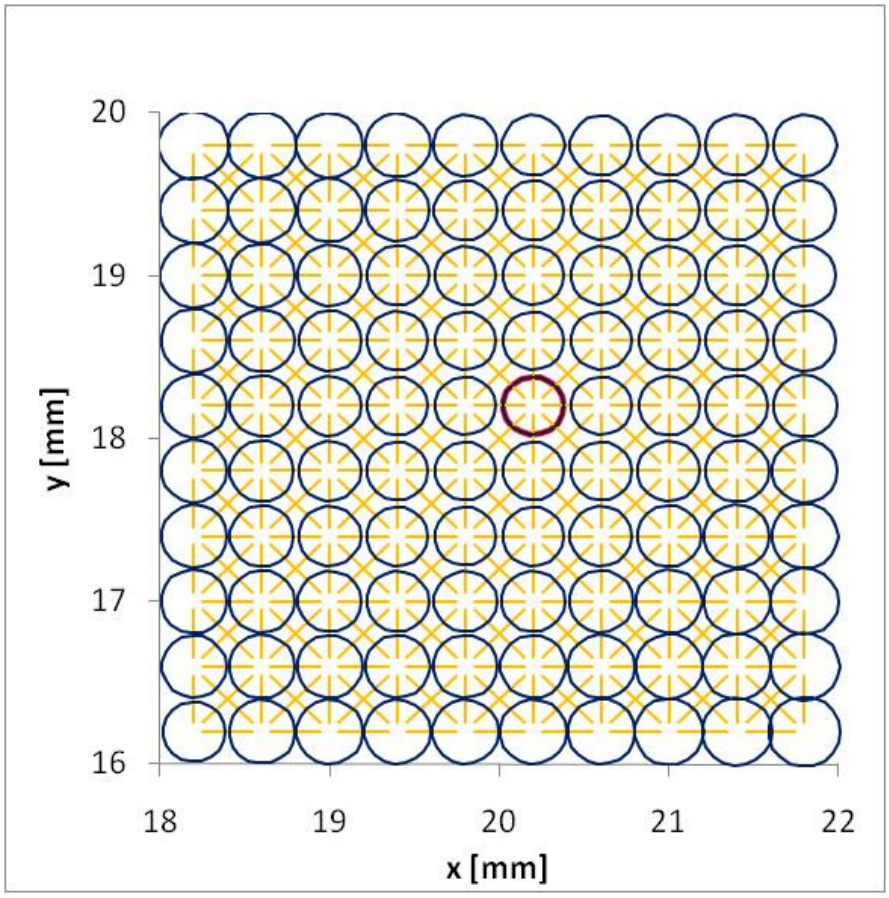

Figure 6-21: Occurrence of coalescence type C1

6.2.2. *Nominal values for activation superheat and bubble departure radius values*

This case differs from the previous because of the introduction of the uncertainty parameters in the values of bubble departure radius and activation superheat. The uncertainty parameters will be imposed equal to 10% of the nominal value. This means that for each of these two parameters, for each nucleation site and each time that this becomes active (except for the first activation) a random value is automatically and independently chosen by the code for the parameter, in a range ±10% of the nominal value. The value was chosen from the analysis of experimental results developed at the University of Edinburgh (Hutter et al., 2009) and it has been introduced to explain the importance of taking into account the uncertainty in the input data in the code. It must be noted that the uncertainty value applied to the superheat is a fraction of the superheat itself, so that its value can never be lower than zero (that would lead to the unrealistic case of an activation temperature lower than the saturation temperature). The simulations were run this time to simulate 10 s, in order to allow a better statistics respect to the previous case (when a long simulation was not required due to the regularity of the bubble growth). The total computational time was approximately equal to 120 hours, equivalent to ~ 12 hours per simulated second. As before, the effects of the site distribution on the superheat distribution and variations, on the bubble growth, on the activity of the sites and on coalescence will be studied.

Superheat variations and bubble growth

The superheat variations at the nucleation site and the bubble growth histories at four different sites belonging to different zones (#1 in Zone 1; #32 in Zone 3; #79 in Zone 4; #100 in Zone 5, the same analysed for the previous case in Figure 6-15) are shown for the total length of simulations (i.e. until t = 10 s) in Figure 6-22, a) and for the initial stage (i.e. until t = 1 s) in Figure 6-22, b). Also in this case the transient (t < 0.5 s) and quasi-steady state (t > 0.5 s) phases are easily recognizable from the analysis of the superheat variations. For the transient phase a fast decrease phase (t < 0.15 s, where the superheat quickly drops from its initial value of 2.25 K to ~ 1 K) and a settlement phase (0.15 s < t < 0.5 s, where the superheat slightly oscillates around its average value) can be identified. However, this case greatly differs from the previous one without uncertainties: the maximum superheat variations, already during the quasi-

steady phase, are smaller than 0.11 K, approximately 0.275 times smaller than for the case without uncertainties. This leads to a much flatter superheat distribution for the whole surface. However, in this case, the average superheat is larger (~ 1.05 K) than in the previous case (~ 0.8 K), showing a less effective heat removal. This effect is due to a strong thermal interaction between adjacent nucleation sites and to the different bubble sizes (as shown by the different bubble departure radii, which determine also occurrence of horizontal coalescence type C2 (i.e. between bubbles of significantly different size), other than only C1 (similar size) as it occurred in the previous case.

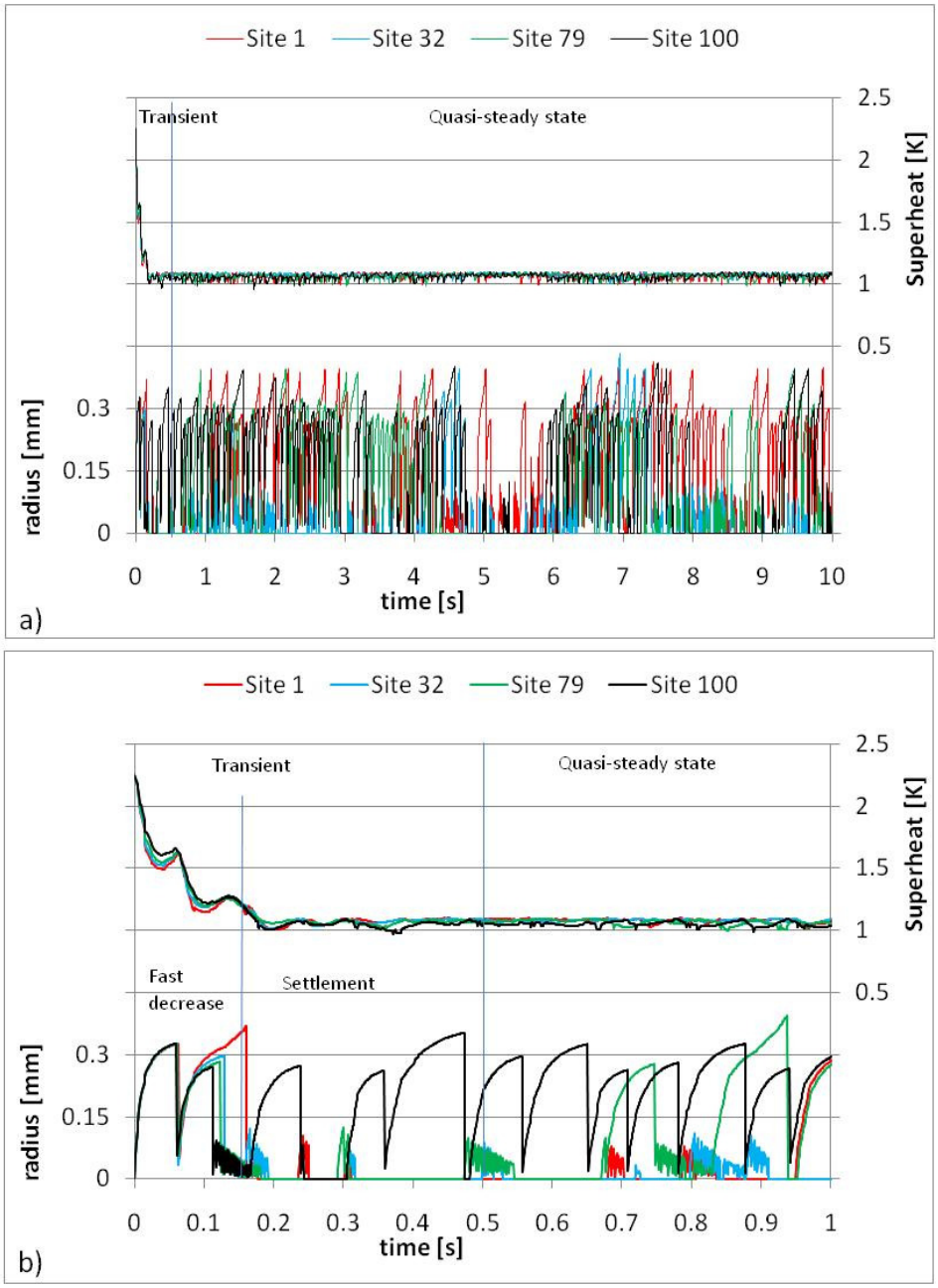

Figure 6-22: Superheat variation at the nucleation site and bubble growth histories for the nucleation sites #1, #32, #79 and #100. Uncertainties = 10%

The bubbles are now growing out of phase (causing the loss in regularity of activation observed in the previous case), due to the introduction of the uncertainty parameters that modify the final bubble size and consequently the heat removal and mesh interaction. In fact, when the bubble departure radius is modified, also the maximum contact area, the mesh radius and refined mesh size are modified, leading to different heat flux contribution both at the base and at the dome of the bubble. Moreover, larger mesh radius could cause interference between refined mesh distributions at adjacent site.

The waiting time, growth time and period of the bubbles depending on the site identification number are shown in Figure 6-23. The values are very scattered, but with the help of exponential interpolation lines shown also in the figure, a general increase of the three variables with the site identification number can be observed. The average value of the waiting time ranges from ~ 4 (site #1) to ~ 11 ms (site #100) while the growth time ranges from ~ 5.5 to ~ 12 ms, but with smaller variations between sites. The bubble period ranges from ~ 10 to ~ 24 ms. However, very scattered values can be observed at specific nucleation sites, with for instance maximum growth times equal to

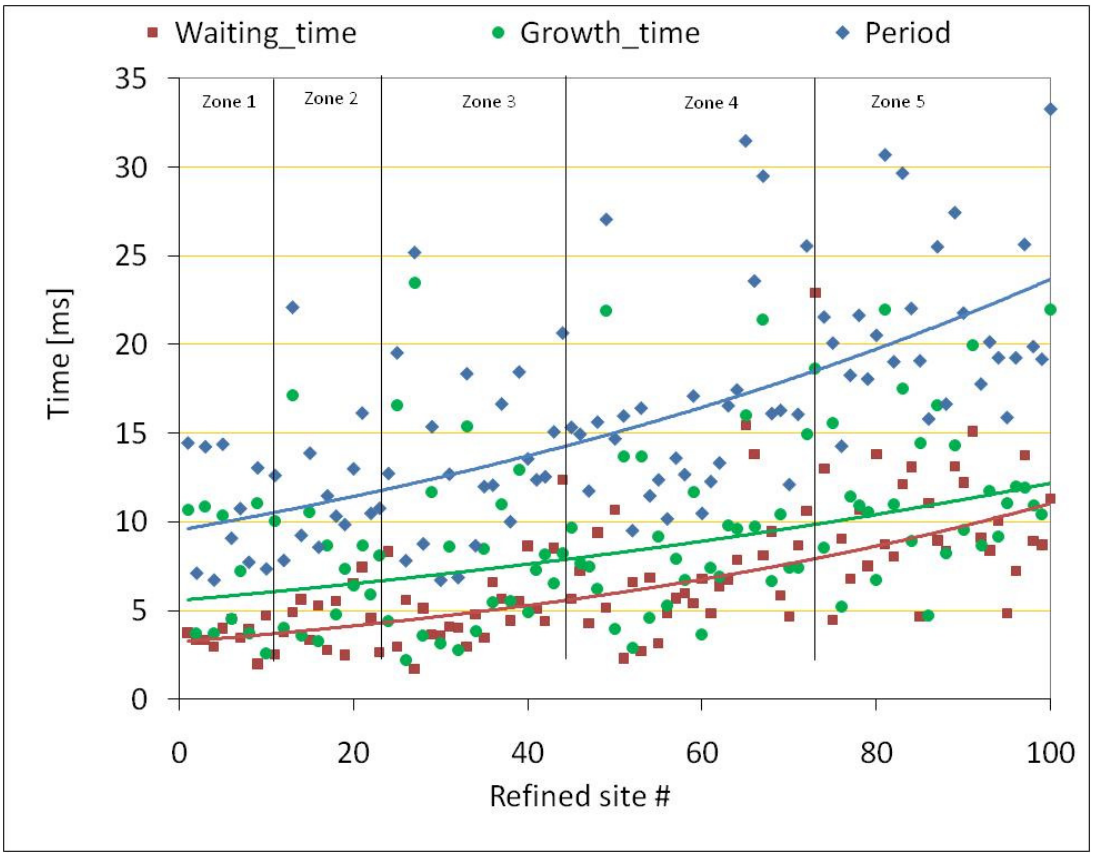

Figure 6-23: Waiting time, growth time and period for the refined sites in case of uncertainty parameters equal to 10%

~ 24 ms (almost double than the average value), due to coalescence phenomena analysed in the following paragraphs.

The bubble distribution at the different nucleation sites is shown in Figure 6-24 for all the active standard sites at different time steps. It is evident that while for the case at t = 0.1 s the bubbles are growing similarly to the previous simulations with no uncertainty parameters, for the other cases, t = 0.2, 2.1 and 9.9 s, respectively a), b), c), the bubble distribution becomes irregular with the bubbles growing out of phase. In fact, at t = 0.2 s the first effects of breaking the symmetry is visible in the central region, although in the external region the bubbles are still growing almost regularly. Instead, at t = 5.3 and 9.9 s, the loss of regularity is complete: big bubbles (also larger than the nominal bubble departure radius) are generally surrounded by much smaller bubbles or by areas where bubbles do not grow at all.

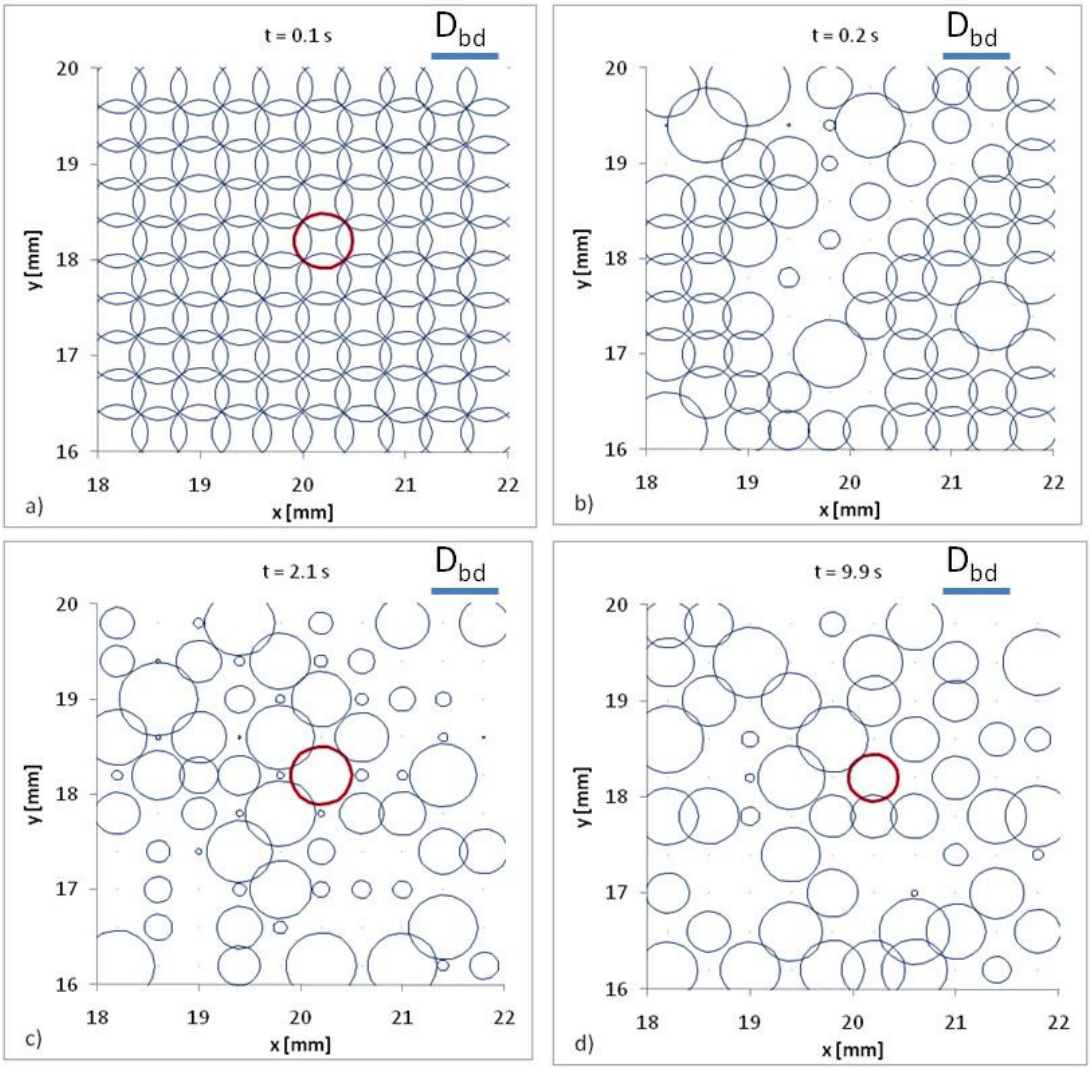

Figure 6-24: Bubble distribution at the standard sites at different time steps when the uncertainty parameters are equal to 10%

The superheat distribution along the horizontal line passing through Site #1 is shown in Figure 6-25 for the same time steps shown in Figure 6-24 (t = 0.1, 0.2, 2.1 and 9.9 s). The superheat distribution at t = 0.1 s appears already not symmetrical, although all the bubbles have similar radii. The difference in superheat is due to the different bubble departure radii that lead to different maximum contact area radii and different triple contact line areas. This determines slightly different heat transfer removal and consequently different bubble growth rates. The asymmetry becomes more evident already at t = 0.2 s mostly in the central region, where the bubbles grow completely out of phase, while for the external region the bubbles continue to grow similarly to each other. At the following time steps, the distribution of bubbles at the active sites becomes more irregular. For specific sites, the local superheat variations interest an area significantly larger than the contact area, as it occurs for instance for Site #11 (x = 19.4 mm) at t = 2.1 s or for Site #19 (x = 21 mm) at t = 9.9 s. This occurs when a bubble grows surrounded by much smaller bubbles or inactive sites: in this area the other sites have a small heat removal capability so that the superheat locally increases. However, local variations between the centre of the nucleation sites and the area outside the contact area are ~ 0.05 K, much smaller than the sensitivity of the experimental sensors currently used at the University of Edinburgh.

From analysis of the bubble growth in Figure 6-22 and Figure 6-24, it seems that

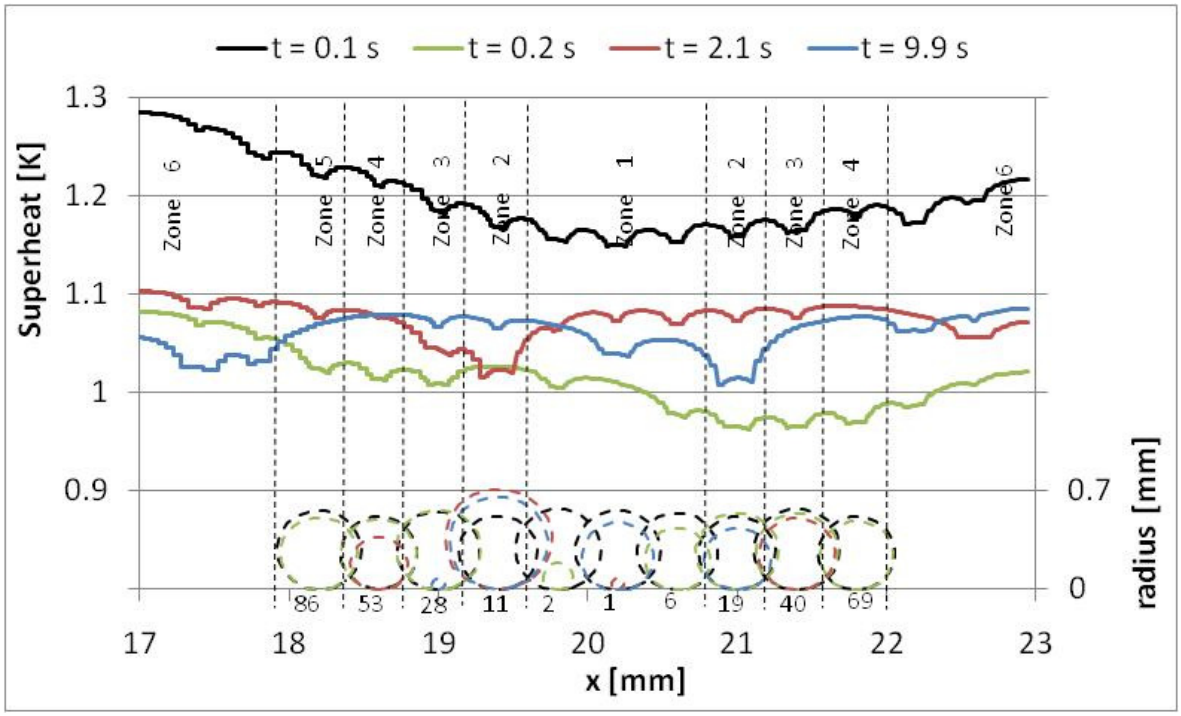

Figure 6-25: Superheat distribution along a line passing trough the centre of the plate

some sites do not become active or produce only very small bubbles (i.e. departing with very small bubble departure radii) due to the presence of large bubbles at close distance, while others have a bubble departure radius significantly larger than the nominal value of 0.33 mm, up to ~ 0.42 mm, much larger than the maximum bubble departure radius when the maximum of the uncertainty parameter is accounted ($0.33 \cdot 1.1 = 0.363$ mm). Moreover, in some cases (as for instance for Site #1 at t ~ 0.5 s and for Site #79 at t ~ 0.95 s), the bubble radius increase rate suddenly changes, due to the increase in volume that occurs when a bubble is incorporated following a coalescence event type C2, according to Equation 3.21, as specifically analysed in the following section. This phenomenon modifies both the contact area (and then the heat transfer through it) and the bubble dome area (and then its heat contribution to the bubble growth).

The 2-dimensional superheat distribution at t = 2.1 s for the entire area is shown in Figure 6-26, at the same time step shown in Figure 6-25 c): it is clear how the superheat distribution is not uniform: some of the nucleation sites determine larger superheat drops, reaching minimum values of ~ 1.01 K, as in the regions indicated by a white arrow, while some other regions have large areas (occupied by several nucleation sites) where the superheat is above 1.1 K, as for instance for the regions indicated by a red arrow.

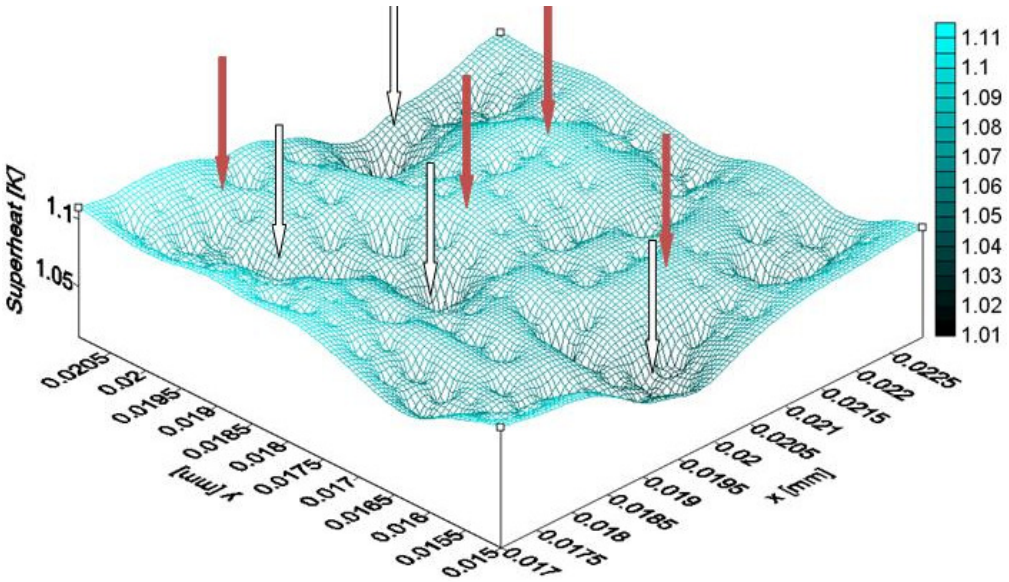

Figure 6-26: 2-dimensional superheat distribution with uncertainty parameters equal to 10%

Activity of the sites

From Figure 6-22 it is clear that all the sites have different activities. However, if the total activity of the sites is analysed during the quasi-steady state, it appears that the sites do not have a completely random behaviour, as it can be seen from analysis of Figure 6-28 a). This figure graphically associates the activity of each site to a circle with the radius representing the activity itself. The total activity takes into account all the times a site becomes active, including also the small bubbles that have to depart due to either the mesh interference or to coalescence type C2 (i.e. for bubbles with similar radii). In this case, it seems that an alternating bubble growth for adjacent sites is present. For instance, the total activity at Site #1 is ~ 274 activations/s, while the closer Sites #2, #4, #6 and #8 have activity equal respectively to ~ 490, ~ 425, ~ 381 and ~ 418 activations/s, ranging from ~ 1.4 to ~ 1.78 times the activity at Site #1. Moreover, it seems clear that the total activity decreases with the distance from the centre, due to the slightly higher superheat towards the edges of the substrates, mostly during the first stage of the simulations. The values of the total activity of each site are shown in Figure 6-27. For the total activity, the decrease effect towards the external region is clear, with an average value decreasing from ~ 350 for low site identification numbers to ~ 150 activations/s for large site identification numbers. The imaginary dotted line connecting the points helps in understanding the alternating effect on activity at adjacent sites. It is also possible to see that the effect is more evident for low numbers for each zone, as confirmed in Figure 6-28. This implies that on the left side of each zone, the difference in activity for adjacent sites is much larger than on the right side.

If only the activity due to the production of large bubbles is counted (i.e. when the bubbles at departure have departure radii larger than 0.1 times the nominal bubble departure radius) the activity drastically drops to values close to the case with uncertainty parameters equal to zero, as it can be seen in Figure 6-28. The average value is approximately 5 activations/s: the activity decrease with the site identification number

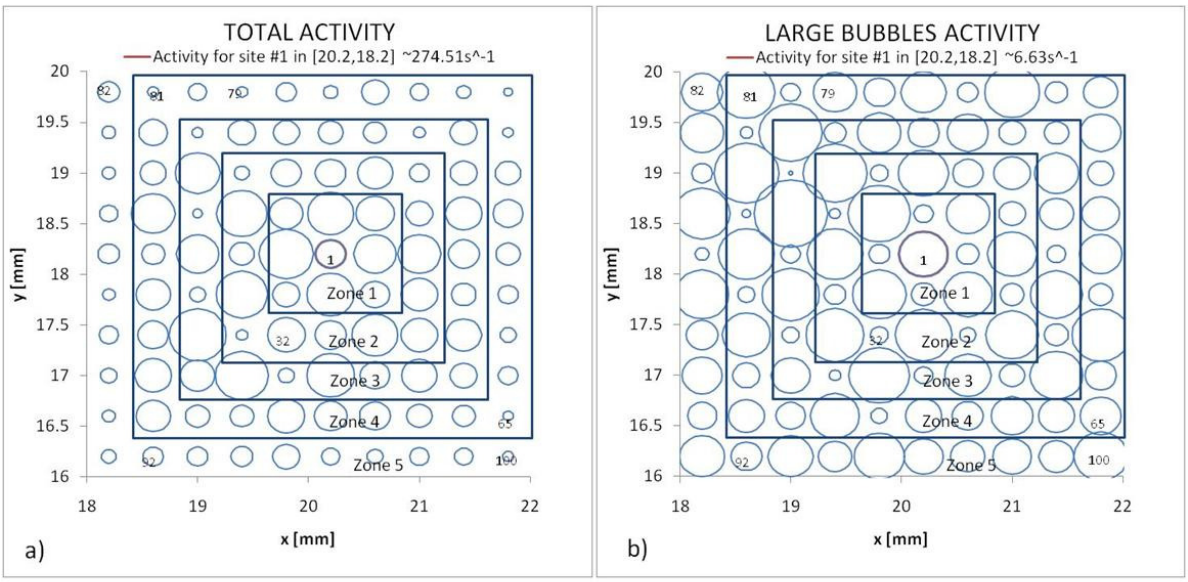

Figure 6-27: Activity of the nucleation sites for all the bubbles and only the large bubbles for the case with uncertainty parameter equal to 10%

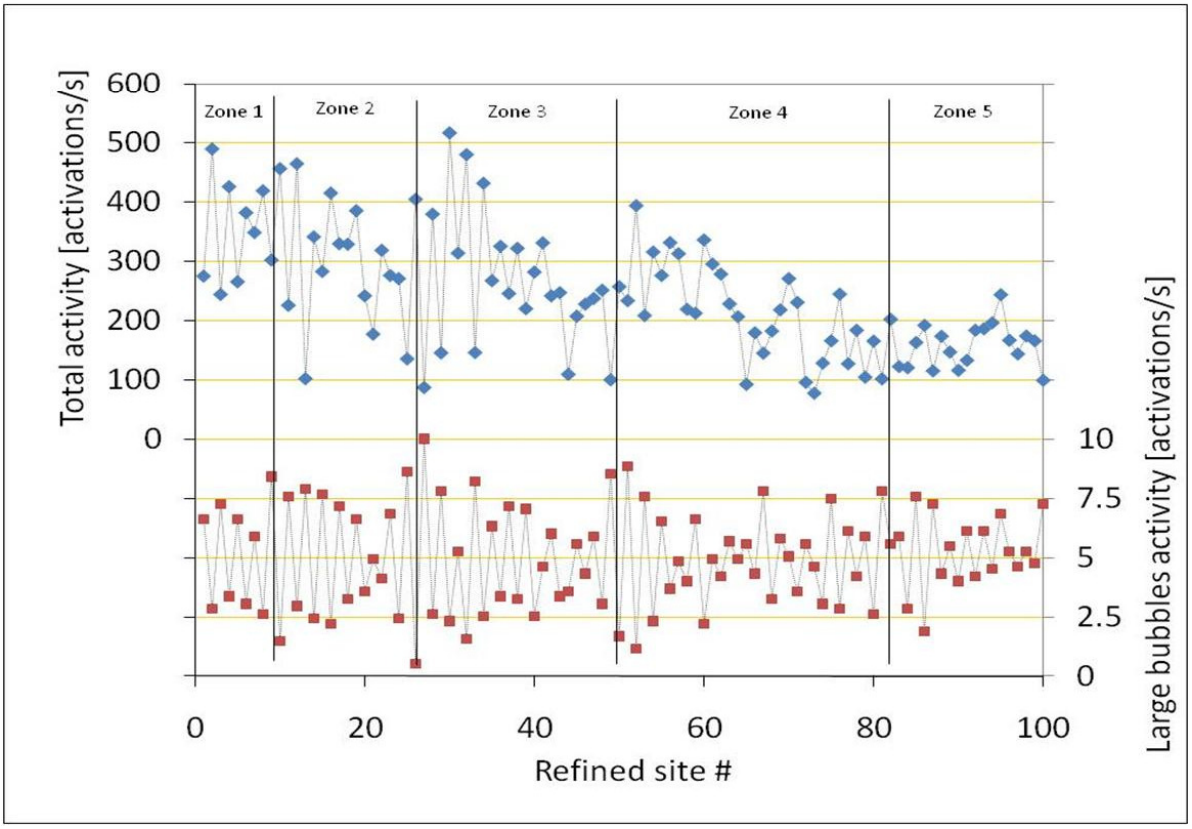

Figure 6-28: Average activity of the nucleation sites during the quasi-steady state when using the uncertainty parameters equal to 10%. a) Total activity. b) Large bubble activity

disappears and the difference in activity for adjacent sites is much larger (if the relative value is considered), ranging from 10 to almost 0 activations/s (leading to percentage variations of 100%). Figure 6-28 b) shows that the alternating effect at adjacent sites is much more evident if only the large bubbles are considered, mostly in the central area, where the difference in the radii of the circles is clear.

Horizontal coalescence

The occurrence of coalescence is graphically shown in Figure 6-29: a) represents the number of events for the type C1, i.e. occurring between bubbles of similar radii, while b) is for the type C2, i.e. for bubbles with a radii ratio larger than 2. Figure 6-29 c) and d) represent the same of respectively a) and b) but restricted to Zone 1. In both cases, the lines represent the mutual occurrence (i.e. either site #i coalesce in #j or vice versa). In both cases, the implemented coalescence models are highly simplified and further studies are required to refine them. However, the following results show that coalescence phenomena may have a large effect on bubble growth and activation of the nucleation sites.

It is clear that most of the events type C1 occur between bubbles at sites not immediately adjacent, while for type C2 the interaction can occur only for immediately adjacent sites, due to the fact that type C2 requires a closer distance to occur. For each figure, the length of the line connecting two sites represents the frequency of occurrence of the type of coalescence between the two sites themselves scaled to the maximum coalescence occurrence value. The circles are used only to better identify the nucleation sites, but they do not refer to any particular instant or bubble distribution during simulations. Sites connected by longer lines represent the ones where coalescence between the two occurred most. It appears that in zone 1 coalescence type C2 has an approximately equal frequency of occurrence. Instead, the type C1 was more likely to occur only for some of the sites. For instance, the occurrence between #1 and #3 is very similar to the one between #1 and #5, and more than double of occurrence between #2 and #4 or between #1 and #4. It must be highlighted that the lengths in the two figures are not comparable since scaled with different parameters.

It also appears that both types of coalescence have larger frequency in the inner region, mostly for type C1 than in some external regions. The frequencies for the coalescence type C1 and C2 for the sites #1 to #10 for the quasi-steady state are listed respectively in Table 21 and Table 22.

.

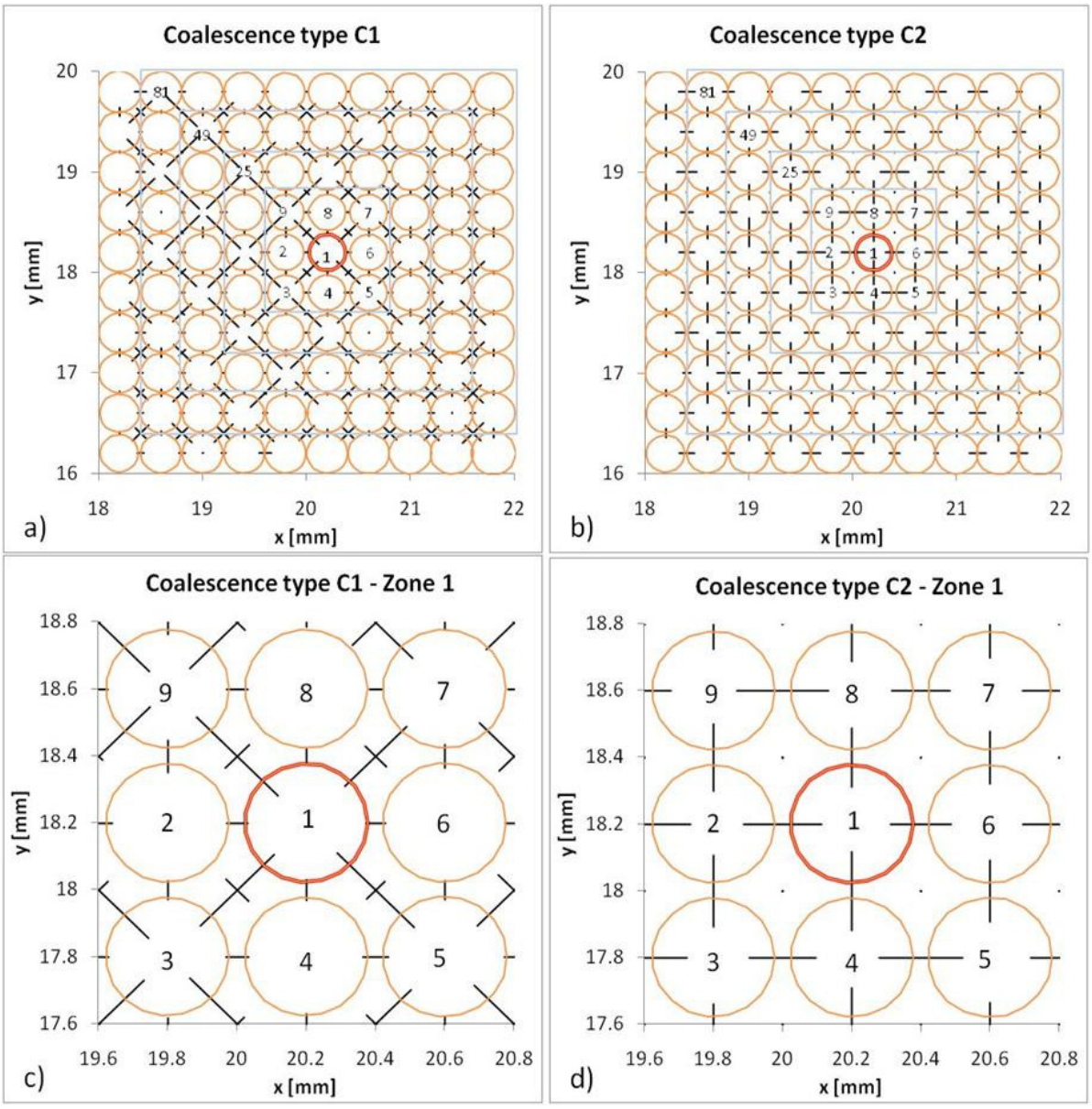

Figure 6-29: Occurrence of coalescence type C1 (a, c) and C2 (b, d)

For type C1, the table is filled only in the upper triangle because the interaction is always mutual between the sites, while for type C2 only the diagonal is left blank (i.e. when #i = #j). The values represent the frequency in events/s. In Table 21, for instance the value at the row corresponding to site #1 and column corresponding to site #3 is 4.95 events/s. This indicates at which frequency coalescence type C1 between #1 and #3 (1 <--> 3) occurs. However, from analysis of Figure 6-29 c), a numerical effect seems to be present due to the numbering of the sites. In fact, the frequency of coalescence for sites with odd identification number is significantly larger than for sites with even identification number, when coalescence with the sites located across the diagonal is considered. For instance, the frequency of coalescence between site #1 and sites #3 or #9 is significantly larger than of coalescence between site #2 and sites #4 or #8. This is connected to the lower activity of sites with even identification number shown in Figure 6-28. In Table 22 instead, at the same position (row #1 and column #3) the value 12.11 events/s indicates only the frequency of occurrence of bubble at site #1 incorporated by bubble at site #3 after coalescence type C2 (but not the contrary, indicated instead in the position at row #3 and column #1).

Table 21: Coalescence type C1 frequencies for site #1 to #10

Coalescence type C1										
	#1	#2	#3	#4	#5	#6	#7	#8	#9	#10
#1		1.26	4.95	1.26	5.16	1.16	4.11	0.84	5.47	0
#2			1.16	1.16	0	0	0	1.26	2.11	0.21
#3				1.37	0	0	0	0	0	0
#4					1.37	1.05	0	0	0	0
#5						1.05	0	0	0	0
#6							1.47	1.26	0	0
#7								0.63	0	0
#8									1.16	0
#9										1.05

Table 22: Coalescence type C2 frequencies for site #1 to #10

Coalescence type C2										
	#1	#2	#3	#4	#5	#6	#7	#8	#9	#10
#1		12.11	0.32	21.16	0.53	14	0.32	13.47	0.32	0
#2	42.53		32.95	0.21	0	0	0	0	26.63	0
#3	0.32	11.37		18.42	0	0	0	0	0	0
#4	36.42	0	28.84		42.74	0.11	0	0	0	0
#5	0.11	0	0	13.68		18.95	0	0	0	0
#6	28	0	0	0.21	26.21		24	0	0	0
#7	0.11	0	0	0	0	13.79		18.11	0	0
#8	29.68	0.21	0	0	0	0.11	23.68		37.68	0
#9	0.32	17.37	0	0	0	0	0	24.74		6
#10	0	0.21	0	0	0	0	0	0	31.79	

From Table 21, the frequency for sequentially numbered sites (for instance 1 and 2 or 2 and 3) is between 1 and 1.5 events/s (for the sites #1 to #10). From Table 22 it is noticeable the asymmetry in the frequency of occurrence of coalescence type C2 (bubble at site #i is incorporated by bubble at site #j with respect to the opposite case). However, if the two events are both counted, the frequency for sequentially numbered sites is approximately equal to values between 37 and 62 events/s (for the sites #1 to #10).

The bubble growths at Site #1 and at the four surrounding sites immediately adjacent (#2, #4, #6 and #8) are shown in Figure 6-30, together with the superheat variations at the nucleation site #1 for the time period between 1.5 and 2 s of simulations. Four different phenomena are visible, indicated with an arrow and identified with the letters A, B, C and D. For the event A (1.585 s < t < 1.65 s) four time steps are identified (numbered from 1 to 4). The bubble growths and the superheat variations along the line connecting sites #2, #1 and #6 are shown in Figure 6-31. For all the case, the superheat variations at the base are very small (less than 0.1 K) and Site #2 never becomes active. At t = 1.585 s (event A1), the bubbles at sites #1 and #6 have similar radii (the one at site #1 is slightly larger) and due to the close distance, the two domes interfere so that coalescence type C1 occurs. However, since the bubble radii for the bubble at site #1 is close to the departure radius, the contact angle and contact area are very small, so that the superheat variations are small as well. When the bubble at site #1 departs at t = 1.59, a new bubble starts growing, and at t = 1.608 s (Event A2),

bubble at site #1 is going to coalescence into bubble at site #6 (type C2, since $r_{b2} < 0.5\ r_{b6}$).

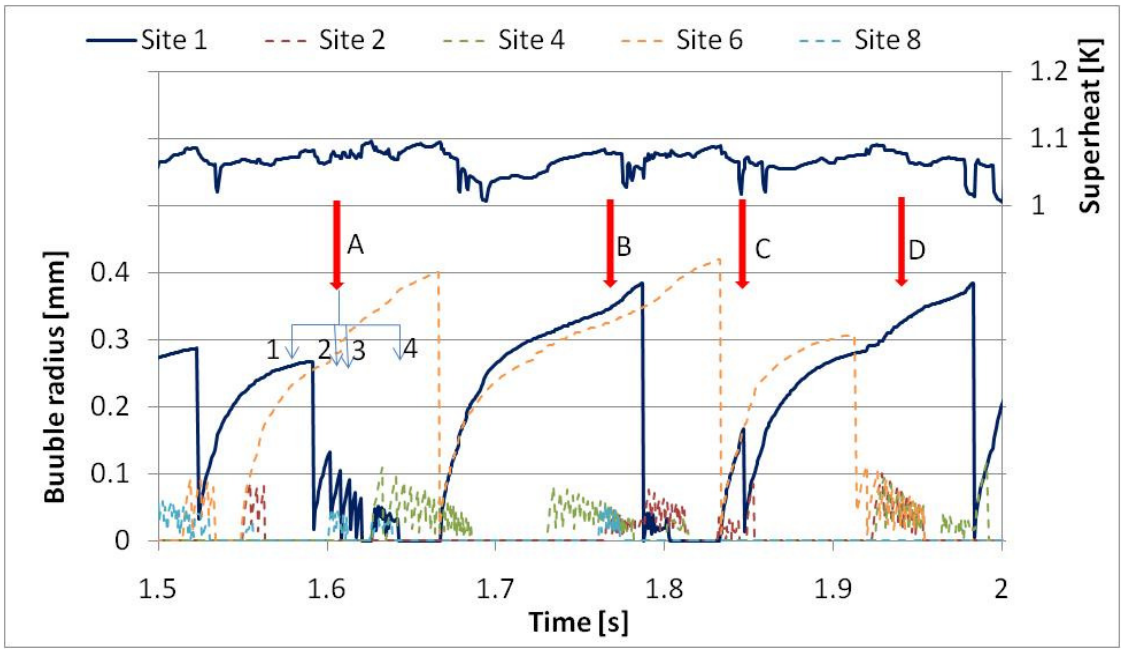

Figure 6-30: Bubble growth histories and superheat variations at Site #1 and the surrounding adjacent sites (#2, #4., #6, #8)

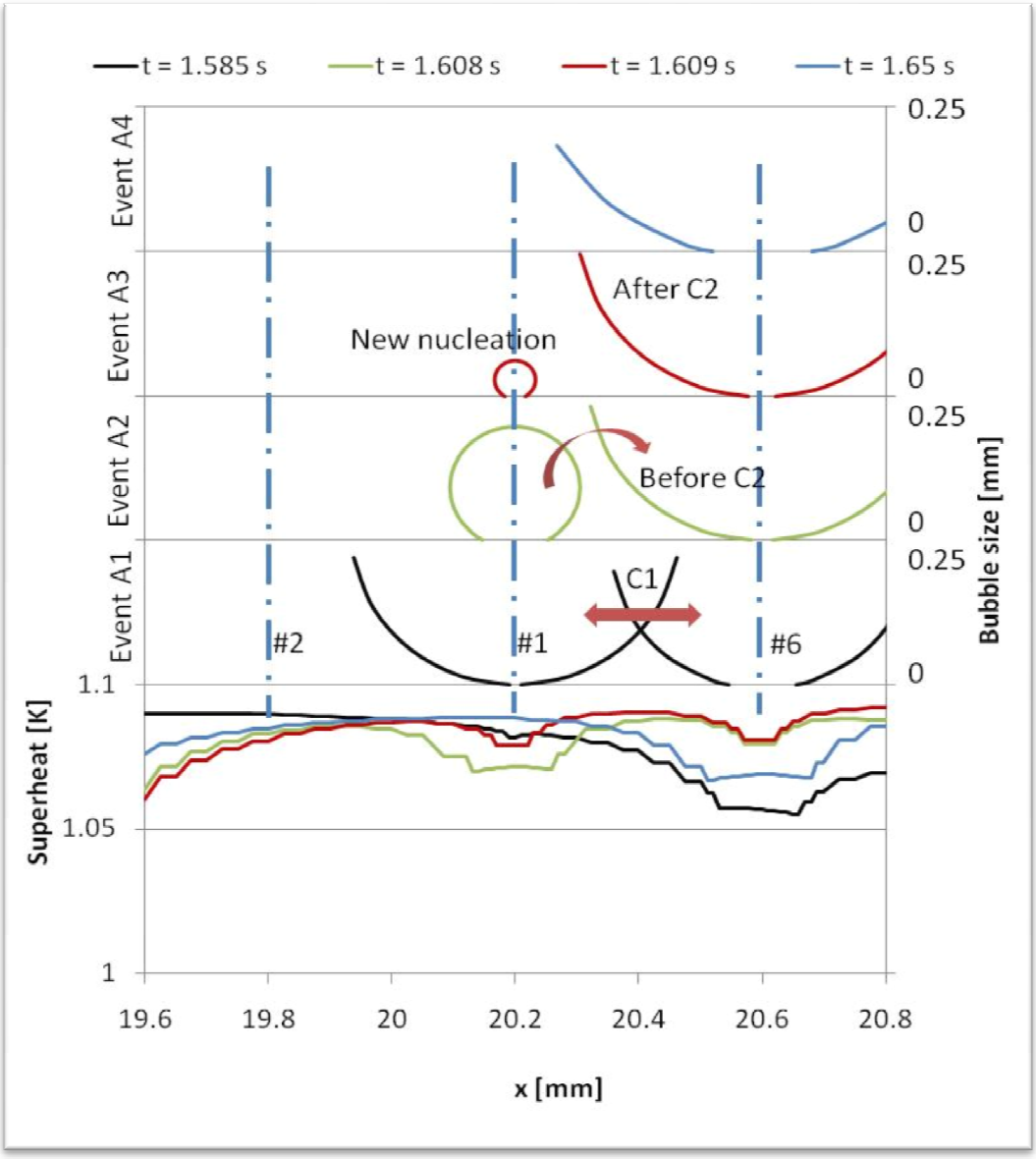

Figure 6-31: Bubble growth and superheat distribution along the line passing through the nucleation sites #2, #1 and #6

This event forces the bubble at site #1 to disappear (after which a new small bubble is here generated at t = 1.609 s, Event A3) and the bubble at site #6 to undergo an increase of the bubble radius and bubble growth rate (Figure 6-30), as well as an increase of the bubble departure radius according to Equation 3.21. The bubble departure radius is further increased by sequential coalescence events type C2, not only of bubbles generated at site #1, but also at site #4 and #8 (not shown in Figure 6-31). During the two events A2 and A3 the superheat variation at site #6 does not significantly change, while at site #1 the variation is larger due to the sudden change in the size of the contact area. At t ~ 1.649 s, site #1 becomes completely inactive: since

the superheat in this area is still larger than the activation superheat (as shown in the upper part of Figure 6-30), the inactivity is due to interference of the refined mesh with the ones of the surrounding sites. At t = 1.65 s, site #1 is shown inactive in Figure 6-31, and the superheat in that region further increased.

Event B is essentially similar to event A2, with bubbles at sites #1 and #6 having both large bubble radii and coalescing (type C1). However, in this case, both bubbles at sites #1 and #6 have incorporated bubbles from adjacent sites following coalescence type C2, as evident from analysis of the bubble growth rate and the production of small bubbles at the other sites. Event C instead represents the case in which site #1 is forced to become inactive because of the limitations in the mesh distribution, according to Equation 3.1. This conclusion is derived by the absence in variation in bubble growth rate or bubble radius for the bubble at site #6 and confirmed by analysis of the coalescence event data. Event D represents the opposite case with respect to event A2, with bubble at site #1 incorporating this time bubble at sites #6, #2, and #4.

6.3. Large distribution of nucleation sites on Titanium immersed in water

This section analyses the effects of a large distribution of 100 potential standard nucleation sites on a thin metal foil (Titanium, 25 µm thick) immersed in water at atmospheric pressure and saturation conditions. In particular, superheat variations across the substrate, activation of the sites and occurrence of coalescence, as well as the possibility of inhibition or seeding of sites due to the activity of neighbour nucleation sites will be studied. The input data for the single bubble growth will be the same used in the validation process (Section 5.3.4): the uncertainties parameters for the activation superheat and bubble departure radius will be set equal to zero in this case so that the nominal values are imposed. A summary of the input data is shown in Table 23.

Table 23: Input data for a large distribution of sites for titanium in water

Substrate [Titanium] 36 x 36 mm²		δ_H 25 µm	ρ_H 4500 $\frac{kg}{m^3}$	c_H 523 $\frac{J}{kgK}$	k_H 21.9 $\frac{W}{mK}$	$\dot{q}$ = 50 $\frac{kW}{m^2}$
Liquid [Water] 1Atm, 100 °C		ρ_v 0.5974 $\frac{kg}{m^3}$	ρ_L 958 $\frac{kg}{m^3}$	c_L 4216 $\frac{J}{kgK}$	k_L 0.677 $\frac{W}{mK}$	H_{fg} 2257300 $\frac{J}{kg}$
Single bubble growth and Heat Transfer	**Exper**	t_g 18.1 ms	r_{bd} 2.665 mm	ΔT_{act} 15.5 K	f_{decr} 0.6	ΔT_{IN} 17.5 K
	Numer	HT model *ML*	HTC_{maz} ~ 80 $\frac{kW}{m^2}$	f_D 1.84	φ_0 30°	Natural convection Eq. 3.7, f_{enh} = 1.42
Numerical data		Δt 0.5 µs	w_{xy} 0.5 mm	n_{vL} 2	n_R 7	*Number of sites* 100 standard

The nominal bubble departure radius is set r_{bd} = 2.665 mm (approximately 8 times larger than the bubble departure radius for FC-72 on silicon) and the growth time t_g = 18.1 ms. The micro-layer model (M*L*) for the heat transfer at the base of the bubble has been selected according to the experimental results analysed in Golobič et al. (2006). However, in this case, the maximum *HTC* has been increased to 80.5828 $\frac{kW}{m^2}$ with respect to the value used during the validation process, ~ 60 $\frac{kW}{m^2}$, in order to allow a smaller initial value of the apparent contact angle (φ_0 = 30°, with respect to the value used during the validation process, φ_0 = 45°). This allows a closer spacing between nucleation sites and then more chances to observe coalescence without incurring numerical limitations due to interference of the refined mesh distribution. The initial value for superheat was set equal to 17.5 K to guarantee conditions similar to the ones described in the validation process for the unaffected area outside the contact area. The simulated metal foil was a square 36 mm long (much larger than for the silicon case, 6 mm) in order to have the same number of standard sites (100) located in a square arrangement with a distance between adjacent nucleation sites *S* = 3.23 mm. This value has been chosen in order to maintain the distance to bubble departure radius ratio used

for the silicon case (1.21). The centre of the plate is supposed in x = 20 mm and y = 18 mm, as it was for the silicon cases analysed in Section 6.2. Moreover, the edge effects are less important because of the lower thermal capacity of the plate for Titanium. The distribution of the 100 refined sites is shown in Figure 6-32. No unrefined sites have been simulated. The dotted line represents only an imaginary line drawn in order to help in identifying the numbering of the sites, ordered as for the silicon case. Five zones were also distinguished (Zone 1, sites 1 to 9; Zone 2, sites 10 to 25; Zone 3, sites 26 to 49; Zone 4, sites 50 to 81; Zone 5, sites 82 to 100). Also in this case, only two vertical layers in which the thickness of the substrate is divided were simulated.

The total length of simulations is 10 s because of the much larger computational times: 22.5 hours per simulated second, approximately 4 times the computational time observed in the case described in Section 6.2.1. This is due to the much larger superheat variations in the metal foil at each activation as observed during the validation process, to the larger dimensions of the substrate and to its smaller thickness.

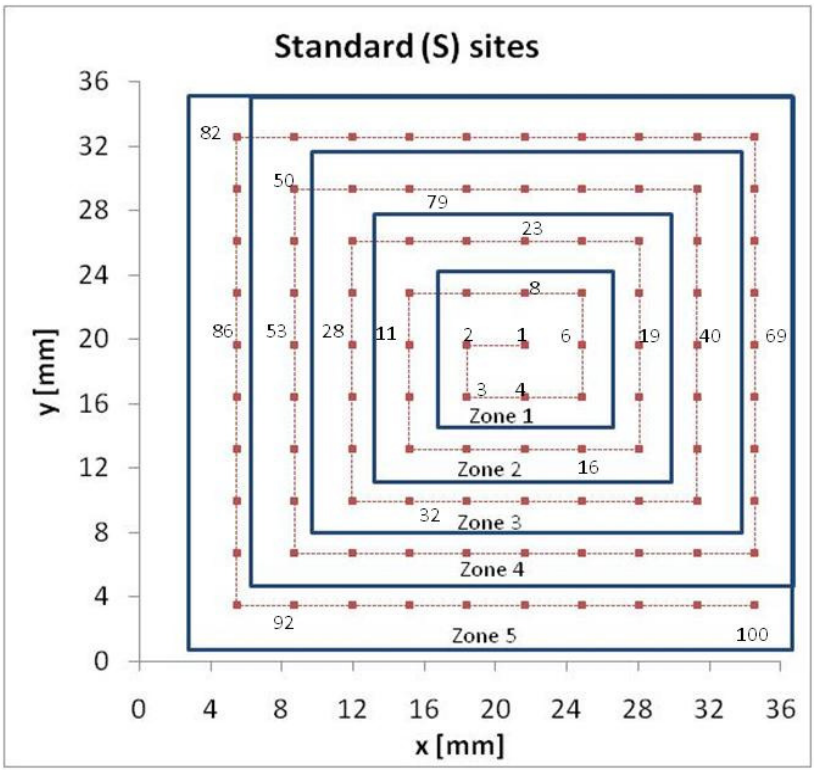

Figure 6-32: Site distribution for titanium immersed in water with distance between sites 3.23 mm

Superheat variations and bubble growth

The superheat variations at the nucleation site and the bubble growth histories for four different sites belonging to different zones (site #1 in Zone 1; #32 in Zone 3; #79 in Zone 4; #100 in Zone 5, the same analysed for the previous case in Figure 6-15 and Figure 6-22 for the silicon cases) are shown for the initial stage (i.e. $t < 0.75$ s) in Figure 6-33, a) and for the final stage (9.75 s $< t <$ 10 s) in Figure 6-33, b). The transient period

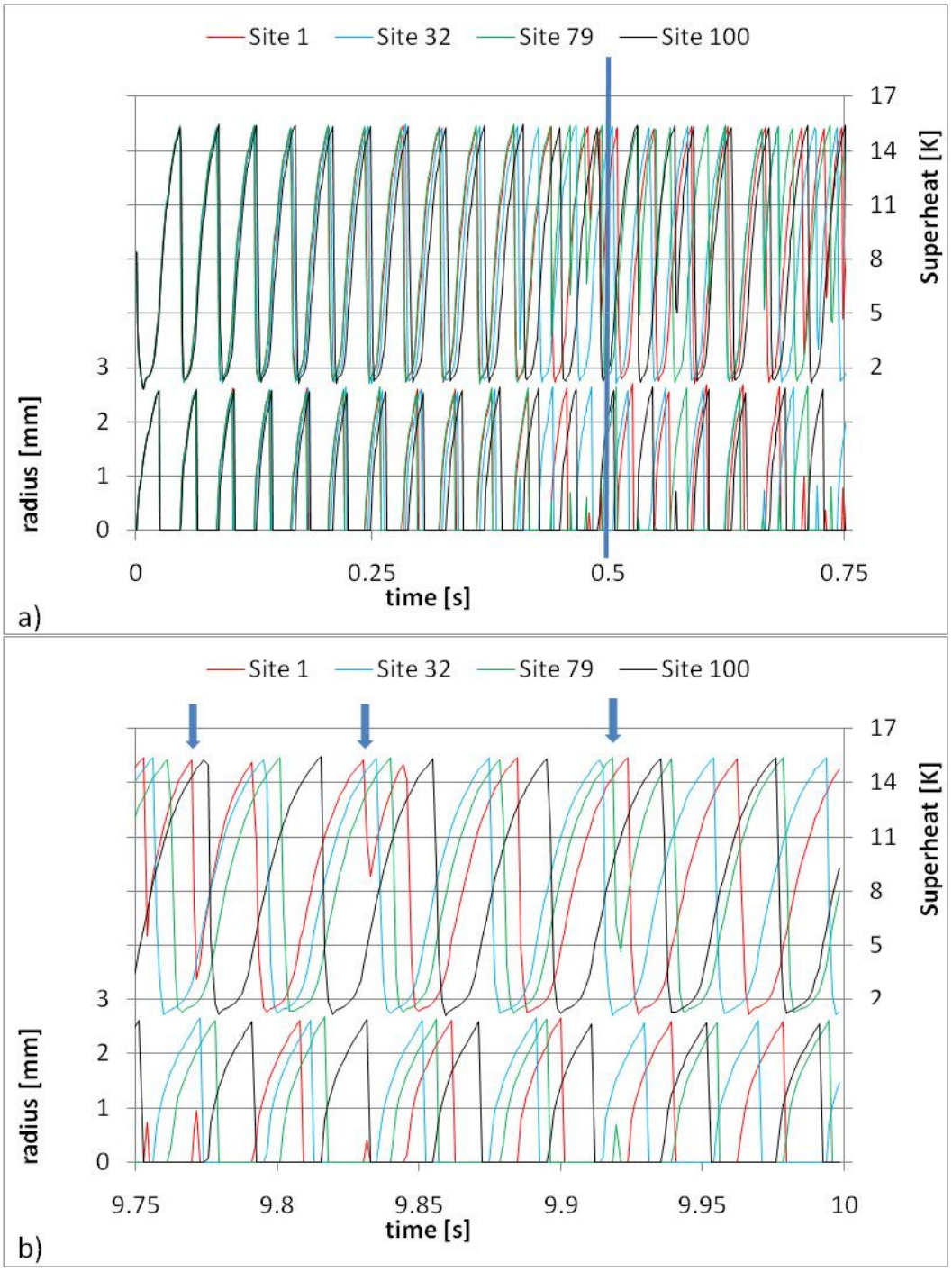

Figure 6-33: Superheat variation at the nucleation site and bubble growth histories for the nucleation sites #1, #32, #79 and #100 on titanium. Uncertainty parameters = 0%

seems negligible in this case, with the superheat at the nucleation site immediately fluctuating between ~ 1.9 and 15.5 K. However, the average values will be considered only for events occurring after the initial 0.5 s, in order to have a comparison with the data previously obtained for the silicon substrate. Moreover, it is after an initial period that the sites seem loosing synchronization in bubble growth, as evident from Figure 6-33. The loss in synchronization is connected to the larger variations in superheat that lead to an average superheat always lower than the activation value (15.5 K) and then to significant waiting times during which the superheat recovers. For this reason, although the sites were arranged regularly and identical input data were imposed, the bubbles seem to grow independently from each other and small thermal interaction effects in the lateral direction across the substrate can be detected. However, the presence of bubbles departing with small radii (indicated with the arrows in Figure 6-33, b, at t ~ 9.77 and ~ 9.83 s for site #1 and at t ~ 9.92 s for site #79) highlights that coalescence phenomena (as analysed in detail in the following section) are taking place. In these cases, the superheat suddenly decreased when the site became active, followed by an increase immediately after departure of the small bubble until the superheat reached the activation value and a new bubble nucleated. This case strongly differs from both the simulations for silicon (with and without uncertainty parameters). In fact, for silicon, when the uncertainty parameters were set equal to zero (see Section 6.2.1), all the sites were synchronized with very regular activations for the entire length of simulations, while for titanium, the loss of synchronization occurs very soon (the bubbles at the four sites grow perfectly in phase only for the first six bubble cycles, $t < 0.25$ s). For the case on silicon with uncertainty parameters equal to 10% (see Section 6.2.2), the sites strongly interacted between each other with occurrence of alternate bubble growth and sequential coalescence, while for titanium it appears that the sites act more independently, and sequential coalescence does not occur. This highlights that thermal interactions across the substrate are much smaller for titanium due to the smaller thickness and lower thermal capacity. Moreover, the presence of departure of bubbles with small radii and consequent variation of the superheat helps in better explaining the flatter superheat for silicon, due to the sequential activation and deactivation of sites.

The dependence of the time-average values for waiting time, growth time and period on the site identification number (and then indirectly on the distance of the site from the centre of the substrate) is shown in Figure 6-34, together with the exponential interpolation lines. It is evident that the three variables increase with the site identification number. In this case, the differences between sites are much less marked than in the case of silicon, and generally negligible. The waiting time ranges between ~ 20 and ~ 23 ms, while the growth time ranges from ~ 9 to ~ 14 ms, with a resultant period ranging from ~ 29 to ~ 37 ms. However, from comparison of these values with Figure 6-33 (b), the growth time to reach the nominal bubble departure radius is significantly larger (~ 19 ms for site #1 and ~ 20 ms for site #100) than the average values. The lowering effect is due to the presence of bubbles departing with small radii. The growth time to reach the nominal bubble departure radius, contrarily to the cases for silicon, is very similar to the case of an isolated bubble: in fact, while for titanium the average superheat variations are not strongly affected by the presence of a large number of sites, for silicon, the average superheat dropped from ~ 8 K for the isolated site (Compare Section 4.2.5) to ~ 1 K for the large site distribution (100 nucleation sites, as shown in Sections 6.2.1 and 6.2.2). This highlights that the thermal interactions

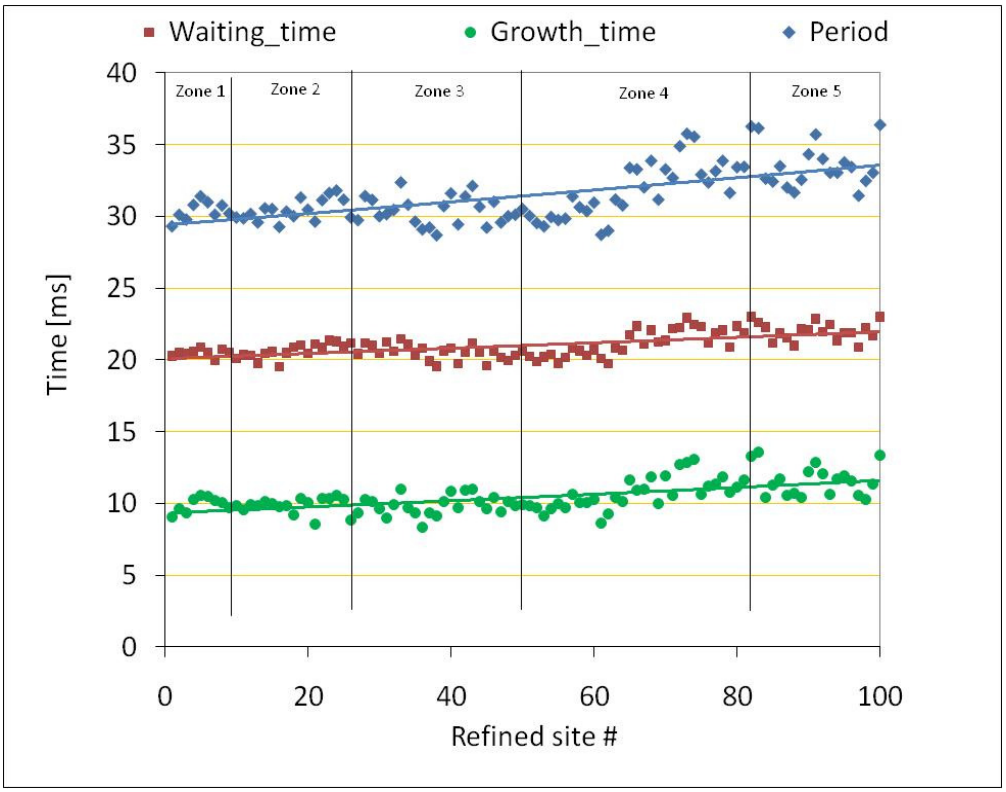

Figure 6-34: Waiting time, growth time and period for the case with titanium and uncertainty parameters equal to 0

through the solid substrate are much stronger for silicon, due to the higher thermal capacity and to the larger thickness.

The bubble distribution at different time steps (t = 0.25, 0.55, 0.65 and 9.5 s) is shown in Figure 6-35. By contrast with the cases for a silicon substrate with uncertainty parameters equal to zero (Section 6.2.1), for titanium foils the bubbles lose the initial synchronization in bubble growth at very small simulated times, as it is evident already at t = 0.25 s, Figure 6-35, a). Here, most of the sites are active, but the radii slightly differ and some of them are inactive, with clear left-right symmetry in activation. The symmetry effect becomes also more evident when the sites start to activate more independently, as it occurs in the central and lower part of the substrate for t = 0.55 and 0.65 s, as highlighted by brown arrows respectively in Figure 6-35, b) and c). However, this phenomenon is visible only until t ~ 0.7 s. A valid explanation of the more marked symmetry in the lower and central part with loss of symmetry on the upper part of the substrate could not be provided. The symmetry itself and the apparent larger activity in the lower part of the substrate during the first stage of simulations may have been generated by a chaotic behaviour of the system. Moreover, it seems that the sites activate in clusters defined for the purposes of this analysis as "groups of close sites with similar bubble growth characteristics", which assume particular geometries, for the entire length of simulations and an example of it is indicated by green arrows in Figure 6-35, d) for t = 9.5 s, although in this case the symmetry is completely lost. A complete analysis of the presence of chaotic behaviour and activation in clusters is beyond the goal of this project. For the cluster analysis precise rules to unequivocally identify the groups acting similarly should be identified. Several studies have been developed also in fields very different from boiling heat transfer, for instance in the field of data mining (Abonyi and Feil, 2007), in marketing studies or in analyses of geographical distribution of diseases (Olsen et al., 1996).

The activation in clusters is shown in Figure 6-36 for t = 1.8 s: the superheat colour map is compared to the bubble size (white dashed line) and the contact area (white continuous line). Several clusters are visible, indicated by the arrows in the figure, most of them with a very small contact area size. The superheat in the inner part of the contact areas is always low, in most cases very close to 1 K (blue areas). The areas around inactive sites have a much larger superheat, some of them already close to the activation value (15.5 K) while others are recovering from previous activations.

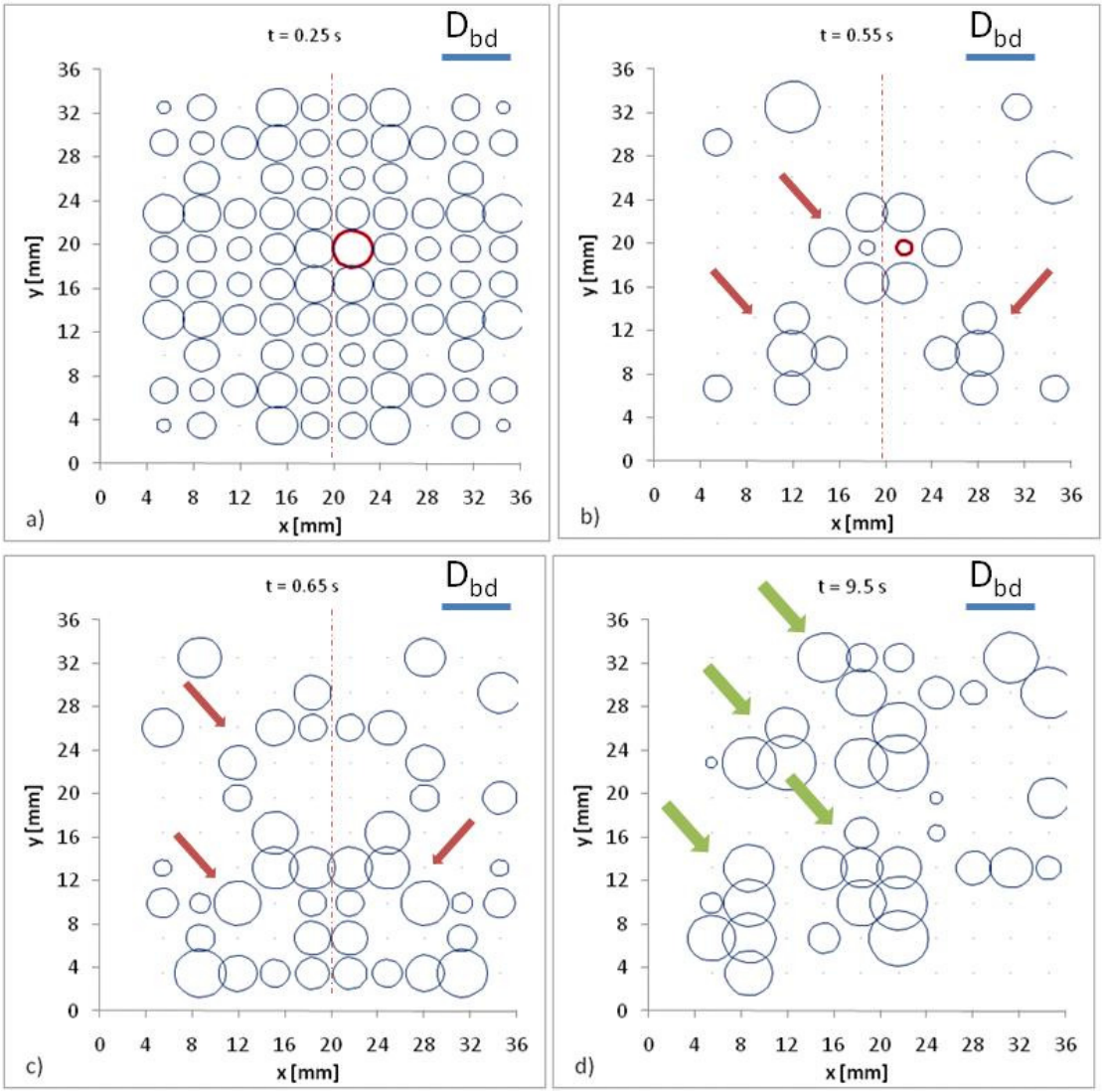

Figure 6-35: Bubble distribution at the standard sites on titanium at different time steps when the uncertainty parameters are equal to 0

The superheat distributions along the line passing through the centre of nucleation sites #1, #2 and #6 at the same time steps shown in Figure 6-35 is shown in Figure 6-37. At t = 0.25 s the ten sites (#1. #2, #6, #11, #19, #28, #40, #53, #69 and #86) are all active and the superheat variations between the regions outside the contact areas and the centres of the sites are very large (~ 15 K). The activation of the sites strongly affects the superheat variations, but its effect is limited in space (the radius of the area influenced by the growing bubble is in this case, as well as for the case with only 7 nucleation sites described in Section 5.3.4 during the validation process, of the order of the distance between nucleation sites) due to the very small thickness of the substrate, which limits the propagation of thermal effects in the lateral direction. The variations are significantly smaller when the bubble size is small (as occurs for instance for site #1 and #2 at t = 0.55 s or for site #6 at t = 9.5 s), and localised to a narrower area around the nucleation site. During the final stage of the bubble growth, the area subjected to large superheat variations is much larger than at the beginning, although the contact area is similar, due to the larger heat transfer removal when the contact area was at its maximum. On the other hand, when the site is not active and the superheat is locally

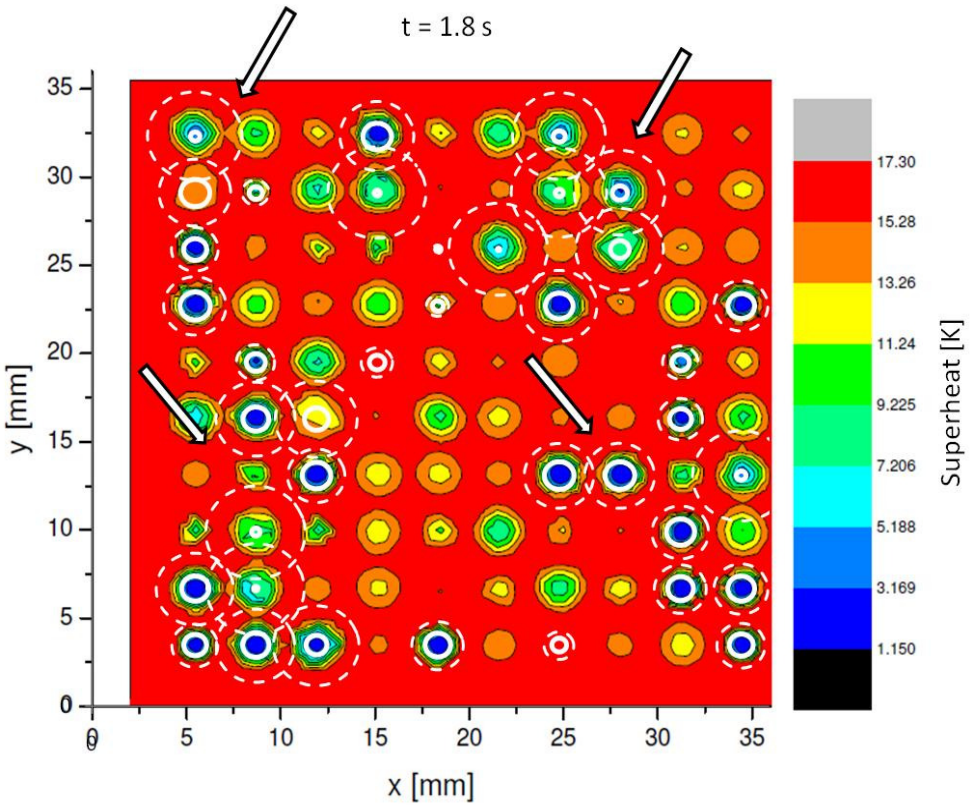

Figure 6-36: Superheat colour map and bubble and contact area radii

increasing to reach the activation conditions again, the variations affect an area similar to the area that is affected by the presence of the bubble. Examples of the superheat recovery period during the waiting times are for sites #19 and #28 at t = 0.55 s or for sites #2 and #40 at t = 0.65 s.

The 2-dimensional superheat distribution for half of the substrate (x > 20 mm) at t = 0.6 s is shown in Figure 6-38. Along the line for x = 20 mm, only sites #19, #28 and #69 are active (as already shown in Figure 6-37), with very large superheat variations (~ 15 K). For the other sites located along the line the superheat is recovering and its variations are smaller than 6 K. The superheat variations for all the other sites are difficult to define from the 2-D distribution, although for some sites (indicated with a brown arrow) the variations are clearly less marked.

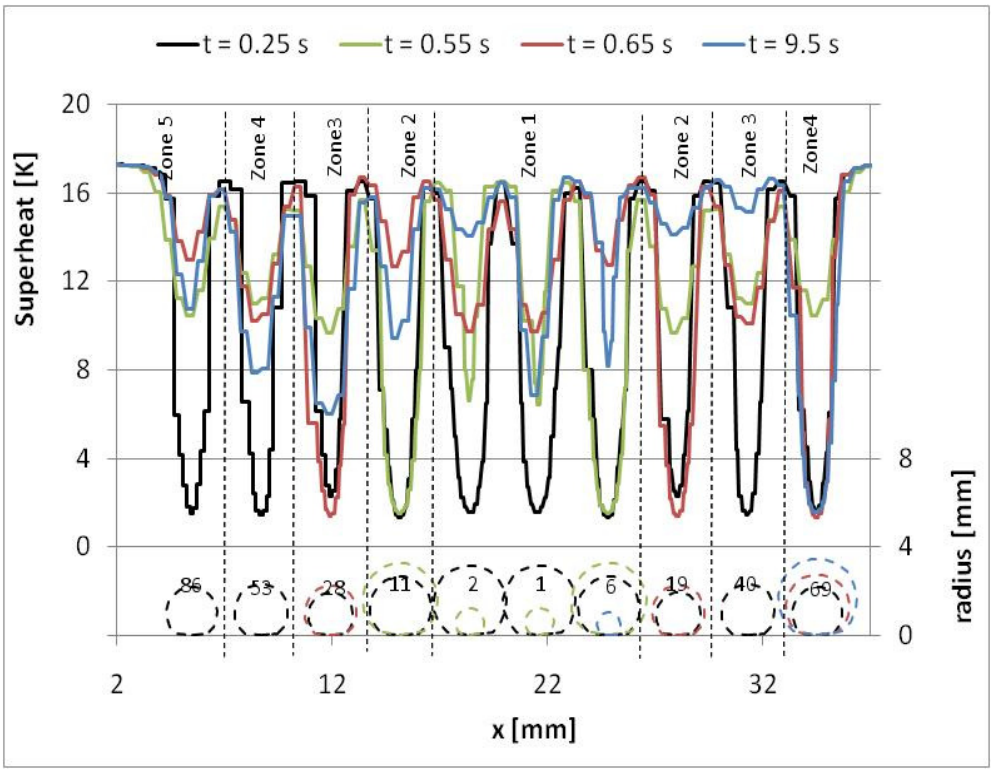

Figure 6-37: Superheat distribution along a line passing trough the centre of the plate

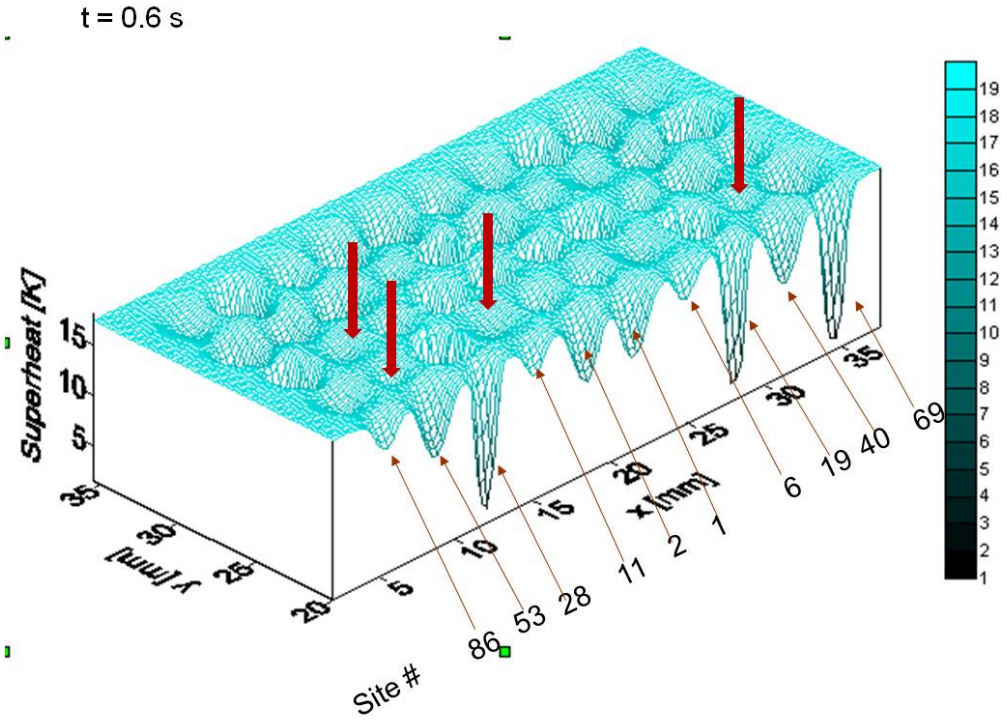

Figure 6-38: 2-dimensional superheat distribution

Activity of the sites

Figure 6-39 shows the total activity (for $t > 0.5$ s) of the sites, with the graphical visualization (a) and depending on the site identification number (b). Both the figures highlight that the average activity is almost uniform over the entire surface, with just a small decrease towards the periphery of the substrate. The values range from ~ 34 activation/s at site #1 to ~ 29 activation/s at site #100. If only the large bubbles are considered (i.e. only those that reach at least half of the size of their nominal bubble departure value) the activity significantly drops Figure 6-39 (b), mostly for the sites with low identification number (i.e. those located in the central part of the substrate). In this case, activity values range from 18.4 activations/s at site #1 to 23.4 activations/s at site #100.

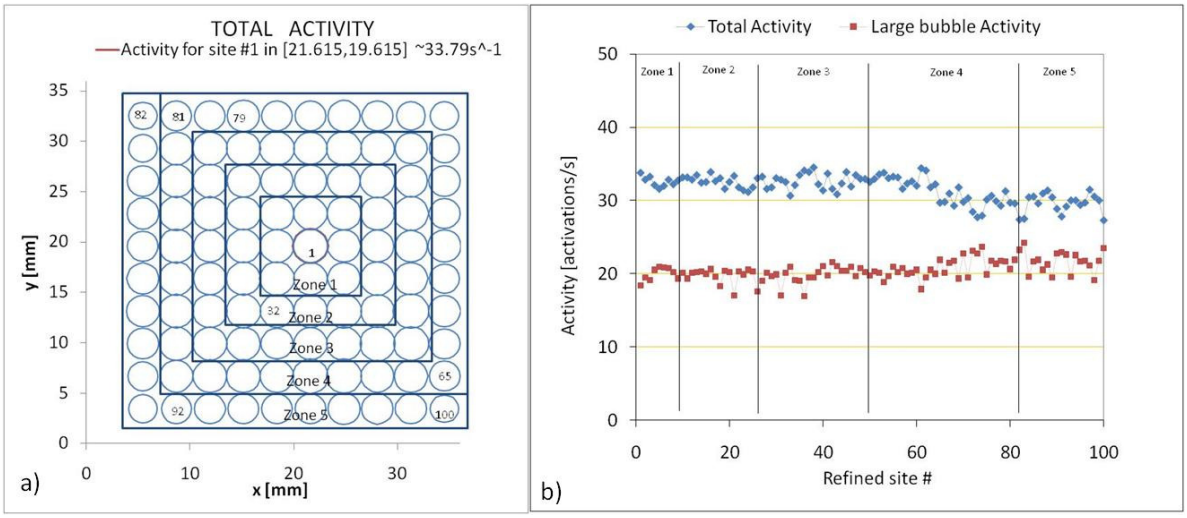

Figure 6-39: Total activity of the nucleation sites: a) spatial distribution; b) depending on the nucleation site identification number

Horizontal coalescence

The analysis of occurrence of horizontal coalescence shows that both coalescence types C1 and C2 occur almost uniformly across the entire surface, but while type C1 involves all the eight sites surrounding a specific one (apart for those located close to the edges of the site distribution), type C2 involves only the four closest sites, since the distance between the others is too large to allow this type of coalescence. Also in this case, as already mentioned before, it is important to specify that the models suggested for coalescence are crude and highly simplified and further studies are required to refine them. The frequency of occurrence of the two types of coalescence is summarised for the sites with identification number from #1 to #10 in Table 24 for type C1 and in Table 25 for type C2. As in the previous case for the silicon substrate, for type C1, the table is filled only in the upper triangle. The frequencies are comparable with those for silicon and uncertainty parameters = 10% (compare Table 21). For type C2 the frequencies are much smaller (compare Table 22), due to the absence of sequential coalescence. This phenomenon is connected to the waiting time, i.e. the time for the superheat to recover to the activation value after departure. For silicon, the superheat was always very close to the activation value, while for titanium the site may require several milli-seconds before the conditions for activations are again satisfied. This aspect is visible in Figure 6-40, events A and B: in the first case, after departure of a small bubble at site #1 due to coalescence, the site requires ~ 17 ms to become active again, while for event B the required time is ~ 11 ms. The difference depends on the size of the small departed bubble and on the superheat drop at the nucleation sites during its growth. At t ~ 9.9 s

(event C) it is possible to observe the coalescence type C2, when site #1 incorporates the bubble at site #4, and undergoes a large increase of the bubble radius and of the bubble growth rate.

Table 24: Coalescence type C1 frequencies for site #1 to #10

Coalescence type C1										
	#1	#2	#3	#4	#5	#6	#7	#8	#9	#10
#1		1.37	0.63	1.58	0.95	0.84	1.26	1.05	0.95	0
#2			1.68	1.26	0	0	0	0.74	1.26	0.53
#3				1.47	0	0	0	0	0	0
#4					0.53	0.63	0	0	0	0
#5						0.32	0	0	0	0
#6							0.74	1.05	0	0
#7								1.37	0	0
#8									1.68	0
#9										1.47

Table 25: Coalescence type C2 frequencies for site #1 to #10

Coalescence type C2										
	#1	#2	#3	#4	#5	#6	#7	#8	#9	#10
#1		14.12	0	10	0	14.12	0	15.88	0	0
#2	7.65		8.24	0	0	0	0	0	11.18	0
#3	0	10		15.88	0	0	0	0	0	0
#4	8.24	0	13.53		2.94	0	0	0	0	0
#5	0	0	0	7.06		7.65	0	0	0	0
#6	10	0	0	0	4.12		13.53	0	0	0
#7	0	0	0	0	0	12.35		7.65	0	0
#8	7.06	0	0	0	0	0	8.24		12.35	0
#9	0	13.53	0	0	0	0	0	10.59		9.41
#10	0	0	0	0	0	0	0	0	10.59	

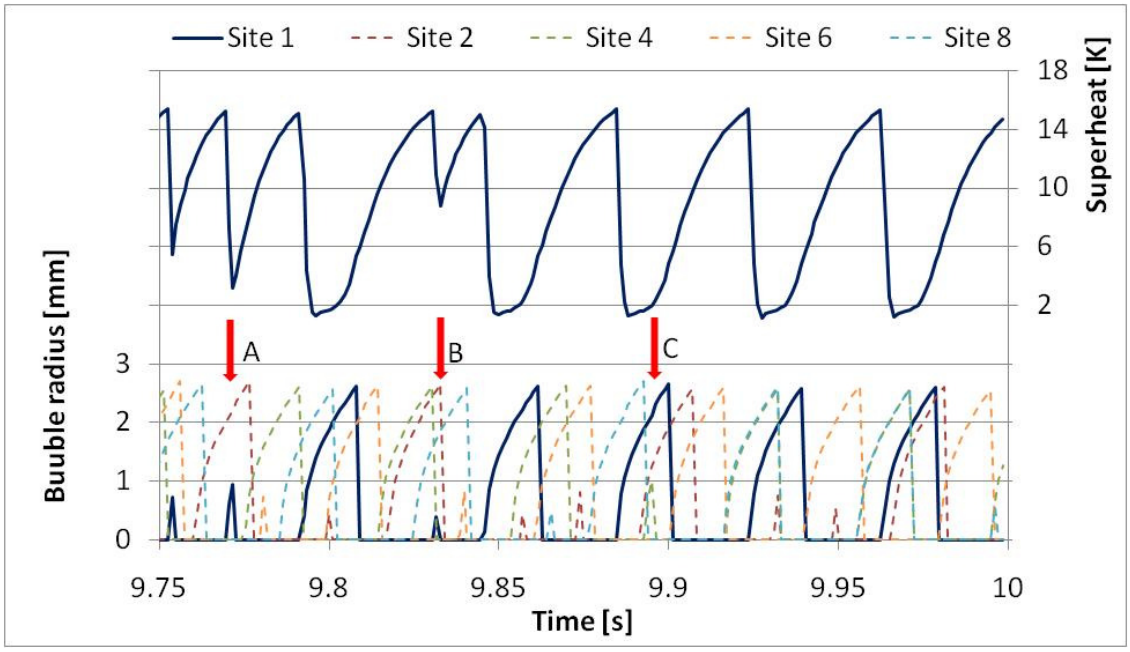

Figure 6-40: Bubble growth histories involving coalescence and superheat variations at Site #1 and the surrounding adjacent sites (#2, #4., #6, #8)

6.4.Summary

This section aimed to analyse the effects of a large distribution of nucleation sites, both on silicon (6 x 6 mm^2; 0.38 mm thick) and on titanium (36 x 36 mm^2; 25 µm thick) substrates. 100 refined nucleation sites were simulated in both cases. The analysis started with preparatory cases on silicon to study the effects of thermal interactions between a small number of sites (2, 3 or 4) and the effects of the arrangement of the sites on an intermediate number of nucleation sites (49). From this analysis, a square distribution of nucleation sites, with spacing between sites able to allow the two types of coalescence (C1 and C2, depending on the relative size of the coalescing bubbles) without interference of the mesh distribution ($S \sim 2x1.21r_{bd} = 2.42r_{bd}$) was chosen. This ratio was used for both simulations on silicon and on titanium. The input data for the bubble growth and activation of the sites were imposed equal to the values used in the validation process (Section 5.3.4) for a small number of nucleation sites, and assumed valid for a larger distribution. For silicon, two cases were studied: in the first case, the nominal values for bubble departure radius and activation superheat were imposed; for the second, these two parameters were randomly adjusted at each activation during the simulations with uncertainty parameters equal to 10% of the nominal values, in order to take into account possible uncertainties in measurements.

From the numerical point of view, simulations on silicon substrate were much faster (~ 12-15 hours per simulated second) with respect to the titanium case (~ 22 hours per simulated second), due to the smaller size of the substrate and to the smaller differences in superheat across the substrate in the first case.

From the physical point of view, a stronger thermal interaction between sites was recognisable for the silicon case, leading to lower average superheat around the nucleation sites for a large distribution of sites with respect to an isolated site. This led also to much larger growth times, due to the smaller heat flux contribution at the base of the bubble. Moreover, the superheat distribution across the substrate became flatter. On the contrary, for the titanium case all the sites appear to act more independently, and the superheat variations to be very similar between an isolated site and a large distribution. The growth times are also comparable.

This section showed that the code is able to deal with completely different conditions, ranging from a very thin metal substrate (titanium) with bubble radii equal to 2.665 mm to thicker non-metal substrate (silicon) with higher thermal capacity and bubble radii approximately 8 times smaller than in the previous case. The capacity of the code in adapting its mesh distribution and the ease in modifying correlations and conditions according to the different situations simulated make it a very powerful instrument to investigate thermal interactions despite of the simplicity of some of the models, as for instance the one for horizontal coalescence.

7. Conclusions

This study presented the main results obtained by a numerical code designed to reproduce and predict the superheat variations, the bubble growth and site activation for bubbles growing on the upper surface of a solid substrate horizontally immersed in a liquid at saturation conditions, with potential nucleation sites located at specified positions. The code is based on a hybrid approach, merging the complete 3-dimensional, time-dependent numerical solution for the temperature variation in the solid substrate with semi-empirical models for the bubble growth and heat transfer on its upper surface.

The code, rearranged from a numerical point of view in collaboration with Dr R. Nelson at Los Alamos Nuclear Laboratory in order to make it suitable for parallel computing, was also improved from the physical point of view according to theoretical studies and on the basis of experimental evidence, from results mainly produced at the Universities of Edinburgh and Ljubljana. Among the improvements, the code flexibility to reproduce a wider range of conditions was increased by introduction of two different heat transfer models applied to the base of the bubble. This made the code suitable to simulate both the micro-layer and contact line heat transfer models, according to different liquid to solid substrate materials couplings (although the choice of which model is to be used must be specified by the user). Other than the heat transfer models, the bubble growth was strongly refined with respect to the original version of the numerical code by the introduction of the simplified sub-models for the heat contribution at the dome of the bubble and for the bubble shape changes during the bubble growth according to the shrinking of the contact area during the detachment phase (always assuming a truncated sphere shape). Finally, two simple models to crudely take into account coalescence effects between two or more bubbles according to their relative sizes were introduced: those represented the first approach to consider interaction mechanisms on the liquid side.

The effects of the introduced modifications for FC-72 on a silicon substrate (0.38 mm thick) were studied via a sensitivity analysis with respect to a base case based on the experimental bubble growth (obtained as average value of eight different sequences

at the same experimental conditions) combined with the spatial average value of the superheat variation below the bubble over an area slightly larger than the bubble size. It was concluded that both the inclusion of a model for the heat contribution at the dome of the bubble and a model for shrinking of the bubble growth could significantly modify the bubble growth and therefore their contributions could not be neglected. In particular, an increase of the heat contribution at the dome of the bubble reduced the bubble growth rate during the first stage and increased it during the last stage of the bubble growth (if the bubble growth time was forced to match the experimental value). By contrast, the introduction of the shrinking of the bubble contact area during the last stage of the bubble growth reduced the evaporation contribution at the base and then the bubble growth rate during the last phase, so that it was increased during the first stage. Both the micro-layer and contact line heat transfer models were able to reproduce the correct bubble growth time, although the superheat variations at the nucleation site significantly differ in the two cases. Unfortunately, their variations were always lower than the maximum sensitivity of the sensors (±0.5 K) used during the experiments with FC-72 on silicon, so that the current sensors were incapable to follow the superheat variation at the specified experimental conditions. However, for different experimental conditions, as for instance Golobič et al. (2006) or Kiger and Moghaddam (2008), it was shown that the superheat variations may be much larger. The simulations of the variations over an area simulating the sensors (square shape, 0.84 mm long, located around the nucleation site) aiming at reproducing the experiment results at the University of Edinburgh were shown to be even smaller than variations at the nucleation site and very similar for the two heat transfer coefficient models. Numerical results clearly predicted the impossibility for the current experimental instrumentation to measure superheat variation during the bubble growth, so that further investigation in this area with the current experimental facilities seems to be unable to provide more detailed information.

The sensitivity analysis also investigated the effect of changes in the main input data: according to that, it was concluded that the only significantly influent datum was the activation superheat, although its variations was limited to value always larger than the theoretical superheat necessary for activation (so that no waiting time was expected). Its increase led to a more uniform bubble growth rate, while the other analysed input data (i.e. the initial value of the apparent contact angle, the heat transfer model at the base of the bubble and the use of standard or unrefined sites) did not

significantly alter the bubble growth history, if the experimental growth time was forced to be matched.

The capability of the code to adapt to different experimental conditions (i.e. variable input heat flux at the bottom of the substrate leading to different measured average superheat and bubble departure radii) was proved, although the heat transfer coefficients below the growing bubbles needed to be tuned to match the average bubble growth times. The comparison of numerical results for FC-72 on silicon for the validation process with the experimental results (produced at the University of Edinburgh) showed that the code is able to reproduce the bubble growth rate and superheat variation for five experimental cases. An analysis of the superheat variation at a fixed isolated nucleation site for a case at sub-atmospheric pressure for a long observation time (~ 4 s) showed that the code is able to reproduce well transient superheat variations, provided that the irregularity in activation experimentally observed (leading to long terms periods of regular activity alternating with others of total inhibition, both of the order of seconds) is imposed by the user during simulations. Moreover, a comparative analysis was also carried out for thin metal foils (titanium, 25 µm and platinum, 6 µm thick) immersed in saturated water at atmospheric pressure conditions for the validation process, in order to reproduce the experimental results produced at the University of Ljubljana. An impressive similarity in the dimensionless heat transfer coefficients at the nucleation sites versus dimensionless growth times was discovered here for the first time, very surprising due to the essentially different characteristics of the two substrates in properties and thickness. The application of a correlation obtained according to these experimental data to numerical cases based on the micro-layer model (this time without tuning of the heat transfer coefficients at the base of the bubble, replaced by tuning of the heat evaporation contribution at the dome) showed a very good agreement when the superheat variations (of the order of 15 K, much larger than in the case for silicon on FC-72) and heat flux variations were compared. The analysis of results for a distribution of 100 potential nucleation sites allowed concluding that the substrate-liquid combination strongly affects the variation of superheat and the relative influence area. The distance between nucleation sites was chosen comparable to the bubble departure radius (the heat transfer coefficient data from the single bubble growth obtained during the validation process for both the cases of silicon on FC-72 and titanium on water were assumed still applicable). It was shown that for titanium in water the superheat variation was very similar to the single bubble

case. By contrast, for silicon on FC-72 the average superheat at the nucleation site dropped from ~ 8 K for the single bubble case to ~ 1 K (and then comparable to the activation superheat) for the large distribution.

A further conclusion that was reached was that uncertainties in the input data and the possibility of occurrence of coalescence may play a very important role in the regularity of activation of the sites and the growth of the bubbles. In fact, a significantly different behaviour was observed for the case of silicon on FC-72 whether the nominal values for activation superheat and bubble departure radii were used or not. The introduction of uncertainty parameters to correct the nominal values, randomly chosen each time a site became active, introduced differences in the average activity of the sites, which all acted in phase in the case of nominal input data instead. This was due mainly to the variable maximum contact area radii (due to the variable bubble departure radii when uncertainty parameters were used) which may lead to mesh refinement limitations and occurrence of horizontal coalescence between bubbles of significantly different sizes (which did not occurred in the previous case and that is the only one of the two considered sub-models for coalescence that produces effects on the bubble growth of two adjacent bubbles). This suggests that this phenomenon cannot be neglected: further studies are required to refine the current crude model, also according to experimental findings. Considering the case when the uncertainty parameters were used, the site activation frequency was not uniform for all the sites over the whole surface, showing a distribution with alternating more active sites.

The case of titanium on water, only developed for the nominal values (i.e. without taking into account the uncertainty parameters), showed a completely different behaviour: in this case the sites lost regularity in activation after only few activation cycles. Activation in clusters seemed to occur, although the final average activation frequency was similar for all the sites. Both type of coalescence occurred in this case, although for the type for dissimilar sizes the frequency was greatly smaller than for the case of silicon on FC-72.

Summarising, it can be concluded from this analysis that the code is able to simulate very different conditions for the single bubble growth or a small number of sites, as a thin metal foil on water against a non-metallic thicker substrate on a dielectric liquid, with significantly different bubble departure sizes and superheat variations. Some uncertainties in simulations were shown, arising from numerical procedures adopted to reduce the computational time: these might be eliminated by calculations on

a large cluster of parallel computers with an increased level of detail of the mesh distribution. Comparison of experimental and numerical results for bubble growth and superheat variations showed a good agreement. Moreover, it was shown that the code is able to simulate large distributions of nucleation sites, as required by the original objectives of this project, although an experimental validation of the results was not possible because of lack of time in the construction of a new test section and successive comparison with results from simulations. Further studies in this area could significantly contribute to the understating of the interaction phenomena between nucleation sites in order to shed light on the complex nucleate boiling phenomena.

8. Discussion and Future work

This chapter aims to analyse some of the key points of the nucleate boiling heat transfer process according to how they have been faced during this PhD project and draw some guidelines for future developments and improvements. Particularly focus will be put on the following aspects:

- Heat evaporation at the dome of the bubble;
- Heat transfer model at the base of the bubble, and in particular the contact line model (as supported by Stephan and co-workers and experimentally observed by Kiger and Moghaddam, 2008), the micro-layer model (supported by results from Golobič and co-workers) and possibility of sliding bubble phenomena;
- Coalescence phenomena;
- Site activation, bubble departure and waiting time.

8.1. Heat evaporation at the dome of the bubble

Two main contributions can be accounted for the bubble growth. The first one is the evaporation at the base of the bubble and is mainly connected to the wall superheat. The second contribution is the heat transfer between the liquid and the bubble at the curved dome of the bubble. This model has a very long history from the beginning of the previous century: analytical models were suggested for hemispherical bubble growth on a wall in uniform and non-uniform temperature fields by Plesset and Zwick (1954), Cooper and Lloyd (1969) and others, as already analysed in Section 2.3. These models become inaccurate as the bubble centre develops motion away from the wall, so that numerical studies as the one suggested by Dhir (2001) became necessary. A complete simulation of the latter would require solution of the Navier-Stokes equations on the liquid and vapour sides. Several numerical models have been developed to take into account this contribution and most of them agree that this may provide a large contribution to the bubble growth, the importance mainly depending on the size of the bubble. Among others, Son et al. (1999) used boundary functions to simulate the bubble liquid-vapour interface and noted that the entity of the contribution at the dome depends on the bubble radius with respect to the thickness of thermal boundary layer. For small

radii, the bubble is still located inside the thermal boundary layer and evaporation occurs all around the bubble itself, as shown in Figure 8-1 (a). On the contrary, when the bubble grows out of the thermal boundary layer, only the heat provided through the portion around the bubble base is taken into account, as shown in Figure 8-1 (b). The figure shows the simulated bubble profile (as a function of the dimensionless radius r/l_0 and height y/l_0) and the isothermal lines at different dimensionless time steps (t/t_0), highlighting that the largest temperature gradient occurs in the proximity of the area where the bubble dome apparently meets the liquid and the solid wall, generally called triple contact line area. The Stephan model also assumes a heat contribution through the interface between liquid and vapour, simplified by a 2-dimensional heat conduction model in Stephan and Hammer (1994). The contribution was numerically shown to be significant for a bubble growing in propane/n-butane on a copper wall (Stephan et al., 2009). Neglecting this contribution as it occurred in the original model suggested by Golobič et al. (2004) may lead to overestimation of the heat flux at the bubble base and consequently to incorrect superheat variations in proximity of the bubble contact area. A simple semi-empirical model was instead introduced during this project (see Section 3.2.4). The model was based on the hypothesis that a thin liquid thermal layer (assumed at the activation temperature) constantly covers the bubble for the entire length of the

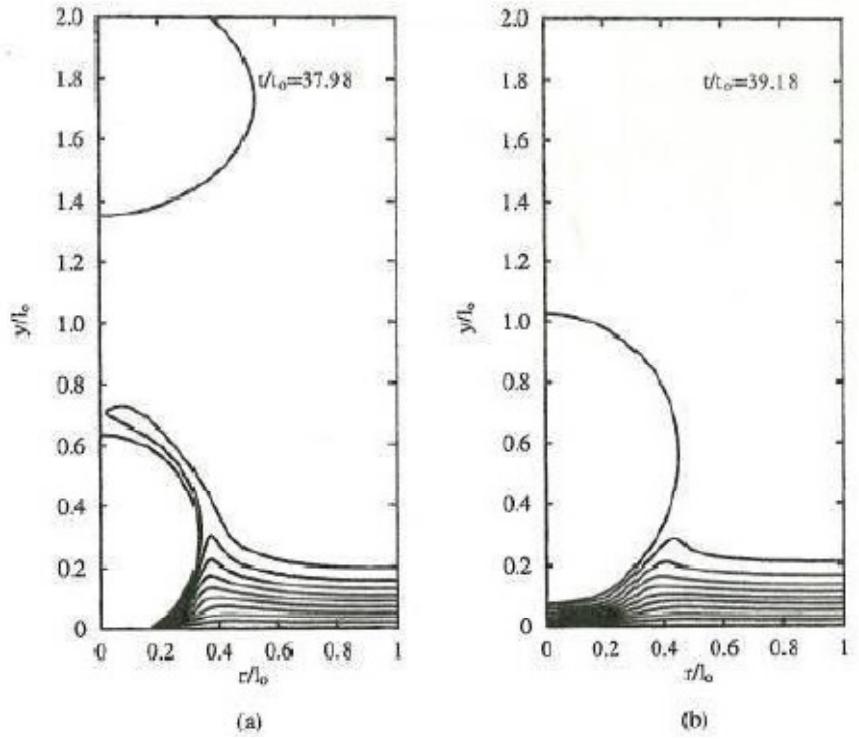

Figure 8-1: Bubble growth inside (a) and outside (b) the thermal layer (Son et al., 2008)

bubble growth causing a temperature gradient between the liquid and the vapour. Although crude, this led to very significant contributions to the bubble growth depending on the combination of the substrate-liquid characteristics. The bubble growth on metal foils analysed in Sections 5.3.4 and 6.3, with the radius of the bubbles larger than 1 mm in diameter is an important example of a numerical case where this contribution was fundamental. Also, heat evaporation at the dome was found of primary importance in varying the bubble growth rates for small bubbles growing on a silicon wafer immersed in FC-72 (Section 4.3.5). The availability of more accurate experimental results related to the bubble growth rates and possibly able to distinguish between the different heat contributions could provide the guidelines for the creation of a more refined semi-empirical model that may replace the existing one. A possible solution could take into account for instance the heat contributions at the different stages of the bubble growth and be based on the two sub-models, depending on the bubble size with respect to an empirical fixed liquid macro-layer thickness.

8.2. Heat transfer model at the base of the bubble

At the moment, two models are the most accredited for the heat transfer contribution at the base of the bubble. The first model is the contact line model, which has been strongly supported by the team led by P. Stephan (compare Stephan et al., 2006 and analysed here in more detail in Section 4.3.6). This model assumes that the bubble is growing with the apparent shape of a truncated sphere. In the area where the bubble dome undergoes a large variation in the curvature (apparently defining the bubble contact area), a high heat transfer coefficient contribution is supposed, as schematically shown in Figure 8-2 (a). In the inner area, a small heat transfer contribution from the substrate to the bubble growth is assumed, due to the presence of an absorbed film. This phenomenon has been experimentally observed by Kiger and Moghammed (2008), for a silicon substrate (60 μm thick) immersed in FC-72 at atmospheric pressure, for very high substrate superheats (~ 20-30 K).

Large superheat variations (~ 10-20 K) have been observed at the triple contact line area measured by a series of sensors radially disposed around the nucleation site, corresponding to large heat flux peaks (~ 200-400 kW/m^2). This model is in contrast with the micro-layer model supported by the team led by Golobič (compare for instance Golobič et al., 2006 and 2009), based on experimental measurements of the temperature variations on the back of very thin metal foils (6 or 25 μm) by using an Infra-Red high speed camera. For this model, the numerical elaboration of the experimental superheat data allowed deriving the heat flux and heat transfer coefficient distributions between the foil and the liquid or the bubble. According to their results, the heat flux presents a crater-shape distribution with its maximum in proximity of a circular area corresponding to the triple contact line. On the contrary, the heat transfer coefficient presents a central peaked distribution that decreases towards the triple contact line annular region, as schematically shown in Figure 8-2 (b). The micro-layer model supposes that a liquid film is constantly trapped between the vapour dome and the solid substrate, its thickness decreasing towards the centre of the contact area. Criticisms have been moved in Stephan et al. (2009) to the experimental data supporting this model, inferring that since the effect of errors in measurements was not analysed, the accuracy of the description of the model could not be verified.

Whether the contact line or micro-layer models is the model that most likely describes the mechanism has not been determined yet, but it is likely that both models are possible depending on the characteristics of the bubble nucleation and growth and consequently on the characteristics of the substrate, liquid and their coupling. Kenning

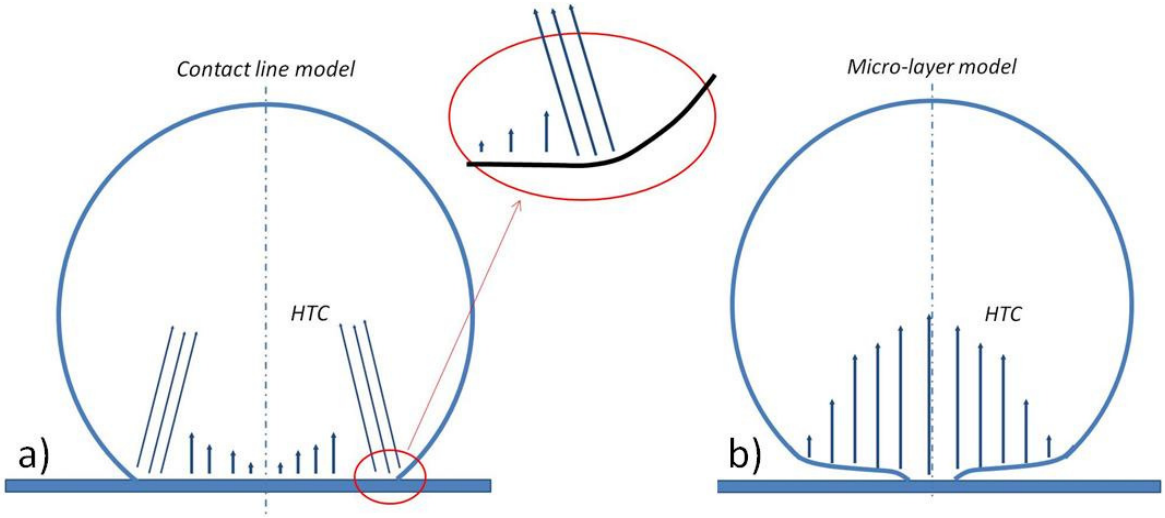

Figure 8-2: Contact line (a) and micro-layer (b) model schematics

(1999), reviewing the models proposed by Chester (1978), inferred that the two competitive models seem to be reasonable for similar conditions, depending on how the surface is treated before the experiments. In particular, the role of wettability was analysed: the use of the same surface and refrigerating liquid could not guarantee similar bubble growth phenomena if the method by which the surface was polished was changed. This could lead for instance to small bubbles generated at high frequency rather than large bubbles at low frequency. Moreover, it was shown during this study that the two different models could be applied to different conditions obtaining a good agreement. However, due to a lack of experimental evidence in the analysed results, further investigation is required to determine to which conditions each model may be applied.

Further uncertainty in the choice of the model is generated by experimental observation of sliding bubbles (Golobič et al., 2009), schematically shown in Figure 8-3. If the contact line model was assumed, the dry area supposed below the bubble (since direct contact between vapour and substrate was assumed) would make it unlikely for the bubble contact area to easily deform or move. On the contrary, for the micro-layer model, the presence of the liquid layer could facilitate deformation of the shape. Eventually, the bubble could completely detach from the nucleation site because of the combined effect of fluid movements and change in curvature. In that case, the micro-layer model could be considered as an intermediate stage leading to a sliding bubble.

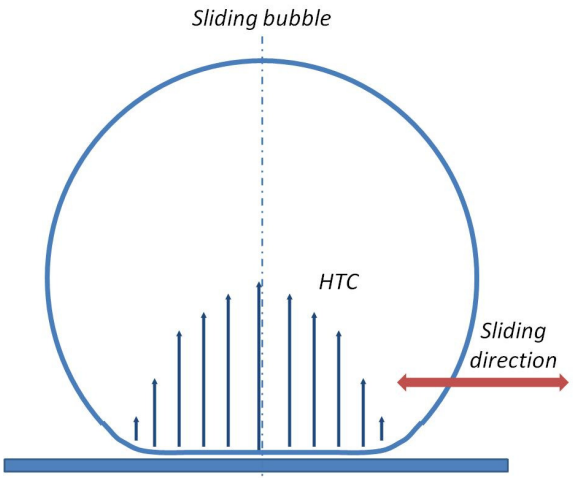

Figure 8-3: Sliding bubble

However, if the contact line model seems to be less appropriate to describe this bubble growth scenario, the micro-layer model presents inconsistencies that still must be explained. Supposing that the heat contribution at the bubble base is due to evaporation of the thin micro-layer, the thickness of the micro-layer should decrease with time. This would lead to an increase of the heat transfer coefficients with time. Instead, analysis of experimental data proposed by Golobič et al. (2006 and 2009) and elaborated in Section 5.3.4 showed that, despite the fairly very different substrate characteristics in the two examples analysed, the scaled heat transfer coefficients at the centre of the contact area assume very similar increasing-decreasing behaviours (Figure 5-11), with very low values during the final stages of the bubble growth.

Another aspect that should be considered for both the models is whether a dry zone is present in the inner part of the contact area, and which fraction of the apparent contact area it covers. Here, a zero heat transfer coefficient due to the direct contact of vapour with the substrate wall should be observed. The presence of a low but not zero heat flux would instead indicate the presence of liquid traces. This aspect has been recently reviewed by Kenning et al. (2009), by comparison of the experimental results for the two models (Golobič et al., 2006 and 2009 in support of the micro-layer model and Wagner et al., 2007 in support of the contact line model). However, it was pointed out in this study that uncertainties in measurements and in the definition of the input data (as for instance the input heat source) are too large to definitely exclude one or the other possibility.

In Chapter 4, Section 4.2.6, a comparison of the two models applied to a silicon substrate was carried out, showing that the evaporation model at the base of the bubble do not significantly affect the superheat distribution outside the contact area and the bubble growth conditions. However, a complete different behaviour should be expected for thin metal layers, due to the lower thermal capacity of the substrate. The application of two models has been analysed during this PhD project in particular in Chapter 5 (for the validation of the model) and in Chapter 6 (for the study of the effects of thermal interactions between sites for a large distribution of nucleation sites). The micro-layer model was applied to the simulations of thin metal foils (6 or 25 μm thick) immersed in water, while the contact line model was applied to a significantly thicker silicon wafer (380 μm thick) immersed in FC-72.

An improvement of the present models could be made in order to take into account possible conditions leading to bubble sliding phenomena, for instance by evaluation of the forces balance or of the superheat variation below the growing bubble.

8.3. Coalescence

8.3.1. Horizontal coalescence

Horizontal coalescence has been proved to have a very important role in the heat transfer mechanisms and bubble activity for bubbles growing at close distance. At present, several models have been developed to take into account this phenomenon, but they mostly focus on high heat fluxes conditions leading to stems production. The phenomenon has been extensively studied: among others, Zhang and Shoji (2003) experimentally confirmed the occurrence of horizontal coalescence for distance between nucleation sites to bubble departure diameter ratio (S/D_{bd}) lower than 1.5. Similar results were recently obtained by Hutter (2009) for bubbles growing on a silicon substrate (0.38 mm thick) immersed in FC-72 at a pressure of 0.5 bar, and distance between the nucleation sites equal to 0.84 mm. The frequency of occurrence strongly increased with the average wall superheat, with a maximum of 60 Hz for wall superheat of ~ 12.5 K.

A crude model for horizontal coalescence has been introduced in the numerical model used for simulations during this PhD project. This includes two sub-models depending on the relative size of the coalescencing bubbles. The model has been shown to have a large effect on the results. In particular, from the numerical point of view, the occurrence of alternate bubble growing at adjacent sites due to mesh restrictions was reduced. From the heat transfer point of view, occurrence of coalescence led to smaller average superheat variations in the area around the nucleation sites during the bubble growth for bubbles of significantly different sizes, as shown in Section 6.2.1 for silicon in FC-72. This was due to the combined effects of a higher bubble departure frequency and of the presence of two (or more) bubbles growing at close distance. These results showed that despite the simplicity of the used model, this phenomenon could strongly affect the nucleation site activity and superheat variations. A clearer understanding of the phenomena involved in this process could greatly help in the definition and introduction of a simplified but more accurate model that could refine or replace the present one.

8.3.2. *Vertical and declining coalescence*

Vertical and declining coalescence have been described in Section 2.8. Their contributions have not been included in the present model because the phenomena involve an already departed bubble interacting with one still attached to the heated wall. The process was believed to have little effect on the heat transfer mechanisms in proximity of the substrate wall for the area previously occupied by the already detached bubble. Stronger effects are expected on the bubble still growing at the substrate wall, such as modification of the bubble departure radius and increase in the activity of the site. Moreover, occurrence of vertical coalescence is expected to be less likely for thin metal foils if not at high heat fluxes, contrarily to what happens for silicon substrates, due to the high thermal capacity and to the average high superheat (that lead to very short or zero waiting times). Recently, Hutter (2009) and Hutter et al. (2009) described the effects of occurrence of vertical coalescence on bubble growing on a silicon substrate (0.38 mm thick) immersed in FC-72 at variable pressures (0.5, 0.75 and 1.0 bar) with applied heat flux of 4.8 kW/m^2 corresponding to an average superheat of 7.9 K. A schematic representation of the phenomenon is shown in Figure 8-4. After a first bubble (V_{top}) has departed, a second one immediately nucleates at the same site (V_{bot}) and the two coalesce in the vertical direction in one larger bubble (V_{coal}). The time scale for the bubble growth and the volumes depend on the average wall superheat. Shorter bubble growth times were observed following vertical coalescence, with the second bubble pulled away from the surface at much smaller bubble departure radii than the first one. A strong variation in bubble departure radii could lead to significantly different heat fluxes at the contact area. Should it happen, the superheat distribution could be affected. However, from analysis of simulation results described in Section 0, the superheat variation always assume very small values, so that at the considered

Figure 8-4: Vertical coalescence, schematic representation (Hutter, 2009)

conditions the variations would be undetectable with the sensors used at present at the University of Edinburgh (Hutter et al., 2009).

A simple modification of the model could be achieved by modification of the bubble departure radius for succeeding bubbles, assuming alternate large and small values according to experimental results. The drawback would be the necessity of introduction of a further semi-empirical model to take into account the lifting of the departed bubble.

8.4.Site activation, bubble departure and waiting time

The present model assumes that in normal conditions a bubble departs when its radius reaches a fixed value (if coalescence does not occur) called bubble departure radius. In this case, the shape at departure is almost a perfect sphere with an approximately zero contact area radius. Natural convection conditions are immediately restored following departure of the bubble. Then, if the superheat at the nucleation site is higher than the activation superheat imposed and if there are no mesh limitations (due to the presence of other nucleation sites in the region surrounding the specific site), a new bubble nucleates. In the other case, the superheat has to locally recover to allow nucleation, so that a non-zero waiting time (i.e. the time elapsed between departure of the first bubble and nucleation of the new one) is detected. An example of the first type of events was shown for simulations (described in Section 5.3.2) reproducing the bubble growth on FC-72 on Silicon experimentally observed in Hutter (2009). On the other hand, the presence of significant waiting times was detected in simulations reproducing the experiments on thin metal foils immersed in water developed by Golobič et al. (2006 and 2009), as described in Section 5.3.4, although the simulated waiting times were significantly shorter than in the experiments. The value of superheat at the departure of the bubble is strongly connected to vertical coalescence. However, in simulations, the model does not currently take into account the effects of possible temperature gradients in liquid and solid fields at departure of the bubble. Possible alternative solutions could be studied both for the activation and departure mechanisms and for the heat transfer conditions following the bubble departure. For instance, the activation of the sites could be supported by more specific conditions on the superheat gradient other than on its absolute value, while the departure mechanisms could be based on the balance of the forces acting on the growing bubble. Regarding the heat transfer conditions during the waiting time, a model to take into account the sudden

contact of the hot wall with cold liquid in the area previously covered by the bubble contact area could be introduced in order to replace the natural convection conditions now immediately restored after bubble departure.

8.5.Numerical aspects

From the numerical point of view, the code still presents some weaknesses. It has been highlighted that in some cases (as for instance for coalescence phenomena in Section 6.2.2 or the missed activation of site #100 described in Section 6.2.1) the order in which the nucleation sites have been identified may affect the final results. Moreover, the effect of numbering on the activation for close-spaced sites has been analysed in Section 3.2.3, highlighting the possibility of having numerical alternating bubble growth. The problem cannot be completely eliminated, although the new method introduced for the mesh refinement can significantly limit its consequences by using a larger number of intermediate refinement steps, n_{cR}. In this case, interference between refined cells will be limited, but the increase of n_{cR} would lead to significantly higher computational times.

A further improvement to the code could be the introduction of a procedure that randomly selects the site order at each time step. The use of this procedure would be useful for a large number of nucleation sites, where it is necessary the simulation of close spaced sites otherwise limited by the presence of adjacent already growing bubbles.

A last improvement would be the introduction of a procedure that selects the position of the sites randomly or according to a specific distribution (for instance the Poisson or Normal distribution). This would allow extending the use of the code from a distribution of sites with specified positions (representing artificial micro-cavities) to industrial substrates, in which the position and characteristics of the cavities depend on the finish of the surface and they are generally not evaluable if not statistically.

9. References

3M. 2006. Speciality Materials, Fluorinert Liquid FC-72, Product information.

Abonyi, J. and Feil, B. 2007. Cluster analysis for data mining and system identification. Birkhäuser Basel

Bankoff, S.G. 1958. Entrapment of gas in the spreading of a liquid over a rough surface. *A.I.Ch.E.*, Vol. 4, pp 24-26

Basic, S., Skerget, L. and Hozjan, S. May 2006. Hydrodynamics of partial nucleate boiling by PIV technique. *ECI International Conference on Boiling Heat Transfer*, Spoleto

Benjamin, R.J. and Balakrishnan, A.R. 1996. Nucleate pool boiling heat transfer of pure liquid at low to moderate heat fluxes. *International Journal of Heat and Mass Transfer*, Vol. 39, pp 2495-2504

Benjamin, R.J. and Balakrishnan, A.R. 1997. Nucleation site density in pool boiling of saturated pure liquids: effect of surface microroughness and surface and liquid physical properties. *Experimental Thermal and Fluid Science*, Vol. 15, pp 32-42

Calka, A. and Judd, R.L. 1985. Some aspects of the interaction among nucleation sites during saturated nucleate boiling. *International Journal of Heat and Mass Transfer*, Vol. 28, pp 2331-2342

Chai, L.H., Peng, X.F. and Wang, B.X. 2000. Nonlinear aspects of boiling systems and a new method for predicting the pool nucleate boiling heat transfer, *International Journal of Heat and Mass Transfer*, Vol. 43, pp 75-84

Chaptun, S., Watanabe, M. and Shoji, M. 2004. Nucleation site interaction in pool boiling on a heated surface with triple artificial cavities. *International Journal of Heat and Mass Transfer*, Vol. 47, pp 3583-3587

Chekanov, V.V. 1977. Interaction of centers in nucleate boiling. *Teplofizika Vysokikh Temperature*, Vol. 15, pp 121-128

Chen, T. and Chung, J.N. 2002. Coalescence of bubbles in nucleate boiling on microheaters. *International Journal of Heat and Mass Transfer*, Vol. 45, pp 2329-2341

Chesters, A.K. 1978. Modes of bubble growth in the slow-formation regime of nucleate pool boiling. *International. Journal of Multiphase Flow*, Vol. 4, pp 279-302

Chopra, A. 1992. Interaction of bubbles forming at adjacent nucleation sites. M. Eng. Thesis, McMaster University, Canada

Cooper, M.G. 1969. The microlayer and bubble growth in nucleate pool boiling. *International Journal of Heat and Mass Transfer*, Vol. 12, pp 915-933

Cooper, M.G. 1984. Heat flow rates in saturated nucleate pool boiling – a wide ranging examination using reduced properties. *Advanced in Heat Transfer*, Vol. 16, pp 157-239

Cooper, M.G. and Lloyd, A.J.P. 1969. The microlayer in nucleate pool boiling. *International Journal of Heat and Mass Transfer*, Vol. 12, pp 895-913

Demiray, F. and Kim, J. 2004. Microscale heat transfer measurements during pool boiling of FC-72: effect of subcooling. *International Journal of Heat and Mass Transfer*, Vol. 47, pp 3257-3268

Dhir, V.K. 2001. Numerical simulations of pool-boiling heat transfer. *A.I.Ch.E. Journal*, Vol. 47, pp 813-834

Dhir, V.K. 2006. Mechanistic prediction of nucleate boiling het transfer – Achievable or a hopeless task?. *Journal of Heat Transfer - Transactions of ASME*, Vol. 128, pp 1-12

Eddington, R.I, Kenning, D.B.R. and Korneichev, A.I. 1978. Comparison of gas and vapour bubble nucleation on a brass surface in water. *International Journal of Heat and Mass Transfer*, Vol. 21, pp 855-862

Eddington, R.I. and Kenning, D.B.R. 1979. The effect of contact angle on bubble nucleation. *International Journal of Heat and Mass Transfer*, Vol. 22, 1231-1236

Engelberg-Forster, K. and Greif, R. 1959. Heat transfer to a boiling liquid – mechanism and correlations. *Journal of Heat Transfer - Transactions of ASME*, Vol. 81, pp 43-53

Forest, T.W. 1982. The stability of gaseous nuclei at liquid-solid interfaces. *Journal of Applied Physics*, Vol. 53, pp 6191-6201

Forster, H.K. and Zuber, N. 1954. Growth of a vapour bubble in a superheated liquid. *Journal of Applied Physics*, Vol. 25, No. 4, pp 474-478

Forster, H.K. and Zuber, N. 1955. Dynamics of vapour bubbles and boiling heat transfer. *A.I.Ch.E. Journal*, Vol. 1, No. 4, pp 531-535

Gerasimov, D.N., Kondratyeva, V.A., Rudavina, M.N. and Sinkevich, O.A. May 2006. False chaos in boiling. *ECI International Conference on Boiling Heat Transfer*, Spoleto

Golobič, I. and Gjerkeš, H. 2001. Interactions between laser-activated nucleation sites in pool boiling. *International Journal of Heat and Mass Transfer*, Vol. 44, pp 143-153

Golobič, I. and Gjerkeš, H. 2002. Measurement of certain parameters influencing activity of nucleation sites in pool boiling. *Experimental Thermal and Fluid Science*, Vol. 25, pp 487-493

Golobič, I., Bašelj, M., Papez, A., Petkovsek, J. and Kenning, D.B.R. August 2006. Bubble coalescence in pool boiling on a thin foil investigated by high-speed IR thermography. *13th International Heat Transfer Conference*, Sydney

Golobič, I., Pavlovič, E., Hardenberg, J., Berry, M., Nelson, R.A., Kenning, D.B.R. and Smith, L.A. 2004. Comparison of a mechanistic model for nucleate boiling with experimental spatio-temporal data. *Trans IChemE*, Vol. 82, pp 435-444

Golobič, I., Pavlovič, E., Strgar, S., Kenning, D.B.R. and Yan, Y. 1996. Wall temperature variations during bubble growth on a thin plate: computation and experiments. *Eurotherm seminar No.48*, pp.25-32

Golobič, I., Petkovsek, J., Bašelj, M., Papez, A. and Kenning, D.B.R. 2009 Experimental determination of transient wall temperature distributions close to growing vapor bubbles. *Heat and Mass Transfer*, Vol. 45, pp 857-866

Guo, Z. and El-Genk, M.S. 1994. Liquid microlayer evaporation during nucleate boiling on the surface of a flat composite wall. *International Journal of Heat and Mass Transfer*, Vol. 37, No. 11, pp 1641-1655

Haider, S.I. and Webb, R.L. 1997. A transient micro-convection model of nucleate pool boiling. *International Journal of Heat and Mass Transfer*, Vol. 40, pp 3675-3688

Han, C.Y. and Griffith, P. 1965a. The mechanism of heat transfer in nucleate pool boiling - part I. *International Journal of Heat and Mass Transfer*, Vol. 8, pp 887-904

Han, C.Y. and Griffith, P. 1965b. The mechanism of heat transfer in nucleate pool boiling - part II. *International Journal of Heat and Mass Transfer*, Vol. 8, pp 905-913

Hardenberg, J., Kenning, D.B.R., Xing, H. and Smidth, L.A. 2004. Identification of nucleation site interactions. *International Journal of Heat and Fluid Flow*, Vol. 25, pp 298-304

Hardenberg, J., Kono, T., Kenning, D.B.R., McSharry, P.E. and Smith, L.A. August 2002. Identification of boiling nucleation sites by non-orthogonal empirical functions (NEF) analysis of thermographic data. *Proceedings of the 12th International Heat Transfer Conference*, Grenoble, Vol. 3, pp 377–382

He, Y., Shoji, M. and Maruyama, S. 2001. Numerical study of high flux pool boiling heat transfer. *International Journal of Heat and Mass Transfer*, Vol. 44, pp 2357-2373

Hsu, Y.Y. 1962. On the size range of active nucleation cavities on a heating surface. *Journal of Heat Transfer - Transactions of ASME*, Vol. 84, pp 207-216

Hutter, C. 2009. Experimental Pool Boiling Investigation of FC-72 on Silicon with Artificial Cavities, Integrated Temperature Micro-Sensors and Heater, Ph.D. Thesis, The University of Edinburgh, Edinburgh, UK

Hutter, C., Cummins, G., Lin, H., Karayiannis, T.G., Kenning, D.B.R., Sefiane, K. and Walton, A.J. September 2009, *ECI International Conference on Heat Transfer and Fluid Flow in Microscale*, Whistler, Canada

Ivey, H.J. 1967. Relationships between bubble frequency, departure diameter and rise velocity in nucleate boiling. *International Journal of Heat and Mass Transfer*, Vol. 10, pp 1023-1040

Judd, R.L. 1988. On nucleation site interaction. *Journal of Heat Transfer - Transactions of ASME*, Vol. 110, pp 475-478

Judd, R.L. and Chopra, A. 1993. Interaction of the nucleation processes occurring at adjacent sites. *Journal of Heat Transfer - Transactions of ASME*, Vol. 115, pp 955-962

Judd, R.L. and Hwang, K.S. 1976. A comprehensive model for nucleate pool boiling heat transfer including microlayer evaporation. *Journal of Heat Transfer - Transactions of ASME*, Vol. 98, pp 623-629

Judd, R.L. and Lavdas, C.H. 1980. The nature of nucleation site interaction. *Journal of Heat Transfer - Transactions of ASME*, Vol. 102, pp 461-464

Kern, J. and Stephan, P. 2003. Theoretical model for nucleate boiling heat and mass transfer of binary mixtures. *Journal of Heat Transfer - Transactions of ASME*, Vol. 125, pp 1106-1115

Kenning, D.B.R. 1992. Wall temperature patterns in nucleate boiling. *International Journal of Heat and Mass Transfer*, Vol. 35, pp 73-86

Kenning, D.B.R. and Yan, Y. 1996. Pool boiling heat transfer on a thin plate: features revealed by liquid crystal thermography. *International Journal of Heat and Mass Transfer*, Vol. 39, pp 3117–3137

Kenning, D.B.R. September 1999. What Do We Really Know About Nucleate Boiling?. 6th UK National Heat Transfer Conference, Edinburgh, pp 143-167

Kenning, D.B.R., Kono, T. and Wienecke, M. 2001. Investigation of boiling heat transfer by liquid crystal thermography. *Experimental Thermal and Fluid Science*, Vol. 25, pp 219-229

Kenning, D.B.R., Golobič, I. and Petkovsek, J. September 2009. Pool boiling: global correlations and mechanistic studies. *UK National Heat Transfer Conference*, London

Kiger, K.T. and Moghaddam, S. September 2008. Microscale measurements and analysis of surface temperature and heat flux in single-bubble nucleate boiling of saturated fluorocarbon liquids. *ECI International Conference on Heat Transfer and Fluid Flow in Microscale*, Whistler

Kim, J., Huh, C. and Kim, M.H. 2007. On the growth of bubbles during saturated nucleate pool boiling at sub-atmospheric pressure. *International Journal of Heat and Mass Transfer*, Vol. 50, pp 3695-3699

Knowles, S. 1984. Interaction between bubble emission phenomena at adjacent nucleation sites. *Unpublished research, Mech. Eng. Dep.*, McMaster University

Koffman, L.D. and Plesset, M.S. 1983. Experimental observations of the microlayer in vapor bubble growth on a heated solid. *Journal of Heat Transfer - Transactions of ASME*, Vol. 105, pp 625-632

Lee, R.C. and Nydahl, J.E. 1989. Numerical calculation of bubble growth in nucleate boiling from inception through departure. *Journal of Heat Transfer - Transactions of ASME*, Vol. 111, pp 474-479

Levy S., 1959, Generalized correlation of boiling heat transfer. *Journal of Heat Transfer - Transactions of ASME*, Vol. 81, pp 37-42

Lorentz, J.J. 1972. The effects of surface conditions of boiling characteristics, Ph.D. thesis, Massachusetts Institute of Technology, Cambridge, Massachusetts

Mallozzi, R., Judd, R.L. and Balakrishnan, N. 2000. Investigation of randomness, overlap and the interaction of bubbles forming at adjacent nucleation sites in pool boiling. *International Journal of Heat and Mass Transfer*, Vol. 43, pp 3317-3330

McSharry, P.E., Ellepola, J.H., Hardenberg, J., Smidth, L.A., Kenning, D.B.R. and Judd, K. 2002. Spatio-temporal analysis of nucleate pool boiling: identification of nucleation sites using non-orthogonal empirical functions. *International Journal of Heat and Mass Transfer*, Vol. 45, pp 237-253

Mei, R., Chen, W. and Klausner, J.F. 1995a. Vapor bubble growth in the heterogeneous boiling –I. Formulation. *International Journal of Heat and Mass Transfer*, Vol. 38, pp 909-919

Mei, R., Chen, W. and Klausner, J.F. 1995b. Vapor bubble growth in the heterogeneous boiling –II. Growth rate and thermal fields. *International Journal of Heat and Mass Transfer*, Vol. 38, pp 921-934

Mikic, B.B. and Rohsenow, W.M. 1969. A new correlation of pool-boiling data including the effect of heating surface characteristics. *Journal of Heat Transfer - Transactions of ASME*, Vol. 91, pp 245-250

Mikic, B.B., Rohsenow, W.M. and Griffith, P. 1970. On bubble growth rates. *International Journal of Heat and Mass Transfer*, Vol. 13, pp 657-666

Mitrovic, J. 1998. The flow and heat transfer in the wedge-shaped liquid formed during the growth of a vapour bubble. *International Journal of Heat and Mass Transfer*, Vol. 41, 1771-1785

Moghaddam, S. and Kiger, K.T. 2009. Physical mechanisms of heat transfer during single bubble nucleate boiling of FC-72 under saturation conditions – I. Experimental investigation. *International Journal of Heat and Mass Transfer*, Vol. 52, pp 1284-1294

Moore, F.D. and Mesler, R.B. 1961. The measurement of rapid surface temperature fluctuations during nucleate boiling of water. *A.I.Ch.E. Journal*, Vol. 7, pp 620-624

Mosdorf, R. and Shoji, M. 2004. Chaos in nucleate boiling – nonlinear analysis and modelling. *International Journal of Heat and Mass Transfer*, Vol. 47, pp 1515-1524

Mosdorf, R. and Shoji, M. 2006. Temperature fluctuation at twin cavity in nucleate boiling – wavelet analysis and modelling. *International Journal of Heat and Mass Transfer*, Vol. 49, pp 3156-3166

Mukherjee, A. and Kandlikar, S.K. 2007. Numerical study of single bubbles with dynamic contact angle during nucleate pool boiling. *International Journal of Heat and Mass Transfer*, Vol. 50, pp 127-138

Myers, J.G., Yerramilli, V.K., Hussey, S.W., Yee, G.F. and Kim, J. 2005. Time and space wall temperature and heat flux measurements during nucleate boiling with constant heat flux boundary condition. *International Journal of Heat and Mass Transfer*, Vol. 48, pp 24289-2442

Nukiyama, S. 1934. The maximum and minimum values of the heat Q transmitted from metal to boiling water under atmospheric pressure. *International Journal of Heat and Mass Transfer*, Vol. 9, pp 1419-1433

Olek, S., Zvirin, Y. and Elias, E. 1990. Bubble growth predictions by the hyperbolic and parabolic heat conduction equations. *Wärme- und Stoffübertragung*, Vol. 25, No. 1, pp 17-26

Olsen, S.F., Martuzzi, M. and Elliot, P. 1996. Cluster analysis and disease mapping--why, when, and how? A step by step guide. *British Medical Journal*, Vol. 313, pp 863-866

Parker, J.L. and El-Genk, M.S. 2005. Enhanced saturation and subcooled boiling of FC-72 dielectric liquid. *International Journal of Heat and Mass Transfer*, Vol. 48, pp 3736-3752

Pasamehmetoglu, K.O. and Nelson, R.A. 1991. Cavity to cavity interaction in nucleate boiling: the effect of heat conduction within the heater. *A.I.Ch.E. Journal*, Vol. 87, pp 342-351

Pioro, I.L., Rohsenow, W. and Doerffer, S.S. 2004. Nucleate pool-boiling heat transfer. II: assessment of prediction methods. *International Journal of Heat and Mass Transfer*, Vol. 47, pp 5045-5057

Plesset, M.S. and Zwick, S.A. 1954. The growth of vapor bubbles in superheated liquids. *Journal of Applied Physics*, Vol. 25, No. 4, pp 493-500

Prosperetti, A. and Plesset, M.S. 1978. Vapour-bubble growth in a superheated liquid. *Journal of Fluid Mechanics*, Vol. 85, No. 2, pp 349-368

Qi, Y., Klausner, J.F. and Mei, R. 2004. Role of surface in heterogeneous nucleation. *International Journal of Heat and Mass Transfer*, Vol. 47, pp 3097-3107

Rohsenow, W.M. 1952. A method of correlating heat transfer data for surface boiling of liquids. *Journal of Heat Transfer - Transactions of ASME*, Vol. 74, pp 969-976

Sadasivan, P., Unal, C. and Nelson, R.A. 1993. MACRO3D, A Three-Dimensional finite volume computer code for the analysis of high heat-flux nucleate boiling. LA-UR-93-1835 (N-6-93-R101)

Sadasivan, P., Unal, C. and Nelson, R.A. 1995. Nonlinear aspects of high heat flux nucleate boiling heat transfer. *Journal of Heat Transfer - Transactions of ASME*, Vol. 117, pp 981-989

Shoji, M. and Takagi, Y. 2001. Bubbling features from a single artificial cavity. *International Journal of Heat and Mass Transfer*, Vol. 44, pp 2763-2776

Shoji, M., Zhang, L. and Chaptun, S. April 2005. Nucleation site interaction in pool nucleate boiling - Serial experiments using artificial boiling surfaces -. *6th World Conference on Experimental Heat Transfer, Fluid Mechanics, and Thermodynamics*¸ Matsushima, Miyagi

Shoukri, M. and Judd, R.L. 1978. On the influence of surface conditions in nucleate boiling – the concept of bubble flux density. *Journal of Heat Transfer - Transactions of ASME*, Vol. 100, pp 618-623

Son, G. and Dhir, V.K. 2008. Numerical simulation of nucleate boiling on a horizontal surface at high heat fluxes. *International Journal of Heat and Mass Transfer*, Vol. 51, pp 2566-2582

Son, G., Dhir, V.K. and Ramanujapu, N. 1999. Dynamics and heat transfer associated with a single bubble during nucleate boiling on a horizontal surface. *Journal of Heat Transfer - Transactions of ASME*, Vol. 121, pp 623-631

Son, G., Ramanujapu, N. and Dhir, V.K. 2002. Numerical simulation of bubble merger process on a single nucleation site during pool nucleate boiling. *Journal of Heat Transfer - Transactions of ASME*, Vol. 124, pp 51-62

Stephan, K. and Abdelsalam, M. 1980. Heat-transfer correlations for natural convection boiling. *International Journal of Heat and Mass Transfer*, Vol. 23, pp 73-87

Stephan, P. and Fuchs, T. May 2006. Local heat flow and temperature fluctuations in wall and fluid in nucleate boiling systems. *ECI International Conference on Boiling Heat Transfer*, Spoleto

Stephan, P. and Hammer, J. 1994. A new model for nucleate boiling heat transfer. *Wärme- und Stoffübertragung*, Vol. 30, pp 119-125

Stephan, P., Fuchs, T., Wagner, E. and Schweizer, N. May 2009. Transient local heat fluxes during the entire vapor bubble life time. *ECI International Conference on Boiling Heat Transfer*, Florianópolis

Stralen, S.J.D., Sohal, M.S., Cole, R. and Sluyter, W.M. 1975. Bubble growth rates in pure and binary systems: combined effect of relaxation and evaporation microlayers. *International Journal of Heat and Mass Transfer*, Vol. 18, pp 453-467

Sultan, M. and Judd, R.L. 1978. Spatial distribution of active sites and bubble flux density. *Journal of Heat Transfer - Transactions of ASME*, Vol. 100, pp 56-62

Sultan, M. 1981. Interaction of the nucleation phenomena at adjacent sites in nucleate boiling. Ph.D. Thesis, Mechanical Engineering Department, McMaster University. Hamilton, Canada

Sultan, M. and Judd, R.L. 1983. Interaction of the nucleation phenomena at adjacent sites in nucleate boiling. *Journal of Heat Transfer - Transactions of ASME*, Vol. 105, pp 3-9

Theofanous, T.G. and Patel, P.D. 1976. Universal relations for bubble growth. *International Journal of Heat and Mass Transfer*, Vol. 19, pp 425-429

Tong, L.S. and Tang, Y.S. 1997. *Boiling heat transfer and two-phase flow*, Washington, Taylor & Francis

Tong, W., Bar-Cohen, A., Simon, T.W. and You, S.M. 1990. Contact angle effects on boiling incipience of highly-wetting liquids. *International Journal of Heat and Mass Transfer*, Vol. 33, pp 91-103

Ünal, H.C. 1976. Maximum bubble diameter, maximum bubble growth time and bubble growth rate. *International Journal of Heat and Mass Transfer*, Vol. 19, pp 643-649

Wang, C.H. and Dhir, V.K. 1993a. Effect of surface wettability on active nucleation site density during pool boiling of water on a vertical surface. *Journal of Heat Transfer - Transactions of ASME*, Vol. 115, pp 659-669

Wang, C.H. and Dhir, V.K. 1993b. On the gas entrapment and nucleation site density during pool boiling of saturated water. *Journal of Heat Transfer - Transactions of ASME*, Vol. 115, pp 670-679

Weng,

Yang, S.R. and Kim, R.H. 1988. A mathematical model of the pool boiling nucleation site density in terms of the surface characteristics. *International Journal of Heat and Mass Transfer*, Vol. 31, pp 1127-1135

Zeng, L.Z., Klausner, J.F. and Mei, R. 1993. A unified model for the prediction of bubble diameters in boiling systems – I. Pool boiling. *International Journal of Heat and Mass Transfer*, Vol. 36, pp 2261-2269

Zhang, L. and Shoji, M. 2003. Nucleation site interaction in pool boiling on the artificial surface. *International Journal of Heat and Mass Transfer*, Vol. 46, pp 513-522